



**The influence of moisture on pyroclastic density current
dynamics and deposits: implications for understanding
volcanic stratigraphy**

being a thesis submitted in fulfilment of the
requirements for the degree of

Doctor of

Philosophy in Earth Science

at the University of Hull

by

Nemi Jessica Walding BSc (University of Plymouth)

May 2025

Acknowledgements

The past three years have been an incredible adventure. I've done more than I can imagine in terms of travelling, learning, and becoming a published scientist. None of these experiences would have been possible without my amazing supervisory team. Their confidence and support throughout my application process, my first-year tears and stress, my second-year adventures and escapades, my third-year panic-induced job applications, and my frenzied writing periods have been the backbone of my work.

Becky, thank you for your enthusiasm and wisdom. You're a massive inspiration to me as an academic parent and an awesome scientist. I'm beyond grateful for all our chats, from running ultramarathons to navigating academia and, of course, for your knowledge and impact on my research. Our weekly coffee chats have kept me sane and calm, and I am beyond grateful for your time.

Pete, thank you for adopting me into your home when completing lab work (thanks, Holly and Stanley!), introducing me to the best gyros in Bristol, using (and potentially destroying) your lab equipment and, of course, your knowledge and input. Your excitement is contagious, and I always leave a week of lab work feeling rejuvenated and beyond excited.

Natasha, thank you for keeping me sane! You've truly been a wonderful, calming presence throughout the whole process. Your knowledge of everything, but especially fieldwork (and **grammar** and spelling checks!!), has been instrumental to my work. I'm so glad to have been able to work with you both in Santorini and Tenerife. I especially miss our morning Tenerife swims (followed by copious amounts of churros).

To Dan and Anna – your support throughout this process is greatly appreciated. I am beyond grateful to you both for your input and enthusiasm for my project. To my Tenerife gang, Graham, Johnathan, Alex, and Maisy, each Tenerife trip is an absolutely wild ride. May we all drink barraquitos together again someday!

My office gang and friends, Luke (& Caitlin), Charlie and Lucia. It's been a pleasure spending the last 2 years crammed in an office with you, surrounded by dying plants and fueled by coffee and cake. Tom – thank you for putting up with me during first year. Our office wobbles and chats kept me stable, and I'm very grateful that I got to share my first year with you! Eamonn, Josh, Bobby – the Hull City Boozers. I

appreciate our outings to watch football, pilgrimages to Pave and trips to Propaganda. See you post viva, lads. Hal – cheers, lad, and have a Moretti on me like. To the absolute love of my life and best friend, Sarah. You are truly the best, most supportive and incredible friend a gal could ask for, I love you long time.

To my amazing Dad, thank you for your continued support (financially and mentally!). Don't worry; I won't get a normal job soon. To the rest of my family (Mum, Katie, John, Julianne, Grandma, Bill, Adrian and Pauline), thank you for always being there.

Abstract

Pyroclastic Density Currents (PDCs) are hazardous, multiphase currents of heterogeneous volcanic material and fluid. Moisture can enter a PDC system through internal (e.g., pre-eruptive) or through external processes during transport. Prior to this thesis, the impact of moisture on PDC systems has been largely overlooked, and the role of moisture on PDC behaviour, properties of pyroclastic materials and the resulting depositional architecture formed during PDC-forming eruptions has not been addressed. The work outlined in this thesis utilises geomechanical, geotechnical and analogue models alongside fieldwork observations to gain a better insight into the role and behaviour of moisture in PDC systems.

This work demonstrates that the addition of moisture into pyroclastic material alters the angle of repose, cohesion, and shear strength. This changes material properties from flowable to non-flowable and impacts the fluidisation profiles and gas escape structures formed. Further investigation of pyroclastic material using geotechnical equipment has shown that shear strength increases at low moisture contents and shear thickening behaviours occur at high moisture contents. This indicates that moisture-rich layers are more likely to resist shearing and be preserved in volcanic successions.

Characterisation of PDC deposits in Tenerife have revealed distinct erosional and remobilisation behaviours of flow-unit ash layers that are associated with varying moisture conditions. Additionally, experiments utilising a fluidised flume, and the sectioning of a ballotini current and substrate in gelatine, have allowed internal features to be observed. The addition of moisture to the substrate effectively suppressed erosion, remobilisation, and the formation of various features within the substrate.

These results are crucial for understanding flow unit architecture and estimating the frequency of PDC emplacement units during explosive eruptions. A greater understanding of PDC deposits and the processes that formed them is essential for improving our interpretation of current conditions and deposit formation which is essential for future hazard assessments.

Contents

Acknowledgements	i
Abstract	iii
Contents	iv
List of Figures	x
List of Tables	xvi
Glossary	xviii
Funding	xx
Chapter 1 Introduction	1
1.1 Research Approach	3
1.2 Research Questions and Objectives	5
1.3 Thesis outline and structure	5
Chapter 2 Literature Review	9
2.1 Physical Characteristics of PDCs	9
2.2 Dynamics in PDCs	10
2.3 Particle Formation and Characteristics	13
2.4 Interparticulate Forces	17
2.5 Sedimentation and deposition	19
2.6 Moisture in PDC Systems	21
2.6.1 The temperature problem and phase changes	25
2.6.2 The influence of moisture on industrial applications	27
2.6.3 Moisture influence on PDC flow and deposits	28
2.7 Modelling PDCs	29
2.7.1 Analogue Modelling of PDCs	29
2.7.2 Numerical Modelling of PDCs	31
2.8 Inspiration: Modelling cohesion in turbidity currents	32
2.9 Capillary Cohesion in PDC Modelling	34
2.10 Author's Perspective and Positionality	34

Chapter 3 : Cohesional behaviours in pyroclastic material and the implications for deposit architecture	36
3.1 Abstract	36
3.2 Introduction	36
3.2.1 Moisture in PDCs and their resulting deposits.....	38
3.2.2 Capillary cohesion.....	40
3.3 Methodology	41
3.3.1 Source material and sample preparation	41
3.3.2 Material characterisation and cohesive behaviour tests	42
3.3.3 Limitations	48
3.4 Results	49
3.4.1 Material properties	49
3.4.2 Fluidisation experiments	52
3.4.3 Key observations.....	57
3.5 Discussion	57
3.5.1 Gas Escape Structures	58
3.5.2 Application to natural gas escape structures	61
3.5.3 Mechanism for secondary explosions	61
3.5.4 Implications for deposit remobilisation and preservation.....	64
3.5.5 Implications for PDC flow dynamics.....	65
3.6 Conclusion	66
Chapter 4 : Behaviours of pyroclastic and analogue materials, in dry and wet environments, for use in experimental modelling of pyroclastic density currents	68
4.1 Abstract	68
4.2 Introduction	68
4.2.1 Material selection in experimental PDC modelling	70
4.2.2 Moisture in a PDC system	75
4.2.3 The influence of moisture on experimental modelling materials.....	75

4.3	Methods and materials	77
4.3.1	Pyroclastic and analogue samples	77
4.3.2	Scaling.....	79
4.3.3	Wetting process	79
4.3.4	Particle size and shape analysis.....	80
4.3.5	Experimental procedure	80
4.3.6	Statistical analysis	82
4.3.7	Limitations	83
4.4	Results I: behaviour of material in dry conditions.	83
4.4.1	Particle size analysis	83
4.4.2	Bulk and tapped densities	86
4.4.3	Angle of repose	87
4.4.4	Fluidisation.....	89
4.5	Results II: behaviour of material in wet conditions	92
4.5.1	Bulk and tapped densities.	92
4.5.2	Angle of repose	94
4.5.3	Fluidisation.....	96
4.6	Discussion	99
4.6.1	Controls on the behaviour of pyroclastic material	99
4.6.2	The importance of the proportion of fines content.....	100
4.6.3	Age, Composition and Environment Effects	102
4.6.4	Implications for PDCs and their Deposits.....	102
4.6.5	Material recommendations for experimental modelling	105
4.7	Conclusions	112
Chapter 5 : The influence of moisture on ash strength: implications for understanding volcanic stratigraphy.		114
5.1	Abstract	114
5.2	Introduction	114

5.2.1	Changes in variables: flow and deposit.....	116
5.2.2	This work and aim.....	117
5.3	Terminology, Materials and Methods	119
5.3.1	Fieldwork Terminology	119
5.3.2	Experimental Materials	121
5.3.3	Experimental Methods	125
5.4	Variations in ash layer strength on Tenerife	127
5.4.1	“Dry” ash layer contact	127
5.4.2	Sheared accretionary lapilli ash layer contact.....	130
5.4.3	“Wet” ash pellet layer contact.....	134
5.4.4	Ash layer remobilisation	137
5.4.5	Questions raised by the fieldwork.....	139
5.5	Experimental results.....	140
5.5.1	Direct shear box tests	140
5.5.2	Ring shear tests	141
5.5.3	Particle size and shape analysis.....	143
5.5.4	Drop Tests	144
5.6	Discussion	145
5.6.1	Dry Deposit.....	145
5.6.2	Moisture-affected deposits	146
5.6.3	Implications for interpreting PDC stratigraphy and hazard	149
Chapter 6 : Capturing shear instabilities, pulses and current behaviours at the flow boundary zone of granular currents.....		151
6.1	Abstract	151
6.2	Introduction	151
6.2.1	Current–substrate interaction and erosion.....	152
6.2.2	Understanding current-substrate interaction through analogue modelling.....	154
6.2.3	Aims	155

6.3	Methods and material preparation.....	156
6.3.1	Flume set-up.....	156
6.3.2	Materials.....	157
6.3.3	Setting and Sectioning	157
6.3.4	Data collection and analysis.....	158
6.3.5	Deposit architecture classification	159
6.4	Results	166
6.4.1	Comparison of current mobility and pulses over substrate conditions of 0 wt.% and 2.5 wt.% moisture	166
6.4.2	Sedimentary features observed in a substrate of 0 wt.% moisture.....	166
6.4.3	Sedimentary features observed in a substrate of 2.5 wt.% moisture.....	169
6.4.4	Sedimentary feature interpretation	171
6.4.5	Multi-stepped feature formation at the current-substrate boundary.....	171
6.4.6	Extent of Remobilisation	176
6.5	Discussion	178
6.5.1	Dry shear structures and multi-stepped shearing	178
6.5.2	Multi-stepped feature formation	179
6.5.3	The effect of adding moisture to the substrate	179
6.5.4	Application to geophysical flows.....	182
Chapter 7	Discussion and Conclusions	189
7.1	Implications for the behaviour of wet and dry pyroclastic materials.....	190
7.1.1	Static environments	190
7.1.2	Dynamic environments	192
7.2	Implications for ignimbrite stratigraphic architecture.....	195
7.2.1	Deposit heterogeneity	195
7.2.2	Erosion, preservation and remobilisation.....	196
7.3	Implications for flow dynamics	198
7.4	Wider Implications and Future Work	199

7.4.1	Re-thinking flow units	199
7.4.2	Rethinking the flow boundary zone model	201
7.4.3	Understanding PDCs in time and space	204
7.4.4	Secondary hazard generation	207
7.4.5	Flow migration, entrainment and bulking.....	207
7.4.6	What about altered ash?	208
7.4.7	Cold, wet PDCs: Limitations and future work.....	209
7.5	Conclusions	210
References		211
Appendix A - Supplementary Material for Chapter 3.....		247
Appendix B - Supplementary Material for Chapter 4.....		248
Appendix C - Supplementary Material for Chapter 5		256
Appendix D - Supplementary Material for Chapter 6.....		268

List of Figures

Figure 1.1. PDC travelling down the flanks of Mount Merapi, Indonesia, 2006. (©Merapi Volcano Observatory, Yogyakarta, Indonesia; Pallister and Newhall, 2007).	1
Figure 1.2. Illustrative sketch and photos showing the mechanisms of PDC formation. a. Lateral blast at Mt St Helens, 1980 (© Keith Ronnholm, Mt St Helens Institute Website) b. Sustained Column Collapse PDC at Ngauruhoe, 1975 (© Graham Haycocks, New Zealand Geological Survey) c. Lava Dome Collapse at Soufriere Hills, Montserrat, 2009 (© MVO/Government of Montserrat). d. PDC travelling down the NW flank of Mayon Volcano, Philippines, 1984 (©Olimpio Pena, Philippine Institute of Volcanology and Seismology). Figures adapted from Branney and Kokelaar (2002).	2
Figure 2.1. Fluidisation mechanisms in a PDC, a) grain-self fluidisation, where the upward movement of gas is initiated from the incorporation of gas from substrate interaction, plants or by exsolution of juvenile clasts; b) bulk-self fluidisation, where gas is entrained beneath the flow front and c) sedimentation fluidisation, where the downward movement of particles causes an upward movement of gas. Particles are spherical in the figure but represent any characteristic found in natural pyroclastic material (i.e., change in size, density, composition, etc.).	10
Figure 2.2. Unsteadiness in a single-surge and sustained current. In the quasi-steady phase, the parameter value, U, fluctuates around the average. Where U is a parameter (such as velocity or concentration) and t is time.	11
Figure 2.3. Conceptual model of PDC regimes from Lube et al. 2020, Fig 1a and Fig 3 a-e.	12
Figure 2.4. Scanning Electron Microscope image of Taupo 1 sample used in Chapters 5 and 6. Note the particle size, shape (angular, elongate and shard-like), and composition (glassy).	15
Figure 2.5. Simplified illustration showing comminution processes during PDC propagation. Rounded particles and ash concentration increase as particles move from proximal to distal locations. Furthermore, as a PDC loses energy, the dominant regime will move from a collisional flow-dominated regime to a more frictional-dominated regime at the flow boundary zone.	16
Figure 2.6. Different states are associated with moisture increase in a granular material. A) pendular state, b) funicular state and c) capillary state. Figure is adapted from Kim and Hwang, 2003.	18
Figure 2.7. Simplified diagram showing stratigraphic scenarios where different flow units could be interpreted a) where a deposit is delineated by ash or pumice fall, b) where there is a clear compositional variation in the deposit sequence and c) where a clear scour is present and crosscuts the underlying deposit.	19
Figure 2.8. key ignimbrite lithofacies: a) massive lapilli tuff (mLT) lithofacies in the Poris formation of Tenerife. b) Lithic breccia (lBr) overlying mLT lithofacies on Santorini. c) stratified (s) and cross-stratified tuff (xsT) layers interbedded with pumice fall deposits on Tenerife d) gas escape pipes (pip) forming from a charcoal fragment in Eugene, Oregon.	21
Figure 2.9. Schematic illustration of a PDC interacting with sources of moisture across a landscape, which can potentially enter the PDC system and resulting deposits.	23
Figure 2.10. Phase diagram of water, controlled by temperature and pressure. At a certain pressure or temperature, a phase change will occur from gas to liquid by condensation and from liquid to gas by vapourisation.	27

Figure 3.1. Schematic illustration of a PDC interacting with sources of moisture across a landscape which have the potential to enter the PDC system and resulting deposits.	39
Figure 3.2. Particle mass fraction of volcanic material.	43
Figure 3.3. Representative static angle of repose (SAoR) cone formation of V1 – V6 at 0 – 10 wt.% moisture addition. Numbers next to each cone show the average cone height (°).	50
Figure 3.4. a) SAoR for volcanic material with varying moisture percentages with standard deviation error bars; b) DAoR critical angle of volcanic material with varying moisture percentages with standard deviation error bars.....	50
Figure 3.5. Examples of the structure recognised across the experiments.	53
Figure 3.6. A-F Fluidisation profiles of V1 – V6 with increasing moisture (0.00 – 10.00 wt.%). Symbols show gas escape structure formation.	54
Figure 3.7. The gas velocity (cm/s) required to initiate gas escape structures depending on moisture percentage (%). Symbols represent different experimental suites from this study (circles), Wilson (1980) (hourglass) and Roche et al. (2001) (crosses).	60
Figure 3.8. Moisture-influenced model of secondary explosion formation by a) a defluidising wet deposit and b) a defluidising dry deposit with external influences of water.	64
Figure 4.1. GSD plot of pyroclastic (solid line) and analogue (dashed line) materials used throughout the experiments. Materials in legend are organised by logarithmic particle size mean (with cornstarch the finest grained material used) (\emptyset) for this and subsequent figures.....	83
Figure 4.2. Bulk and tapped bulk density results of dry pyroclastic and analogue materials. Results were used to calculate Hausner ratio and Carr's index to determine flowability. Flowability field values are from Gorle and Chopade (2020). Materials are in order of particle size mean (\emptyset). Standard deviation of BTD, uncertainty and error can be found in Supplementary Material 4B.....	86
Figure 4.3. Comparison of particle a) methods of moments logarithmic mean size, b) fines content, c) sphericity, d) symmetry, e) Sauter mean diameter and f) Sauter mean * sphericity ($D_{32} \cdot SPHT$) against SAoR and DAoR values of pyroclastic and analogue materials. Materials are listed in order of fines content (%). Standard deviation, error and uncertainty is shown in Supplementary Material 4B.....	88
Figure 4.4. Images demonstrating the key behaviours described in these experiments showing a) bubbling, b) channelling, c) pocketing, d) explosive channelling, e) cracking (from Walding et al., 2023) and f) diffusive cracking features seen in the present fluidisation experiments.....	90
Figure 4.5. Fluidisation profiles of pyroclastic and synthetic materials at 0 wt.% moisture. Tung 1-6 values obtained from Walding et al., 2023. Materials are in order of particle size mean (\emptyset).	92
Figure 4.6. Changes in Hausner Ratio and Carr's Index as a function of water addition to the material for a) 0.5 wt.% and b) 5 wt.%. Flowability field values are from Gorle and Chopade (2020). Standard deviation, error and uncertainty of BTD can be found in Supplementary Material 4B.....	93
Figure 4.7. a) SAoR at 0 and 5 wt.% moisture and b) DAoR at 0 and 2.5 wt.% moisture of pyroclastic and analogue materials and fine content (%). Materials are listed vertically in order of fines content % from cornstarch to Tung 6. Standard deviation, error and uncertainty is in Supplementary Material 4B.	95
Figure 4.8. Fluidisation behaviours of pyroclastic and analogue materials at 0, 0.5, 1, 2.50 and 5 wt.% moisture addition a) Colima, b) Atitlan, c) Ballotini 1, d) Milos e) Fine Sand, f) Taupo 2, g) Taupo	

1, h) Industrial Pumice i) Ballotini 2. Symbols show fluidisation behaviours of material. Data is presented in material mean size order. Fluidisation results from Tung 1 – 6 are in Supplementary Material 4D.	98
Figure 4.9. Loading plot from PCA analysis (Lê, Josse and Jussion, 2008; Kassambara and Mundt, 2020; R Core Team, 2023). Dim1 and Dim2 are the principal components and show percentages. Each variable used in the data set is showed as a vector. The direction of the vector indicates the correlation between the variable and the principal component, while the length of the vector represents the magnitude of the correlation (\cos^2). Vectors that group together or point in similar directions may indicate similarities or underlying relationships. Additional data can be found in Supplementary Material 4E.	100
Figure 5.1. Conceptual model depicting how variable deposition of ash fallout layers in proximal and distal locations during unsteady PDC activity can complicate interpretations of flow units and eruption history. As a single PDC undergoes waxing and waning through time and, therefore, changes in run out through time (column a, t^0 - t^4), co-ignimbrite ash is deposited during episodes of local hiatus. Distally (column c), the final deposit may appear to have multiple ‘flow units’ (dashed line), but only one unsteady PDC was active throughout. Proximally (column b), no evidence of hiatus or ‘flow-units’ are evident (model based on field correlations presented in Dowey et al., 2024).	118
Figure 5.2. Illustration to show how ash layers recording hiatus in an ignimbrite succession may be (a) preserved, (b) eroded, or (c) remobilised by subsequent PDC activity, either due to waxing of a sustained unsteady current or by renewed activity following a complete cessation in PDC activity.	119
Figure 5.3. i) Ash-rich lapilli-tuff (LT1, LT2 and LT3) in contact with tuff (T1 & T2) within the Cueva Honda member of the Poris Formation at Montaña Magua. a. ii) Location map, log at GR: 2811282, 01626695, Supplementary Material 5D. See lithofacies terminology in Supplementary Material 5B. b. Interpretation of the formation of deposits shown in Log 1 through time (t) (see text for explanation).....	129
Figure 5.4. a. i) Accretionary lapilli layer (mTacc) in contact with overlying thin tuff (T) layer, observed in the Magua Member of the Poris Formation at Montaña Magua [GR: 2811244, 01626702]. Accretionary lapilli are sheared at the contact (star). a.ii) Diffuse stratified accretionary lapilli unit (dsTacc) in contact with overlying lapilli-tuff layer (mLT). Accretionary lapilli are fragmented at the contact. a. iii) Location map, log at GR: 2811244, 01626702, See Supplementary Material 5E. See lithofacies terminology in Supplementary Material 5B. 4b. Interpretation of formation of i) the lower contact (5.4. a. i) showing granular shear occurring at the flow boundary zone in log 2, and ii) the more cryptic upper contact shown in log 2 (see text for full explanation).	133
Figure 5.5. Ash pellet (pelT1 & 2) layers documenting an episode of PDC hiatus in this area. The ash pellet layers (pelT1 and 2) of the Jurado Member of the Poris ignimbrite (Brown & Branney, 2004) are in erosive scouring contact with the lithic breccia (lBr) facies above (red dashed line). i) Ash pellet contact (pelT1) is overlain by lapilli tuff (mLT2). Feature A indicates remobilisation. The second ash pellet layer (pelT2) is overlain (in erosive contact) by the lithic breccia unit (lBr). ii) Location map, log at GR: 2810693, 01627006, See Supplementary Material 5F. See lithofacies terminology in Supplementary Material 5B. Flow direction is north to south b) Interpretation panels	

showing (t_1) the formation of the ash pellet layers and (t_2) erosion of ash pellets and lapilli tuff by subsequent lithic-rich PDC activity (see interpretation text for full explanation).	135
Figure 5.6. i) Ash layer (T^*) in contact with overlying lithic-rich facies (lBr) in the Jurado and Tamadaya Member of the Poris Ignimbrite (Brown & Branney, 2004) at the Poris Quarry location. Note the ‘peeling up’ and lifting of the coherent zone of ash ii) Location map, log at GR: 2810696, 01627001, See Supplementary Material 5G. See lithofacies terminology in Supplementary Material 5B. Flow direction is north to south b) Interpretation panels showing the formation of this striking feature at the ash layer contact (see text for full explanation).	138
Figure 5.7. Direct shear box test of Tung 4 at 0 wt.% (black) and 1 wt.% (blue) moisture contents. Note that the yield stress was not reached. See Supplementary Material 5E.	140
Figure 5.8. a) Atitlan 2, b) Brown Tuff and c) Taupo 1 shearing profiles of material at varying moisture contents (0 and 1 wt.%). B shows peak stress, and a dashed red line highlights the yield stress and separates areas of elastic response (left-hand side of the graph) and plastic hardening (right-hand side of the graph).	142
Figure 5.9. Particle size analysis of material before and after the ring shear experiments.	143
Figure 5.10. Drop test completed on Taupo 1 sample at b) 0 wt.% moisture, c) 50 wt.% moisture and d) 60 wt.%. Arrows show the movement of the ball from a) falling, b) and d) moving through the material and c) showing the bouncing movement of the ball on impact with the deposit. See Supplementary Material 5J.	145
Figure 5.11. Schematic showing dry (left) and wet (right) ash layers forming from dry and moist plume fallout, co-ignimbrite fallout and dilute PDC deposition. At the dry locality, a subsequent PDC entrains (1) the loose ash material, possibly leading to bulking (2) in the current. The final deposit shows a cryptic or missing ash layer. In the wet scenario, moisture in the substrate is inferred by the presence of accretionary lapilli and ash pellets, which lead to an overall more cohesive deposit of greater shear strength (3). Furthermore, where lithics are present (4), high moisture substrates can experience shear thickening. This results in the preservation of “wet” ash layers, which are recorded.....	147
Figure 6.1. Unsteadiness in a sustained, long-lived current. In the quasi-steady phase, material pulses (i.e., an increase in velocity) can form. U is a change in current parameter (e.g., velocity, concentration) and t is time.....	154
Figure 6.2. Experimental flume set-up as outlined in and adapted from Rowley et al, (2014) showing the porous plate (green) and substrate (black). The experiments recorded in this work utilise the first chamber to supply a gas flux to the material. Chambers 2 and 3 hold the unfluidised loose substrate.	156
Figure 6.3. a) Block divisions within the flume (A-E). The arrow shows the current direction, and the dashed red lines show the partitioning of deposit blocks at a distance away from the hopper. b) The lateral division of slices (1, 2 and 3) in shaded dark aquamarine, and c) illustrates the schematic used throughout this work to indicate the position within the flume.....	159
Figure 6.4. a) Flume run 1 (0 wt.% moisture substrate) and b) flume run 2 (2.5 wt.% moisture substrate) current front velocity (m/s) against distance (cm). The velocities of the pulse front are recorded (dashed line) and end where they meet the current front, can no longer be traced or where current motion ceases completely.	166

Figure 6.5. Panel of Flume Run 1, Section 1, A-E. The substrate had a moisture addition of 0 wt.%. A is proximal (i.e., where the substrate starts), and E is distal (i.e., down-flume where the substrate ends and the run out of the current stops). Feature type, frequency, angle and aspect ratio are described. Feature classification and descriptions can be found in Table 6.1. Panel sections for Flume Run 1 (sections 2 and 3) can be found in Supplementary Material 6C. Current videos can be found in Supplementary Material 6F.....	168
Figure 6.6. Panel of Flume Run 2, Section 1, A-E. The substrate had a moisture addition of 2.5 wt.%. A is proximal (i.e., where the substrate starts), and E is distal (i.e., down-flume where the substrate ends and the run out of the current stops). Feature type, frequency, angle and aspect ratio are described. Feature classification and descriptions can be found in Table 6.1. Panel sections 2 and 3 for Flume Run 2 can be found in Supplementary Material 6E. Current videos can be found in Supplementary Material 6F.....	170
Figure 6.7. a) Remobilisation events sequenced from the deposit in Flume run 1, Section 2 from 17 to 22.5 cm (a.i – a.iii) b) Flow front (solid black line) and pulse (dashed grey line) velocity from 17 – 22 cm and c) Current thickness through time at 17 (± 1.0) cm.....	173
Figure 6.8. a) Remobilisation events sequenced from the deposit in Flume Run 1, Section 2 from 69 to 72 cm (a.i – a.iii) b) Flow front (solid black line) and pulse (dashed grey line) velocity from 69 – 72 cm and c) Current thickness through time at 69 (± 1.0) cm.....	174
Figure 6.9. Conceptual model showing the stepped flow boundary zone caused by unsteady, multiphase shearing episodes. Pulses are "energetic episodes" such as an increase in velocity in the current. a) Velocity profile and the stepped flow boundary zone, b) Resulting feature formation which represents stepped shearing at the flow boundary zone. t1, t2 and t3 are different points in time. At t3, velocity is thought to be sustained, unsteady or to decrease as the final current deposition takes place. The current velocity profiles are based on Smith et al. (2023).....	175
Figure 6.10. Remobilisation height of features (from the top of the substrate to the top of the highest feature) and average remobilisation are (%) against down-flume distance (m) for a) flume run 1 at 0 wt.% substrate and b) flume run 2 at 2.5 wt.% substrate. Section q Section 1 is at the side wall, section 3 is at the flume centreline, and Section 2 is the divisor between the two.	177
Figure 6.11. Modelled basal shear velocities for currents over dry (0 % model) and wet (2.5 % model) substrates. Simulated features have lengths that range from 0.1 to 10 cm at 0.1 cm intervals. Flow front velocities from the flume experiments (min and max for 0 wt.% (black) and 2.5 wt.% (blue) are plotted to show the modelled minimum and maximum wavelengths formed at these velocities.	181
Figure 6.12, Schematics of a) a dry, loose substrate from Branney and Kokelaar (2002) and a b) moist, cohesive or lithified substrate from this work, with indicative concentration and velocity profiles. The FBZ (red dashed line) can migrate vertically, reflecting erosion and deposition at the current-substrate boundary. In b) erosion into the underlying substrate is suppressed due to the associated shear strength of the substrate.....	186
Figure 6.13. The control of critical shear stress on erosion and deposition by a current in a) loose dry conditions and in b) moist, cohesive or lithified substrate.....	188

Figure 7.1. Schematic showing the maximum packing density of pyroclastic material with increasing percentage of large particles with small volumes of moisture, as inferred in this work (adapted from Shakor et al., 2022)	192
Figure 7.2. Maximum gas escape velocity against fines content for the samples analysed in Chapters 3 and 4. Samples exhibiting “easier” fluidisation behaviours, such as bubbling, channelling and diffusive cracking are shown as circles, those exhibiting “intermediate” behaviours, such as drying profiles and pocketing as shown as diamonds and those exhibiting “difficult” behaviours such as explosive channelling and racking are shown as crosses. Colours show different moisture additions from 0 (green) to 10 (pink).	194
Figure 7.3. a) Field localities in the Poris ignimbrite in Tenerife showing moist layers of accretionary lapilli (upper left picture) and pellets (lower left picture). For more detail see sections 5.4.2 and 5.4.3. b) Experimental examples completed in Chapter 6, Section 6.4.3 showing shearing (top right) of a cohesive deposit and remobilisation of cohesive clumps (bottom right).	197
Figure 7.4. Schematic image showing a PDC through time and the resulting flow units that can be interpreted at different locations (1, 2, 3) from the vent. At location 1, one flow unit is recorded. At location 2, two flow units are recorded, and at location 3, four flow units are recorded. Figure adapted from Dowey et al. (2024)	200
Figure 7.5. Comparison of the FBZ as presented in Branney and Kokelaar (2002) and interpreted in this thesis. a) granular flow-dominated FBZ with schematic concentration and velocity profiles with a dry, loose substrate and a b) moist, cohesive or lithified substrate from this work. c) a traction dominated FBZ with schematic concentration and velocity profiles with a dry, loose substrate and a d) moist and cohesive substrate, e) a fluid escape dominated FBZ with schematic concentration and velocity profiles with a dry, loose substrate and a f) moist, cohesive or lithified substrate. The FBZ (red dashed line) can migrate vertically, reflecting erosion and deposition at the current-substrate boundary.	203
Figure 7.6. a) field images from the Brown Tuff PDC deposit in Lipari, Italy, overriding a pumice fall layer. In the boxes, i) shows stringer features and ii) shows flame-like features remobilised from the underlying pumice fall. The current direction is from right to left. b) Additional flume experiments completed as part of this work. The substrate is dry and loose (0 wt.% moisture) and has been remobilised by the current to form flame-like features in the deposit (dashed lines). The current direction is left to right.	205

List of Tables

Table 3.1. Table showing particle size mean (logarithmic), particle size median (logarithmic), particle range, fines content ($< 63 \mu\text{m}$), geometric mean, logarithmic (ϕ) Method of Moments used for Mean, Sorting, Sphericity, Skewness, and Kurtosis. Sauter mean diameter calculated from Breard et al (2019). Geldart Group Classification (Geldart, 1973) based on mean size of particle.	44
Table 3.2. Relationship between Carr’s Compressibility Index (CI), Hausner Ratio (HR), and flowability behaviours. From Gorle and Chopade, 2020.	46
Table 3.3. Flowability based on angle of repose results (Al-Hashemi & Al-Amoudi, 2018).	47
Table 3.4. Loose and tapped bulk density, the Hausner ratio, Carr Index and Flowability. Uncertainty and Error (\pm) of the experiment.	49
Table 3.5. Types of behaviour of gas escape observed with increasing moisture in volcanic material.	59
Table 4.1. Compilation of published works on material properties of analogue and pyroclastic material used in experimental modelling. The values represent the properties of the material used in a range of static and dynamic studies. SAoR – Static Angle of Repose, DAoR – Dynamic Angle of Repose.	73
Table 4.2. Pyroclastic samples used in the reported experiments, reporting formation processes, chemical composition, location of sample collection and references (where applicable).	78
Table 4.3. Analogue samples used in the experiments. Ballotini 1 and 2 represent the size variation of the two material samples used.	79
Table 4.4. Material properties of both pyroclastic (sample names shaded dark grey below) and analogue materials (shaded pale grey). These include logarithmic particle size mean and particle size median, particle range, fines content ($< 63 \mu\text{m}$), geometric mean (ϕ), and employ the method of moments for calculating mean, sorting, sphericity, symmetry, skewness, and kurtosis. The Sauter mean diameter is computed following the methods outlined in Breard et al (2019). Additionally, the Geldart Group Classification (Geldart, 1973) is determined based on the logarithmic mean particle size. Table is ordered by logarithmic particle size mean.	84
Table 4.5. Dry pyroclastic material in comparison to analogue material for use in experiments. ‘X’ is where fluidisation behaviours were present. ‘-’ is where fluidisation behaviours were not present. ‘n/a’ symbolises experiments that did not take place.	107
Table 4.6. Wet (0.5, 1, 2.5 wt.%) pyroclastic material in comparison to analogue material for use in experiments. ‘X’ is where fluidisation behaviours were present. ‘-’ is where fluidisation behaviours were not present. ‘n/a’ symbolises experiments that did not take place.	110
Table 5.1. Experimental material source location, chemical composition, formation mechanisms and the test completed in this work. DS – direct shear, RS – ring shear and DT – drop test. References detail material characteristics, collection and location.	121
Table 5.2. Material properties of both pyroclastic and cornstarch material. These include logarithmic particle size mean and particle size median, particle range, fines content ($< 63 \mu\text{m}$), and geometric mean (ϕ). The method of moments is employed for calculating Mean, Sorting, Sphericity, Symmetry, Skewness, and Kurtosis. The Sauter mean diameter is calculated following Breard et al. (2019). Material properties explored further in Walding et al., 2023; 2024. The table is ordered by particle size mean.	Error! Bookmark not defined.

Table 6.1. Sedimentary features observed in this work, their characteristics and descriptions and how they have been measured in this work.	160
---	-----

Glossary

A Glossary of terms used throughout this work, based on the descriptions by Branney and Kokelaar (2002).

Architecture – The structure of an ignimbrite deposit, including three-dimensional changes in thickness, arrangement of lithofacies and geometry.

Ash aggregates - Clustering of ash particles from the presence of cohesive forces, cementation or baking. Ash aggregates can be accretionary lapilli or pellets.

By-passing – The overpassing of a current over a substrate where material is neither deposited nor eroded.

Cohesion – The forces that control the “sticking together” of particles. This can be due to the presence of clay minerals, interstitial liquid or electrostatic forces.

Dynamic – Moving or flowing such as material in a current or a fluidised deposit.

Flow boundary zone (FBZ) – A zone that consists of the uppermost part of the current and lowermost part of the deposit. Lithofacies are determined by the behaviours at this zone. The flow boundary zone moves vertically upward where, or when, the deposit is aggrading and vertically downward where, or when, the deposit is eroding.

Flow unit – A deposit of an individual or unsteady PDC which is delineated by evidence of current cessation (i.e., pumice fall, ash fall, chemical composition, scouring).

Fluidisation – The expansion of a granular material due to the movement of a fluid.

Ignimbrite – the ash- and pumice-rich deposit formed from PDCs.

Lapilli tuff – Lithofacies described as being poorly sorted fine to coarse ash with sub-angular to sub-rounded lithic and pumice lapilli. Can be massive or stratified. Tuff is described for units comprising < 50 % ash. Records deposition from the main body of a PDC.

Lithofacies – The distinct features of a deposit. For example, unique characteristics such as stratification, grain size, shape, sorting and composition which characterise it as being emplaced in a particular environment/mechanism.

Pulse – Movement of material in a current that forms spontaneously during current propagation.

Remobilisation – The entrainment and subsequent deposition of material.

Shear thickening – non-Newtonian behaviour where a material behaves like a solid under increased shear stress or impact.

Static – Stationary deposit. Unmoving such as material in a deposit.

Unsteadiness – Fluctuating current conditions which can be from source (e.g., changes in mass flux) or from spontaneous waxing and waning within the current (e.g., pulses).

Waning – A decrease in a certain parameter (e.g., velocity) through time at a fixed location.

Waxing – An increase in a certain parameter (e.g., velocity) through time at a fixed location.

Yield stress – The stress (applied force per unit area) required to result in permanent or plastic deformation without any further increase in load.

Funding

This project has been funded by the EU Horizon 2020 programme (Project GEOSTICK 712525) through a University of Hull scholarship. Additional grants have been received and facilitated conference attendance, fieldwork, lab work, training and overseas research. Thank you to the University of Hull Doctoral College Conference Presentation and Training Fund, Sir Philip Reckitt Educational Trust Grant, IAVCEI Conference Travel Grant, Yorkshire Geological Society Fearnside's Award, BSRG Gillian Harwood Fund, BSG NERC Advanced Training Short Course, Utrecht Network Young Researchers Grant, Energy and Environment Institute Research Impact and Support Fund, Volcanic and Magmatic Studies Group Student Bursary Award, Turing Scheme Grant, GW4 Volcanology Community Enterprise Grant, Geological Association Meetings Award and British Society of Rheology Student Travel Grant.

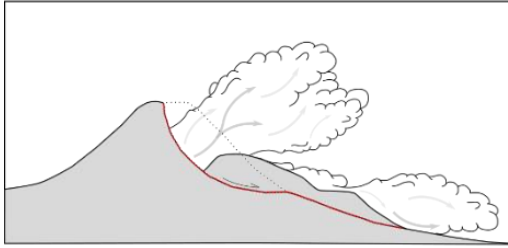
Chapter 1 Introduction

Pyroclastic Density Currents (PDCs) are a volcanic hazard often formed from explosive volcanic eruptions or from dome collapse events (Fig. 1.1). They are rapidly moving, high-temperature (up to 1000 °C) currents of heterogeneous volcanic material and gas that can surmount topographic barriers and form extensive deposits far away from the source (Fisher, 1979; Wilson, 1985; Cas & Wright, 1988; Woods et al., 1998; Branney & Kokelaar, 2002; Dufek, 2016). They can be highly destructive (Valentine, 1998) and have caused the deaths of over 90,000 people since 1600 A.D. (Auker et al., 2013). Currently, around 100 million people living at risk from PDCs (Lube et al., 2020), therefore, the understanding of their complexities, and how currents react to variations in internal and external factors is pivotal in volcanic hazard assessment. PDCs can be initiated from short, unsteady eruption styles (e.g., gravitational collapse of lava domes, lateral blasts, partial column collapse) or more sustained and steady eruption styles (e.g., continuous column collapse) (Fisher, 1979; Branney & Kokelaar, 2002; Sulpizio et al., 2014) (Fig. 1.2).

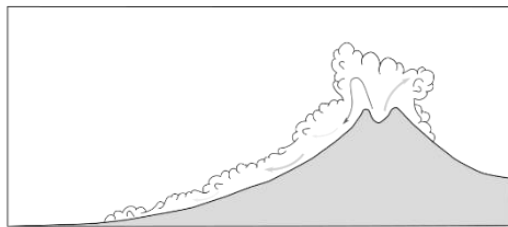
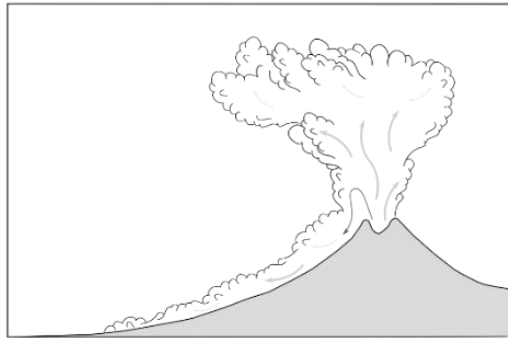


Figure 1.1. PDC travelling down the flanks of Mount Merapi, Indonesia, 2006. (©Merapi Volcano Observatory, Yogyakarta, Indonesia; Pallister and Newhall, 2007).

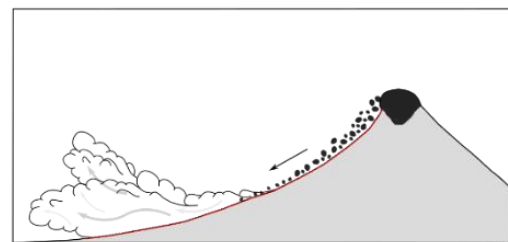
a) Lateral Blast



b) Sustained Column Collapse - Plinian and low fountaining



c) Lava Dome Collapse



d) Single Pulse Collapse

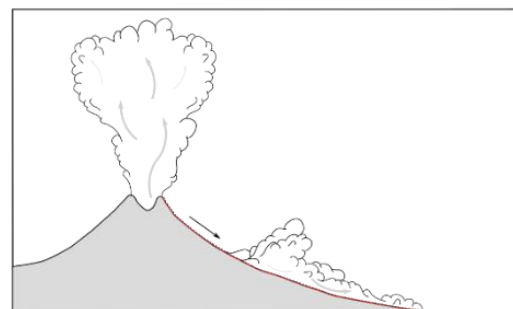


Figure 1.2. Illustrative sketch and photos showing the mechanisms of PDC formation. a. Lateral blast at Mt St Helens, 1980 (© Keith Ronnholm, Mt St Helens Institute Website) b. Sustained Column Collapse PDC at Ngauruhoe, 1975 (© Graham Haycocks, New Zealand Geological Survey) c. Lava Dome Collapse at Soufriere Hills, Montserrat, 2009 (© MVO/Government of Montserrat). d. PDC travelling down the NW flank of Mayon Volcano, Philippines, 1984 (©Olimpio Pena, Philippine Institute of Volcanology and Seismology). Figures adapted from Branney and Kokelaar (2002).

“Ignimbrite” is a word which has taken a range of overlapping but subtly different meanings in the literature, and here the term is used to identify ash- and pumice-rich deposits formed from sustained PDCs (Sparks, 1976; Branney & Kokelaar, 2002). Ignimbrite deposits can be complex both laterally and vertically as a result and reflect spatial and temporal changes in flow dynamics and interactions with topography (Branney and Kokelaar, 1997, 2002; Williams et al., 2014; Dowey et al., 2024). Lithofacies terminology can be described as massive or stratified, non-graded to graded and describe any part of the ignimbrite showcasing distinctive features (Cas & Wright, 1988; Branney & Kokelaar, 2002). Changes in the lithofacies characteristics are thought to represent changes in the flow-boundary zone (progressive aggradation model of Branney & Kokelaar, 1992, 2002). The flow boundary zone describes the lower part of the current and the upper part of a forming deposit (Branney and Kokelaar, 2002). Therefore, the vertical and lateral changes in lithofacies reflect the variations in the flow boundary zone through time and space and can, with accompanying data, give us an insight into the nature of the current.

Pyroclastic density currents exist as multi-phase gravitational currents, meaning they express both solid (i.e., lithic clasts, pumice, ash) and fluid (gas and water vapour) phases (Burgisser & Bergantz, 2005; Esposti Ongaro et al., 2011, 2012; Lube et al., 2020). The relationship between these two phases can vary instantaneously throughout a current, creating a continuum between dilute (fluid-dominated) and concentrated (particle-dominated mixtures) (Druitt, 1998; Branney & Kokelaar, 2002; Sulpizio et al., 2014). However, PDCs are opaque, so internal processes cannot be observed. Therefore, combining analogue and numerical modelling alongside fieldwork can further our understanding of PDC behaviours.

1.1 Research Approach

PDCs are hazardous and unpredictable. Therefore, observing them is rare and accompanied by challenges of visibility, as they are mostly covered by an opaque overriding cloud of ash. Furthermore, in-situ collection of PDC data are difficult and only provides a small insight into the nature of the current. To better understand PDCs, various approaches have been used to understand the behaviours at play between PDC initiation, propagation and deposit formation. A combined approach of direct current observation (Cole et al., 1998, 2002; Lipman, 2019; Vecino et al., 2022), detailed lithofacies interpretation (Fisher, 1979; Branney & Kokelaar, 1997; Brown et al., 2003;

Smith & Kokelaar, 2013; Brown & Branney, 2013; Douillet et al., 2013, 2013, 2018), small- and large-scale analogue experiments (Dellino et al., 2007; Lube et al., 2015, 2019; Rowley et al., 2014; Smith et al., 2018, 2020; Sulpizio et al., 2014) and advanced numerical modelling techniques (Valentine, 1987; Dufek, 2016; Kelfoun, 2017; Breard et al., 2018) has initiated advances in the understanding of PDCs.

Previous works on other geophysical flows (e.g., turbidity currents, snow avalanches, debris flows) and engineering flows (e.g., granular or powder processing and transport) have contributed towards a greater understanding of PDC behaviour and have helped advance the field. Despite this progress, data is limited due to the natural complexity of these currents.

Despite the ongoing research and advances in understanding PDCs, they continue to be a threat to global communities (Naismith et al., 2020). The 3rd of June 2018 Volcan de Fuego eruption (Guatemala) generated a devastating series of PDCs which resulted in the deaths of an estimated 2,900 people and the loss of 5,000 homes (Naismith et al., 2020). With an increased understanding of these flows, more detailed hazard assessments of PDC-forming eruptions can be created. Hazard assessments rely on detailed field mapping or computer simulations and models. Understanding the internal dynamics and behaviours of PDCs contributes to validating these assessments and benefiting communities vulnerable to explosive volcanic events.

Moisture may be introduced into a PDC system from the ambient atmosphere (e.g., humidity, precipitation), the source of the eruptive material (e.g., phreatomagmatic eruptions), interactions with bodies of water, saturated sediment, or even vegetation. However, the impact of moisture on pyroclastic material is unknown. Introducing moisture into dynamic current or static deposit packages will likely introduce variations in particle and resulting material properties. This may influence current behaviour or have implications for deposit architecture.

This thesis contributes to this broad body of work aiming to better understand PDCs and how to better reconstruct their behaviour from ignimbrite stratigraphy. It builds on recent advances in analogue modelling techniques and combines this with field study and geotechnical approaches.

1.2 Research Questions and Objectives

Understanding complex ignimbrite architectures can contribute to more accurate approximations regarding the frequency and evolution of PDC-forming volcanic eruptions. However, due to changes in current and substrate behaviour, the reliability and traceability of individual flow units may be challenging.

This thesis aims to determine the impact of moisture on pyroclastic material, the consequent implications on static and dynamic behaviours, and the understanding of volcanic stratigraphy. It sets out to determine how specific substrates, such as important current hiatus layers and moisture-rich or -depleted layers, may be preserved or not in the volcanic record. Understanding the erosional or preservational potential of ignimbrite material may contribute to a more accurate definition, interpretation, and understanding of stratigraphic sequences. This work utilises fieldwork, experimental analogue modelling, and geomechanical tests to investigate these parameters. This research will contribute to a new understanding of the influence of moisture on PDCs, allow better assessments of PDC architectures, and initiate exciting research that could be incorporated into numerical and hazard modelling.

The thesis-specific research questions are:

RQ1: What controls the behaviour of dry and wet pyroclastic material in both static and dynamic environments?

RQ2: How does moisture and material type affect deposit heterogeneity and architecture?

RQ3: What influences the preservation or erosion of substrate materials; particularly those that may mark PDC hiatuses?

RQ4: How do changes in moisture result in substrate entrainment or remobilisation within a flow?

RQ5: How do changes in moisture within the substrate affect flow dynamics (i.e., velocity, run-out, mobility)?

1.3 Thesis outline and structure

Chapter 1 introduces a brief overview of the thesis, outlining a general description of PDCs and the methodology used. The overall thesis research questions, aim, and objectives are then addressed, as well as the thesis outline and structure.

Chapter 2 is a comprehensive literature review of the understanding of PDCs, from their formation, transportation dynamics and, finally, deposition. A section is dedicated to modelling PDCs before discussing the literature gap where this work lies.

Chapter 3 investigates the role of moisture in pyroclastic material and resulting cohesion behaviours. These are investigated in static and dynamic conditions that show variations in material strength and have significant implications for deposit architecture. Results from the dynamic experiments highlight the impact of moisture on gas escape structures within a deposit. This chapter has been published as “*Cohesional behaviours in pyroclastic material and the implications for deposit architecture*” in the *Bulletin of Volcanology* (Walding et al., 2023). I conceptualised this work, developed and executed the experimental suite, validated and completed the formal analysis and visualisations, and developed the original draft of this work. Co-authors contributed to the discussion of results, amendments, and comments to the final manuscript.

I thank Jacob Nash, Mark Gilbertson, and Samuel Mitchell for access to and development of the fluidisation chamber at the University of Bristol and Ulrich Küppers is thanked for supplying the pyroclastic material used in these experiments. Two anonymous reviewers and L. Pioli contributed to the final review process.

Throughout this published work the term “cohesion” and “cohesivity” is used to describe the changes in Angle of Repose seen with the addition of moisture. When a granular material is released freely onto a surface, the particles will arrange themselves to form a natural slope, where the maximum slope before collapse is called the static “Angle of Repose”. The Angle of repose has been explored in granular science to investigate the physical and mechanical properties, such as the friction coefficient, shear strength and the flowability of granular material (Zhou et al., 2002; Beakawi Al-Hashemi and Baghabra Al-Amoudi, 2018; Dai et al., 2022). The addition of cohesion increases the shear strength of the material due to the formation of interparticle capillary forces. Therefore, changes in shear strength are a product of the addition of moisture to the angle of repose pile and this term has been substituted throughout the thesis.

Chapter 4 expands on the research from Chapter 3 and incorporates a wider suite of pyroclastic materials alongside a suite of analogue materials to explore the behaviour of moisture. The results from this work characterise pyroclastic and analogue materials in dynamic (i.e., flowing), static (i.e., stationary), wet and dry conditions and explore friction

and fluidisation behaviours. Adding moisture can lead to fundamental changes in material properties, significantly impacting geomechanical, fluidisation and flowability behaviours. This work begins to validate a suite of analogue materials against pyroclastic material in a range of conditions for use in experimental modelling. This chapter has been published as “*Behaviours of pyroclastic and analogue materials, in dry and wet environments, for use in experimental modelling of pyroclastic density currents*” in *Volcanica* (Walding et al., 2024). I conceptualised, validated and completed the formal analysis, investigation, original draft and visualisation of this work. Rebecca Williams, Pete Rowley and Natasha Dowey contributed to conceptualising, supervising, and writing reviews and edits. Anna Bird and Dan Parsons contributed to the review and editing of this work.

Ullrich K  ppers, Tom Johnson, Ermanno Brosch, and Gert Lube are thanked for providing the pyroclastic samples used in these experiments. I thank Jacob Nash, Mark Gilbertson, and Samuel Mitchell for access to and development of the fluidisation chamber at the University of Bristol. Louis Chambers and Caitlin Malon are thanked for their assistance in the laboratory. Magnus Johnson and Andy Richardson advised on the statistical analysis. Finally, Eric Breard and Ermanno Brosch are thanked for their thoughtful comments and review during the publication process.

Chapter 5 investigates field relationships between ash aggregate layers and overlying ignimbrite facies within the Poris Ignimbrite on Tenerife. Three interactions have been identified – in dry, low moisture and high moisture conditions – each displaying distinct erosional and remobilisation behaviours. The results show that at both low and high moisture conditions, pyroclastic material increases in yield strength. Furthermore, at high moisture conditions, shear thickening is seen in ash material. This chapter is titled “*The influence of moisture on ash strength: implications for understanding volcanic stratigraphy*” and has been submitted to *Bulletin of Volcanology*. I conceptualised, validated and completed the formal analysis, investigation, original draft and visualisation of this work. Additionally, I developed this idea and established the collaboration with Mark Thomas and Sara Osman at the University of Leeds. Rebecca Williams, Natasha Dowey and Pete Rowley contributed to conceptualising, supervising, and writing reviews and edits. Mark Thomas and Sara Osman contributed to initial lab work discussions, supervision, writing reviews and edits. Richard Brown (University of Durham) is acknowledged for sharing knowledge, time, and locations. Dr Anna Bird provided insightful comments on this piece of work. Thank you to all pyroclastic

material donations that have been shipped and sent to us to complete this work (Gert Lube, Ermanno Brosch, Ulli Kueppers and Tom Johnson). Finally, I am thankful to Kirk Handley and Gary Martin for the equipment and advice.

Chapter 6 explores behaviours between a fluidised granular current and a loose stationary substrate in an experimental flume. The final deposit is set in gelatine and sectioned into slices to enable a 3D longitudinal reconstruction of the deposit. Sedimentary features formed are crucial in reconstructing erosional and depositional behaviours at the current-substrate boundary. Both current dynamics (e.g., unsteadiness and mass flux) and substrate strength (i.e., cohesion) can have fundamental controls on resulting behaviours (e.g., erosion or deposition). The results identified complex stepped shear features forming in dry substrate conditions (0 wt.%) which are thought to be driven by the sustained, unsteady current and the presence of a high-velocity pulse moving through the area. The experiments were also completed on wet (2.5 wt.%) moisture substrates and the addition of moisture into the substrate, suppresses erosion and remobilisation, resulting in the formation of discrete clumps of cohesive material and less intricate shear features. The findings show that increased cohesion in the substrate requires higher current velocity and shear stress to induce erosion and remobilisation. This study applies these interactions to gain insight into the flow boundary zone in PDCs. This has implications for understanding substrate coherence and cohesion in depositional and erosional models, impacting our interpretations of stratigraphic architecture and deposits.

Experiments were completed at the University of Bristol, using equipment funded by a British Society of Geomorphology ECR Grant held by Peter Rowley. Jordan Chenery is thanked for his assistance in the lab.

Chapter 7 collates the research presented in chapters 3 to 6 and answers the research questions and objectives outlined in Chapter 1. The work is summarised by concluding remarks and a discussion of areas for future research.

Chapter 2 Literature Review

2.1 Physical Characteristics of PDCs

PDCs do not exist as a simple homogeneous, monodisperse system; they are complex and enigmatic. PDCs are described as a multiphase flow with a solid and fluid component (Lube et al., 2020). The solid, granular phase of a PDC consists of volcanic and lithic material, which is influenced by interparticulate forces and particle characteristics such as concentration, size, density and shape (Branney & Kokelaar, 2002; Cole et al., 2002; Brown et al., 2003; Darteville, 2004; Douillet et al., 2013). The fluid phase of buoyant gas and vapour can result in intricate interactions of pore pressure, fluidisation, drag and turbulence.

Fluidisation within a flow influences PDC behaviour and mobility, promoting long run-out distances (Sparks, 1976, 1978; Wilson, 1984; Branney & Kokelaar 1992, 2002; Roche, 2012; Aravena et al., 2021; Breard et al., 2017, 2023; Salatino et al., 2024). It is described as the effect of an movement of fluid (gas or liquid) into a granular material, which overcomes the force of gravity and supports the flow (Sparks, 1976; Cocco and Chew, 2023; Branney & Kokelaar, 2002). As a particle becomes fluidised, the effects of drag surrounding it causes variations in surrounding gas velocity and expansion of the bed (Girolami et al., 2008; Gilbertson, 2019). The solid phase of a PDC includes volcanic and lithic materials, with properties like particle size, shape and density influencing the fluidisation of material.

Fluidisation in PDCs can be initiated during emplacement (e.g., fines experiment of Chédeville & Roche, 2018) and maintained throughout the flow by other fluidisation mechanisms (Branney & Kokelaar, 2002). Grain self-fluidisation (Fig. 2.1a) is caused by exsolving gas from hot juvenile glass shards and pumice (Sparks, 1978) and/or from substrate evaporation (steam generated from surface precipitation, combustion of plant matter). Bulk self-fluidisation (Fig. 2.1b) is where clasts become supported by ingestion of ambient air into the front/head of the PDC (Chedeville & Roche, 2015).

Sedimentation fluidisation (Fig. 2.1c) is where particle settling and sorting during compaction cause interstitial fluid movement.

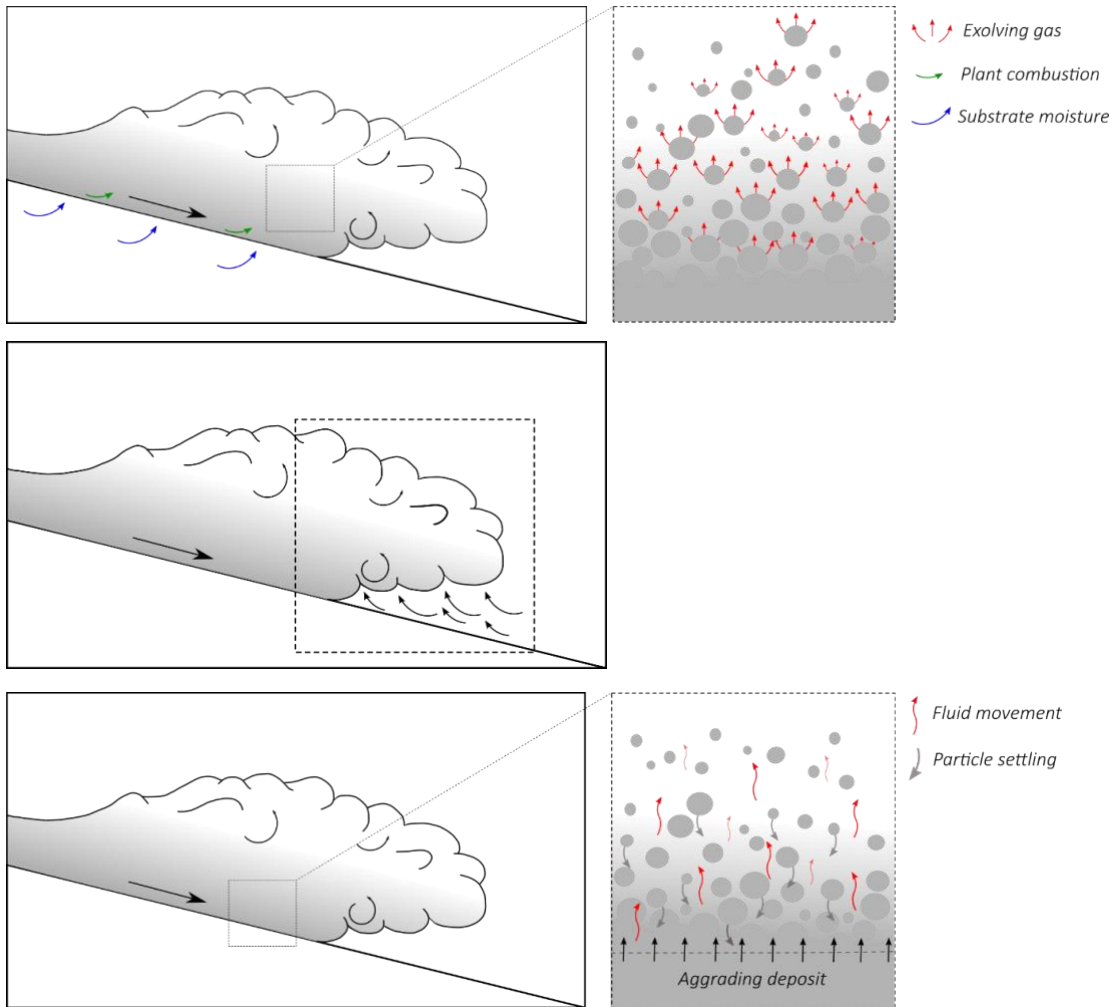


Figure 2.1. Fluidisation mechanisms in a PDC, a) grain-self fluidisation, where the upward movement of gas is initiated from the incorporation of gas from substrate interaction, plants or by exsolution of juvenile clasts; b) bulk-self fluidisation, where gas is entrained beneath the flow front and c) sedimentation fluidisation, where the downward movement of particles causes an upward movement of gas. Particles are spherical in the figure but represent any characteristic found in natural pyroclastic material (i.e., change in size, density, composition, etc.).

2.2 Dynamics in PDCs

PDCs are inherently unsteady (Fig. 2.2), which depends mainly on their formation (i.e., sustained or short-lived lava dome collapse; Fig. 1.2) (Branney & Kokelaar, 2002).

Unsteadiness within a PDC can lead to waxing and waning, which is an increase or a decrease in a certain parameter (such as velocity due to changes in mass flux, topography, particle concentrations etc.) at a certain instant in time (Branney & Kokelaar, 2002; Sulpizio & Dellino, 2008). PDCs are also **non-uniform** in nature, meaning, that changes in certain parameters (slope, concentration, sedimentation, elutriation, clast abrasion, changes in substrate) will result in changes in current

behaviour through time and space (Branney & Kokelaar, 2002). Within a single current, these unsteady and non-uniform fluctuations can result in erosion, by-passing or deposition by the current. For example, a waning current may deposit, and a waxing current may erode (Branney & Kokelaar, 2002). Additionally, unsteadiness can lead to pulses forming within a flow, which can be generated from initial conditions or spontaneously generated during propagation (Rowley et al., 2014; Smith et al., 2018; Andrews, 2019; Brosch & Lube, 2020; Rowley et al., 2023). Therefore, the deposits of unsteady, fluctuating eruptions can be complex (Sulpizio & Dellino, 2008; Dowe et al., 2024).

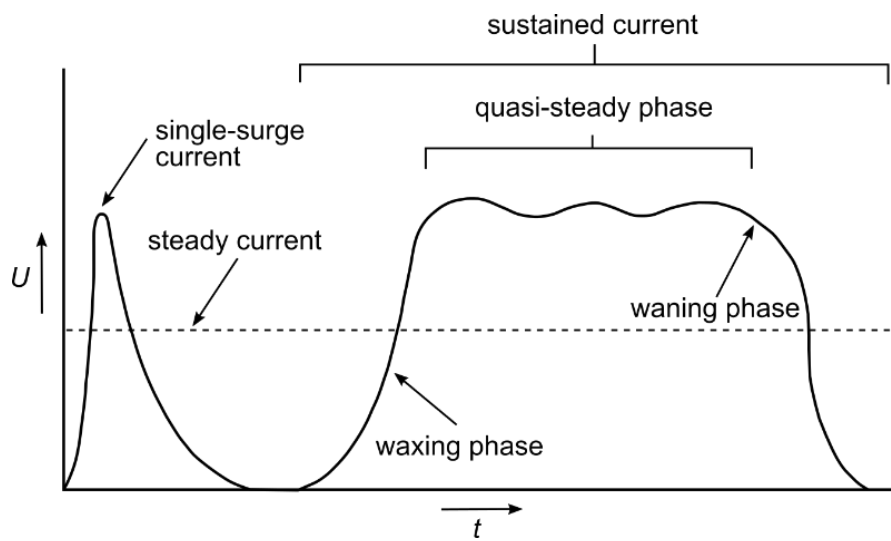


Figure 2.2. Unsteadiness in a single-surge and sustained current. In the quasi-steady phase, the parameter value, U , fluctuates around the average. Where U is a parameter (such as velocity or concentration) and t is time.

Particle concentrations within a PDC can exhibit a wide continuum, from a dilute, low-concentrated current of predominantly ash-rich material to a dense, highly concentrated current (Sparks et al., 1973; Branney & Kokelaar, 1992, 1997, 2002; Cole et al., 2002; Brown & Branney, 2004). Previously, these have been described as pyroclastic surges and contrasting pyroclastic flow deposits (Fisher & Schmincke, 1984; Cas & Wright, 1988; Druitt, 1998). However, more recent works consider these dense and dilute end members instead as part of a PDC spectrum consisting of particles in a collisional-frictional regime and a turbulent-kinetic regime (Branney & Kokelaar, 2002; Dufek, 2016; Breard & Lube, 2017; Douillet et al., 2019; Lube et al., 2020).

Particles in a *dilute regime* are suspended in a turbulent flow, where forces are gravity and drag-dominated, and particles and gas influence each other's behaviour, i.e., one or two-way coupling (Fig. 2.3, Branney & Kokelaar, 2002; Douillet et al., 2019; Lube et

al., 2020). Dilute regimes can be located in the upper flow region of dense PDCs (i.e., as a phoenix cloud or co-ignimbrite cloud) or as a fully dilute PDC. Turbulent eddies and instabilities within the flow transport particles and cause entrainment of surrounding ambient air (Andrews, 2014; Dufek, 2016; Dellino et al., 2019).

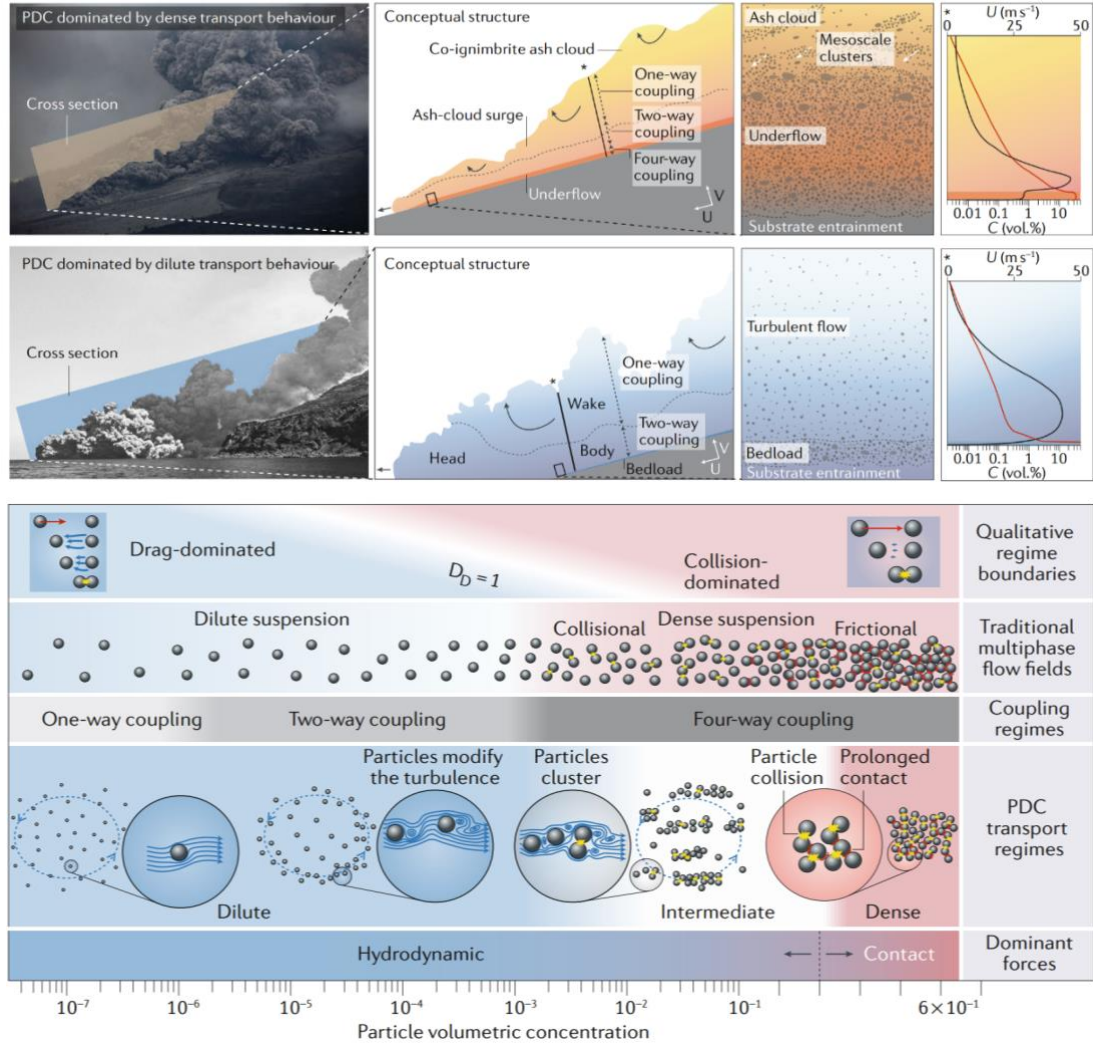


Figure 2.3. Conceptual model of PDC regimes from Lube et al. 2020, Fig 1a and Fig 3 a-e.

Conversely, the **concentrated flow regime** is dominated by particle-particle interactions, i.e., four-way coupling (Fig. 2.3; Lube et al., 2020). Due to this, particle characteristics, such as size, density and shape, can vary extensively and are important factors in controlling behaviours. Most particles during the transport of a concentrated flow occur within a basal granular or underflow. However, the observations of the basal flow are typically obscured by an opaque co-ignimbrite cloud (Fig. 2.3, Breard & Lube, 2017; Sulpizio et al., 2014; Lube et al., 2020).

Finally, the **intermediate regime** consists of “moderate particle concentrations”, characterized by varying distributions of dense and dilute concentrations (Fullmer &

Hrenya, 2017; Lube et al., 2020; Brosch & Lube, 2020). The clustering of material within intermediate regimes is believed to be due to particle-induced collisions and instabilities within the fluid phase (Fig. 2.3., Weit et al., 2019; Lube et al., 2020). Clustering within a flow can impact the sedimentation rate by dramatically increasing the mass of the basal flow (~5 %, Breard et al., 2016), sustain pore-pressures and impact momentum through changes in viscosity and friction (Breard et al., 2016; Breard & Lube, 2017; Fullmer & Hrenya, 2017; Lube et al., 2020).

In reality, a PDC is likely to exist on a spectrum and may display one or all these regimes at any one point during its lifespan. Variations in particle concentration within the flow will influence the deposit formed and changes in deposition or erosion. Unsteadiness in the current, resulting in waxing and waning, will fundamentally impact flow regimes and, therefore, the resulting deposits. This is important in better linking flow to product and understanding PDC behaviour.

2.3 Particle Formation and Characteristics

The physical characteristics of particles within PDCs, such as density, shape and size, heavily influence flow behaviour. Changes in particle characteristics depend on initial eruptive formation and transportation processes.

The characteristics of an eruption (e.g., explosive or effusive) are related to the mass flux of magma, relationships with the environment (i.e., hydrosphere, conduit geometry and stability) and fragmentation (Zimanowski et al., 1997; Buttner et al., 1999; Rose & Durant, 2009; Mueller et al., 2015; Aravena et al., 2018).

Fragmentation of magma is initiated by the expansion of gases derived from exsolving magma due to over pressurisation (Alidibirov & Dingwell, 2000) and/or interactions with the hydrosphere (Zimanowski et al., 1997). Unstable conditions, such as the rapid rise of magma in a conduit, lava dome or flank collapse, can cause gases within a magma to be in nonequilibrium with the surrounding melt (Sparks, 2003; Cashman et al., 2017). Such conditions can cause dissolved gases to exsolve from the magma, converting magmatic-derived thermal energy into kinetic energy through the fragmentation threshold, resulting in particle formation (Wohletz, 1983; Dellino & Volpe, 1995, 1996; Alidibirov & Dingwell, 2000; Zimanowski et al., 2003; Spieler et al., 2004).

Magmatic interaction with the hydrosphere, named phreatomagmatic, can induce highly explosive eruptions (Self & Sparks, 1978; Woheltz, 1983; Lorenz, 1987; Moitra et al., 2020). Water within a phreatomagmatic system can be derived from interactions with groundwater, external water (i.e., precipitation events) and surface water (i.e., melting of ice, water-saturated sediment, lake water and sea water) (Lorenz, 1987; Nemeth et al., 2001; Autin-Erickson et al., 2008). The impact of fluid within the initial eruption can be reflected in the surrounding deposits and in the literature is sometimes termed a “wet-eruption”. Resulting wet-eruption deposits classically show a high fines content and the presence of accretionary lapilli (Nemeth et al., 2001; van Eaton et al., 2012).

As a current propagates, lithic- and pumice-rich regions form due to the density organisation of particles (Calder et al., 2000). Pumice has a density range of $\sim 200\text{--}1100\text{ kg m}^{-3}$ and lithics $1300\text{--}2700\text{ kg m}^{-3}$, depending on composition (Dade & Huppert, 1996; Calder et al., 2000). In proximal (closer to source) regions, denser lithics can be more abundant, which can be influenced by eruption column dynamics (Palladino & Valentine, 1995; Calder et al., 2000; Valentine, 2020). Pumice is less dense than lithics and can continue to more distal flow regions (Calder et al., 2000), although, larger lithics can also be transported by saltation and rolling (Calder et al., 2000; Branney & Kokelaar, 2002). Currents with higher lithic concentrations show longer runout than pumiceous-rich flows. This is due to lithics' higher terminal fall velocity (Palladino & Valentine, 1995; Rodriguez-Sedano et al., 2016). The density variations between lithics and pumice within an ignimbrite deposit can result in grading variations (Sparks, 1976).

Particle shape can be important in particle trajectories within a flow and packing in a deposit. Shape morphologies can be described in several ways; for example, a particle can be described as being spherical or hair-like and have smooth, highly porous or glassy textures, as seen in volcanic particles (Dellino & La Volpe, 1995; Dellino et al., 2005; Bagheri & Bonadonna, 2016; Diogaardi et al., 2017; Connolly et al., 2020). Even though natural particles can display various shapes, analogue and numerical studies use perfectly spherical beads to reduce shape complexity and promote better fluidisation behaviours (see section 2.9, Geldart, 1973; Bagher & Bonadonna, 2016). For example, irregular particles can result in significantly larger drag forces than spherical particles (Dellino et al., 2005; Connolly et al., 2020). Drag is also highly dependent on the Reynolds number (Re), which helps to predict flow patterns and particle trajectories (Connolly et al., 2020). Irregular particle shapes have a greater effect when the Re number is high, associated with more turbulent flow regimes (Bagher & Bonadonna,

2016; Diogaurdi et al., 2017). Furthermore, particle surface changes, such as in the presence of vesicles can increase drag (Liu et al., 2015). Particle shape and size significantly affect and control the packing or arrangement of a material in its deposited state (Jia & Williams, 2001).



Figure 2.4. Scanning Electron Microscope image of Taupo 1 sample used in Chapters 5 and 6. Note the particle size, shape (angular, elongate and shard-like), and composition (glassy).

PDC deposits are heterogeneous and display a range of clast and particle *sizes* (Fig. 2.4, Kaminski & Jaupart, 1998; Cole et al., 2002). Variations in particle sizes can be attributed to initial vent dynamics (fragmentation of magma, vent stability), erosional sedimentation processes as the current propagates (abrasion and attrition) and segregation within the flow (Sparks, 1976; Dufek & Manga, 2008).

The concentration of ***fine ash*** (< 2 mm) during eruptions increases with explosivity (Wohletz, 1983; Buttner et al., 1999; Zimanowski et al., 2003; Rose & Durant, 2009). The formation of ash results from both pre-eruptive (i.e., initial magma fragmentation) and eruptive (i.e., transport and sedimentation mechanism) processes. Ash can be transported by a buoyant plume, as seen in Pinatubo 1991 (VEI 6), where ash reached 34 km in height (Darteville et al., 2002), or during PDC propagation. During the 1980 Mount St. Helens eruption (VEI 5), the directed PDC blast transported large volumes of volcanic material 27 km from the source (Wilson, 1980; Belousov et al., 2007). In

larger eruptions, such as the 25.4 ka Oruanui Taupo eruption (VEI 8), 320 km³ of ash-rich ignimbrite material was transported and deposited up to 60 km from the eruption source (Wilson, 2001; van Eaton et al., 2012).

Fine ash concentration can be increased during transport by clast interaction and comminution processes (Fig. 2.5, Sparks, 1978; Walker, 1981; Woheltz & Krinsley, 1982; Buttner et al., 1999; Dufek & Manga, 2008). Increased collisional and frictional rates can vary due to interactions with particles and their surroundings, such as movement through a volcanic conduit or within energetic, dense regions of PDCs (Dufek & Manga, 2008; Rose & Durant, 2009; Kueppers et al., 2012; Dufek et al., 2012; Mueller et al., 2015). Field observations comparing Plinian fallout units with associated ignimbrite deposits show significantly more rounding of clasts in the latter (Manga et al., 2011; Mueller et al., 2015). The increased sphericity of clasts, high ash concentrations, and abrasion of particle rims within PDC deposits implies strong internal mechanical processes during transport and deposition (Fig. 2.5, Walker, 1981; Woheltz, 1983).

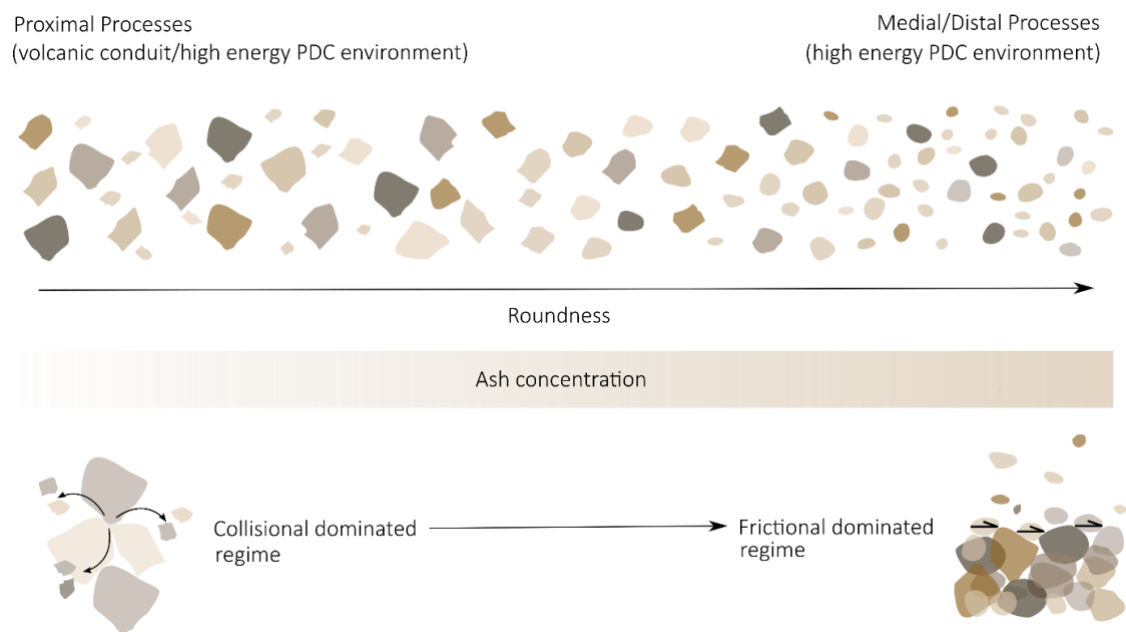


Figure 2.5. Simplified illustration showing comminution processes during PDC propagation. Rounded particles and ash concentration increase as particles move from proximal to distal locations. Furthermore, as a PDC loses energy, the dominant regime will move from a collisional flow-dominated regime to a more frictional-dominated regime at the flow boundary zone.

The variability of particle characteristics results in complex interactions between particles and their surrounding fluid medium. For example, the size of particles will influence interparticulate forces and overall surface area. Variations in shape will impact particle trajectories and packing. Even composition will ultimately affect where

a particle is positioned within a flow, and the behaviour of interparticulate forces will depend on porosity and permeability at the particle scale. These behaviours are fundamental in understanding pyroclastic material from particle to bulk scale, to enable a better overall understanding of pyroclastic material and wider PDC behaviours.

2.4 Interparticulate Forces

Cohesion influences the movement, settling and deposition of particles, making it a key factor in predicting flow behaviour and deposit formation. This importance is not limited to geophysical flows; it has also been extensively highlighted in industrial processes, such as powder processing and transportation (Mirsha et al., 2020; Lu et al., 2020)

Cohesive forces between particles can arise from various mechanisms, including electrostatic attractions (Schumacher & Schmincke, 1995; James et al., 2002, 2003), van der Waals forces, and hydrostatic interactions like capillary and liquid bonding. In volcanic systems like PDCs, all these interparticle forces are present, highlighting the need for their consideration in accurately modelling and understanding these systems.

During explosive volcanic activity, fine, dry ash particles can become positively and negatively charged, creating *electrostatic attraction* between particles (Gilbert & Lane, 1994; James et al., 2000). Volcanic plumes, which can carry significant electrical charges, develop as these charged particles interact within the plume. Without a conductive path to the earth, the charged volcanic ash particles can either attract or repel each other (Schumacher & Schmincke, 1995), influencing aggregation, settling behaviour, and the overall dynamics of the plume.

Van der Waals forces act between atoms, molecules and particles (Louati et al., 2015; Shang et al., 2020; Yehuda & Kalman, 2020) and are fundamental in many interparticle interaction processes. These forces are important in aggregation, flocculation, adhesion and surface tension (Israelachvili & Jacob, 2011). The strength of van der Waals forces is known to diminish as the distance between particles increases (Shang et al., 2020), making them especially important in short-range interactions where they contribute significantly to particle cohesion and behaviour in both natural and industrial systems. Electrostatic and van der Waals forces are all evident throughout volcanic systems, manifesting in phenomena such as fine ash clustering, aggregation and the occurrence of electric storms during eruptions, (McNutt & Williams, 2010; Brown et al., 2012). At

elevated temperatures, it is generally assumed that the dominant interparticulate forces are electrostatic and van der Waals forces. However, as distance increases and entrainment occurs, temperatures will decrease (Benage et al., 2016) and introducing moisture into the system will change the dominant interparticle forces to *hydrostatic* (Koos, 2014). This shift to the prevalence of hydrostatic forces has been seen in ash aggregation (Brown et al., 2012); electrostatic attraction is dominant where humidity levels are below 71 % (Telling et al., 2013). As humidity rises, the influence of moisture-related cohesion becomes more pronounced, highlighting the complex interplay between temperature, humidity and cohesive forces in volcanic ash.

As water begins to condense within the system, liquid bridges begin to form between particles. This is the transition from a non-capillary to a capillary state (Kim & Hwang, 2003) and will result in changes in cohesion and strength behaviours (Kim and Hwang, 2003; Delenne et al., 2013). At low moisture contents, depending on unique material characteristics (i.e., size, shape, porosity, etc.), particles are said to be in a pendular state (Fig. 2.6a, Kim & Hwang, 2003; Delenne et al., 2013; Koos, 2014). In the pendular state, water is placed as a thin film surrounding particles (Kim & Hwang, 2003; Koos, 2014). Increasing moisture content forms a capillary network between particles (Fig. 2.6b, funicular state, Kim & Hwang, 2003). Eventually, the capillary state is reached at high water contents, where capillary bonds completely support particles (Fig. 2.6c, Kim & Hwang, 2003; Koos, 2014).

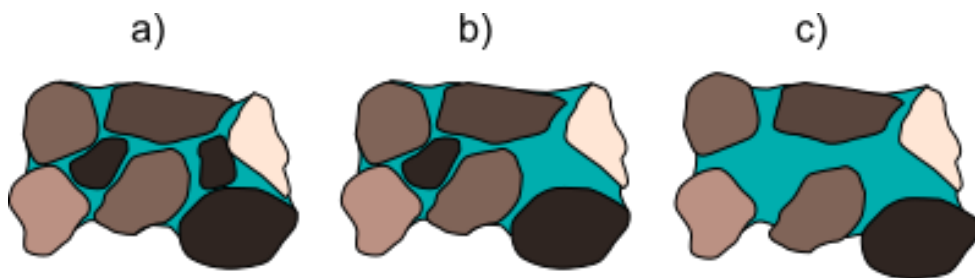


Figure 2.6. Different states are associated with moisture increase in a granular material. A) pendular state, b) funicular state and c) capillary state. Figure is adapted from Kim and Hwang, 2003.

Interparticulate forces can result in clumping and agglomeration between particles, which affects their final physical particle shapes (e.g., size, shape, and density), particle trajectories, settling rates, and deposition. Within a PDC system, it is suggested that all forces (i.e., electrostatic, van der Waals, and hydrostatic) will be present. Hydrostatic forces will dominate in areas of high moisture, such as humid or wet environments, forming capillary bonds between particles where the water has condensed.

2.5 Sedimentation and deposition

The “en-masse” model has been previously thought to control deposition in dense PDCs (Sparks et al., 1973; Sparks, 1976; Wright & Walker, 1981; Fisher & Schmincke, 1984). In this case, material is deposited where it is within the current. For example, a single “plug-like” movement of material may occur where internal variations are present within the flow and deposit at that location.

However, it is now widely accepted that a PDC will deposit material by the **progressive aggregation model** (Fisher, 1966; Branney & Kokelaar, 1992, 2002). The progressive aggregation model interprets certain deposit characteristics (lithofacies) as reflecting flow processes at the point of deposition at the flow boundary zone (FBZ). The FBZ incorporates the lower part of the current and the uppermost layer of particle aggregation within an accumulating deposit, where steady or stepwise aggradation can take place (Branney & Kokelaar, 2002; Sulpizio & Dellino, 2008).

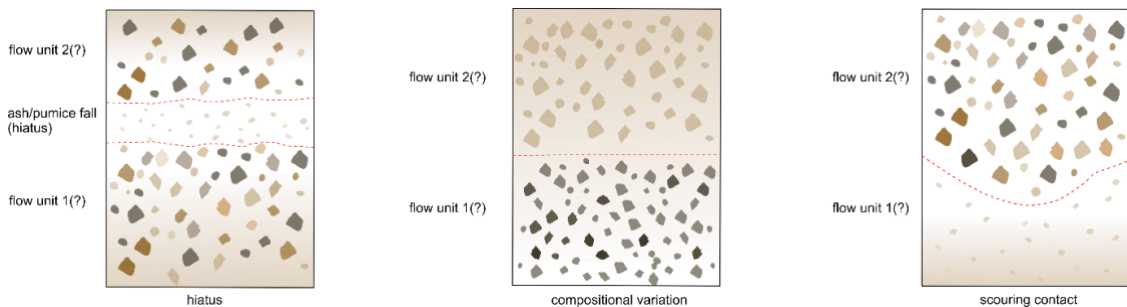


Figure 2.7. Simplified diagram showing stratigraphic scenarios where different flow units could be interpreted a) where a deposit is delineated by ash or pumice fall, b) where there is a clear compositional variation in the deposit sequence and c) where a clear scour is present and crosscuts the underlying deposit.

The FBZ can exhibit as four end members (Branney & Kokelaar, 2002). These include direct fallout-dominated flow FBZ, where pyroclasts deposit directly, with low current velocities preventing particle interactions, fluid escape and segregation. This results in a non-stratified deposit formed by individual particle settling velocities. Traction-dominated FBZ has low clast concentrations and interactions in an area of low shear. This can produce stratified deposits and the formation of bedforms. In granular flow FBZs, clast concentrations and interactions are dominant, and shearing is high. Finally, fluid escape-dominated FBZs have high particle concentrations, where sedimenting grains push fluid upwards, which slows down particle settling velocities (Branney & Kokelaar, 2002). Behaviours at the FBZ will directly influence the type of material

deposited, and the architecture of the deposit will be influenced by current dynamics (e.g., eroding, bypassing, or depositional flow).

Architectural packages of material in an ignimbrite can be subdivided into flow units (Sparks, 1976), where a flow unit is a stratigraphic package that records the passage of an individual PDC (Fig. 2.7). A flow unit is defined by evidence of a PDC hiatus, often recorded as a change in lithofacies. Lithofacies are defined as a deposit package distinguished by variations in stratification, particle size, shape, sorting, fabric and composition which record a particular depositional environment (Smith, 1960; Fisher, 1979; Wright et al., 1981; Fisher & Schmincke, 1984; Cas & Wright, 1988; Branney & Kokelaar, 2002; Sulpizio, 2005; Brown et al., 2010; Pacheco-Hoyos et al., 2020; Dowe & Williams, 2022). In the literature, flow units can be delineated by pumice-fall layers, ash-fall layers, compositional variations or marked by clear erosional scouring or reworked surfaces (Fig. 2.7, Sparks et al., 1973; Sparks & Walker, 1977; Wright & Walker, 1981; Sigurdsson & Carey, 1989; Branney & Kokelaar, 1992; Pittari et al., 2006; Brown & Branney, 2013; Cavazos-Álvarez & Carrasco-Núñez, 2020). Flow units are uncertain when distinct hiatus (i.e., a localised cessation in PDC activity) layers are not observed (Baez et al., 2020). The presence of a paleosol layer represents a longer time period in the sequence and, therefore, distinguishes between separate eruptive sequences (Branney & Kokelaar, 2002).

Branney and Kokelaar (2002) introduced a lithofacies scheme for ignimbrites, which allowed ignimbrites to be described, interpreted, and compared to the current behaviours during deposition. Here, some key lithofacies are briefly explored.

Massive lapilli-tuff (mLT) is characterised by poor sorting, an ash matrix, and varying concentrations of pumice and lithic lapilli (Fig. 2.8). Typically, it lacks internal stratification and is interpreted as forming in a fluid escape-dominated FBZ. **Lithic Breccia (lBr)** is characterised by large lithic blocks set in a fines-poor or fines-rich matrix (Fig. 2.8). It is typically associated with large PDC events, such as caldera collapse. Deposition is thought to be by fluid escape or granular flow processes.

Stratified and cross-stratified tuffs (sT, xsT) consist of fine tuff to lapilli, characterised by small-scale stratification (Fig. 2.8) and it is interpreted to form from a tractional-dominated flow or from ash fallout. Furthermore, these lithofacies can be subdivided into moist (< 100 °C) and dry deposition (> 100 °C). During moist deposition, bedding angles are steeper than the angle of repose, soft-state deformation is present, and pellets

are often formed (Fig. 2.8). This reflects moist deposition behaviours induced by internal flow or external (e.g., rainfall) conditions (Branney & Kokelaar, 2002).

Vertical pipes, sheets, and pods of clast-supported, crystal and lithic-rich, fines-poor material are common features in massive ignimbrites (Fig. 2.8, lithofacies code: *pip*). These structures form due to fluid escape during rapid deposition and compaction during in-situ deposition of a deposit. They can indicate gas escape in a deposit due to thermal expansion, plant combustion or steam production.

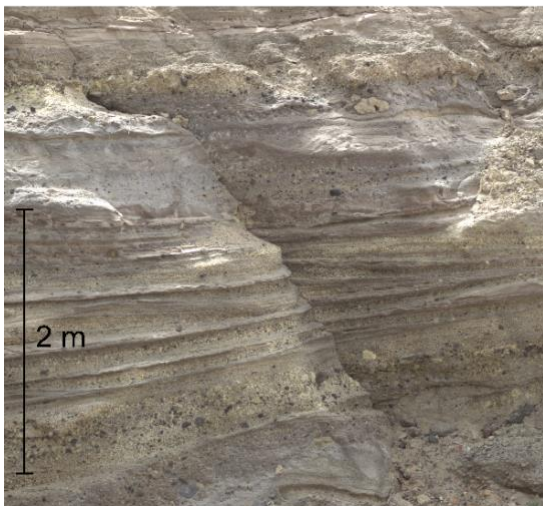
a) mLT



b) mLT and lBr



c) xsT interbedded with pumice fall



d) pip in mLT



Figure 2.8. key ignimbrite lithofacies: a) massive lapilli tuff (mLT) lithofacies in the Poris formation of Tenerife. b) Lithic breccia (lBr) overlying mLT lithofacies on Santorini. c) stratified (s) and cross-stratified tuff (xsT) layers interbedded with pumice fall deposits on Tenerife d) gas escape pipes (pip) forming from a charcoal fragment in Eugene, Oregon.

The interpretation of lithofacies is essential for understanding behaviours at the flow boundary zone (FBZ) during deposition. By interpreting variations in lithofacies strength and cohesion (such as the presence of a wet deposit), depositional processes and environments can be reconstructed which in turn helps guide our understanding of the FBZ.

2.6 Moisture in PDC Systems

Water can enter a PDC system through external or internal processes (Fig. 2.9). A PDC can be water-rich from initial eruptive activity, defined as phreatomagmatic, but, as a

PDC propagates, additional factors may result in water being incorporated into the current.

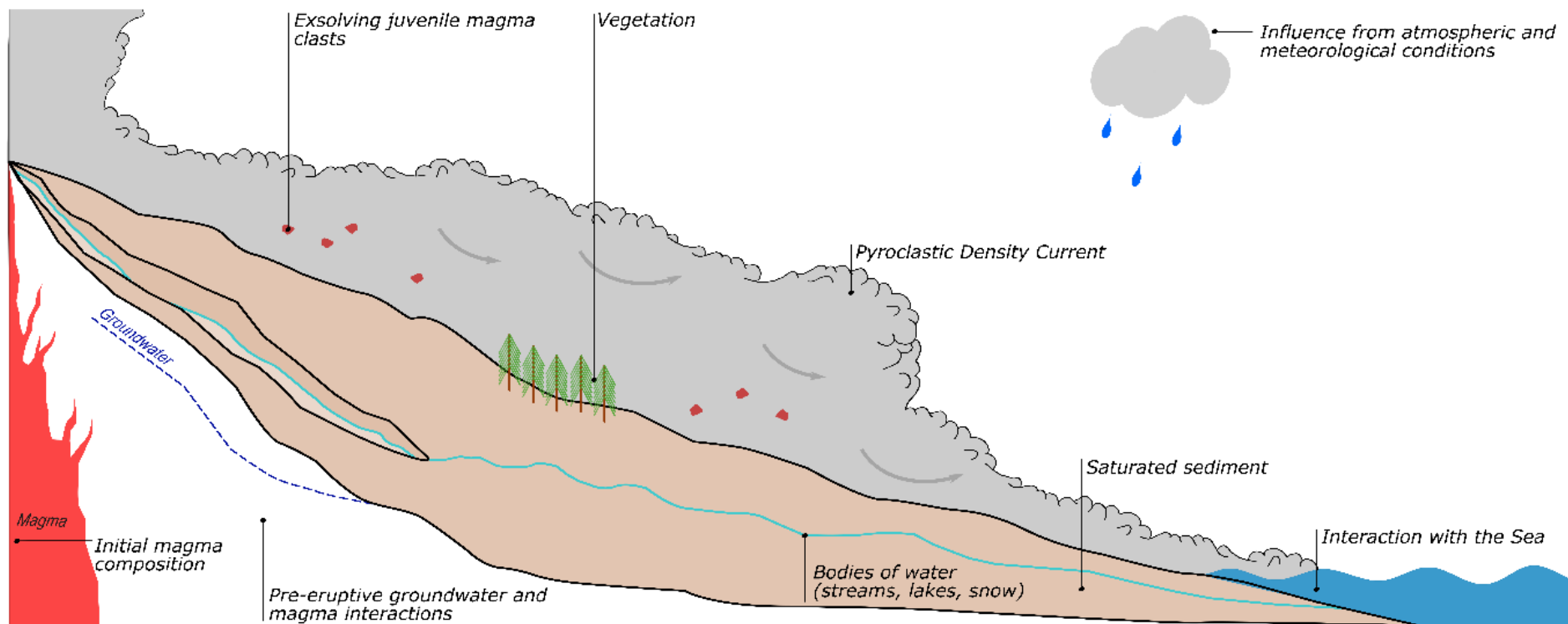


Figure 2.9. Schematic illustration of a PDC interacting with sources of moisture across a landscape, which can potentially enter the PDC system and resulting deposits.

Groundwater (Fig. 2.9) can be found at depth surrounding volcanic edifices or shallowly perched in a permeable substrate. The interaction of magma and groundwater has been attributed to high-pressure and violent behaviour, as seen in phreatomagmatic and phreatic eruptions (Morrissey & Mastin, 2000; Hurwitz, 2003). Combinations from initial mixing conditions between groundwater, meteoric, brine-rich and magma types all influence the magma water content prior to an eruption (Sparks, 1978). Furthermore, if the **initial magma conditions** are wet, juvenile magmatic clasts will exsolve during transport, releasing water and other volatiles (Fig. 2.9). Sparks (1978) modelled how low (0.7 wt. %) and high (6 wt. %) initial water content in juvenile clasts could impact the fluidisation behaviours of the flow. Results highlighted that a magmatic clast from an initial wet magma (i.e., rhyolitic) could still have a residual water content of 0.6 -0.8 wt % during transport of a PDC.

During transport, moisture can be introduced into turbulent regions of the flow through the **entrainment of ambient air** (Fig. 2.9). Rose & Durant (2009) showed that a rising co-ignimbrite cloud may entrain up to 60 times more moisture than a Plinian column. Atmospheric moisture levels (i.e., humidity) are defined by the ratio of water vapour to dry air (Pepin et al., 2017; Camuffo, 2019). **Humidity** is very closely related to elevation. Volcanoes can vary in height and topography, from below sea level to > 6500 m in elevation (Ojos Del Salado: 6893 m.a.s.l). This is known to affect moisture levels, as precipitation patterns vary with topography (Barclay et al., 2006; Duane et al., 2008). As elevation, and therefore altitude, increases, water vapor levels decrease. For instance, at 5 km elevation, water vapor can drop to less than 10% of its ground-level percentage (Hartman, 2016). On the other hand, topography can directly influence local precipitation patterns, with areas of higher elevation receiving greater volumes of precipitation compared to coastal regions (Barclay et al., 2006). Globally, water vapor concentrations vary with latitude, being about 10 times greater at the equator than at the poles (Hartman, 2016). This is because tropical regions, with their warmer climates, can hold more moisture in the air. However, meteorological impacts, such as snowfall and other precipitation events, tend to increase in frequency as one moves away from the tropics, especially in temperate and polar regions. This combination of geographical factors will affect moisture availability, for example, approximately 45% of active volcanoes are located in the tropics (Barclay et al., 2006). A PDC can incorporate water by vaporization from traversing **bodies of water**, such as streams, (crater) lakes, sea and snow (Fig. 2.9. Darteville et al., 2002). Although these observations are rare, PDCs

flowing into the sea have been seen to generate small-scale explosions on interaction with the water (Cole et al., 1998, 2002). Small-scale experiments by Freundt (2003) replicated these observations in a flume. Heated ash (400 °C) interacted with a body of water, generating minor steam explosions. Experiments of Walder (2000b) modelled the dynamics between static hot pyroclastic material and snow. Results showed that interactions with the snow promoted rapid vaporisation and caused unstable fluidisation of the boundary between pyroclastic material and the snow. This caused bubbling of the material, convective particle movement and scouring between the boundaries.

Substrates can become water-laden and saturated due to rainfall, groundwater levels or melting of snow/ice beneath a PDC (Fig. 2.9). As a high-temperature PDC is transported over a water-saturated substrate, they can interact, forming a local incorporation of steam and moisture. The vaporisation processes, turning water into steam (referred to as “sediment flashing” within the literature; Wilson, 1980; Brown & Branney, 2013), are thought to increase the mobility of a current, forming an upward pore pressure gradient, which in turn may increase fluidisation (Branney & Kokelaar, 2002).

Finally, the ***pyrolysis of plant matter*** (Fig. 2.9) into charcoal fragments can be seen throughout ignimbrite deposits (Cunningham, 1964; Scott et al., 2008; Hudspith et al., 2010) and is often used in charcoal reflectance for temperature analysis of currents (Efford et al., 2014b). Furthermore, in modern-day large eruptions (Mount Pele, 1902; Mount St Helens, 1980; Montserrat, 2002), large areas of vegetation have been removed by PDCs moving over the area (Hudspith et al., 2010).

These examples highlight how moisture can be incorporated into a PDC system through pre-eruptive conditions and interaction with bodies of water, substrates, and atmospheric influences during propagation. Although minor, moisture incorporation can influence the behaviour and deposits of PDCs.

2.6.1 The temperature problem and phase changes

Measurements of PDC temperature have been derived from in-field measurements (Cole et al., 2002), charcoal reflectance analysis (Scott & Glasspool, 2005; Wibowo et al., 2018), pyroclast thermoremanent magnetization (Cioni et al., 2004; Benage et al., 2016) and vegetation analysis (Efford et al., 2014a). The temperature within a PDC system can vary widely. Low temperature (< 100 °C) currents are interpreted to form

from phreatomagmatic interactions (Sparks & Wilson, 1990; Yamamoto et al., 1999), while high temperatures currents are interpreted to form from magmatic processes and can reach more than 700 °C (Cioni et al., 2004; McClelland & Druitt, 1989; Bardot, 2000; Lesti et al., 2011). The temperature will depend on other external factors such as entrainment rate, current permeability of the system and external moisture incorporation (McTaggart, 1960; Sparks, 1976; Dufek, 2016; Benage et al., 2016; Breard et al., 2019; Shimizu et al., 2019).

In the upper regions of the flow, pressures may approximate atmospheric levels with cooler temperatures. Pressure and temperature will increase in the denser parts of PDCs (Breard & Lube, 2017). Changes in temperature and pressure can result in the conversion of water vapour into droplets (i.e., decrease in temperature, increase in pressure) or vice versa if heated/decompressed. Consequently, the moisture content in PDCs and resulting deposits can vary over time and space. For instance, the rapid transformation of water into steam during granular PDC interactions with wet substrates can create a new source of gas, enhancing the mobility and fluidisation of the current, while the influence of moisture from precipitation and atmospheric conditions may be more likely to affect the dilute portion of the current. All of these factors can modify the location and rate of gas to liquid (or vice versa) phase changes within the system.

Phase changes refer to the transition of water in its varying states (i.e., solid, liquid, and gas, Fig. 2.10). Vaporisation describes the transition of a liquid to a gas and typically occurs at high temperatures ($> 100\text{ }^{\circ}\text{C}$) and pressures (Pa). Condensation describes the transition of a gas to a liquid, where water vapour cools and forms water droplets. Therefore, at any point within a PDC system, depending on temperatures and pressures, condensation rates will change (Fig. 2.10).

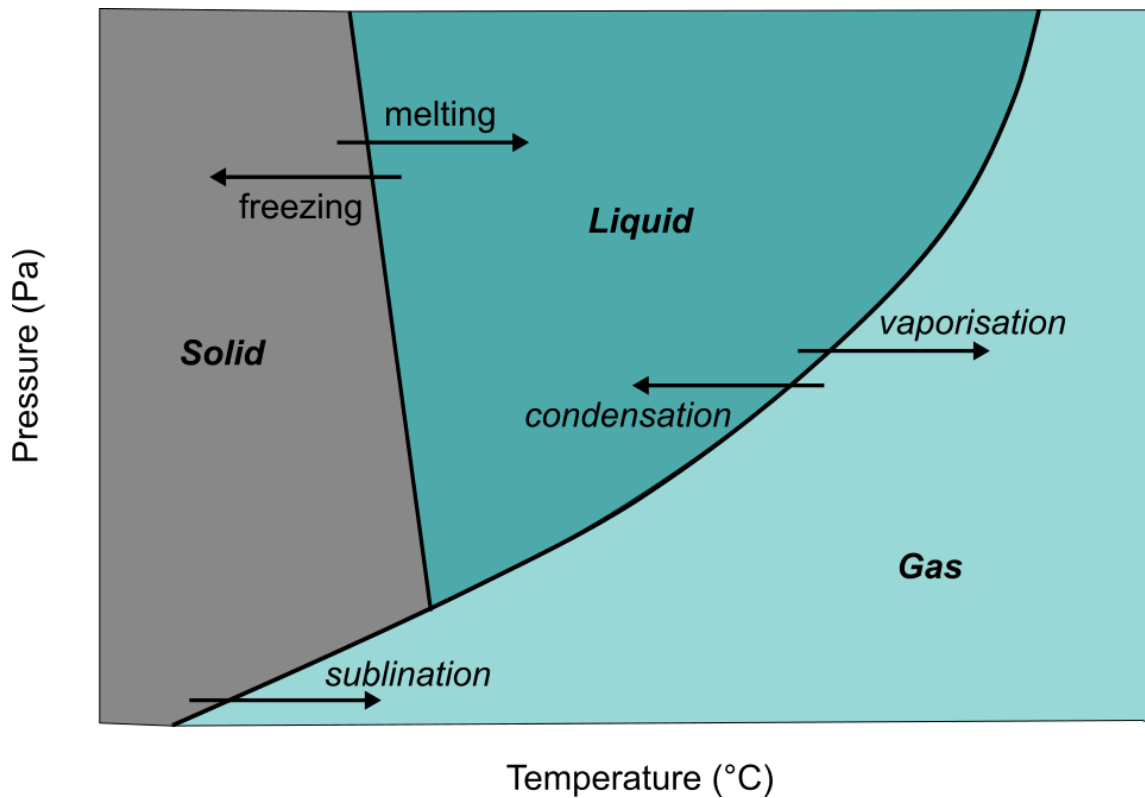


Figure 2.10. Phase diagram of water, controlled by temperature and pressure. At a certain pressure or temperature, a phase change will occur from gas to liquid by condensation and from liquid to gas by vaporisation.

When discussing the influence of moisture within a “system,” this term serves as a general framework for understanding its fundamental impacts. It does not capture the intricate complexities and interactions present in natural systems. Moisture interacts with and alongside complex relationships between temperature, pressure, particle characteristics, and environmental conditions that collectively shape the behaviour of PDC systems.

2.6.2 The influence of moisture on industrial applications

This impact of moisture on PDC dynamics is relatively unknown, but behaviours can be inferred from surrounding literature, such as the powder processing industry. Solid particles make up almost 50 % of the material used in industries like powder coating, pharmaceutical manufacturing, industrial and food processing, to name a few (Han et al., 2020; Macri et al., 2020). The particles are transported, so understanding the behaviours of the bulk flow during transport is pivotal to the efficiency of the operation (Marci et al., 2020; Ripp & Ripperger, 2010). Various parameters, such as changes in temperature, humidity, and particle characteristics, can contribute to interparticle cohesion. Temperature and moisture are often controlled during industrial processes due to their large effect on the fluidisation properties of a material. The presence of moisture

forms liquid bridges between particles, decreasing their ability to flow and leading to clumping, clogging, and particle aggradation (Lu et al., 2018; Groen et al., 2020).

2.6.3 Moisture influence on PDC flow and deposits

A PDC can become cold from the heat loss to the atmosphere and wet from the introduction of moisture (section 2.6). Decreasing temperatures may result in condensation of water vapour and the formation of capillary bonds between particles (Section 2.4, Fig 2.6). As seen in industrial applications, the presence of moisture in a granular current may alter current dynamics, such as fluidisation. This can induce material aggregation and clumping, potentially resulting in changes in flow behaviour, sedimentation rates, deposition, and resulting lithofacies (e.g., the presence of accretionary lapilli or ash pellets) (Brown et al., 2012; Szulc et al., 2024).

Ash aggregation describes the clustering of volcanic ash (< 2 mm) through contact or interstitial forces. Therefore, aggregation promotes a more rapid settling velocity of fine particles and introduces aggregates into transport and depositional processes (Gilbert & Lane, 1994; Rose & Durant, 2009; Brown et al., 2012). Aggregates can be described by the influence of water (dry to moist) and can form spherical to sub-spherical, layered and flattened pellets (Brown et al., 2010, 2012). Ash aggregates have been described extensively in ash fall deposits (Schumacher & Schmincke, 1991; Schumacher et al., 1995; Brown et al., 2010, 2012; Costa et al., 2010) and can also be observed in the deposits of PDCs (Schumacher & Schmincke, 1991; Brown et al., 2010). Therefore, aggregates can be useful as stratigraphic markers (i.e., hiatus of flow and settling of ash fall) and may allow the interpretation of internal conditions within a PDC (e.g., the presence of moisture; Gilbert & Lane, 1994; Brown et al., 2010; Van Eaton & Wilson, 2012).

The presence of liquid increases aggregation rates (Gilbert & Lane, 1994; Mueller et al., 2016). Experiments completed by Mueller et al. (2016) demonstrated that the rate of aggregation increases with humidity. Ash pellets form from the interaction of ash and moisture in a co-ignimbrite cloud or an eruption plume (Brown et al., 2010). If the pellets fall through a PDC they loft (moving vertically upwards and downwards) to accrete thin layers of ash, forming accretionary lapilli (Brown et al., 2010). Although liquid bonding forces are strong, they are unlikely to survive transport and depositional processes within a PDC, as evidenced by fragmented accretionary lapilli in deposits (Colombier et al., 2019; Brown et al., 2012). Therefore, it has been suggested that

another mechanism must be involved to strengthen the aggregate structure. The presence of a secondary variable, such as the precipitation of salt (Colombier et al., 2019; Rossi et al., 2021) and the presence of certain chemical compounds (NaCl, Mueller et al., 2016), can increase aggregate formation rates and strengthen the structure.

Ash aggregates have greater fall velocities than their surrounding particles, and therefore, in a PDC system, they may result in changes in size distribution (Lane et al., 1993; Gilbert & Lane, 1994; James et al., 2002). Ultimately, due to the variations in size, this could lead to changes in the fluidisation properties of the material, which will, therefore, impact sedimentation and depositional rates.

2.7 Modelling PDCs

Modelling provides an attractive way to simulate a range of geophysical currents that often-put lives at risk or equipment in danger of any in-situ monitoring (Wilson et al., 2014; Scharff et al., 2019). Furthermore, the simplification of modelling allows variables to be focused and refined before incorporating into larger, more complex systems. Analogue experiments validate data and underpin the basic geophysical properties that can then be applied to generate new or update existing numerical models.

2.7.1 Analogue Modelling of PDCs

Analogue models are attractive because they enable the modelling of complex natural geophysical systems and processes in less hazardous and more accessible environments (Roche et al., 2008; Rowley et al., 2014; Smith et al., 2018, 2020; Walding et al., 2022, 2024). Additionally, analogue experiments allow researchers to control and manipulate a wide range of specific parameters (i.e., size, concentration, moisture, density, shape and temperature), enabling more detailed investigation into controls and behaviours of natural processes.

The investigation of PDCs in analogue modelling has considered dilute currents (Andrews, 2014), dense currents (Rowley et al., 2014; Smith et al., 2018, 2020) and interactions of PDCs moving into water (Freundt, 2003), to name a few. In dense PDC modelling, the currents can be with or without an interstitial fluid phase being present (i.e., fluidised or unfluidised). Fluidisation in a PDC plays an important role in their high mobility and is thought to be a result of excess pore pressure and entrainment (Sparks, 1976, 1978; Wilson, 1984; Branney & Kokelaar, 1992, 2002; Roche, 2012;

Aravena et al., 2021; Breard et al., 2017, 2023; Salatino et al., 2024). The relatively new incorporation of fluidised material into experimental flumes has allowed new insight into PDC behaviour (Eames & Gilbertson, 2000; Roche et al., 2004; Girolami et al., 2008; Rowley et al., 2014; Smith et al., 2018, 2020). The current material can be fluidised in the hopper or lock-gate (Roche et al., 2002, 2004; Girolami et al., 2008) or by the upward movement of gas through a porous base (Rowley et al., 2014; Smith et al., 2018, 2020; Walding et al., 2022) and is determined by the minimum fluidisation velocity (U_{mf}) (Cocco and Chew, 2023). The U_{mf} of a material is determined where the influx of gas creates a high enough drag force to overcome the effect of gravity (Cocco and Chew, 2023)

Using Geldart's (1973) classification, materials can be categorised based on their fluidisation behaviour. Geldart (1973) separated powders into four distinct groups (A-D), differentiated by their fluidisation behaviours, where powders can exhibit a 'very poor' to 'excellent' fluidisation state based on particle size, shape and density. Group A (30 – 100 μm) and Group B (100 μm – 1 mm) powders tend to expand uniformly during fluidisation and often display the most favourable fluidisation behaviours (e.g., homogeneous bubbling and channelling). In contrast, the finest particles (< 20 μm) in Group C are dominated by the presence of interparticulate forces (e.g., electrostatic cohesion and van der Waals). Therefore, fluidisation behaviours are usually poor. Group D (> 1 mm) particles are the largest and require higher gas velocities for effective fluidisation. Group D has moderate to poor fluidisation and often demonstrates slugging, channelling, and spouting behaviours (Leturia et al., 2014).

To match the fluidisation behaviours of PDCs and to minimise variability in other particle parameters such as shape, density, and roughness, the most common analogue material used to date are ballotini beads, commonly Geldart Group A and B. Using mean particle diameters below ~150 μm generally ensures these materials can easily fluidise at gas velocities achievable in the laboratory (Roche et al., 2004; Montserrat et al., 2012; Rowley et al., 2014; Breard et al., 2019). The benefits of using ballotini are that, as well as their excellent fluidisation behaviours, they are widely available for use. However, they do not capture the total particle variability of natural pyroclastic material.

In small-scale experiments, natural pyroclastic material has been used to investigate gas escape structures and flow behaviour (Roche et al., 2001, 2004; Dellino et al., 2007).

However, the high degree of polydispersity of natural material (e.g., density, size, roughness, composition) can introduce challenges such as scaling limitations and complications with uniform fluidisation (Wilson, 1984). Some of these issues have been mitigated using large-scale flow experiments which use natural, representative pyroclastic samples which can match bulk flow properties of natural PDCs over longer timescales (Dellino et al., 2007, 2010; Lube et al., 2015; Brosch et al., 2021).

2.7.2 Numerical Modelling of PDCs

Numerical modeling is a crucial tool in advancing our understanding of PDCs. This approach integrates mathematical, physical and chemical equations to approximate and validate PDC behaviours, deposits and analogue models (Kelfoun, 2017; Kavanagh et al., 2018). Importantly, numerical models play a vital role in improving hazard assessments of PDCs (Rossano et al., 2004; Kelfoun, 2017; Lube et al., 2020).

Modeling PDCs is challenging due to the complex parameters involved (Dufek, 2016). These can include current concentrations, pore-pressures and fluidisation, particle characteristics, unsteadiness and entrainment (Esposti Ongaro et al., 2020). In addition, secondary interactions, such as: temperature, substrate entrainment, erosion, remobilisation, deposition, fragmentation, aggregation, meteorological conditions, rheology, topography and uniformity through time introduce further complications and computational expenses. These parameters are incorporated into numerical models using simplified equations of mass, momentum and energy (Esposti Ongaro et al., 2020).

Numerical models of PDCs have focused on steady dilute or dense regions of the currents eventually evolving into more sophisticated transient and multiphase models in a 2D or 3D space (Sparks et al., 1978; Wilson et al., 1980; Valentine and Wohletz, 1989; Dobran et al., 1993; Neri et al., 2003; Darteville, 2004, 2005; Esposti Ongaro et al., 2011, 2020). The *depth averaged model* approach simplifies currents into stratified layers of particle concentration and density in terms of a “dilute” upper current and a “dense” lower current (Neri et al., 2007; Kelfoun, 2017; Shimizu et al., 2019; Shimizu et al., 2023), where the dilute region of the current is dominated by fluid-particle interactions, the dense region by particle-particle interactions and the overall behaviours are determined by the transfers of mass, momentum and energy between them (Shimizu et al., 2023). *Multiphase models* are more complex and use the compressive and incompressible Reynolds Average Navier-Stokes Equations (RANS) allowing the

transfer of equations between gas and solid mixtures in a continuum (Burgisser and Bergantz, 2002; Lube et al., 2020).

Numerical models can be useful to scale-up processes, incorporate a large range of fluid and particle regimes and gain an insight to internal processes (velocity, concentration, shear) at any point throughout the simulated current. Despite advances in numerical models and computational fluid dynamic (CFD) approaches, accurately simulating the full evolution and behaviours of PDCs remains a complex challenge (Doronzo et al., 2011; Lube et al., 2020).

2.8 Inspiration: Modelling cohesion in turbidity currents

Turbidity currents are the movement of sediment downslope, driven by gravity. The density contrast between the sediment and ambient fluid (water) is the main driving mechanism (Baas et al., 2005). Similarly to PDCs, the deposits of these currents (turbidites) show various sedimentary fabrics and structures which can be used to interpret processes that take place in deep-water currents (Marr et al., 2001). Turbidity currents were long modelled with no additional cohesive materials (i.e., clay, organic material), which contradicts what is widely observed in deposits. A recent effort to consider the role of cohesive materials has led to an understanding that their addition causes sediments to act differently (Project GEOSTICK 712525), thus, introducing new uncertainty and perhaps misinterpretation of behaviours, bedforms and deposits (Baas et al., 2016).

Adding cohesive materials into 3D flume experiments changed material properties and current behaviour (Baas & Best, 2002; Baas et al., 2009). With increasing clay concentration in the flow, flocs begin to form. Flocs are an aggregate of clay particles that result from van der Waals and electrostatic charges (Dyer & Manning, 1999; Baker et al., 2017; Baker & Baas, 2020). By increasing clay content further, the clay particles form strong liquid bonds between one another, called gelling (Baas et al., 2016; Baker et al., 2017). Furthermore, by increasing clay content, current behaviours can change, resulting in rheological and plastic changes in the current (Maar et al., 2001; Baas & Best, 2002; Baas et al., 2009, 2016). Baas and Best (2002) examined these flow behaviours in more detail and found that with increasing clay concentrations, the flow transitioned from an initial turbulence-dominated current to a region of laminar shear (plug flow). A transitional phase was also observed, where clay particles flocculated together but were easily broken and disrupted in high shear.

As a turbidity current passes over a substrate, it may erode (named bulking) or deposit, contributing to changing current dynamics (Parker et al., 1987). Parker et al. (1987, and references within) elucidated that with increasing entrainment of substrate material, a turbidity current may be able to self-accelerate.

Baas et al. (2016) demonstrated varying substrate-current interactions, the resulting deposits and the key parameters affecting the relationship between the substrate and the current. These relationships were described as by-passing, where the current neither erodes nor deposits material, so there is no interaction between the current and the substrate; deposition, where the particle settling velocity is greater than the shear velocity of the current; erosion, where the shear stress of the current is greater than that of the substrate; deformation, where the substrate deforms plastically; and mixing, where material is eroded and deposited resulting in a scoured surface with a mixed deposit zone containing both current and substrate material. These varying styles of interaction relate to the relationship between the current (i.e., erosive capability), the sediment and the substrate (i.e., the resistance of the substrate), which will depend on particle characteristics, such as size, shape, density as well as interparticulate forces (i.e., capillary and van der Waals). The understanding of current-substrate interaction in turbidity current research is similar to that of the flow boundary zone (FBZ) in PDCs. However, the FBZ model (Branney & Kokelaar, 2002) overlooks the complex properties of the substrate, a factor that has been neglected in the model.

The relationship between the flow and substrate has been observed through features like scour marks, rip-up clasts and impact marks (Marschalko, 1970; McCaffrey et al., 2001; Clark and Stanbrook, 2001; Eggenhuisen et al., 2011; Hofstra et al., 2015; Baas et al., 2021). These features are a direct result of the forces at the flow-substrate interface, which control the extent of erosion. Additionally, variations in topography, particle density, size, composition, moisture, and temperature further complicate flow and substrate behaviour (Baas et al., 2005, 2016; Meiburg and Kneller, 2010). Interaction between the flow and substrate may lead to erosion, bulking and material preservation. In natural systems, these processes can result in the removal or preservation of material packages and bulking. In PDC systems, bulking is less well understood but is thought to amplify the hazard as it can potentially increase the volume and mobility of the current (Mangeney et al., 2007, 2010; Roche et al, 2013; Farin et al, 2014; Dufrense, 2012).

2.9 Capillary Cohesion in PDC Modelling

A fundamental gap in PDC knowledge is understanding the effect of moisture, especially in small quantities. Moisture presence is indicated by pellet formation (Reimer, 1983; Schumacher & Schmincke, 1995; Brown et al., 2012; Diaz-Vecino et al., 2023) and interaction with bodies of water (Cole et al., 2002) yet has been neglected in current PDC research. Perhaps, similar to the discoveries in clay-rich turbidity currents, moisture-induced cohesion may fundamentally impact PDC behaviour and our stratigraphic understanding.

Analogue models have explored the effect of fluidisation in water-saturated conditions (Roche et al., 2001) and on steam generation on encountering water (Freundt, 2003; Dufek et al., 2007). But, in most analogue experiments, steps are taken to minimise the moisture content of the materials used to reduce the effects of cohesion. This typically involves drying samples in an oven for 24 hours to eliminate adsorbed moisture and reduce the impact of cohesion (Druitt et al., 2004, 2007; Girolami et al., 2008, 2015).

The research in this thesis have begun to explore the exciting behaviour of moisture in PDC systems. Moisture can have fundamental implications for runout, fluidisation, and resulting deposits. Therefore, moisture should be incorporated into experiments for a better overall understanding of PDC hazards and for more accurate and reliable data to be used in models for hazard planning and mitigation control.

2.10 Author's Perspective and Positionality

Over the past few decades, understanding of PDCs has increased from global contributions and multidisciplinary approaches. However, these enigmatic flows are still relatively poorly understood compared to other geophysical flows. This work aims to expand the knowledge surrounding the lesser-explored role of moisture on pyroclastic material behaviour, which I believe may be crucial in understanding PDC deposit architecture and flow dynamics in wet, humid environments or where water interaction is significant. In the subsequent chapters, an interdisciplinary approach integrating geotechnical, geomechanical and fluid dynamics perspectives is utilised to better understand capillary cohesion and its impact on fluidisation, material strength and shear behaviours.

At the core of this research is the ongoing effort surrounding integrating field studies, analogue models and numerical simulations into hazard planning and risk assessments.

This thesis emphasises the importance of continued contributions from multidisciplinary methodologies to benchmark PDC models accurately. This work aspires to contribute to future advancements in PDC modelling and hazard assessment by addressing the moisture component.

Chapter 3 : Cohesional behaviours in pyroclastic material and the implications for deposit architecture

3.1 Abstract

Pyroclastic Density Currents (PDCs) are hazardous, multiphase currents of heterogeneous volcanic material and gas. Moisture (as liquid or gas) can enter a PDC through external (e.g., interaction with bodies of water) or internal (e.g., initial eruptive activity style) processes and the presence of moisture can be recorded within distinct deposit layers. We use analogue experiments to explore the behaviour of pyroclastic material with increasing addition of moisture from 0.00 – 10.00 wt.%. Our results show that: 1) the cohesivity of pyroclastic material changes with the addition of small amounts of moisture; 2) small increases in moisture content change the material properties from a free-flowing material to a non-flowable material; 3) changes in moisture can affect the formation of gas escape structures and fluidisation profiles in pyroclastic material; 4) gas flow through a deposit can lead to a moisture profile and resulting mechanical heterogeneity within the deposit, and 5) where gas escape structure growth is hindered by cohesivity driven by moisture, pressure can increase and release in an explosive fashion. This work highlights how a suite of varied gas escape morphologies can form within pyroclastic deposits resulting from moisture content heterogeneity, explaining variation in gas escape structures as well as providing a potential mechanism for secondary explosions.

3.2 Introduction

Pyroclastic density currents (PDCs) are hazardous, rapidly moving and often high-temperature volcanic phenomena. These currents are multiphase mixtures of heterogeneous juvenile material, atmospheric gas, and accessory lithic fragments. The high mobility of PDCs has in part been attributed to the onset of fluidisation (Sparks, 1976, 1978; Wilson, 1984; Branney & Kokelaar, 1992, 2002; Roche, 2012; Aravena et al., 2021; Breard et al., 2017, 2023): the upward movement of gas counterbalances the force of gravity and supports the flow (Sparks, 1976; Branney and Kokelaar, 2002; Cocco et al., 2014). The ability of the material to flow, or its ‘flowability’, depends upon interparticle forces (van der Waals, electrostatic or capillary forces). These forces can be influenced by bulk composition and material physical properties such as particle size, density, shape, and moisture content (Roche et al., 2004; Rios, 2006; Druitt et al., 2007; Leturia et al., 2014).

Fluidisation in PDCs can be initiated from formation and maintained throughout the course of the flow by transport on steep slopes, flow channelisation (Kelfoun & Gueugneau, 2022), substrate evaporation (i.e., steam generated from interaction with surfaces with moisture content or bodies of water), bulk self-fluidisation or ambient air entrainment (Sparks, 1978; Branney & Kokelaar, 2002; Chedeville & Roche, 2015; Valentine & Sweeney, 2018; Kelfoun & Gueugneau, 2022; Breard et al., 2023). Sedimentation fluidisation (or, hindered settling) and particle-self fluidisation is the interstitial gas movement driven by particle settling and compaction (Aravena et al., 2021; Roche, 2012; Breard et al., 2017; Chedeville & Roche, 2018). On or after deposition, the material will defluidise and particles segregate, forming gas escape structures (i.e., fines depleted elutriation pipes, Wilson, 1980; Cas & Wright, 1991).

Previous analogue investigations into fluidisation behaviours of pyroclastic material and segregation structures have been completed on dry (0 % water content; Wilson, 1980, 1984) and saturated (80 ± 15 % water content; Roche et al., 2001) natural pyroclastic material. Experiments completed by Wilson (1980, 1984) used non-cohesive, poorly sorted pyroclastic mixtures, and added an influx of gas into the deposit. This resulted in poor fluidisation, along with the creation of gas escape structures dictated by particle size and density. In a study by Roche et al. (2001), aqueous fluidisation within a water-saturated deposit of volcanic material was investigated. These findings revealed that fluid-escape pipes formed easily under conditions of low water flux, leading to localised separation of particle sizes and densities. Combining the results from both experiments, we can conclude that natural pyroclastic material will exhibit aggregative fluidisation, where fluidisation is inhomogeneous throughout the deposit through creation of bubbling and channelling (Branney & Kokelaar, 2002; Pacheco-Hoyos et al., 2020). This behaviour arises due to the particle size and density range, regardless of the medium used for fluidisation.

Understanding how moisture, through adsorption of atmospheric humidity, impacts powder material has important industrial applications. Experiments have explored fluidisation behaviours of industrial material with the addition of small volumes of moisture by controlling environmental humidity levels. With the introduction of moisture into a material, van der Waals forces are no longer dominant, and liquid bridges connect particles through capillary cohesion, resulting in poor fluidisation behaviours (Wormsbecker & Pugsley, 2008; Ludwig et al., 2020; Yehuda & Kalman, 2020). A study by Wormsbecker and Pugsley (2008) looked at gas fluidisation

behaviours in a semi-saturated (30, 20, 15 and 5 wt.% moisture) powder. Results showed a significant change in fluidisation behaviour associated with the addition of moisture, which were observed in conjunction with the drying states of the material from 30 to 5 wt.%.

3.2.1 Moisture in PDCs and their resulting deposits

Moisture (i.e., water vapour or liquid water) can enter a PDC system during formation at source or as PDCs propagate (Fig. 3.1). Eruption columns can be water-rich due to phreatomagmatic interaction (Self & Sparks, 1978; Hurwitz, 2003; Houghton et al., 2015; Shimizu et al., 2023) or atmospheric conditions (Vecino et al., 2022). During transport, internal clasts of juvenile magma will exsolve and release water vapour and other volatiles. Experiments have highlighted how magmatic clasts may hold 22-86 % vol. residual gas and water content during initiation of PDC transport (Sparks, 1978). Water vapour diffusion times depend on particle size, where larger, more porous clasts are thought to release gas more rapidly, and temperature changes, where cooler temperature reduces diffusivity of gas (Sparks, 1978).

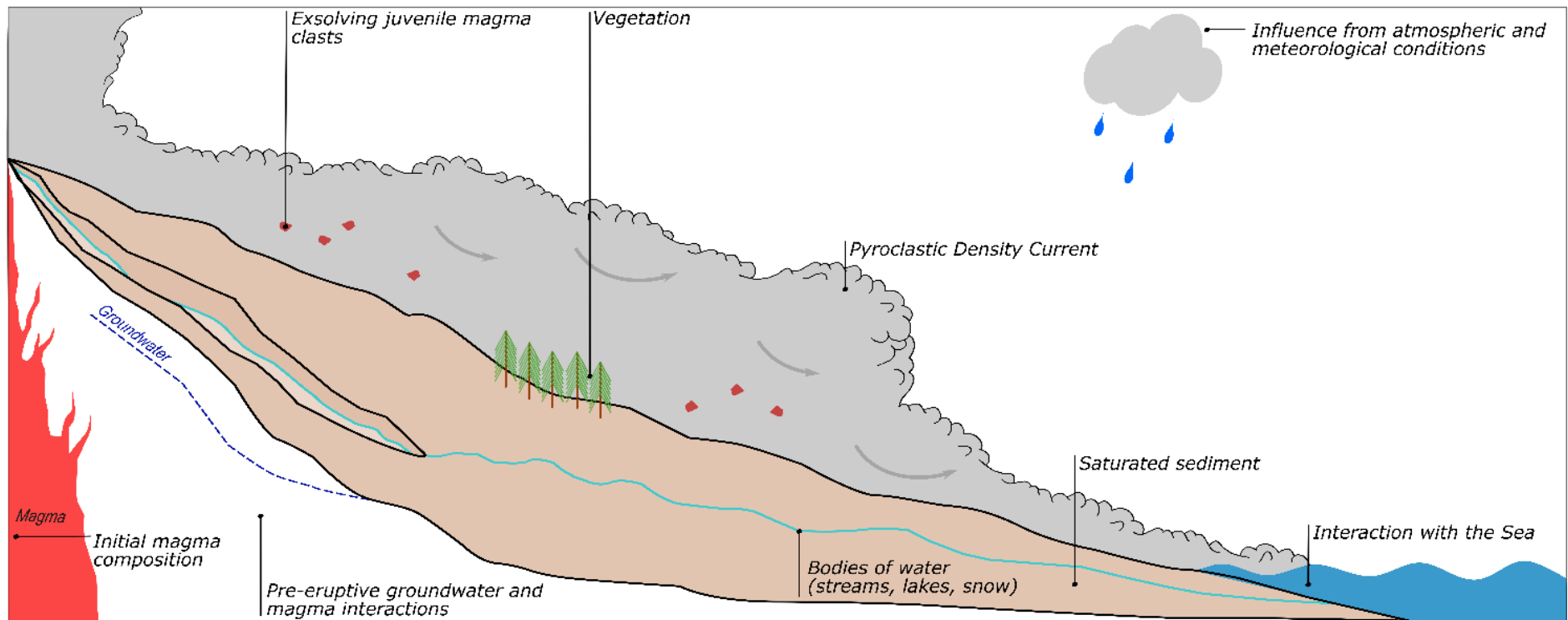


Figure 3.1. Schematic illustration of a PDC interacting with sources of moisture across a landscape which have the potential to enter the PDC system and resulting deposits.

Moisture may be introduced through a combination of atmospheric (e.g., humidity; Pepin et al., 2017; Camuffo, 2019), topographic (e.g., height; Barclay et al., 2006; Duane et al., 2008; Hartman, 2016), climatic (e.g., global location; Barclay et al., 2006) and meteorological (e.g., precipitation) conditions. Furthermore, periods of intense rainfall have been proposed to affect the onset of volcanic activity (Barclay et al., 2006; Sahoo et al., 2022 and references therein). Matthews et al. (2009) documented that within 24 hours of heavy rainfall, the probability of lava dome collapse at Soufrière Hills Volcano, Montserrat (during the period 1998-2003) increased, resulting in higher moisture availability to the resulting PDCs.

Interaction with external bodies of water (i.e., streams, lakes, sea, snow; Darteville et al., 2002; Cole et al., 1998; 2002), water saturated substrate (Moyer & Swanson, 1987; Brown & Branney, 2013; Gilbertson et al., 2020) or by the incorporation of vegetation (as observed at Mount Pelé, 1902; Mount St Helens, 1980; Montserrat, 2002; and Fuego Volcano, 2018) can also contribute to moisture within the PDC system. Therefore, we expect moisture content in PDCs and their resultant deposits to be variable in time and space, for example we can expect higher water contents in deposits near bodies of water (i.e., following PDC interaction with a lake or sea water) than perhaps in areas where very small amounts of juvenile water are contributing to the overall moisture content (i.e., exsolving juvenile clasts).

The presence of moisture within PDCs can be demonstrated by the presence of peculiar features in their deposits. Moisture has been linked to the formation of wet ash aggregates (e.g., pellets) in pyroclastic deposits (Brown et al., 2010; Van Eaton & Wilson, 2013), to elutriation pipes that are rooted in areas of evaporating moisture (i.e., vegetation or water-laden sediments; Pacheco-Hoyos et al., 2020) or by secondary hydroeruptions forming in deposits overlying moisture-rich areas (e.g., Mount St. Helens; Moyer & Swanson, 1987). The influence of these relatively small additions of moisture into a PDC system has been largely ignored in analogue and experimental studies, due to the difficulty of using and controlling the characteristics of moisture-affected material. Therefore, prior to experiments, material is generally dried to remove any residual moisture (Druitt et al., 2004, 2007; Girolami et al., 2008, 2015).

3.2.2 Capillary cohesion

The presence of moisture in a PDC, or in a subsequent deposit, will result in cohesive forces within the interparticulate space. A PDC can reach temperatures $> 1000\text{ }^{\circ}\text{C}$ and

the resulting deposit can maintain high temperatures for extended periods of time (Dufek, 2016; Riehle et al., 1995), and it has been assumed that at these temperatures the dominant cohesive forces will be electrostatic and van der Waals forces (Branney & Kokelaar, 2002). However, with increasing distance and entrainment, temperatures will decrease (Benage et al., 2016; Dellino et al., 2021; Pensa et al., 2023) and the introduction of moisture will likely lead to the formation of capillary bridges ('capillary condensation'; Ma et al., 2019), resulting in a change of the dominant interparticulate forces. This is described in Telling et al. (2013), where electrostatic attraction has been observed to be dominant only where water vapour (i.e., humidity) was lower than 71 % and in Chigira and Yokoyama (2005), where capillary cohesion became the dominant cohesive force with the addition of moisture into the granular material.

Previous studies have shown that an increase in water content leads to a drastic change in the physical properties of a given material. For example, in sands, capillary forces were seen to affect the tensile strength of the material until reaching a water-saturated state (Kim & Sture, 2008; Chen et al., 2021). Therefore, at lower temperatures it is highly likely that the introduction of moisture into the dynamic (current) and static (deposit) regions will induce variations in material properties. Changes in tensile strength and yield stress may determine how resistant a material is to shear and erosion and are important in understanding the flow properties of a material (Pierrat & Caram, 1997; LaMarche et al., 2016). Within a PDC deposit, such changes may also influence defluidisation through gas escape.

The experiments detailed herein assess the impact of the addition of small volumes of moisture within natural pyroclastic material. We explore the resulting variations in terms of fluidisation and particle segregation behaviours. Our results provide new and novel insights into the variation of gas escape behaviours and resulting secondary explosions in a defluidising PDC deposit.

3.3 Methodology

3.3.1 Source material and sample preparation

Unconsolidated material collected in 2009 from the 2006 Tungurahua, Ecuador, eruptions (provided by U. Küppers, LMU Munich) has been subjected to a range of characterisation tests to elucidate flowability properties and variations with moisture content. The studied material is dark grey/brown and andesitic in chemistry and was sampled from the PDC material deposited during the 2006 VEI 3 eruption (Eycheenne et

al., 2012). The PDCs, formed from the destabilisation of erupted deposits at the vent (Douillet et al., 2013), reached a maximum of 8.5 km from source and descended 2600 – 3000 m altitude (Hall et al., 2007; Kelfoun et al., 2009).

Samples were dried in an 80 °C oven for 24 hours to ensure the removal of residual and adsorbed moisture and agglomerations were broken-up by sieving prior to addition of water. The experiments were completed using 6 samples of the Tungurahua pyroclastic material (Fig. 3.2, V1 – V6). Samples V1, V4, V5 and V6 were sieved into desired particle size distributions, whereas samples V2 and V3 were kept as sampled at source (ranging from > 74 - 300 µm). For the series of characterisation tests, water was added to the samples based on weight percentage (0.00, 0.25, 0.50, 1.00, 2.50, 5.00, 7.50, 10.00 wt.%). Finally, samples were stirred thoroughly to ensure a homogeneous moisture distribution. All experiments were carried out at room temperature. Whilst the role of temperature may be important in natural material, we were unable to control for this variable in these experiments.

3.3.2 Material characterisation and cohesive behaviour tests

3.3.2.1 Particle size and shape analysis

Particle analysis of the pyroclastic material was undertaken using a CAMSIZER X2.

This uses particle imaging to build particle shape and size characteristics for dry samples. The maximum resolution for particle size and shape of the CAMSIZER is 0.8 µm per pixel. Particles were sieved prior to using the CAMSIZER and samples < 1000 µm were used. Any results from the CAMSIZER erroneously returned as > 1460 µm were removed. The CAMSIZER results allowed us to calculate the sphericity and cumulative size of the samples. The latter were run through GRADISTAT (Blott & Pye, 2001) to obtain the particle size mean ($(\bar{x}) \emptyset$), median ((\emptyset)), range (µm), sorting index ($(\sigma) \emptyset$), sorting ((σG)), skewness ($(Sk) \emptyset$), kurtosis ($(K) \emptyset$), and geometric mean (µm). Using methods from Breard et al (2019), we were then able to calculate the Sauter mean (m) and fines content (%) of the material. All characteristics of each sample are presented in Table. 3.1.

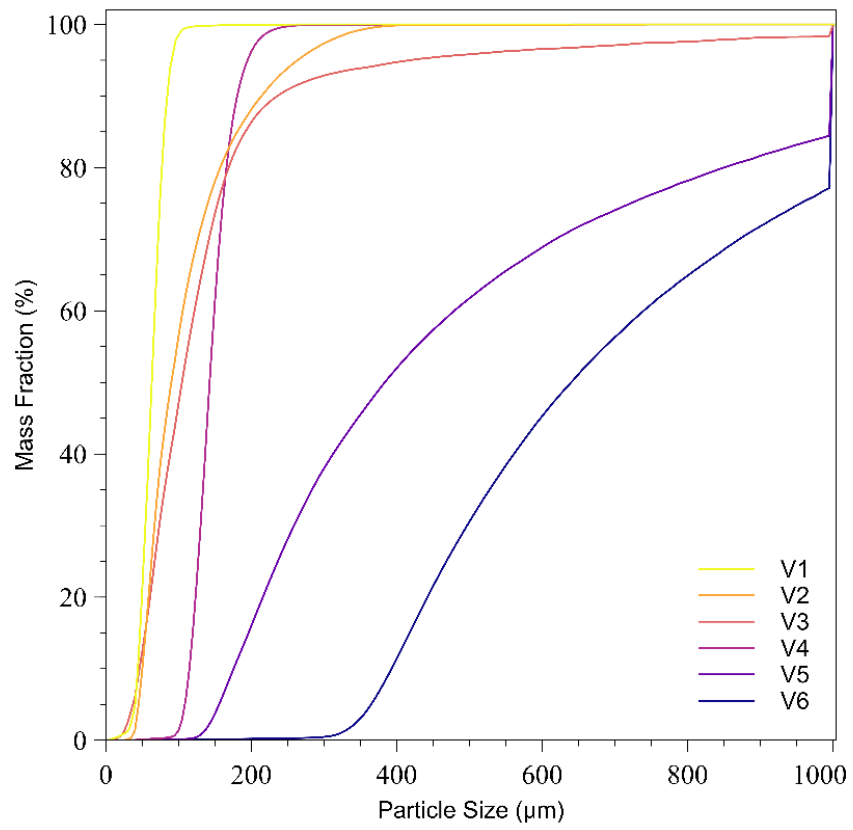


Figure 3.2. Particle mass fraction of volcanic material.

Table 3.1. Table showing particle size mean (logarithmic), particle size median (logarithmic), particle range, fines content (< 63 μm), geometric mean, logarithmic (ϕ) Method of Moments used for Mean, Sorting, Sphericity, Skewness, and Kurtosis. Sauter mean diameter calculated from Breard et al (2019). Geldart Group Classification (Geldart, 1973) based on mean size of particle.

Material	Particle Size Mean (\bar{x}) ϕ	Particle Size Median ϕ	Particle Size Range (μm)	Fines Content (%)	Sorting Index (σ) ϕ	Sorting (σ_G)	Sphericity	Skewness (Sk) ϕ	Kurtosis (K) ϕ	Sauter Mean Diameter (mm)	Geometric Mean (μm)	Geldart Group
V1	3.8	3.7	2.5 – 297.3	35.8	0.4	Well	0.8	1.9	17.0	0.06	72.9	A
V2	3.2	3.3	15 - 425	15.3	0.7	Moderate	0.8	-0.5	2.6	0.01	107.5	A, B
V3	3.1	3.1	5 - 1000	19.3	0.9	Moderate	0.7	-0.6	4.1	0.01	115.0	A, B
V4	2.7	2.7	20 – 650	0.2	0.3	Very well	0.8	0.1	8.5	0.01	153.5	A, B
V5	1.5	1.6	10 – 1000	0.1	0.8	Moderate	0.8	- 0.1	2.5	0.02	347.3	A, B
V6	0.8	0.8	10 - 1000	0.0	0.5	Well	0.8	0.6	8.3	0.03	557.1	A, B

3.3.2.2 Geldart's classification of powders

Geldart (1973) classified powders into four distinctive groups (A-D), each defined by their fluidisation behaviours, which are influenced by particle size and density. These behaviours span a spectrum from 'very poor' to 'excellent'. Group A (30 – 100 μm) and B (100 μm – 1 mm) powders exhibit the most favourable behaviours and expand during fluidisation. On the other hand, Group C, comprising the finest particles ($< 20 \mu\text{m}$) are governed by interparticulate forces. Group D ($> 1 \text{ mm}$) demands higher gas velocities for effective fluidisation. Both group C and D present moderate to very poor fluidisation behaviours, often expressing as slugging, channelling, and spouting (Leturia et al., 2014). The pyroclastic materials used in these experiments (Fig. 3.2) have particle size distributions from 2.5 to 1000 μm and using the particle mean, should exhibit fluidisation behaviours typically of Groups A and B in Geldart's classification.

3.3.2.3 Bulk and tapped density

Carr's Index and the Hausner Ratio are indicative of flowability and interparticulate behaviours (Hausner, 1981) and are useful tools in determining a material's ability to fluidise and flow (Table. 3.2). Carr's Index measures the strength and compressibility of a material (Eq. 3.3; Moondra et al., 2018). The Hausner Ratio determines the packing of the material and how prone the material is to compaction from external forces (Eq. 3.4, Yu & Hall, 1994; Abdullah & Geldart, 1999). A material with a low Hausner ratio indicates better flowability. These parameters are calculated from bulk and tapped density measurements.

Bulk and tapped density measurements describe the mass and volume ratio of a powder or granular material, without and with packing, respectively (Amidon et al., 2017). Tapped density experiments reflect the maximum density achievable through packing. The differences observed in bulk and tapped density measurements are influenced by cohesive attributes of particles (Deb et al., 2018) and can be impacted by the shape and size of a material (Amidon et al., 2017). Given that volcanic ash displays uneven and angular characteristics (see sphericity, Table. 3.1), not all spaces between particles are eliminated. Bulk and tapped density were calculated for dry samples herein to characterize cohesive behaviour prior to the addition of water (method adapted from United States Pharmacopeia, 2015).

Bulk density (ρ_b) was obtained by pouring 100 g of the volcanic material into a 250 mL cylinder and levelling when needed. The unsettled volume was measured, and bulk density calculated using Equation. 3.1. This procedure was completed three times per sample.

Table 3.2. Relationship between Carr’s Compressibility Index (CI), Hausner Ratio (HR), and flowability behaviours. From Gorle and Chopade, 2020.

CI	HR	Flowability
≤ 10	1.00 – 1.11	Excellent
11 – 15	1.12 – 1.18	Good
16 – 20	1.19 – 1.25	Fair
21 – 25	1.26 – 1.34	Passable
26 – 31	1.35 – 1.45	Poor
32 – 37	1.46 – 1.59	Very Poor
> 38	> 1.60	Very Very Poor

The cylinder was tapped at 150 taps/min, with volume measured every minute until levelled. Using the unsettled apparent volume and final tapped volume, the tapped density (ρ_t ; Eq. 3.2), Carr’s Index (CI; Eq. 3.3) and the Hausner ratio (HR; Eq. 3.4) were calculated.

$$\rho_b = \frac{m}{V_0} \quad (3.1)$$

$$\rho_t = \frac{m}{V_f} \quad (3.2)$$

$$CI = 100 \left(\frac{\rho_t - \rho_b}{\rho_t} \right) \quad (3.3)$$

$$HR = \frac{\rho_t}{\rho_b} \quad (3.4)$$

Where m is mass (g), V_0 is the unsettled apparent volume (mL) and V_f is the final tapped volume (mL) (Moondra et al., 2018).

3.3.2.4 Angle of Repose

The Angle of Repose (AoR) refers to the static, and dynamic, friction coefficient and can be investigated through static (funnel) and dynamic (rotating cylinder drum) methods (Al-Hashemi & Al-Amoudi, 2018) to explore cohesive behaviours of a

material (Montanari et al., 2017). AoR results can be interpreted in terms of understanding the flowability of a material (Table 3.3).

Table 3.3. Flowability based on angle of repose results (Al-Hashemi & Al-Amoudi, 2018).

Flowability	Angle of Repose (°)
Very free flowing	< 30
Free flowing	30 - 38
Fair to passable flow	38 - 45
Cohesive	45 - 55
Very Cohesive (non-flowing)	> 55

To determine the static angle of repose (SAoR) for each experiment, samples of 100 g of material were released from a funnel held 35 mm over a circular platform (Mean diameter = 85 mm). The height of the cone was measured, and the angle of repose calculated using Equation 3.5 (Beakawi Al-Hashemi & Baghabra Al-Amoudi, 2018). SAoR is given by L

$$\text{SAoR } (^\circ) = \tan^{-1}\left(\frac{2h}{D}\right) \quad (3.5)$$

Where h is height and D is base diameter (mm). When material did not release freely from the funnel, material was lightly agitated. If the height of the cone reached the base of the funnel, then the funnel was incrementally moved vertically to accommodate the growing cone. This was repeated three times for each experiment.

The Dynamic Angle of Repose (DAoR) was determined by rotating 100 g of material in a clear cylindrical drum at a constant rate (Smith, 2020). This was recorded on video and critical angle (the maximum angle prior to collapse) measurements analysed using ImageJ (Schneider et al., 2012). This was repeated three times.

3.3.2.5 Fluidisation behaviour tests

Experiments to determine the fluidisation behaviours of the pyroclastic material with increasing moisture contents were completed using a rectangular, near-2D fluidisation chamber with a porous base (following Gilbertson et al., 2020). Homogeneous samples of 200 g of pyroclastic material and water were placed into the chamber and carefully levelled. A manometer recorded basal pore pressure changes during each experiment. Gas velocity of dry compressed air (m/s) was increased incrementally until either a

stable, channelised bubbling fluidisation state was achieved, or large amounts of winnowing or pressure build-up occurred. To limit the effects of drying from basal air flow, experiments were carried out with gradual increases in gas flow rate (5×10^{-4} to $2.08 \times 10^{-3} \text{ m s}^{-1}$) for dry sediments and 4.51×10^{-3} to $7.64 \times 10^{-3} \text{ m s}^{-1}$ for moisture added sediments) over a period of 01 min 11 s to 23 min 51 s.

3.3.3 Limitations

To better isolate the effect of moisture on material behaviours, a number of other parameters linked to natural PDCs and their deposits were either held constant or constrained. In nature, pyroclastic material is more polydisperse, and showcases a wider distribution of size, density, shape, composition, and temperature, than the material used in this work. The limitations on the particle size in our experiments originate from: 1) the size of the fluidisation tank and the maximum gas velocity, which dictate the range of material particle sizes that can be used; and 2) the need for effective control of the influence of moisture addition. For instance, the finer fractions of material, characterised by an increased surface area, are more likely to be affected by moisture-related effects (Huang et al., 2009). The fines content of a material governs fluidisation, and fine material will readily fluidise at a lower minimum fluidisation velocity than a coarser material (e.g., blocks from a block and ash flow) (Gilbertson et al., 2020). The samples used in this study are analogous to natural fine fractions of pyroclastic material, such as the fines content of a lapilli-tuff ignimbrite facies, an ash-dominated ignimbrite facies, or a block and ash flow deposit.

Throughout the experiments within this work, samples were dried in an oven at 80°C for 24 hours to facilitate the removal of residual and adsorbed moisture. However, it should be noted that this approach likely did not remove all moisture, as some adsorbed moisture contained in volcanic glass, which would be liberated at higher temperatures ($<500^\circ\text{C}$), would remain. Therefore, the values presented are not absolute but instead represent a percentage increase in addition to the adsorbed moisture within the glass. The exsolution of moisture rates from volcanic glass is not directly comparable and would likely have little effect over the timescales of these experiments. For better quantification of the water content in the pyroclastic material used, thermogravimetric analysis may provide more accurate results.

Our work provides insight to the role of moisture content on pyroclastic material. In the discussion, we begin to explore how other parameters (e.g., size, shape) may impact the

cohesivity and material behaviour where appropriate. A multivariate analysis to quantify the relative control of moisture versus a wide range of other parameters would be an important follow-on study to this work.

3.4 Results

3.4.1 Material properties

The bulk and tapped densities were calculated for pyroclastic samples ranging in sizes from 3.8 ϕ (V1) to coarsest 0.8 ϕ (V6). With increasing particle size, bulk and tapped densities generally decrease (Table. 3.4, Appendix A¹, Supplementary Material 3A). Material flowability, as determined by the Hausner Ratio and Carr Index, is good (V2, V3, V6) and excellent (V1, V4, V5) under the 0 wt.% moisture conditions. The change in flowability between V5 and V6 likely reflects the large increase in geometric mean from 347 (V5) to 557 μm (V6) (Table. 3.1). The excellent flowability in V1, V4 and V5 is likely related to the smaller particle range in V1 and V4 and the low fines content in V5.

Table 3.4. Loose and tapped bulk density, the Hausner ratio, Carr Index and Flowability. Uncertainty and Error (\pm) of the experiment.

Material	Loose Bulk Density (kg m^{-3})	Tapped Bulk Density (kg m^{-3})	Hausner Ratio	Carr Index	Flowability
V1	1310 (± 17)	1420 (± 20)	1.08 (± 0.02)	7.73 (± 0.15)	Excellent
V2	1320 (± 17)	1550 (± 24)	1.18 (± 0.02)	15.13 (± 0.31)	Good
V3	1380 (± 19)	1610 (± 26)	1.17 (± 0.02)	14.28 (± 0.30)	Good
V4	1320 (± 18)	1420 (± 20)	1.07 (± 0.02)	6.59 (± 0.13)	Excellent
V5	1280 (± 16)	1440 (± 21)	1.12 (± 0.02)	10.68 (± 0.21)	Excellent
V6	1180 (± 14)	1370 (± 17)	1.15 (± 0.02)	13.37 (± 0.24)	Good

¹ All appendices for Chapter 3 are in Appendix A. Herein, this will be referred to as ‘Supplementary Material 3A, B, C’ etc...

The static angle of repose (SAoR) increases with increasing moisture across all volcanic samples (V1-6; Fig. 3.3, Supplementary Material 3A). For the 0 wt.% moisture condition, the SAoR ranges from $29^\circ \pm 0.04$ (V2, V4, V5) to $32^\circ \pm 0.04$ (V1, V3). Interestingly, these results show that under 0 % moisture conditions, the SAoR is broadly similar (within 3°) regardless of particle size or sorting (Fig. 3.4a).

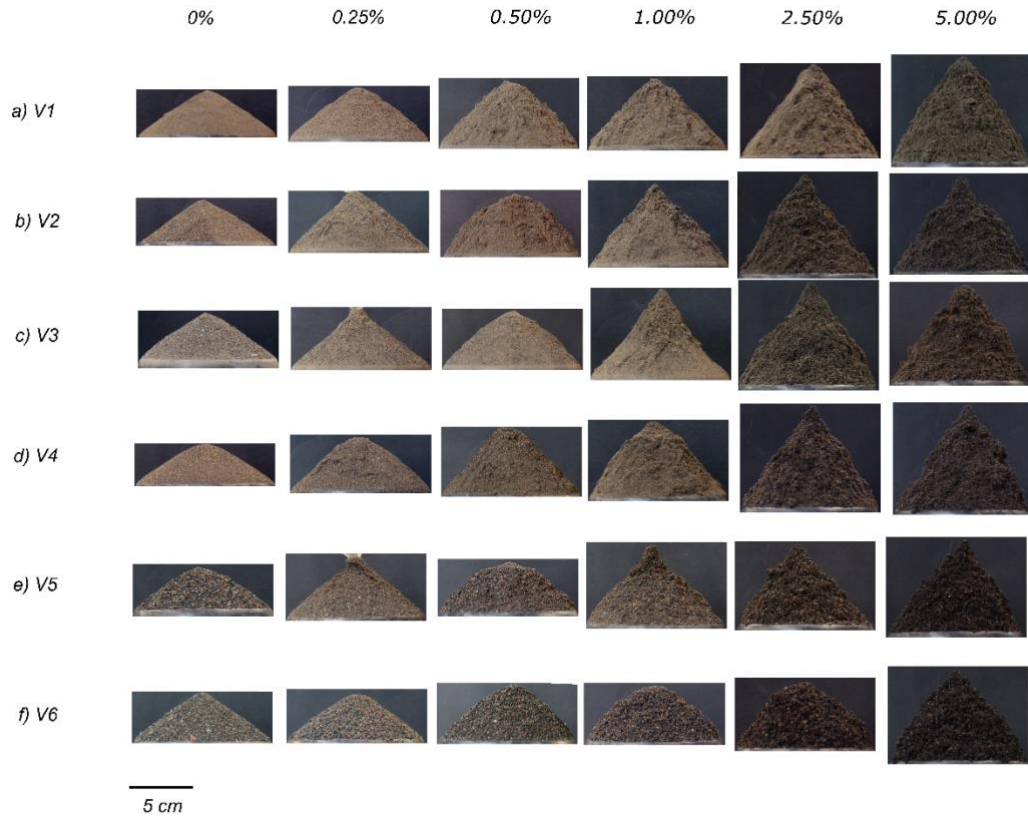


Figure 3.3. Representative static angle of repose (SAoR) cone formation of V1 – V6 at 0 – 10 wt.% moisture addition. Numbers next to each cone show the average cone height ($^\circ$).

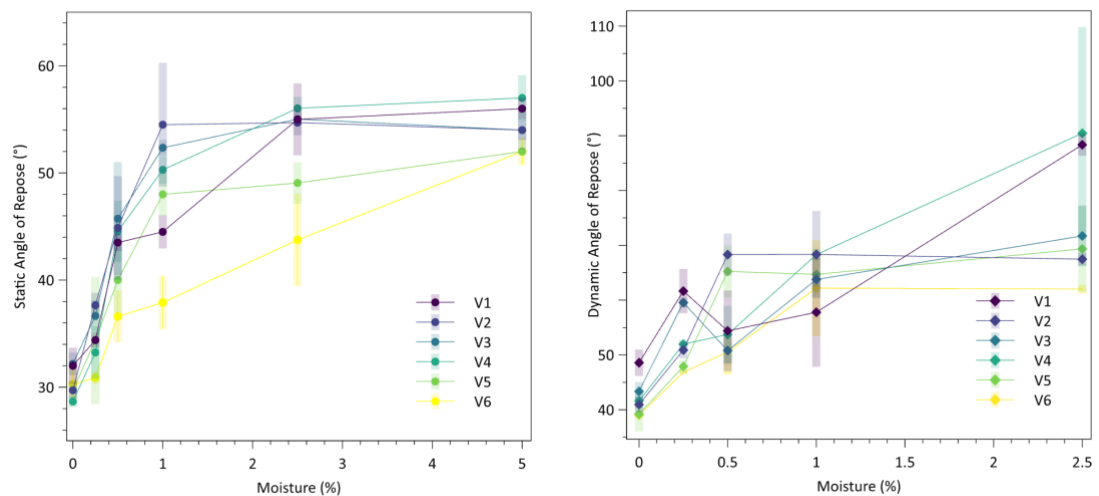


Figure 3.4. a) SAoR for volcanic material with varying moisture percentages with standard deviation error bars; b) DAoR critical angle of volcanic material with varying moisture percentages with standard deviation error bars.

When increasing moisture contents to 5 wt.%, the SAoR values increase to approximately double those achieved with 0 wt.% moisture. However, this relationship is not linear with increasing moisture content (Fig. 3.4a). All materials show a rapid increase in SAoR with moisture to around $36 - 46^\circ$. But beyond a moisture content of 0.5 wt.%, a division is evident between the fine and coarse mixtures; those with lower Sauter mean diameters (V2, V3 and V4) increase to SAoR values of $\sim 55^\circ$ at moisture contents of 2.5 wt.% before becoming invariant with additional moisture content. Mixtures with higher Sauter mean diameters (V5, V6) mostly show a more gradual increase in SAoR with moisture content. V5, with a Sauter mean diameter of 0.02 mm, shows an intermediate behaviour, while V6, with a Sauter mean diameter of 0.03 mm, shows a more linear relationship for SAoR with moisture between 0.5 – 5 wt.%. However, V1, with a Sauter mean diameter of 0.06 mm, shows a rapid increase, similar to V2, V3 and V4. This may be due to the high fines content and sorting index (Table. 3.1).

The sphericity of the samples is shown in Table 3.1. Samples used are from the same parent material, therefore, we see no large variation in particle shape (0.74 – 0.84 in sphericity). In general, the finer material is slightly more angular than the coarser material. We conclude that any differences in sphericity have not influenced the results and small changes in sphericity are not directly related to the cohesive behaviours seen in our experiments.

The results indicate that SAoR is sensitive to increasing values of water in the materials and that relatively small weight percentages can produce very different cohesivities within the mixtures. It is notable that fines-rich mixtures are particularly sensitive to moisture related cohesion, notably at < 2 wt.% moisture, and this is thought to be due to increased surface area and Sauter mean diameter.

Figure 3.4 also shows the relationship of Dynamic Angle of Repose experiments (Fig. 3.4b). Generally, and similar to the SAoR results, there is an increase in the DAoR with increasing moisture. However, in experiments with increasing moisture levels (> 2.50 wt.%), the material was observed to clump, slide, and stick to the outer walls of the drum, complicating the results. Nonetheless, it is important to observe that the Sauter mean relationships detected within the SAoR experiments are not replicated in the DAoR tests.

3.4.2 Fluidisation experiments

Fluidisation behaviours were described via sidewall video analysis of the fluidisation chamber. The observation of gas escape structures (i.e., bubbling, channelling, pocketing, explosive channelling, cracking; Fig. 3.5 a-e) and gas velocity measurements were recorded at varying moisture levels (Fig. 3.6).

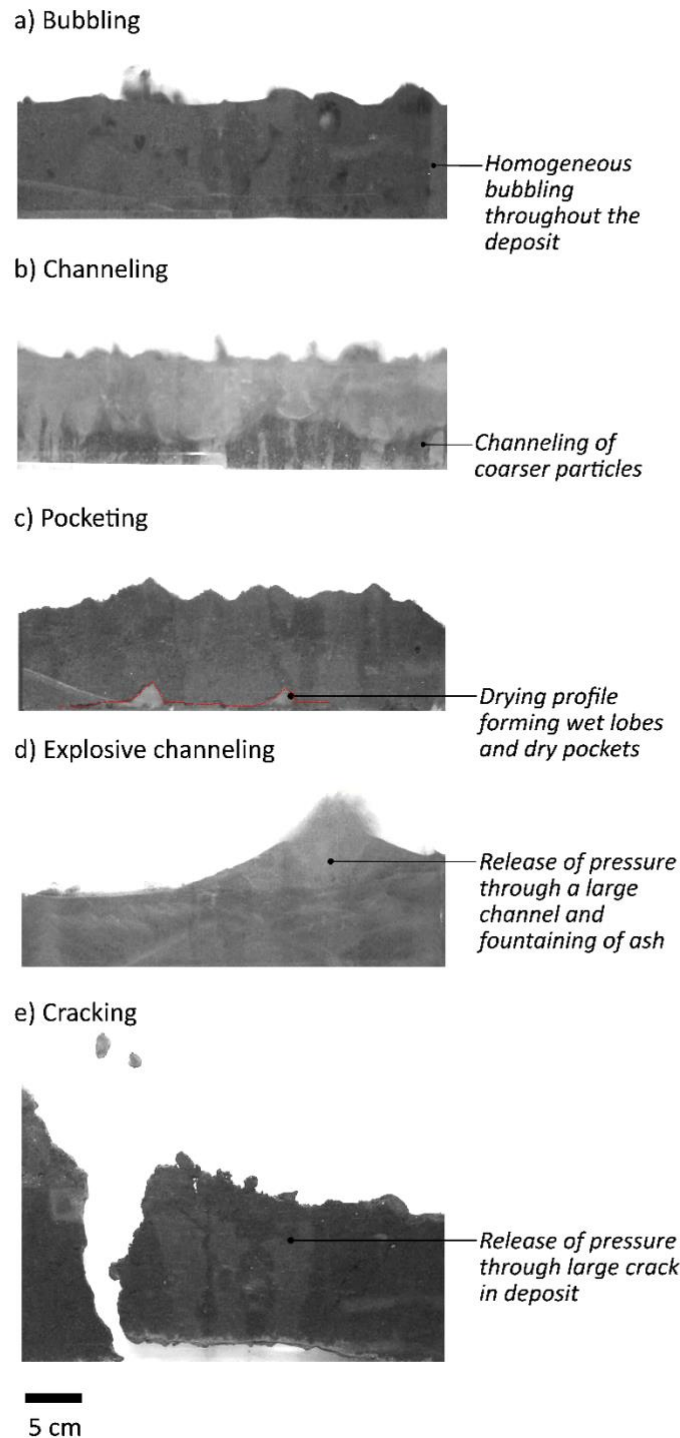


Figure 3.5. Examples of the structure recognised across the experiments.

Bubbling gas escape (Fig. 3.5a) is seen initially in most experiments, where gas bubbles rise from the influx of gas within the deposit. With increasing gas flux, this can lead to channelling, where material is sorted through vertical channels or via pipe structures forming within the deposit (Fig. 3.5b). Drying profiles that migrate through the deposit

are shown in Fig. 3.5c. As drying migrates with non-uniformity in the vertical deposit, formation of areas of wet lobes and bubbling dry pockets can be observed, referred to as pocketing (Fig. 3.5c). Explosive channelling can also be observed in some experiments (Fig. 3.5d); as the material dries from beneath, the upper wet deposit inhibits gas escape and causes a pressure increase and subsequent release (OR3B.1, Supplementary Material 3B). Finally, under the highest moisture contents, material does not form any of the gas escape structures outlined above. Instead, pressure builds until the deposit fractures into cracks where gas can easily permeate through (Fig. 3.5e; OR3B.2, Supplementary Material 3B).

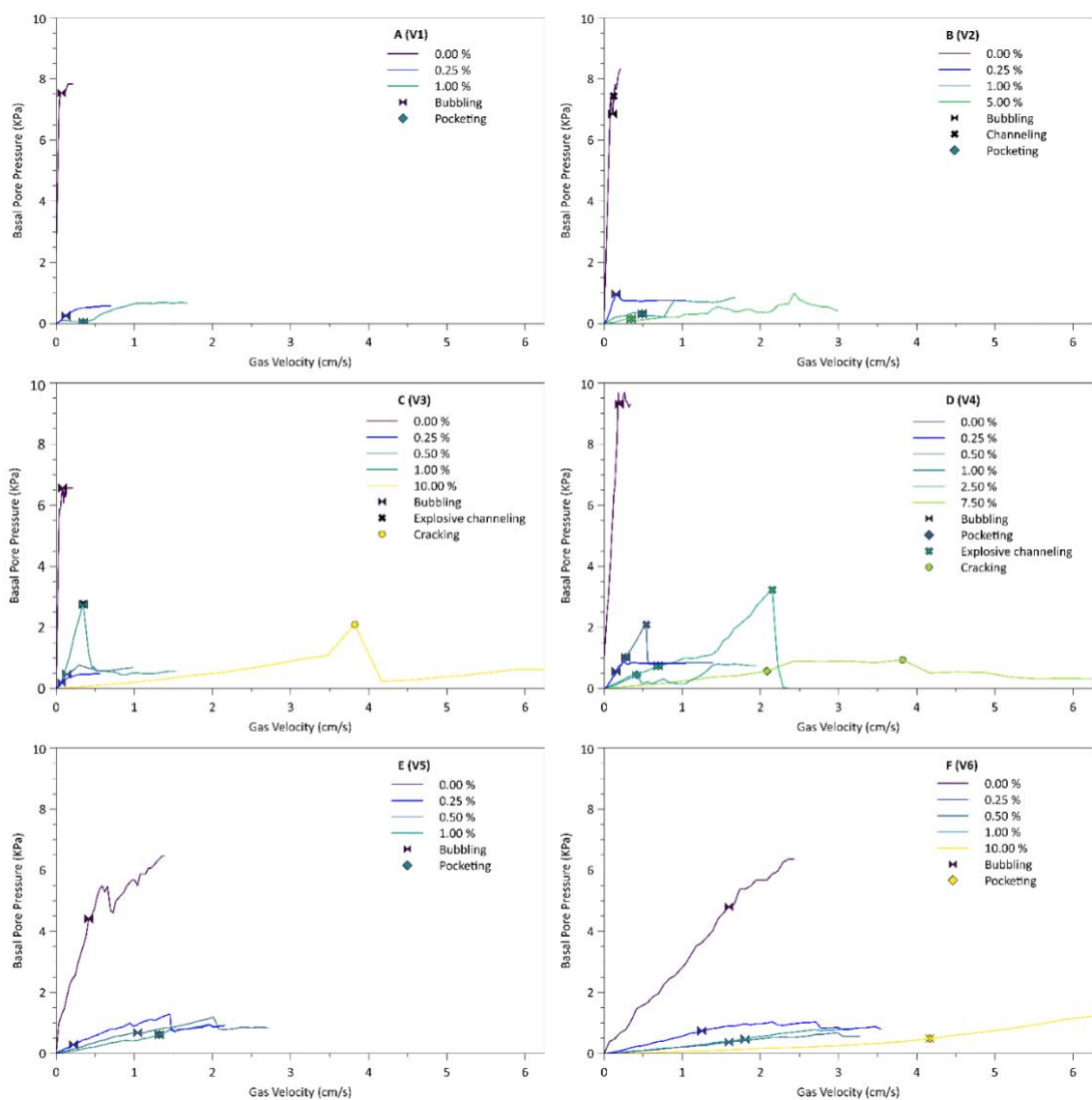


Figure 3.6. A-F Fluidisation profiles of V1 – V6 with increasing moisture (0.00 – 10.00 wt.%). Symbols show gas escape structure formation.

3.4.2.1 0.00 wt.% Moisture

At 0.00 wt.% moisture for mixtures with moderate sorting (i.e., V2, V3, V5), fine material migrates through gas escape channels (Fig. 3.5b) in the lower portion of the

deposit. Bubbling is first seen in the upper fine fraction of the deposit at a minimum gas velocity, U_{mb} , of 0.11 (V2), 0.08 (V3), and 0.42 (V5) cm/s. There is often a separation of fines bubbling in the upper layer, with a mid-area of coarse channelling at a minimum gas velocity for channelling, U_{mc} , of 0.13 (V2) and 0.10 (V3) cm/s as fines are being elutriated, and a coarse material layer at the base of the deposit. Bubbling only affects the finer material.

In the mixtures that are well to very well sorted (i.e., V1, V4), bubbles rise uniformly throughout the whole deposit with a U_{mb} of 0.07 (V1) and 0.19 (V4) cm/s. Within the more coarse, well sorted material (V6), bubbles migrate in a sluggish motion from the base of the deposit, with mostly bubbling (U_{mb} 1.60 cm/s) occurring in the upper half of the deposit and channelling in the lower. This reflects the slight particle size variation of the material used, and therefore the U_{mb} of the coarser material (Fig. 3.5b).

3.4.2.2 0.25 wt.% Moisture

At 0.25 wt.% moisture contents, similar behaviours are observed for V3 (U_{mb} 0.069 cm/s), V5 (U_{mb} 0.22 cm/s) and V6 (U_{mb} 1.25 cm/s) as are observed for 0.00 wt.% moisture. For V2 (U_{mb} 0.15 cm/s), V1 (U_{mb} 0.13 cm/s) and V4 (U_{mb} 0.15 cm/s), bubbling begins at the base of the deposit. However, as the surrounding wet deposit begins to dry, this dry material becomes incorporated into the bubbling deposit. In V2, we again see a separation of channelling and bubbling in the lower and upper deposit.

3.4.2.3 0.50 wt.% Moisture

At 0.50 wt.% moisture, a drying profile can be observed throughout most of the deposit (V4, V5, V6). In the V4 sample, as drying at the base moves throughout the deposit, dry material begins to bubble (U_{mb} 0.28 cm/s), and pressure slowly increases. This is released suddenly (explosive channelling) at 0.54 cm/s through a large channel which cuts through the wet, upper part of the deposit. As the surrounding wet material then begins to dry, it becomes incorporated into the bubbling deposit. In the V5 sample, the drying profile forms lobes of wet material and pockets of dry material. The dry pockets slowly grow until reaching the upper deposit and begin to bubble (U_{mb} 1.04 cm/s). With continued drying as the experiment progresses, similar behaviours to the 0.25 wt.% and 0.00 wt.% moisture levels experiments are observed. After the drying profile has moved through the deposit of V6, similar behaviours to the 0.25 wt.% and 0.00 wt.% moisture experiments are observed (U_{mb} 1.60 cm/s).

For the V3 material, channels of coarser material begin to slowly move towards the surface. Material begins to dry and is then incorporated into the bubbling deposit (U_{mb} 0.14 cm/s).

3.4.2.4 1.00 wt.% Moisture

At 1.00 wt.% moisture, V1, V2, and V4 show portions of material at the base of the deposit drying in pockets. The dry material begins to bubble (U_{mb} 0.35, V1; 0.49, V2; 0.42, V4 cm/s) and as the surrounding wet material begins to dry, it is incorporated into the bubbling deposit. In V5 and V6, a distinctive drying profile moves through the deposit. Again, this creates dry pockets of bubbling material (U_{mb} 1.32, V5; 1.81 V6 cm/s) and wet lobes. In V3, pressure slowly builds as gas velocity is increased. Pressure is suddenly released through the formation of an explosive channel (U_{mb} 0.35 cm/s). The dry deposit then begins to bubble (U_{mb} 0.35 cm/s) and is slowly incorporated into the surrounding drying material.

3.4.2.5 2.50 wt.% Moisture

At 2.50 wt.%, behaviours of V4 show similar results to 1.00 wt.% moisture content: as the base dries, bubbling pockets are formed (U_{mb} 0.70 cm/s) in-between lobes of wet material. In V4, pressure builds until it is suddenly released through an explosive channel (U_{mb} 2.15 cm/s).

3.4.2.6 5.00 wt.% Moisture

At 5.00 wt.%, V2 shows the deposit drying at the base which forms drying and bubbling (U_{mb} 0.35 cm/s) in pockets, and wet lobes.

3.4.2.7 7.50 wt.% Moisture

At 7.50 wt.%, a clear drying profile forms through the V4 deposit, cracks begin to form and move through the deposit until reaching the top and collapsing into pieces (U_{mb} 3.82 cm/s). As gas moves through cracks, there is no dramatic rise and release in pressure.

3.4.2.8 10.00 wt.% Moisture

Finally, at 10.00 wt.%, V3 forms a clear drying profile within the deposit. Pressure builds before being released suddenly at U_{mb} 3.82 cm/s. This forms a large crack in-between wet material. V6 shows a clear drying profile, as pressure slowly rises as small pockets eventually form and dry material begins to bubble (U_{mb} 4.17 cm/s).

3.4.3 Key observations

The fluidisation experiments clearly demonstrate how small additions of water into pyroclastic material can greatly impact fluidisation behaviours and resulting gas escape structures of a defluidising pyroclastic deposit. Two key observations are apparent in the experiments: 1) the drying profile, and 2) pressure build up and release.

The dynamics of the drying profile, as the moisture content is impacted by the fluidising gas, exert a strong control on the distribution of gas escape features, with variations controlled by the grain size of the materials.

As gas flux is increased, a drying profile can move from the base to the top of the deposit. The drying profile forms more easily within the coarser materials (V3 – V6). The profile initially rises uniformly across the bed, before becoming irregular as it reaches the top of the deposit. These profiles are noted as they highlight vertical and lateral moisture heterogeneity within the deposit and their irregular structure determines the formation of drying pockets and wet lobes (Fig 3.5c). At low moisture percentages (< 2.50 wt.%) the drying pockets bubble and the wet lobes begin to dry before being incorporated into the pockets. However, at high moisture contents (> 2.50 wt.%), moisture rich lobes remain throughout the experiment, even at high gas velocities. This shows that within a defluidising deposit, a drying profile will lead to lateral and vertical variations in moisture.

In experiments with moisture contents of 0.50 – 10.00 wt.%, explosive channelling (V3, V4) and cracking (V3, V4) can occur. Across the experiments with 0.50 – 5.00 wt.% moisture contents, a wet impermeable cap was observed to form above the drier underlying deposits, with progressive drying of the vertical profile. Pressure builds under the cap and continues to rise with increasing gas velocity. This eventually results in explosive channelling and a sudden basal pressure drop as the overburden pressure is exceeded. In higher moisture levels (5.00 - 10.00 wt.%) experiments, the deposit does not dry as a relatively uniform rising profile. Instead, pressure builds as the gas velocity is increased until cracks form in the deposit. These cracks act as effective gas escape structures and release the pore pressure.

3.5 Discussion

The impact of moisture on pyroclastic material and PDC behaviour is poorly understood, with previous detailed investigations of fluidisation in pyroclastic material

having focused on dry (Wilson, 1980) and saturated (Roche et al., 2001) end members. However, direct observations have shown that variable amounts of moisture can enter a PDC system (Cole et al., 1998, 2002; Lipman, 2019; Vecino et al., 2022) and accretionary lapilli and ash pellets are believed to provide evidence for the presence of moisture within PDCs (Branney & Kokelaar, 2002; Brown et al., 2010; Druitt, 2014).

Our results show that for the pyroclastic material used within these experiments: 1) the cohesive behaviours and shear strength of pyroclastic material alters drastically, even with very small concentrations of moisture, 2) moisture addition into pyroclastic material can change flow property behaviours from free flowing to non-flowing; 3) changes in moisture affects fluidisation profiles and gas escape structures; 4) a defluidising deposit can lead to a drying profile, and therefore lateral and vertical heterogeneity within the deposit; and 5) pressure can increase where gas escape is hindered by moisture, which can cause dramatic releases of pressure in an explosive fashion. Here we discuss the implications of these findings.

3.5.1 Gas Escape Structures

A variety of gas escape structures were observed in the fluidisation experiments, with many of them related to moisture content. Here we define three main types of behaviour (Table. 3.5). In Type 1 (< 0.50 wt.% moisture) we see partial fluidisation and segregation of heterogenous material through bubbling and channelling. In material with a smaller size range, small vertical bubbling occurs across the entirety of the deposit. During Type 2 (0.50 – 5.0 wt.% moisture), an irregular drying profile develops and moves through the deposit from the base. As the drying profile grows, dry pockets of bubbling material begin to form in between irregular lobes of wet material. Explosive channelling also occurs, which releases pressure and facilitates quicker drying of the whole deposit. Finally, during Type 3 (7.5 – 10.0 wt.% moisture), similar lobe and pocket structures are formed to Type 2 but are accompanied by cracking processes, where fractures in the wet material form to accommodate rapid gas escape. Our experiments represent a defluidising deposit with dry air; in nature we may expect to see defluidisation of moist air, through contact with bodies of water, for example. Our results demonstrate that moisture addition may hinder or prevent fluidisation and gas escape; therefore, a wet air flux may display strikingly different results. This could not be tested experimentally in this work and would benefit from future investigation.

Table 3.5. Types of behaviour of gas escape observed with increasing moisture in volcanic material.

	Type 1	Type 2	Type 3
Moisture Range	0.00 – 0.25 wt.%	0.50 – 5.00 wt.%	7.50 and 10.00 wt.%
Bubbling	Yes	Yes	Yes
Channelling	Yes	Yes	No
Drying Profile	No	Yes	Yes
Pocketing	No	Yes	Yes
Explosive Channelling	No	Yes	No
Cracking	No	No	Yes

Roche et al. (2001) investigated the fluidisation behaviour of pyroclastic material where the material was saturated with water (aqueous state) and subjected to an increase in fluid velocity. The findings of Wilson (1980, 1984) and the experiments herein demonstrate gas escape structures forming from an aerated fluidisation state with an increase in gas velocity. In all experiments, aggregative behaviour was observed, and the gas escape structures that formed were consistently depleted in fines and enriched in dense and coarse material. Importantly, the research of Roche et al. (2001) revealed that aqueous gas escape structures (pipes) formed at lower fluid velocities than the aerated structures in Wilson (1980) (Fig. 3.7). This is due to water having a lower terminal velocity than air.

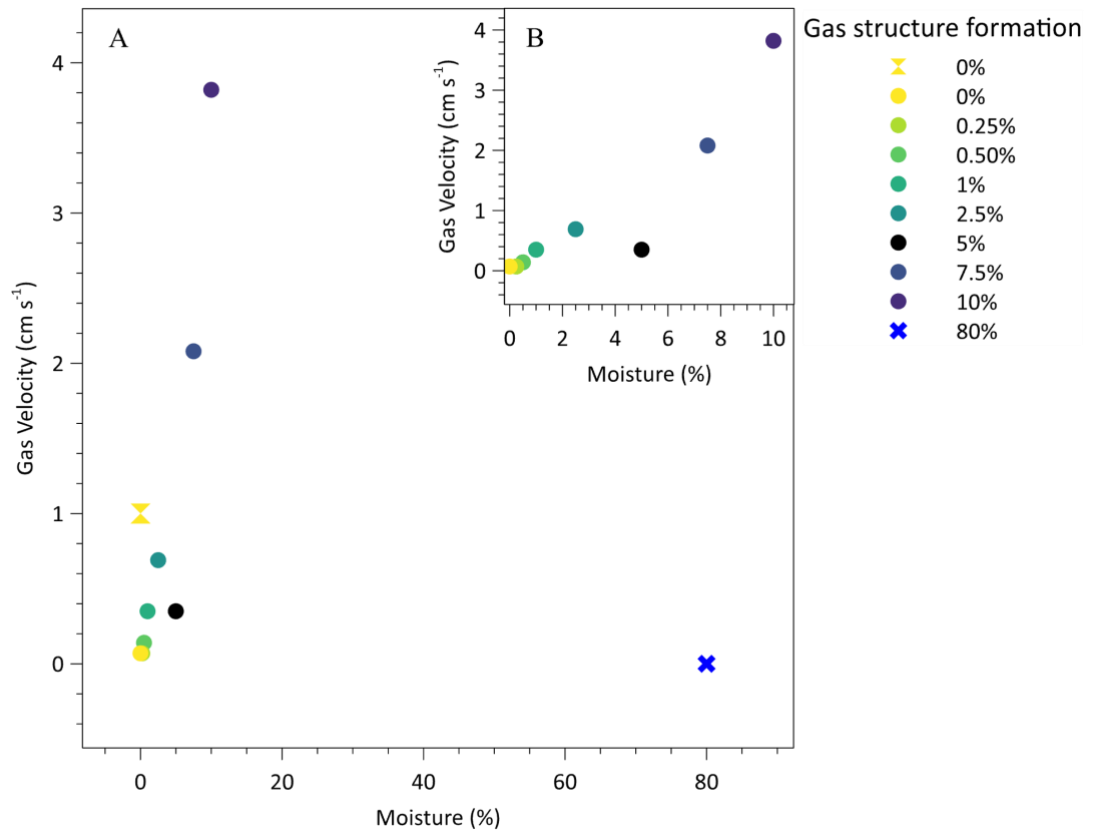


Figure 3.7. The gas velocity (cm/s) required to initiate gas escape structures depending on moisture percentage (%). A) Symbols represent different experimental suites from this study (circles), Wilson (1980) (hourglass) and Roche et al. (2001) (crosses). B) Shows the relationship of results from this study.

Figure 3.7. shows that by increasing moisture within a sample, higher gas velocities are required for aggregative fluidisation. Values from Wilson (1980) are based on the first formation of pipes at 0 wt.% moisture. Our values are from the first formation of gas escape structures at varying moisture percentages (i.e., bubbling at lower moisture percentages, and explosive cracking at the highest). Results from Roche et al. (2001) are based on initial pipe formation at 80 % moisture.

Between 10 and 80 % moisture, a change in the dominant fluidising medium is inferred, from gas to water. Instead of impeding early fluidisation structures, a large increase in moisture leads to more regular structures forming. This can be explained by changing particle-water states with increasing moisture. Future investigation covering increments between 10 and 80 % moisture may be able to define this behaviour change.

Aggregative fluidisation mechanisms will result in the segregation of particles through gas escape structures, where fines are winnowed. The nature of segregation will depend on the particle concentration and the size, shape, density, and relative proportions of clasts (Sparks, 1976; Wilson, 1980, 1984; Branney & Kokelaar, 2002). We find that the

moisture content of the deposit also controls this process; segregation structures can change dynamically with drying or become hindered with increasing moisture influence. This is due to our material being in a predominantly capillary state (Kim & Hwang, 2003; Kim & Sture, 2008). At higher levels of moisture, particles reach a more saturated state, are completely supported by capillary bonds, and fluidisation is no longer inhibited (as seen in Roche et al., 2001; Kim & Hwang, 2003). We observe that even small moisture contents (as low as 0.50 wt.%) into the pyroclastic material used in these experiments may control the formation and nature of gas escape structures.

3.5.2 Application to natural gas escape structures

Our results show that introducing moisture into pyroclastic materials may cause changes in gas escape morphology. Gas escape structures have been recorded and described extensively within field volcanological literature (e.g., Fisher & Schmincke, 1984; Cioni et al., 2015; Pacheco-Hoyos et al., 2020). They have been described as pods and pipes displaying single or branching patterns, or as lenticular, curvilinear, and crescentic shaped (Wilson, 1980; Branney & Kokelaar, 2002; Pacheco-Hoyos et al., 2020). They can be spatially arranged within individual layers or can move through multiple layers and are often fines depleted. Our results demonstrate varied morphologies, including vertical channels, sub-vertical cracks, and pods (created by moisture-rich lobes and dry pockets).

Changes in gas escape structures in pyroclastic deposits are thought to be dominated by heterogeneity within the material (e.g., size, density, shape etc.; Wilson, 1984; Pacheco-Hoyos et al., 2020). We propose that varying moisture levels will also influence changes in gas escape morphology and may explain circumstances where morphological changes are observed when other conditions appear unchanged. More detailed documentation of morphology of field examples may allow for improved interpretations of depositional environment.

3.5.3 Mechanism for secondary explosions

Secondary explosions in pyroclastic deposits form due to the interaction between water and hot material (Van Westen & Daag, 2005). Water in contact with hot pyroclastic material will convert into steam and expand, causing sudden explosive decompression. Secondary explosions form large craters (20 – 80 m depth), can remobilize large volumes of pyroclastic material and can occur for years after the initial eruption (the 1991 Mount Pinatubo generated secondary explosions for up to a year; Riehle et al.,

1995; Van Westen & Daag, 2005). Riehle et al. (1995) modelled cooling, degassing and compaction behaviours within thick pyroclastic deposits. High temperatures were most likely to remain elevated within deposits > 50 m thick, with temperatures cooling mostly by groundwater and rainfall. Keating (2005) modelled that the addition of water on a hot deposit can result in increasing pore pressure, in turn exceeding the overburden pressure. This can result in secondary explosions.

Moyer and Swanson (1987) described three styles of secondary explosions - passive degassing (least explosive), ash fountaining and explosive cratering (most explosive) - controlled by thermal energy and the permeability of the overlying material. Analogue experiments investigating the mechanisms of secondary explosions have been performed by Gilbertson et al. (2020). They identified that vertical changes in size fractions, and therefore a vertical profile of minimum fluidisation velocities, resulted in secondary phreatic explosions. In the experiments of Gilbertson et al. (2020), a deposit capped with coarser material formed an upward doming bed leading to an explosive release of material. This was due to a drag-induced system. The fine-particle layer below acted as a lower minimum fluidisation layer that was unable to fluidise the overlying, coarser layer, resulting in pressure increase and release of gas and particles.

Secondary explosions occur in deposits marked by the occurrence of an active and mobile pore pressure gradient associated with a vertical variation in permeability. Results from our experiments show that increasing moisture levels within the fluidised deposit can lead to impermeable layers forming through drying at the base of the deposit. By increasing moisture throughout our experiments, we observed passive degassing (0 wt.%), ash fountaining (> 0.50 wt.%) and explosive cratering (> 0.50 wt.%) behaviours as described in Moyer and Swanson (1987). After lithostatic pressure of the impermeable wet cap is overcome, explosive channelling (> 0.50 wt.%) and cracking (> 7.50 wt.%) occurs (the 'explosive cratering' of Moyer & Swanson, 1987). Similarly, to these works, our results demonstrate the impact of intermediate permeability on secondary explosion styles. We argue that the change from passive degassing to explosive cratering is not only a consequence of thermal energy in the system, but also of internal degassing of a partially fluidised deposit.

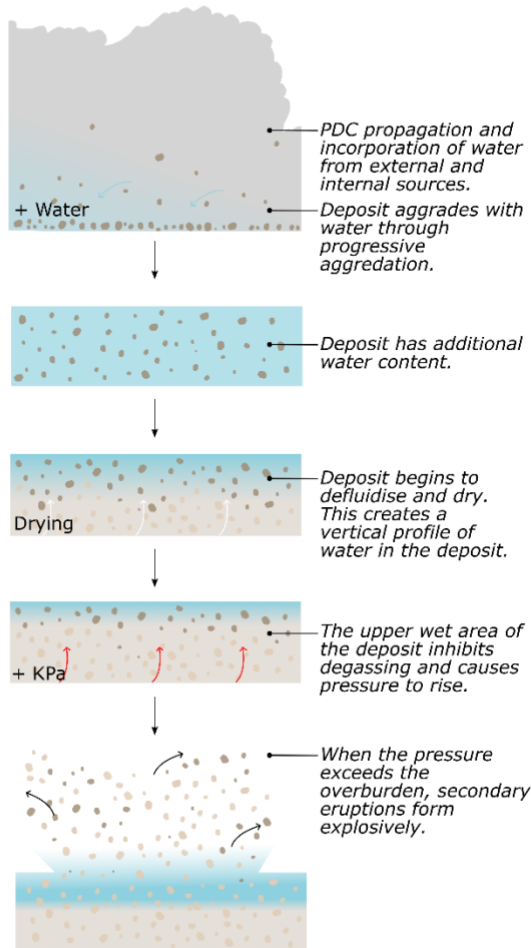
Critically, our results suggest a potential new mechanism for secondary explosions that form in a moisture influenced material (Fig. 3.8a). In our experiments, the addition of water during deposition results in increased cohesion and tensile strength. As the

deposit dries from the base, we see a shift in gas escape as the material begins to dry and bubble. In our model (Fig. 3.8a), the upper moisture rich layer inhibits passive degassing and leads to increased pore-pressure. With increasing pressure in the deposit, the overburden strength of wet material is compromised. The result is a sudden pressure release by explosive channelling and cracking, which mimics similar behaviours seen in secondary explosions in pyroclastic deposits.

In a dry deposit later moistened by water (i.e., precipitation), the upper moisture-rich layers of material will create an overall denser material (Fig. 3.8b). Secondary explosions were observed following the Mt St. Helens 1980 and Mt Pinatubo 1991 events (Keating, 2005) and were attributed to variations in the permeability of pyroclastic deposits caused by the presence of water (e.g., rainfall and lacustrine environments) (Moyer & Swanson, 1987; Manville et al., 2002). It is thought that high pressure towards the base of these pyroclastic deposits (caused by vaporization of water) led to low-permeable layers preventing the balancing of pore pressures throughout the deposit, which resulted in explosive depressurization (Keating, 2005). Keating (2005) suggests that after emplacement, hydrological re-establishment may begin to occur and interaction with hot overlying pyroclastic material may result in the formation of secondary phreatic explosions.

Our moisture influenced model may provide an explanation for the observations of secondary explosions in deposits that have aggraded with the presence of water (e.g., secondary explosions followed the previous location of the Rogue River; Druitt & Bacon, 1986) (Fig. 3.8a) and that have interacted with rain (e.g., Mt Pinatubo, Daag & Westen, 1996) (Fig. 3.8b). Rainfall may create a moisture-rich cap to the deposit that is impermeable to degassing from the lower deposit. The increased moisture from the rain would result in an increased cohesivity, and therefore tensile strength, of the material. With gas escape inhibited, pressure may continue to build until the overburden pressure is reached, and degassing is then allowed to escape through a secondary explosion in the deposit.

a) Defluidising wet deposit.



b) Defluidising dry deposit with external water addition.

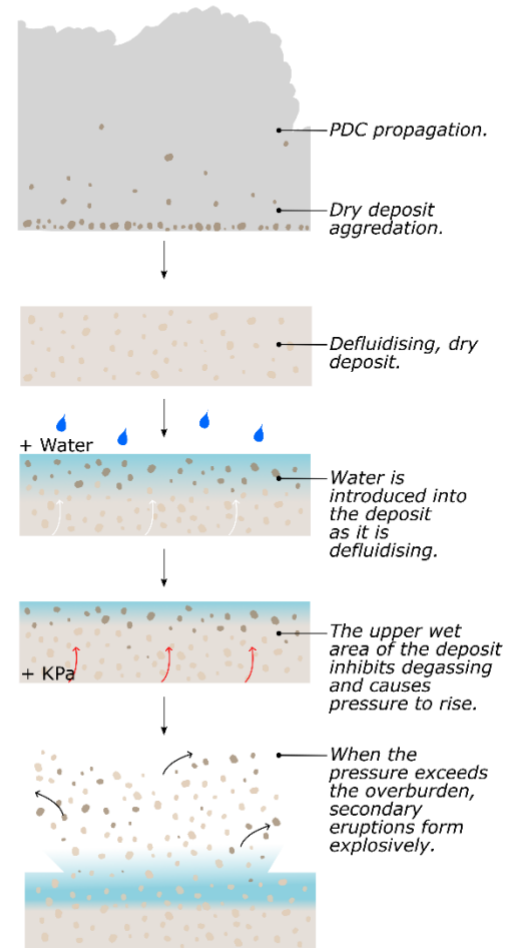


Figure 3.8. Moisture-influenced model of secondary explosion formation by a) a defluidising wet deposit and b) a defluidising dry deposit with external influences of water.

3.5.4 Implications for deposit remobilisation and preservation

The fine ash fraction of a fines-rich deposit will contribute to increased packing of the material (Lam & Nakagawa, 1993; Averardi et al., 2020). In the influence of moisture, we would expect the deposit to hold an increased moisture content in the fines portion in comparison to a coarser portion. Within a material with > 30 % volume of fines, the stress forces begin to be dominated by the fine fraction (Li et al., 2020; Breard et al., 2023). A large volume of fines, both with and without moisture, may dramatically alter the deposition and the preservation potential of these layers. Our results show that small amounts of moisture appear to increase the shear strength of pyroclastic material. A more cohesive deposit may be more resistant to erosion, and remobilisation, meaning

that moist layers may be more likely to be preserved in volcanic successions. Additionally, the formation of a drying profile demonstrates both vertical and lateral variation due to an undulating contact between wet and dry material, resulting in vertical and lateral changes in the tensile strength of a deposit. Therefore, erodibility and preservation of layers may be variable. Future work should aim to quantify cohesivity of material directly and determine yield stress and tensile strength. This will enhance our understanding of material properties and behaviours, allowing us to comprehensively assess their implications for erodibility, remobilisation and preservation.

3.5.5 Implications for PDC flow dynamics

The material behaviours revealed by the BTd, SAoR and DAoR tests raise important questions regarding the impact of moisture within a dynamic, moving PDC. The experiments show that in a dry (0 wt.% moisture) state, the material analysed has a low shear strength as evaluated by the angle of repose. As well as fines concentration, sorting is seen to play a key role (Table. 3.1). This can be seen in V1 (5 wt.% SAoR: 56°), which is well sorted and displays the largest volumes of fines (35.76 %), whereas V4 (5 wt.% SAoR: 57°) is very well sorted and has one of the lowest volumes of fine material (0.15 %). The excellent flowability seen in V4 may result from its sorting and resulting packing behaviour, which is known to affect flow behaviour (Breard et al., 2023). The DAoR results show contrasting behaviours versus the SAoR results when comparing the Sauter mean diameter. This could suggest that particle size has a greater control on material behaviour in static regimes compared to dynamic regimes. Such an observation has wide ranging implications. For example, Breard et al (2023) suggests that long run-out distances in block and ash flows (BAFs) were a result of large degrees of fragmentation, with the current becoming more fines rich, and subsequently the deposit displaying higher packing. These particle size changes result in a dynamically evolving flow, where fines formation and increasing packing behaviour reflect elevated pore-pressure within the flow (Breard et al., 2023). Our experiments (V1, V4) show that both fines content and packing can contribute to good flowability behaviours, with implications for the resulting run-out distance of PDCs. Our experiments are limited by particle size distribution and do not contain any blocks, so are only modelling the behaviours of the finest fraction. However, it is the fines fraction that controls the fluidisation of PDCs (Gilbertson et al., 2020). The role of large blocks in affecting

fluidisation and flowability of PDCs is an important avenue for future research (Sparks, 1976; Branney & Kokelaar, 2002).

The material with the largest volume of fines (V1, V2) is shown to exhibit higher shear strength with increasing moisture (i.e., higher SAoR angle). Sample V4, which is more well sorted, has the highest increase in SAoR values when moisture is added. Our work demonstrates the important role of moisture, even in small amounts, in changing flowability behaviours. We can build a hypothesis that the addition of moisture into a PDC during propagation, with increasing fragmentation of particles and packing during flow, can be a factor in controlling run-out distances – intermediate moisture contents reduce flowability so may reduce maximum runout distances, particularly in flows with enhanced fragmentation.

Our results also indicate that the introduction of moisture reduces material fluidisation. Expanding on this, future research exploring moisture on fluidised currents would be a valuable extension of the current static fluidisation experiments. This would allow for a better assessment of how moisture influences fluidisation and the resulting behaviours in PDCs.

3.6 Conclusion

This work offers insights into the influence of moisture on the behaviour and characteristics of materials deposited from pyroclastic density currents. Our results demonstrate that for certain pyroclastic material: 1) the cohesive behaviours and shear strength of pyroclastic material changes drastically, even for relatively small additions of moisture (> 0.50 wt.%); 2) an increase in moisture can entirely alter flow property behaviour from a free flowing to a non-flowing material; 3) changes in moisture impact fluidisation profiles and gas escape structures; 4) a defluidising deposit can lead to lateral and vertical heterogeneity within the deposit, and 5) pressure can increase where gas escape is hindered by cohesive substrates driven by moisture content, resulting in secondary explosions. Our results build on previous models of secondary explosions in deposits and supports the idea that they are formed because of the development of an impermeable capping layer, here created by the addition of moisture. This work further proposes that moisture within a defluidising deposit profile may hinder or change the formation of gas escape structures, which can then lead to pressure increase and release, with implications for the interpretations of the structures within the deposits. Overall, these findings suggest that moisture plays a critical role in PDC flow dynamics and their

deposits, with implications for erodibility, preservation potential and our broader understanding of deposit architecture.

Supplementary Material for Chapter 3 can be found in Appendix A.

Supplementary Material 3A – Geomechanical data (BTD, SAoR, DAoR) for V1 (Tung 1) to V6 (Tung 6) and uncertainty and error.

Supplementary Material 3B – Online resource 1 and 2 showing fluidisation experiments and pocketing, explosive channelling and explosive cracking gas escape structures.

Chapter 4 : Behaviours of pyroclastic and analogue materials, in dry and wet environments, for use in experimental modelling of pyroclastic density currents

4.1 Abstract

Modelling pyroclastic density currents (PDCs) is a challenging yet essential element of hazard assessment. PDCs are unpredictable and internal processes are often difficult to measure directly. Analogue experiments have been an important tool for investigating internal PDC dynamics. Typically, analogue experiments have removed moisture from experimental materials to limit cohesion. However, this does not represent natural systems well, where moisture can be introduced into a PDC through a variety of processes. In this study, we characterise pyroclastic and analogue materials in dynamic (i.e., flowing), static (i.e., stationary), wet and dry experiments to explore fundamental frictional and fluidisation behaviours. The addition of moisture can lead to changes in material properties, resulting in significant impacts on geomechanical behaviours (size, density, shear strength), fluidisation and flowability. This work highlights the importance of validating the material choice used in modelling experiments, especially in wet conditions.

4.2 Introduction

A pyroclastic density current (PDC) is a volcanic hazard formed during explosive eruptions and dome collapse events. PDCs are rapidly moving, high temperature (up to 1000 °C) currents of heterogeneous volcanic material and gas (Fisher, 1979; Cas & Wright, 1988; Branney & Kokelaar, 2002; Dufek, 2016). They are multiphase flows, where the solid, granular phase consists of both juvenile and entrained material, and the fluid phase contains a combination of volcanic gas and vapour with entrained air (Burgisser & Bergantz, 2005; Ongaro et al., 2011, 2012; Lube et al., 2020).

Internal dynamics within PDC systems are difficult to observe in real time. In-situ data are rare, flows can be unpredictable, and equipment can be damaged by extreme force (Wilson et al., 2014; Scharff et al., 2019). The behaviour of PDCs, including flow runout distance, duration and velocity, is collectively controlled by variations in flow parameters such as mass flux, particle size, particle shape, density, fluid medium and changes in topography (Bursik & Woods, 1996; Branney & Kokelaar, 2002; Andrews & Manga, 2011). Particle size variations, including ash (< 2 mm) concentration, can be

attributed to various factors, including magma composition, fragmentation rate, amount and duration, initial vent dynamics, erosion and sedimentation processes during flow propagation, and current vertical density segregation (Sparks, 1976; Zimanowski et al., 1997; Alidibirov & Dingwell, 2000; Branney & Kokelaar, 2002; Dufek & Manga, 2008; Breard et al., 2023). Particle density contrast can be driven by variation in mixture composition and vesicularity and can lead to further vertical and lateral particle segregation (Doyle et al., 2010). Finally, the temperature and fluid medium (gas or water) in PDCs can contribute to the generation of pore pressure or other controls on interparticle forces, fundamentally affecting particle and bulk material behaviour (Druitt et al., 2007; Lube et al., 2020). Understanding these complex variations is crucial for exploring the dynamics of PDCs.

Advances in the understanding of PDCs have been driven by a combined approach of direct observation (e.g., Cole et al., 1998, 2002; Lipman, 2019; Vecino et al., 2022), detailed geological stratigraphy (e.g., Fisher, 1979; Branney & Kokelaar, 1997; Brown et al., 2003; Smith & Kokelaar, 2013; Brown & Branney, 2013; Douillet et al., 2013, 2013, 2018), small and large scale analogue experiments (e.g., Dellino et al., 2007; Lube et al., 2015, 2019; Rowley et al., 2014; Smith et al., 2018, 2020; Walding et al., 2023) and numerical modelling (e.g., Valentine, 1987; Dufek, 2016; Kelfoun, 2017; Breard et al., 2018). Analogue experiments validate data and underpin the basic geophysical properties that can then be used to generate new or update existing numerical models.

The most common materials used in PDC analogue modelling are soda-lime glass ballotini (microspheres / glass beads). This is due to their widespread availability, narrow and well-defined size distribution, and consistent physical properties (e.g. Roche et al., 2004; Rowley et al., 2014; Chedeville & Roche, 2014; Smith et al., 2018; Gilbertson et al., 2020). However, when trying to simulate the behaviour of polydisperse and non-spherical natural pyroclastic materials, the uniformity of ballotini is not ideal. Given the importance of particle characteristics in controlling frictional behaviours and permeability, the choice of material for analogue experimentation is critical, and yet no known studies have directly compared the behaviour of analogue material to a range of natural pyroclastic samples under both static and dynamic conditions. Recent work has shown the powerful impact of even small (< 1 wt.%) moisture contents on the fluidisation behaviours of pyroclastic sediments (Walding et al. 2023). This work sets out to quantify the static (i.e., motionless material) and dynamic (i.e., material undergoing changes in motion over time) behaviours of various pyroclastic and analogue

materials in dry and “wet” (> 0 wt.% water) environments, for use in analogue modelling. The work aims to investigate the geomechanical behaviours of these materials, to both establish a baseline for material variability under these different conditions (i.e., a flowing current, a stationary substrate or as a defluidising deposit), and to determine the most suitable material for simulation of different natural PDCs. This work adopts the same methodological approach as Walding et al. (2023), expanding the range of pyroclastic material tested and directly comparing behaviours to a range of analogue material.

4.2.1 Material selection in experimental PDC modelling

A variety of analogue materials can be used in experimental modelling to mimic the behaviours of natural material. The choice of analogue materials used in PDC modelling is often justified for their fluidisation properties. Fluidisation plays an important role in PDC mobility (Sparks, 1976, 1978; Wilson, 1984; Branney & Kokelaar 1992, 2002; Roche, 2012; Aravena et al., 2021; Breard et al., 2017, 2023; Salatino et al., 2024) and the formation of deposit structures resulting from defluidisation and degassing (i.e., gas escape structures; Wilson, 1980; Cas & Wright, 1991; Pacheco-Hoyos et al., 2020; Walding et al., 2023). The upward movement of gas can support particles within the flow, opposing the forces of gravity, and reducing contact friction.

The fluidisation of pyroclastic materials can be assessed through experimental set-ups such as the use of fluidisation columns (Wilson, 1984; Roche et al., 2001; Bareschino et al., 2007; Gilbertson et al., 2020; Walding et al., 2023), rotating drums (Valverde & Soria-Hoyo, 2015; Smith et al., 2020; Walding et al., 2023) or flumes (Roche et al., 2004, 2012; Dellino et al., 2007, 2010; Lube et al., 2015; Smith et al., 2018; Brosch et al., 2021). Additionally, the use of numerical modelling can simulate the behaviour of PDCs under different conditions (Ongaro et al., 2002; Darteville et al., 2004; Benage et al., 2016; Kubo Hutchinson & Dufek, 2021). Observations of PDC deposits in the field offer valuable insights into evidence of PDC fluidisation behaviours. This can be through evidence of gas escape in deposits (Fisher & Schmincke, 1984; Cioni et al., 2015; Pacheco-Hoyos et al., 2020) or by observations of recently deposited material (Whelley et al., 2012).

Using the Geldart (1973) classification, pyroclastic materials can be categorised based on their fluidisation behaviour. Geldart (1973) separated powders into four distinct groups (A-D), differentiated by their fluidisation behaviours, where powders can exhibit a 'very poor' to 'excellent' fluidisation state, based on particle size, shape and density. Group A

(30 – 100 μm) and Group B (100 μm – 1 mm) powders tend to uniformly expand during fluidisation and often display the most favourable fluidisation behaviours (e.g., homogeneous bubbling and channelling). In contrast, the finest particles (< 20 μm) in Group C are dominated by the presence of interparticulate forces (e.g., electrostatic cohesion and van der Waals) and therefore fluidisation behaviours are usually poor. Group D (> 1 mm) particles are the largest and require overall higher gas velocities for effective fluidisation. Group D has moderate to poor fluidisation and often demonstrates slugging, channelling, and spouting behaviours (Leturia et al., 2014).

To match the fluidisation behaviours of PDCs, and to minimise variability in other particle parameters such as shape, density, and roughness, the most common analogue material used to date are ballotini beads, commonly Geldart Group A and B (Table. 4.1). Using mean particle diameters below $\sim 150 \mu\text{m}$ generally ensures these materials can easily fluidise at gas velocities achievable in the laboratory (Roche et al., 2004; Montserrat et al., 2012; Rowley et al., 2014; Breard et al., 2019). The benefit of using ballotini is that, as well as its excellent fluidisation behaviours, it is widely available for use. However, it does not capture the full particle variability of natural pyroclastic material.

Pyroclastic material has been used in small-scale experiments, to investigate modelling of gas escape structures and in geomechanical tests to explore material strength and flow behaviours (Roche et al., 2001, 2004; Smith et al., 2018, 2020; Osman et al., 2022; Walding et al., 2023). However, the large polydispersity can lead to issues such as scaling limitations (i.e., having a maximum size range to fit within the limits of experimental apparatus and jamming in small-scale hoppers) and behavioural challenges associated with fluidisation (i.e., large particle polydispersity leading to issues in homogeneous fluidisation of material) (Wilson, 1984; Walding et al., 2023). Some of these issues can be alleviated by using large-scale flow experiments (Dellino et al., 2007, 2010; Lube et al., 2015; Brosch et al., 2021) (Table. 4.1). Additionally, variables introduced by using pyroclastic material (i.e., particle size distribution, particle density, roughness, composition etc.) can lead to added degrees of complexity when modelling using natural pyroclastic materials. Furthermore, it is difficult to get large, homogenous samples of natural materials and in certain areas of the world challenges can arise when trying to obtain natural samples. The nature of each individual sample of material can vary greatly due to changes in sample type (i.e., location of material and volcano), eruption dynamics and age (e.g., weathering and alteration). However, the use of natural

pyroclastic material in experimental modelling is a fundamental step in understanding natural processes and how these vary from the behaviours of analogue material.

Previous studies (such as Breard et al., 2019, Smith et al., 2020, Osman et al., 2022, Walding et al., 2023 and Vale et al., 2024) have explored the use of analogue versus natural material to begin to characterize properties such as material behaviour, shear strength, flowability, fluidisation and permeability. Ballotini (Roche et al., 2004; Smith et al., 2020; Vale et al., 2024) and crushed industrial pumice (Osman et al., 2022; Vale et al., 2024) have been used in a wide range of analogue studies. However, when using natural pyroclastic material, it is often the case that only small amounts of natural material is used from single eruptions (e.g. 232 A.D. Taupo ignimbrite; Breard et al., 2019; Ascension tephra; Osman et al., 2022; andesitic ash sample from Ruapehu; Vale et al., 2024) against which to compare analogue materials against. Table 4.1 collates published works of both analogue and pyroclastic material behaviour used in static and dynamic conditions. In this study, we expand on these exploratory results to investigate the geomechanical behaviours of a wider suite of pyroclastic and analogue material through static, dynamic, dry and wet conditions. Furthermore, we expand on work by Walding et al. (2023) and further investigate the role of water on a suite of pyroclastic materials.

Table 4.1. Compilation of published works on material properties of analogue and pyroclastic material used in experimental modelling. The values represent the properties of the material used in a range of static and dynamic studies. SAoR – Static Angle of Repose, DAoR – Dynamic Angle of Repose.

Literature	Sample	Experiment Type	Mean Size (mm)	Median Size (mm)	Size range (mm)	Fines Content (%)	Bulk Density (kg m ⁻³)	Particle Density (kg m ⁻³)	SAoR (°)	DAoR (°)	Internal Friction Angle (°)
Roche et al., 2004	Ballotini	Dynamic (Flow)	-	-	0.024 - 0.090, 0.106 - 0.212, 0.6 - 0.8	-	1492, 1467, 1450	-	28.5, 24.5, 24	-	-
Dellino et al., 2007, 2010	Somma Vesuvius Pyroclastic Deposits	Dynamic (Flow)	-	1	0.011 - 8	-	-	1630	-	-	-
Lube et al., 2015	Taupo Ignimbrite Mixture	Dynamic (Flow)	-	241-366	0.0014 - 22	4.5 - 17	400 - 2600	-	-	-	-
Smith et al., 2020	Ballotini	Static and Dynamic	0.063.4	-	0.045 - 0.090	-	1450 - 1740	-	10 - 34	14 - 26	-
Smith et al., 2020	Pozzolane Rosso Ignimbrite	Static and Dynamic	0.018 - 0.7	-	0.003 - 3	-	-	-	31 - 61	39 - 53	-
Breard et al., 2017; Brosch et al., 2021	Taupo Ignimbrite Mixture	Dynamic (Flow)	-	-	0.002 - 16	20	-	350 - 2600	39	-	-
Osman et al., 2022	Industrial Pumice (Synthetic)	Static	0.063	-	-	-	602 - 412	-	-	-	36.5

Osman et al., 2022	Ascension Ash	Static	0.063	-	-	-	1019	-	-	-	36.4
Vale et al., 2024	Glass Ballotini	Static	-	-	1-1.4	-	-	2500	-	-	-
Vale et al., 2024	Crushed Pumice	Static	-	-	0.5 – 2.0	-	-	1080	-	-	-
Vale et al., 2024	Ruapehu Ash	Static	-	-	0.5 – 2.0	-	-	2200	-	-	-

4.2.2 Moisture in a PDC system

Moisture, in the form of water vapor or liquid water, can enter a PDC system during its formation, often due to water-rich environments from phreatomagmatic interactions, during its propagation or during and after deposit aggradation. This introduction of moisture can result from a combination of atmospheric conditions (e.g., humidity; Pepin et al., 2017; Camuffo, 2019), topographic factors (e.g., elevation; Barclay et al., 2006; Duane et al., 2008; Hartmann, 2016), and meteorological conditions (e.g., precipitation). Furthermore, PDCs can interact with external bodies of water such as streams, lakes, the sea, and snow (Darteville et al., 2002; Cole et al., 1998, 2002; Vale et al., 2024), as well as water-saturated substrates (Moyer & Swanson, 1987; Brown & Branney, 2013; Gilbertson et al., 2020).

The temperature within a PDC system can vary widely. Low temperature ($< 100\text{ }^{\circ}\text{C}$) currents are interpreted to form from phreatomagmatic interactions (Sparks & Wilson, 1990; Yamamoto et al., 1999) while high temperatures are interpreted to reach in excess of $700\text{ }^{\circ}\text{C}$ (McClelland & Druitt, 1989; Cioni et al., 2004; Bardot, 2000; Lesti et al., 2011; Pensa et al., 2023). Near the surface and in the upper parts of the flow, pressures may be close to atmospheric and temperatures cooler, whereas in the denser parts of PDCs, both pressures and temperatures can increase significantly (Breard & Lube, 2017). Changes in these conditions can lead to the condensation of water vapor into droplets. As a result, the moisture content in PDCs and their resultant deposits can vary in both time and space. For example, the rapid vaporization of water into steam during granular PDC interactions with wet substrates can create a new gas source, increasing the mobility and fluidisation of the current, whereas moisture influence from precipitation and atmospheric conditions may be more likely to affect the dilute regime of the current.

4.2.3 The influence of moisture on experimental modelling materials

When conducting analogue experiments to model PDCs, procedures are often implemented to minimize the moisture content of the material used. This typically involves drying samples in an oven for 24 hours, which helps to remove adsorbed moisture and reduce the effects of cohesion. However, volcanic eruptions and tephra plumes may include a high proportion of water vapour, either from phreatic or

phreatomagmatic eruption processes or from entrainment of moisture from the atmosphere and environment (Self & Sparks, 1978; Pardo et al., 2014, Morrissey & Mastin, 2000; Van Eaton & Wilson, 2012). This can lead to moisture-rich PDCs forming at source. Additionally, moisture can be incorporated into the flow as a PDC propagates, even if initially dry, e.g., from rainfall into the current, travelling over water bodies, or encountering moisture-rich substrates such as vegetation or wet soils (Walding et al., 2023 and refs therein).

Walding et al. (2023) explored the behaviour of small quantities of moisture on fine pyroclastic material ($< 1000 \mu\text{m}$). The findings revealed that the introduction of water ($> 0.50 \text{ wt.}\%$) into pyroclastic material can significantly change the cohesive properties, which in turn alters the flowability from a free flowing to a non-flowing material. This is due to the friction coefficient increasing due to the formation of capillary bridges. Results also demonstrated that changes in moisture content could significantly affect fluidisation profiles and resulting gas escape structures forming within a deposit. Fluidisation experiments of the material showed gas bubbling throughout most experiments (minimum bubbling velocity = $U_{mb} \text{ cm/s}$), with gas bubbles rising from the basal gas supply (Walding et al., 2023). With increasing gas flux, or in more polydisperse mixtures, gas escape can lead to channelling (minimum velocity to induce channelling = $U_{mc} \text{ cm/s}$), where gas pathways are concentrated into vertical channels (approaching Geldart Group D behaviours). With the introduction of water ($> 0.50 \text{ wt.}\%$), drying profiles migrate through the moist deposit and can form areas of wet lobes and bubbling dry pockets (Walding et al., 2023). Explosive channelling (minimum velocity to cause gas escape feature formation = $U_{mx} \text{ cm/s}$) is also observed in experiments of $0.50 - 5.00 \text{ wt.}\%$ water. This is where the material dries, and an upper wet deposit inhibits gas escape leading to a pressure increase and subsequent release. Finally, under the highest moisture conditions, pressure builds under the moist deposit until the deposit fractures into cracks ($U_{mcr} \text{ cm/s}$) where gas can then easily permeate through. This work highlights the impacts of water on pyroclastic material and demonstrates the need to further explore the role of water on PDC flow dynamics and deposit behaviour.

There is a notable gap in research into the behaviours of a range of pyroclastic and analogue materials across static and dynamic experiments, particularly in dry versus wet environments. This lack of comprehensive study may lead to inadequate experimental design, and it is therefore imperative to enhance our understanding of these behaviours.

Doing so will facilitate the validation of analogue materials utilized in experimental modelling and enable the exploration of fundamental characteristics of natural pyroclastic materials. In these experiments, we aim to look at pyroclastic material behaviour in the presence of moisture. These observed behaviours can then be used to infer implications for PDC systems, from flow to deposit.

4.3 Methods and materials

The experimental methods within this paper follow those used in Walding et al. (2023) and are summarised here. More detailed descriptions of the methods used are detailed in Appendix B³, Supplementary Material 4A.

4.3.1 Pyroclastic and analogue samples

Five natural samples of pyroclastic material were chosen to cover a range of physical particle size characteristics (size, shape; fines content; Table. 4.2). Samples were collected from a variety of global locations and represent different eruption styles, lithofacies and geochemical compositions (Table. 4.2). The analogue samples include material that has previously been used in experimental modelling of pyroclastic behaviours (ballotini: Roche et al., 2004; Smith et al., 2018, 2020) and exploratory samples (i.e., cornstarch, Table. 4.3). The pyroclastic samples have maximum particle diameters of 2000 μm and the analogue samples have maximum particle diameters of < 1460 μm (Fig. 4.1a, b). These size ranges were chosen to accommodate the scaling limits of the fluidisation chamber experiment.

³ All appendices for Chapter 4 are in Appendix B. Herein, this will be referred to as ‘Supplementary Material 4A, B, C’ etc...

Table 4.2. Pyroclastic samples used in the reported experiments, reporting formation processes, chemical composition, location of sample collection and references (where applicable).

Material	Eruption/Formation	Composition	Location	References
Tungurahua (1-6)	2006 VEI 3 eruption. Sieved PDC units sampled by U. Kueppers in 2009.	Andesitic	Tungurahua, Ecuador	Hall et al., 2013; Kelfoun et al., 2009; Douillet et al., 2013; Eychenne et al., 2012
Colima	2015 eruption. Sieved PDC units sampled by T. Johnson in 2023	Andesitic	Volcán de Colima, Mexico	Johnson, T. <i>In comms</i> (2023)
Atitlan	Unstudied ignimbrite deposit. Sampled by P. Rowley from massive PDC unit in 2023. GR: 14°40'55.24"N, 91°15'29.15"W	-	Volcán de San Pedro, Guatemala	Rowley, P. <i>In comms</i> (2023)
Taupo (1 & 2)	Taupo 1: Sampled from the proximal fine ash-rich facies from the base of 232 A.D. deposit. Taupo 2: Sampled from 232 A.D. proximal PDC deposits. Sampled by E. Brosch and colleagues.	Rhyolitic	Taupo, New Zealand Taupo 1 – 17 km from vent Taupo 2 – 8km from the vent	Wilson (1985), Brosch et al., 2021
Milos	Basal pyroclastic sequence. PDC units sampled by N. Walding in 2023.	Rhyolitic to Dacitic	Milos, Greece	Zhou et al., (2020)

Table 4.3. Analogue samples used in the experiments. Ballotini 1 and 2 represent the size variation of the two material samples used.

Material	Composition	Material Information
Ballotini (1&2)	Soda lime glass beads	<i>Sourced from Sandblasters.co.uk</i>
Fine Sand	Redhill 110 (silica sand)	<i>Sourced from mineralsmarketing.co.uk</i>
Cornstarch	Cornstarch	<i>Sourced from Harry Harvey Ltd</i>
Industrial Pumice	Unspecified pumice	<i>Sourced from Specialist Aggregates Ltd</i>

4.3.2 Scaling

The work presented here arises from questions about how volcanic materials physically respond to moisture. Although it would be straightforward to analyse natural samples and measure their mechanical response to moisture changes, experimental simulations of natural processes, such as PDC propagation, often utilize various analogous materials instead of pyroclastic sediment. To support this study, we tested a range of these analogue materials alongside natural pyroclastic ones, with the hope that this data will be useful for future research on how these characteristics influence processes within currents, deforming sediments, and other related phenomena.

The scaling of experiments depends on the specific conditions and apparatus design. Therefore, we provide a list of key parameters for each of our tested materials (Table. 4.4). The experiments discussed here examine the mechanical properties of the entire material, though there are limitations, notably, the particle sizes used are restricted to the ash fraction (< 2 mm). This limitation is due to the apparatus, which requires a minimum number of particle diameters to produce repeatable and meaningful data. In natural settings, the particle size distribution can be much broader, which may have impacts on the mechanical properties we are unable to quantify here.

4.3.3 Wetting process

To ensure the removal of residual absorbed moisture in the experiments, all samples were dried for 24 hours at 80 °C. Any agglomerations were broken up by sieving prior to the start of the experiments. For the moisture tests, water was then added to the samples based on weight percentage (0, 0.25, 0.50, 1.00, 2.50, 5.00 wt.%). These moistures were chosen as they have been identified in Walding et al. (2023) as being significant in affecting the cohesive behaviour and the resulting shear strength of

material. Samples were mixed thoroughly to ensure a homogeneous moisture distribution (Walding et al., 2023).

4.3.4 Particle size and shape analysis

Particle analysis of the pyroclastic and analogue material was undertaken using a CAMSIZER X2, which uses particle imaging to establish shape and size characteristics for dry material samples. The CAMSIZER provides a maximum resolution of 0.8 μm per pixel for both particle size and shape. We report particle sphericity (SPHT) values using Eq. 4.1, where P is the measured circumference of the particle and A is the area covered by particle projection. For an ideal sphere, SPHT is expected to be 1, otherwise it is smaller than 1 (Liu et al., 2015).

$$SPHT = \left(\frac{4\pi A_p}{P_p^2} \right) \quad (4.1)$$

Symmetry is measured by how evenly the shape of a particle is distributed around the centre line. For example, asymmetric particles will be < 1 . The cumulative size and shape data from CAMSIZER were subsequently processed using GRADISTAT (Blott & Pye, 2001) to derive various particle size characteristics, using the moments method (Inman, 1952) to calculate logarithmic and geometric particle size mean ($(\bar{x}) \emptyset$), median ((\emptyset)), range (μm), sorting index ($(\sigma) \emptyset$), sorting (σG), skewness ($(Sk) \emptyset$), kurtosis ($(K) \emptyset$), and the geometric mean (μm). The Sauter mean diameter (D_{32}) is a measurement that describes the diameter of a sphere that has the same volume/surface area ratio of a particle (Eq. 4.2, Breard et al., 2019):

$$D_{32}(mm) = 2^{- \left[\mu m(\Phi) + \frac{\log_2}{2} \sigma^2(\Phi) \right]} \quad (4.2)$$

where μm is the geometric mean and σ^2 is the geometric standard deviation (Eq.4.2, in Φ units, Breard et al., 2019). D_{32} values have been used to characterise the fluidisation behaviour of a material (Breard et al., 2019). Following the approach outlined in Breard et al (2019), we calculated the D_{32} (mm) and fines content ($< 63 \mu\text{m}$, %) of the material.

4.3.5 Experimental procedure

Bulk and Tapped Density (BTD) measurements were completed to assess the mass and volume relationships of granular material, both in their initial and compacted states (Amidon et al., 2017). Calculating the material bulk density involved pouring 100 g of the material into a 250 mL cylinder. The initial unsettled volume was measured, and

bulk density calculated (ρ_b ; Eq. 4.3) where m is mass (g) and V_o is the unsettled apparent volume (mL). The cylinder was then tapped at 150 taps/min. The cylinder volume was measured every minute until a stable, levelled reading was completed and tapped density (ρ_t) was calculated using Eq. 4.4 (Supplementary Material 4A), where V_f is the final tapped volume (Moondra et al., 2018). These experiments were repeated with the addition of water (0 – 5 wt.%). The bulk and tapped densities were then calculated to see the effect of adding water. This enabled the calculation of the Carr's Index (CI; Eq. 4.5) and Hausner Ratio (HR; Eq. 4.6), which are important parameters for understanding the flowability behaviours of a material (i.e., how easily a material can flow or move). Carr's index (CI) evaluates a material's strength and compressibility (Moondra et al., 2018). The Hausner ratio (HR) assesses the packing efficiency of the material and its susceptibility to compact under external forces (Yu & Hall, 1994; Abdullah & Geldart, 1999). For example, a low HR signifies good flowability behaviours. BTD experiments were conducted for a representative subset of the entire suite of experiments.

$$\rho_b = \frac{m}{V_o} \quad (4.3)$$

$$\rho_t = \frac{m}{V_t} \quad (4.4)$$

$$CI = 100 \left(\frac{\rho_t - \rho_b}{\rho_t} \right) \quad (4.5)$$

$$HR = \frac{\rho_t}{\rho_b} \quad (4.6)$$

Static and dynamic angle of repose (SAoR and DAoR respectively) experiments were completed to assess the shear strength and flowability of the material (Beakawi Al-Hashemi & Baghabra Al-Amoudi, 2018). For the SAoR experiments, 100 g of each sample was released from a funnel held 35 mm above a circular platform. The cone height was then measured, and the angle of repose calculated using the height of the pile formed and the base diameter of the platform (85 mm). The SAoR is calculated using

$$\text{SAoR } (^{\circ}) = \tan^{-1} \left(\frac{2h}{D} \right) \quad (4.7)$$

where h is height and D is base diameter (mm). The DAoR experiments were completed by using 100 g of material in a rotating drum. Material was rotated and recorded, and the critical angles were measured using ImageJ software (Schneider et al., 2012). SAoR experiments were repeated three times and a subset of DAoR experiments were run to demonstrate reproducibility (Supplementary Material 4B).

Finally, fluidisation experiments investigated the fluidisation behaviours and states of each material at varying moisture contents. This adopted the use of a rectangular, near 2D fluidisation chamber with a porous base (Gilbertson et al., 2020; Walding et al., 2023). Samples of 200 g were placed into the chamber and levelled. A manometer then recorded basal pore pressure changes throughout the experiment. Compressed dry, unheated air was then incrementally passed through the porous base into the chamber and at the points of minimum fluidisation state (i.e., bubbling, channelling etc). The tests were run until either a stable fluidisation state was achieved (bubbling or channelling), excessive winnowing of material occurred or where large pressure was reached without any resulting gas escape structures being formed. Experiments increased the gas flow rate from 0 to 5 cm/s for a period of 0.31 to 3.28 minutes. The short experimental time aided in limiting the effects of material drying. Given time constraints, we decided to focus on completing a range of fluidisation experiments, rather than repeats of fewer experiments.

4.3.6 Statistical analysis

The experiments presented here explore a wide array of variables. We assess the correlation between the different variables by using Spearman's rank correlation coefficient (r_s). The r_s is statistically useful in identifying trends in large data sets and evaluates the monotonic relationship between 2 independent variables (Gauthier, 2001). From this, the confidence interval (%) can be calculated to better constrain relationship correlations for the use of principal component analysis. A principal component analysis (PCA) is used on all samples to summarize the correlated variables as highlighted using the r_s . Data analysis has been completed using the statistical software Microsoft Excel, RStudio (Version 4.3.2, 2023) and the R packages FactoMineR (Lê, Josse & Jussion, 2008), factoextra (Kassambara & Mundt, 2020) and ggplot2 (Wickham, 2009).

4.3.7 Limitations

In nature, pyroclastic materials are more polydisperse than the materials used within these experiments. Their natural variation shows a vast distribution of size, density, shape, composition, and temperature than the parameter space explored in this work. The limitations on particle size ($< 2000 \mu\text{m}$) reflects the limitations of equipment size used in the experiments, such as scaling limits of the fluidisation chamber. Future work encompassing a wider size range could overcome this by using larger fluidisation chamber equipment. At high moisture percentages, the materials used in the DAoR experiments begin to clump, stick and slide to the wall of the drum. Therefore, some DAoR values have been excluded from the results.

4.4 Results I: behaviour of material in dry conditions.

4.4.1 Particle size analysis

The pyroclastic materials used in these experiments (Fig. 4.1) have particle size distributions ranging from 2.5 to 2000 μm and the analogue materials (Fig. 4.1) has a particle size distribution from 2 – 1460 μm . Based on the logarithmic particle mean (Table. 4.4) all materials are expected to exhibit fluidisation behaviours typically associated with Groups A and B in Geldart's classification.

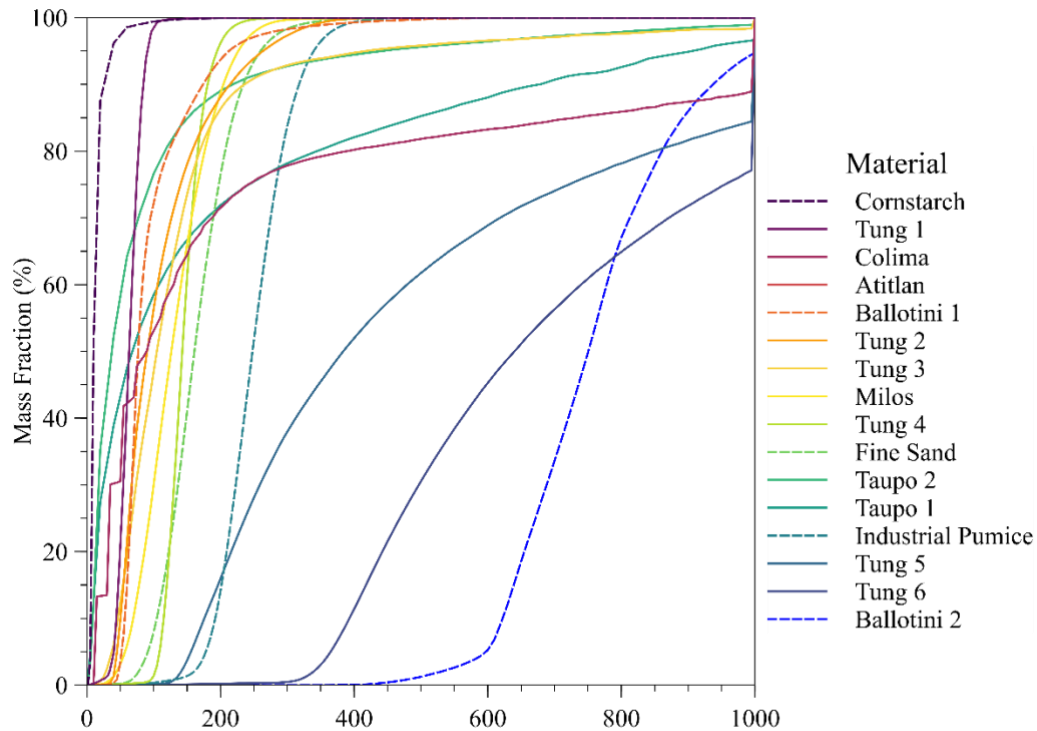


Figure 4.1. GSD plot of pyroclastic (solid line) and analogue (dashed line) materials used throughout the experiments. Materials in legend are organised by logarithmic particle size mean (with cornstarch the finest grained material used) (ϕ) for this and subsequent figures.

Table 4.4. Material properties of both pyroclastic (sample names shaded dark grey below) and analogue materials (shaded pale grey). These include logarithmic particle size mean and particle size median, particle range, fines content (< 63 μm), geometric mean (ϕ), and employ the method of moments for calculating mean, sorting, sphericity, symmetry, skewness, and kurtosis. The Sauter mean diameter is computed following the methods outlined in Breard et al (2019). Additionally, the Geldart Group Classification (Geldart, 1973) is determined based on the logarithmic mean particle size. Table is ordered by logarithmic particle size mean.

Material	Particle Size Mean (\bar{x}) ϕ	Particle Size Median ϕ	Particle Size Range (μm)	Fines Content (%)	Sorting Index (σ) ϕ	Sorting (σ_G)	Sphericity	Symmetry	Skewness (Sk) ϕ	Kurtosis (K) ϕ	Sauter Mean (mm)	Geometric Mean (μm)	Geldart Group
Corn Starch	4.8	4.8	5 – 340	96.2	0.6	Moderately Well Sorted	0.8	0.9	-0.3	4.3	0.02	35.4	A, B, C
Tung 1	3.8	3.7	2.5 – 297	35.8	0.4	Well	0.8	0.9	1.9	17.0	0.06	72.9	A
Colima	3.5	3.6	10 - 1000	84.4	1.5	Poorly Sorted	0.7	0.9	-0.5	2.6	0.04	90.3	A, B, C
Atitlan	3.4	3.8	< 20 - 1780	66.0	1.5	Poorly Sorted	0.8	0.9	-0.9	3.2	0.02	92.4	A, B, C, D
Ballotini 1	3.4	3.6	20 - 655	14.8	0.6	Moderately Well Sorted	0.9	0.9	-0.5	4.7	0.08	92.7	A, B, C
Tung 2	3.2	3.3	15 - 425	15.3	0.7	Moderate	0.8	0.9	-0.5	2.6	0.01	107.5	A, B
Tung 3	3.1	3.1	5 - 1000	19.3	0.9	Moderate	0.7	0.8	-0.6	4.1	0.01	115.0	A, B
Milos	2.9	2.9	15 - 615	8.7	0.6	Moderately Well Sorted	0.7	0.8	0.5	3.3	0.06	132.4	A, B, C
Tung 4	2.7	2.7	20 – 650	0.2	0.3	Very well	0.8	0.9	0.1	8.5	0.01	153.5	A, B
Fine Sand	2.6	2.6	10 – 530	0.8	0.4	Well sorted	0.9	0.9	0.4	4.6	0.14	168.7	A, B, C

Taupo 2	2.4	2.4	< 20 - 2000	52.2	1.0	Moderately Sorted	0.7	0.9	-0.5	4.1	0.04	195.8	A, B, C, D
Taupo 1	2.1	2.2	< 20 - 2000	38.9	1.2	Poorly Sorted	0.8	0.9	-0.5	3.3	0.04	234.6	A, B, C, D
Industrial Pumice	1.8	1.8	5 - 1000	0.1	1.0	Moderately Sorted	0.8	0.9	0.8	4.5	0.24	284.0	A, B, C
Tung 5	1.5	1.6	10 – 1000	0.1	0.8	Moderate	0.8	0.9	- 0.1	2.5	0.02	347.3	A, B
Tung 6	0.8	0.8	10 - 1000	0.0	0.5	Well	0.8	0.9	0.6	8.3	0.03	557.1	A, B
Ballotini 2	0.4	0.4	380- 1460	0.0	0.2	Very Well Sorted	0.9	1.0	-0.1	3.6	0.75	773.1	B, D

4.4.2 Bulk and tapped densities

In dry (0 wt.%) conditions, the finest materials (cornstarch, Colima, Atitlan and Taupo 2) display poor and very poor flowability properties as defined by their HR and CI values (Fig. 4.2, Supplementary Material 4A, 4B).

These correlate with the exceptionally high fines content of these materials (> 52 %). The remaining materials all exhibit fair to excellent flowability, which is influenced by both fines content (< 52 %) and high sorting values (Table. 4.4)

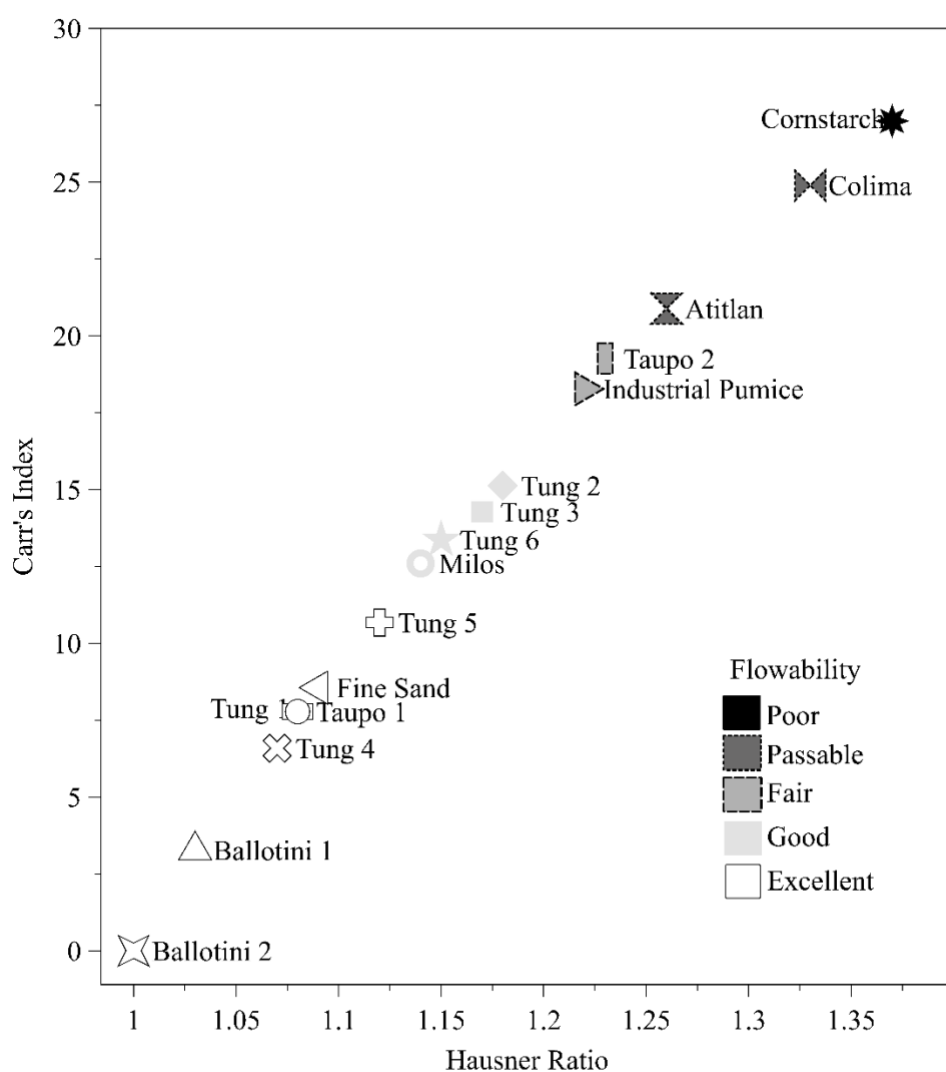


Figure 4.2. Bulk and tapped bulk density results of dry pyroclastic and analogue materials. Results were used to calculate Hausner ratio and Carr's index to determine flowability. Flowability field values are from Gorle and Chopade (2020). Materials are in order of particle size mean (\emptyset). Standard deviation of BTD, uncertainty and error can be found in Supplementary Material 4B.

4.4.3 Angle of repose

At 0 wt.% moisture, the SAoR of the pyroclastic samples range from 28° (std dev = 0.65, Milos) to 43° (std dev = 2.64, 2.76, Taupo 1, Colima), and the analogue materials from 18° (std dev = 0.41, ballotini 1) to 38° (std dev = 1.51, cornstarch) (Supplementary Material 4B). Comparing these results against the materials properties in Table. 4.4, demonstrate that the increase in SAoR correlates to size, shape, and sorting (Fig. 4.3). The DAoR ranges from 39° (std dev = 0.91, 1.84, Tung 5 and 6) to 61° (std dev = 1.70, Atitlan) for pyroclastic samples and from 32° (std dev = 0.41, 0.42, ballotini 1 and 2) to 59° (std dev = 1.51, cornstarch) for the analogue materials. An increase in particle size median results in an increase in both static and dynamic AoR (Fig. 4.3a). Fines content also plays a dominant role on AoR values. As fines contents increase, AoR increases until ~52 % fines where we see a divergence and larger gap between DAoR and SAoR values (Fig. 4.3b). With an increase in D_{32}^*SPHT , we see lower AoR values (Fig. 4.3e, f). Finally, sphericity and symmetry controls on AoR are demonstrated in Figure 4.3c and d, where a decrease in AoR correlates with increasing sphericity and symmetry. This is particularly evident for ballotini 1, which has the highest sphericity (0.90, 0.91) and symmetry values (0.93, 0.93).

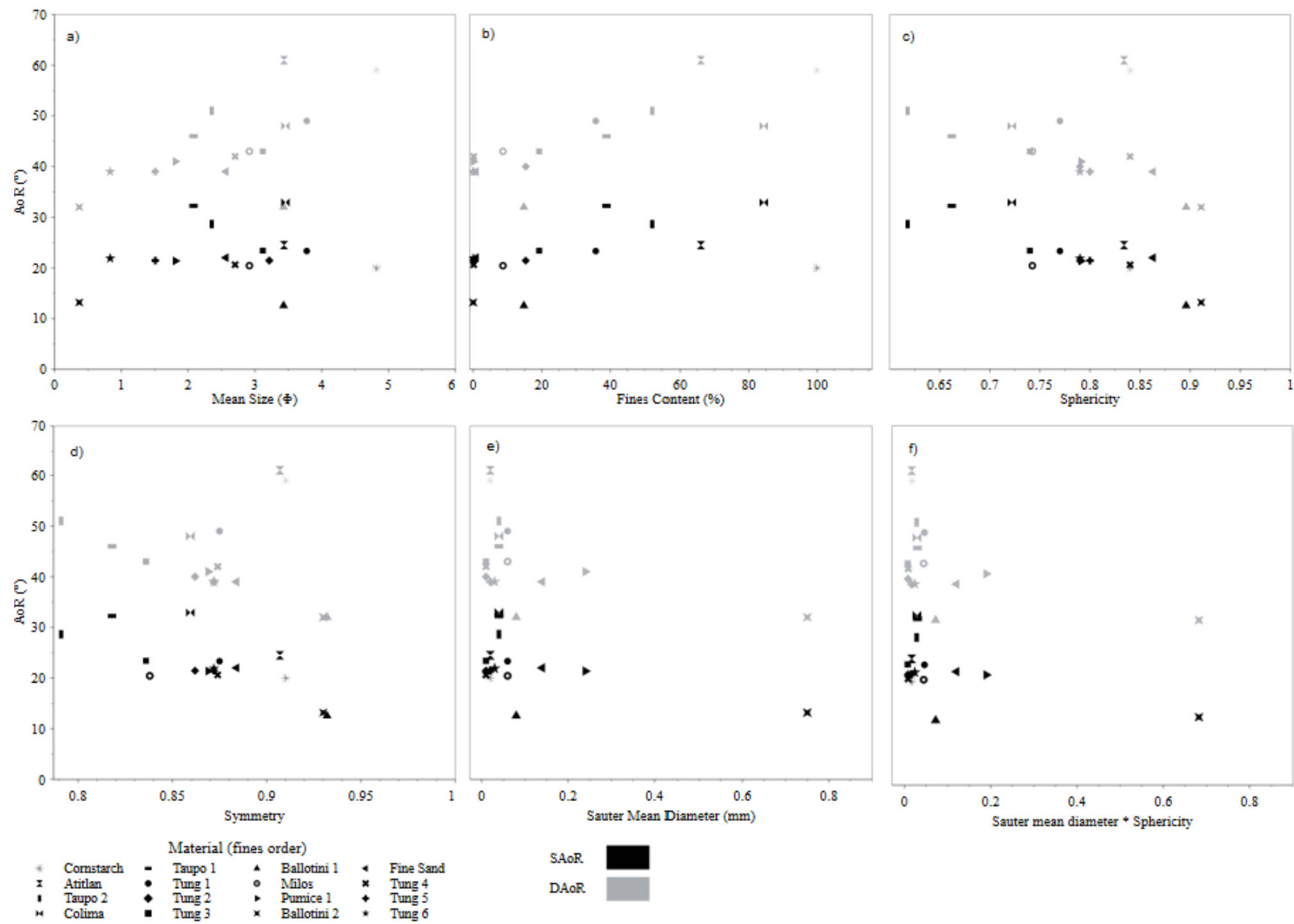


Figure 4.3. Comparison of particle a) methods of moments logarithmic mean size, b) fines content, c) sphericity, d) symmetry, e) Sauter mean diameter and f) Sauter mean * sphericity ($D_{32} \cdot SPHT$) against SAoR and DAoR values of pyroclastic and analogue materials. Materials are listed in order of fines content (%). Standard deviation, error and uncertainty is shown in Supplementary Material 4B.

4.4.4 Fluidisation

Results from the fluidisation experiments were investigated via sidewall video analysis of the fluidisation chamber. We used ballotini to characterise the frictional properties against the sidewall (Perspex) by completing tilt experiments (experimental set-up from Lowes & Perry, 1965). This allowed us to calculate the dry wall friction angle, which showed a value of 21.5° (SD = 2.4). Note that this value is likely to change with the addition of moisture and during fluidisation of material but has not been further explored in these results.

Observations of gas escape structures (e.g., bubbling, channelling) were made and gas velocity was recorded from the base of the chamber. Fluidisation behaviours are categorized into bubbling (U_{mb}), channelling (U_{mc}), explosive channelling (U_{mx}) and cracking behaviours (U_{mcr}) following Walding et al. (2023) (Fig. 4.4). In addition, a new feature is identified in this paper and named “diffusive cracking” (U_{mde}) (Fig. 4.4f, Supplementary Material 4C). Diffusive cracking is defined here as small cracks that can move in-between packages of material and are not fixed (in comparison to cracking, where wet material forms large cracks which only move with increased drying of the material). The individual packages in diffusive cracking can be fluidised, or as gas velocities increase, the packages of material can fracture into smaller packages aiding bubbling and channelling before once again settling into a package and repeating behaviours as mentioned above (Fig. 4.4f).

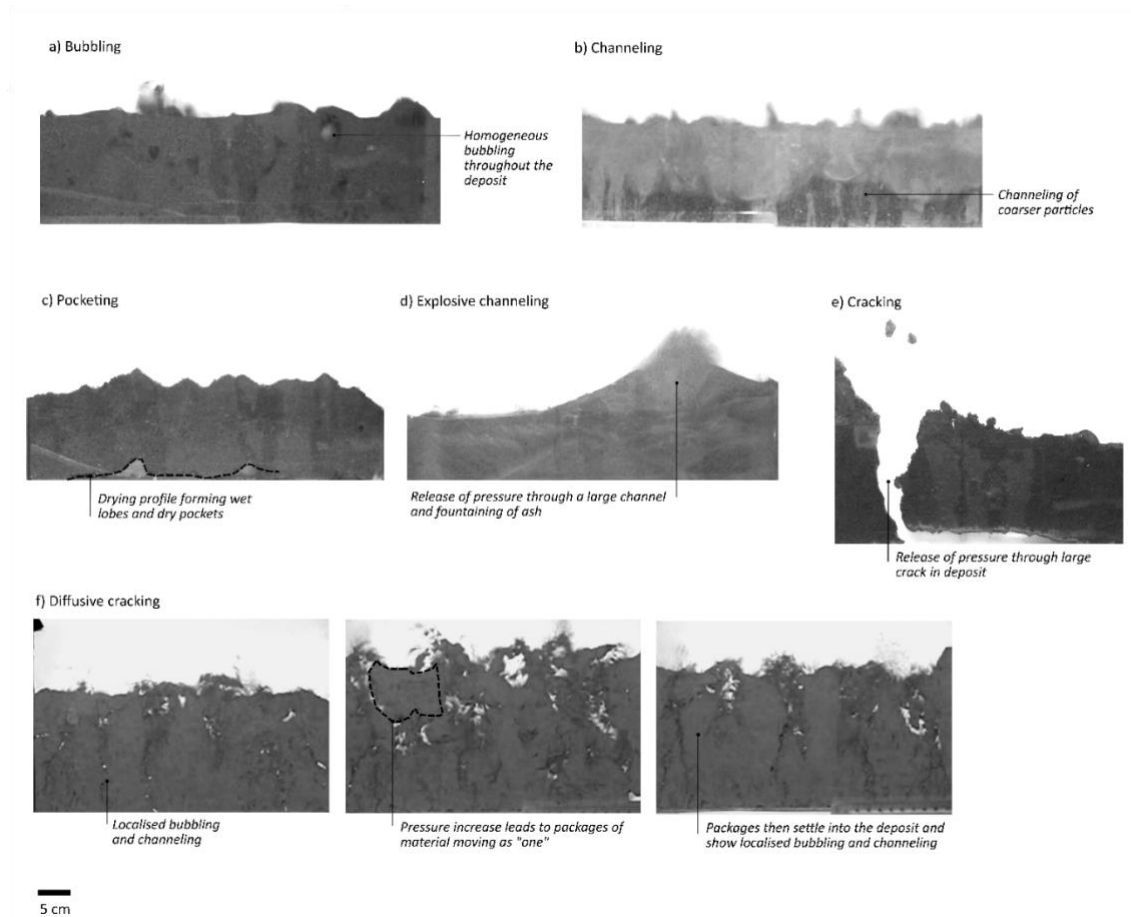


Figure 4.4. Images demonstrating the key behaviours described in these experiments showing a) bubbling, b) channelling, c) pocketing, d) explosive channelling, e) cracking (from Walding et al., 2023) and f) diffusive cracking features seen in the present fluidisation experiments.

4.4.4.1 Pyroclastic Material

At 0 wt.% moisture, the pyroclastic samples exhibit bubbling, diffusive cracking, channelling, and explosive channelling. Milos, Taupo 1 and Taupo 2 display channelling of the coarser material in the lower deposit and bubbling in the upper deposit (U_{mb} : Milos, 0.28; Taupo 1, 0.21; Taupo 2, 0.14 cm/s). However, Colima and Taupo 1 show small amounts of diffusive cracking with no significant change in pressure observed (Fig. 4.4f). At 0 wt.% moisture, both the diffusive cracking (Taupo 1, 0.069; Colima, 0.069 U_{mdc} cm/s) and explosive channelling (Atitlan, 0.069; Colima, 0.208 U_m cm/s) agitate the material and improve heterogeneous bubbling and channelling throughout the whole of the deposit (Fig. 4.4a-f).

The variations in fluidisation behaviours of Atitlan, Colima and Taupo 1 can be attributed to their high fines content (38 – 84 %; Table. 4.5). Fluidisation and U_{mb} values are significantly lower in material with a higher proportion of fines. These are indicative of Geldart Group C behaviours. Taupo 2 also displays a high percentage of

fines (52 %) but does not display cracking or explosive channelling at 0 wt.% moisture. This corresponds to the behaviours seen in the Tungurahua and Milos samples, where sorting is moderate to well sorted.

4.4.4.2 Analogue Material

Fluidisation experiments with the cornstarch were not attempted due to its tendency to disperse into the air. At 0 wt.% moisture, all the other analogue samples tested display bubbling of the deposit (Geldart Group B; Fig. 4.4). In the finer material (ballotini 1), bubbles are small and spherical and form throughout the whole of the deposit (U_{mb} 0.056 cm/s). Ballotini 2 and fine sand are overall coarser and denser materials, so sluggish bubbling is limited to the upper portion of the deposit (U_{mb} : ballotini 2, 2.08; fine sand, 0.417 cm/s). Finally, the industrial pumice has a larger size range than the others and exhibits channelling of the lower coarser material and bubbling (U_{mb} 0.382 cm/s) of the upper finer material (Fig. 4.5). The good fluidisation behaviours of these materials can be attributed to the low fines content (0.00 – 14.78 %) and moderate to well sorting values (Table. 4.4). Furthermore, the fluidisation behaviours of the analogue material at 0 wt.% moisture all exhibit Geldart Group A, B and C characteristics (Geldart, 1973).

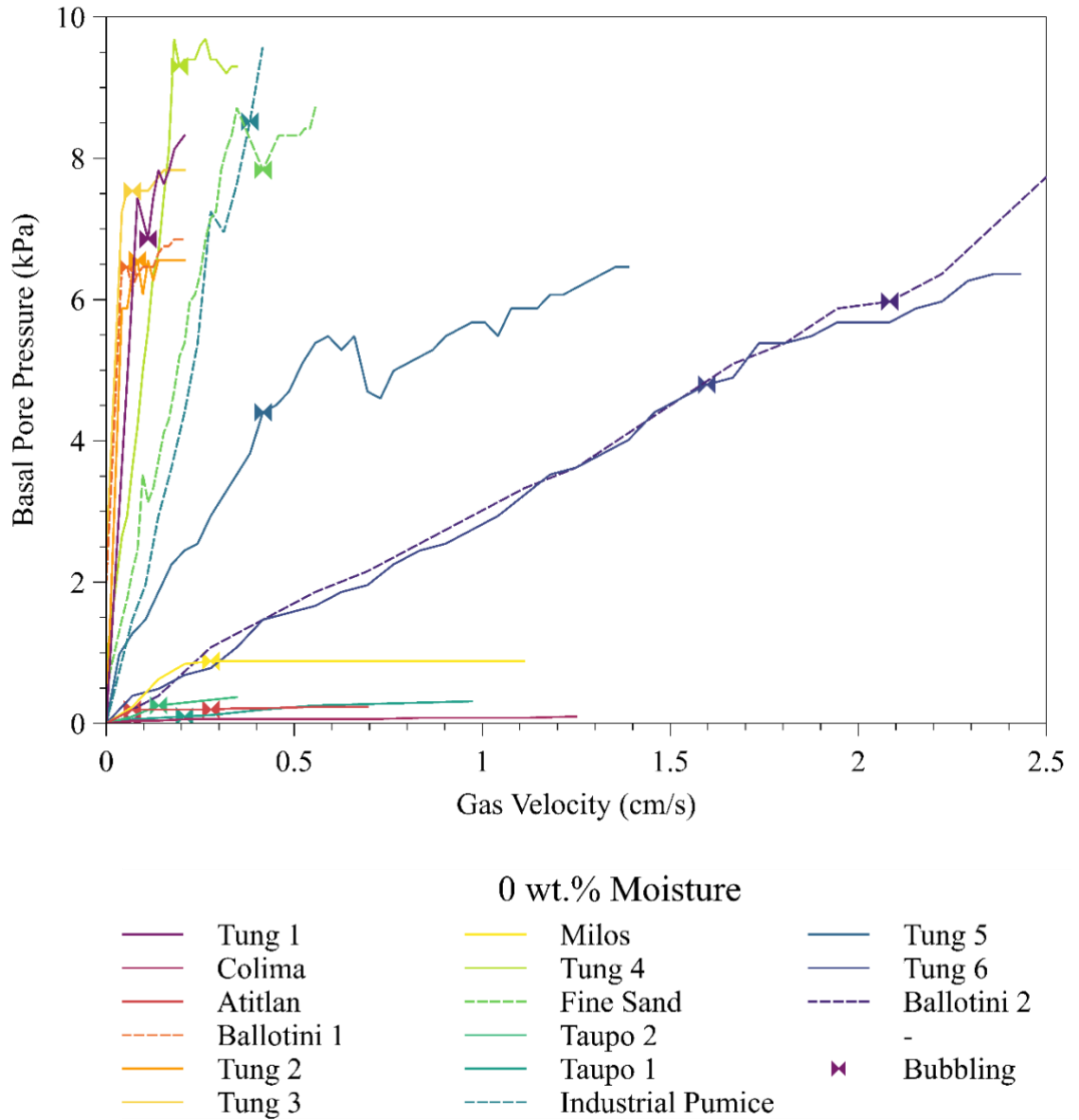


Figure 4.5. Fluidisation profiles of pyroclastic and synthetic materials at 0 wt.% moisture. Tung 1-6 values obtained from Walding et al., 2023. Materials are in order of particle size mean (ϕ).

4.5 Results II: behaviour of material in wet conditions

4.5.1 Bulk and tapped densities.

With increasing moisture contents (0 – 5 wt.%), bulk and tapped densities overall decrease rapidly with an increase from 0 to 0.5 wt.% moisture and then steadily from 0.5 to 5 wt.% moisture (Supplementary Material 4B). However, this is not the case for ballotini 1 and 2. From 0 – 0.5 wt.% moisture, ballotini 2 increases in tapped density before levelling out. The tapped density for ballotini 1 shows a decrease in density from 0 – 1 wt.% moisture before increasing in tapped density from 1 – 5 wt.% moisture. Both particles are highly spherical and hydrophobic, therefore added water may form

capillary bridges between the particles. It is thought that with increasing water, lubrication is increased, allowing for the particles to display overall better packing.

The Hausner Ratio (HR) and Carr's Index (CI) calculations can be used to assess how moisture effects the flowability of a material (Supplementary Material 4B). The largest change seen in both CI and HR from 0 – 5 wt.% moisture are Tung 4 samples and the lowest change was seen in Tung 6. This is thought to be due to the high sorting and small size range of Tung 4 and the high size mean of Tung 6 (Table. 4.4). The CI and HR results show that increasing moisture (0.5 – 5.0 wt.%) has a negative effect on the flow property of the material (i.e., showing poorer and more difficult flowability) (Fig. 4.6). However, this is not the case for Tung 6 which decreases in CI and HR. This is thought to be due to water-induced lubrication and better packing of material.

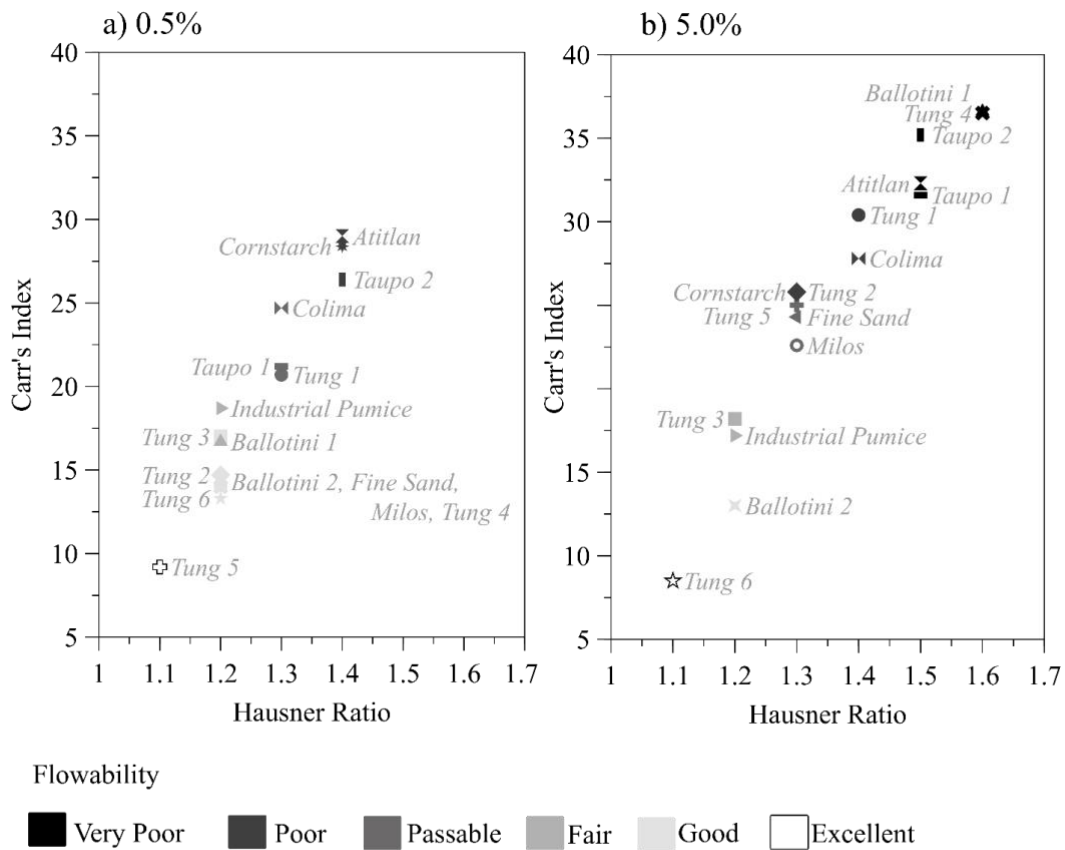


Figure 4.6. Changes in Hausner Ratio and Carr's Index as a function of water addition to the material for a) 0.5 wt.% and b) 5 wt.%. Flowability field values are from Gorle and Chopade (2020). Standard deviation, error and uncertainty of BTD can be found in Supplementary Material 4B.

4.5.2 Angle of repose

An increase in moisture from 0 to 5 wt.% results in an increase in SAoR and DAoR values for pyroclastic and analogue materials and, therefore, a decrease in flowability (Table. 4.9; Supplementary Material 4B). The angle of repose is the steepest angle that a loose slope can naturally form. The forces pulling the particles down slope, the shear stress, is equal to the force that resists down-slope movement (shear strength). The addition of cohesion increases the shear strength of the material due to the formation of interparticle capillary forces. Therefore, changes in shear strength are a product of the addition of moisture to the angle of repose pile (Sheng et al., 2011; Beakawi Al-Hashemi & Baghabra Al-Amoudi, 2018). Further detailed analysis of Tungurahua 1-6 samples can be found in Walding et al. (2023).

4.5.2.1 Pyroclastic Materials

Overall, the highest SAoR change ($> 29^\circ$) from 0 to 5 wt.% moisture are seen in Tung 1, Tung 2, Tung 3, Milos, Tung 4 and Tung 5. From 0 to 1 wt.% moisture, Tung 2, Tung 3, Tung 4 and Tung 5 show a rapid increase in SAoR which then increases at a lower rate from 1 to 5 wt.% moisture (Supplementary Material 4B). In some materials (Tung 2, Tung 3) we see a decrease in SAoR value at 5 wt.% moisture. Taupo 2, Colima, and Atitlan show the smallest change from 0 to 1 wt.% and some of the largest from 1 to 5 wt.% moisture. The lowest overall SAoR change (8°) from 0 to 5 wt.% moisture is Colima. For the DAoR experiments, the highest change from 0 to 2.5 wt.% moisture is Tung 1 (39°) and Tung 4 (48°) and the lowest is Atitlan (-11°) (Fig. 4.7).

The overall largest changes are seen in the Tungurahua and Milos samples. These samples span the size range of pyroclastic mean sizes, are all moderately to well sorted ($0.252 - 0.868$) and show similar sphericity values ($0.74 - 0.84$) (Table. 4.4). These samples also all display the lowest fines content ranging from 0.04 % (Tung 6) to 36 % (Tung 1) (Fig. 4.7). Conversely, the lowest overall changes as seen in Colima, Atitlan, Taupo 1 and Taupo 2 which have a broad size mean, are moderately to poorly sorted ($0.98 - 1.50$) and sphericity values of $0.70 - 0.83$. Notably, these samples display the highest fines content which ranges from 39 % (Taupo 1) to 84 % (Colima) (Fig. 4.7).

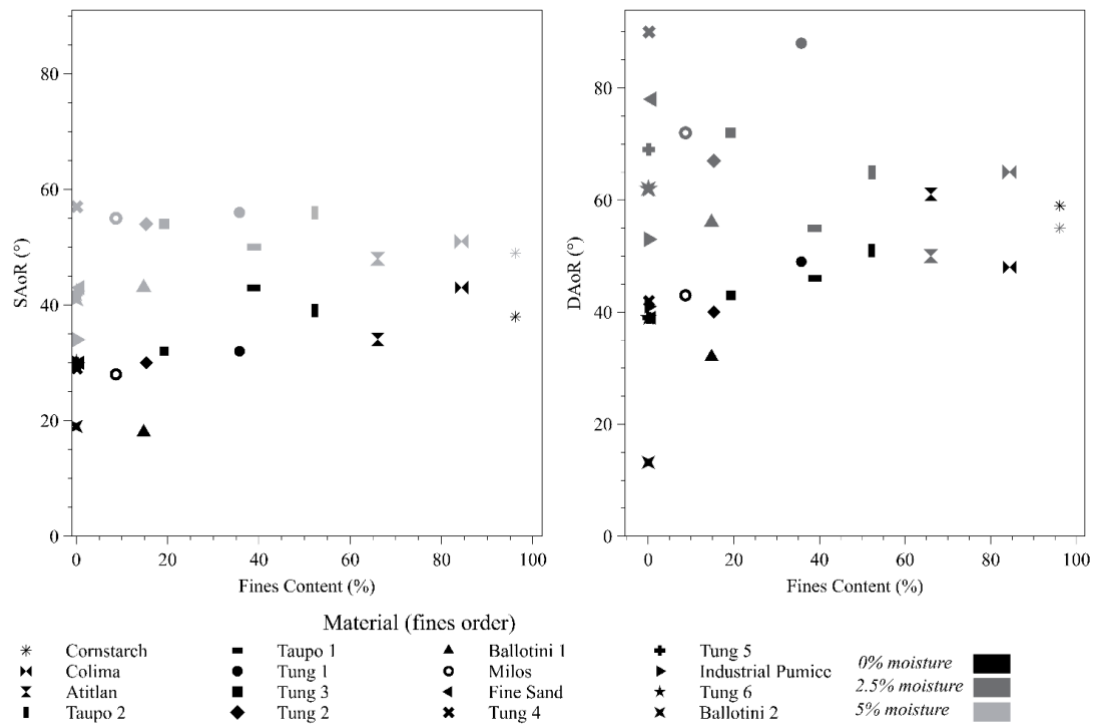


Figure 4.7. a) SAoR at 0 and 5 wt.% moisture and b) DAoR at 0 and 2.5 wt.% moisture of pyroclastic and analogue materials and fine content (%). Materials are listed vertically in order of fines content % from cornstarch to Tung 6. Standard deviation, error and uncertainty is in Supplementary Material 4B.

4.5.2.2 Analogue Materials

Values of SAoR increase with increasing moisture from 0 to 5 wt.%. From 0 to 1 wt.% moisture, ballotini 1 and ballotini 2 show a rapid increase in SAoR (Fig. 4.7). Cornstarch, fine sand and industrial pumice all show a more gradual increase. From 1 to 5 wt.% moisture the SAoR values become steadier and ballotini 1, fine sand and ballotini 2 all show the same or lower values than their 1 wt.% moisture SAoR results. The largest changes can be seen in the ballotini 1 and ballotini 2 samples. These samples are both moderately well to very well sorted (0.62 – 0.24) and have high sphericity values of 0.90 and 0.91 (Table. 4.4, Fig. 4.7). The lowest overall change is cornstarch (11°), which displays the largest size range, sorting value (0.989) and lowest sphericity value (0.79).

The DAoR experiments show a similar pattern, where from 0 to 2.5 wt.% moisture there is an increase of DAoR in ballotini 1 (24° increase), fine sand (39° increase), industrial pumice (12° increase) and ballotini 2 (30° increase). However, the cornstarch shows a decrease of -4° with increasing moisture from 0 to 2.5 wt.%. This is due to the high percentage of fines in cornstarch (96.1 %) compared to the other samples (Table. 4.4).

4.5.3 Fluidisation

The results presented correspond to the observed fluidisation behaviours of both pyroclastic materials (Atitlan, Colima, Milos, Taupo 1 and Taupo 2) and analogue materials (ballotini 1, ballotini 2, fine sand, industrial pumice) utilized in these experiments across water addition of 0.50, 1.00, 2.50 and 5.00 wt.%. A detailed review of the fluidisation behaviors of Tungurahua 1-6 samples can be found in Walding et al. (2023) and Supplementary Material 4D. Overall, results show that with increasing water content, a higher gas velocity (cm/s) is required to fluidise the material. A Geldart Group has been assigned to the fluidisation behaviours observed throughout the experiments (Geldart, 1973; Cocco & Chew, 2023).

4.5.3.1 Pyroclastic Materials

At 0.50 wt.% moisture (Fig. 4.8a, f), Colima (U_{mb} 0.139 cm/s) and Taupo 2 (U_{mb} 0.069 cm/s) display bubbling towards the top of the deposit and diffusive cracking at the base (Geldart Group A and C, Supplementary Material 4C). When the cracking ruptures, the overlying material is agitated and bubbles with the rest of the deposit before settling to the base of the deposit. Atitlan (U_{mb} 0.069 cm/s) and Taupo 1 (U_{mb} 0.069 cm/s) (Fig. 4.8b, g) show bubbling of the upper and channelling of the lower deposit (Geldart Group A, B and C). Milos (Fig. 4.8d) forms pockets of bubbling (U_{mb} 0.972 cm/s) at the base of the material, which increase in size throughout the experiment (Geldart Group B).

At 1.00 wt.% moisture (Fig. 4.8b), Atitlan shows bubbling throughout the upper portion of the deposit (U_{mb} 0.069 cm/s) and channelling in the lower portion (Geldart Group B). Colima, Taupo 1 and Taupo 2 (Fig. 4.8a, f, g) show diffusive cracking in the deposit and some bubbling at 0.556, 0.347 and 0.208 U_{mdc} cm/s (Geldart Group B and C). At higher gas velocities, explosive channelling happens multiple times throughout the deposit but does not release significant amounts of pressure from the base.

At 2.50 wt.% moisture (Fig. 4.8b), Atitlan shows bubbling throughout the upper portion of the deposit (U_{mb} 0.069 cm/s) and channelling in the lower (Group A and C). Explosive channelling occurs at 0.972 cm/s for Colima (Fig. 4.8a) followed by a large pocket forming with bubbling and drying of material (Geldart Group C and A; U_{mb} 1.11 cm/s). Taupo 1 and Taupo 2 (Fig. 4.8f, g) display explosive channelling and cracking (Geldart Group C), but with no observed gas release. Bubbling observed in Taupo 1 (U_{mb} 1.25 cm/s) is sluggish. Small pocketing occurs at the base of the Milos (Fig. 4.8d)

deposit, with no observed bubbling (Geldart Group C). Slow drying continues until the end of the experiment.

Finally, at 5.00 wt.% moisture (Fig. 4.8b), Atitlan again shows similar behaviours as described previously and bubbles at 0.069 cm/s (Geldart Group A). Milos (Fig. 4.8d) shows cracking at 3.19 cm/s and explosive channelling at 4.17 cm/s (Geldart Group C). Taupo 1 (Fig. 4.8f) forms a large pocket at the base of the deposit, slight cracking (1.39 cm/s) and explosive channelling at 1.53 cm/s (Geldart Group C). Finally, Taupo 2 (Fig. 4.8g) bubbles in a sluggish way in the upper deposit (U_{mb} 0.069 cm/s) and displays channelling in the lower deposit. With increasing gas velocity, cracks begin to form and breakaway from each other in “blocks” which rise and fall (Geldart Group C).

Compared to the Tungurahua 1-6 samples (Supplementary Material 4D), Atitlan, Colima, Taupo 1 and Taupo 2 exhibit “higher moisture” fluidisation behaviours (Group C: i.e., cracking and explosive channelling) at significantly lower moisture levels. These materials also display significantly higher fines content (%) than any other samples (Table. 4.4). This may explain why we see more sluggish bubbling behaviour and diffuse cracking happening at a lower moisture content.

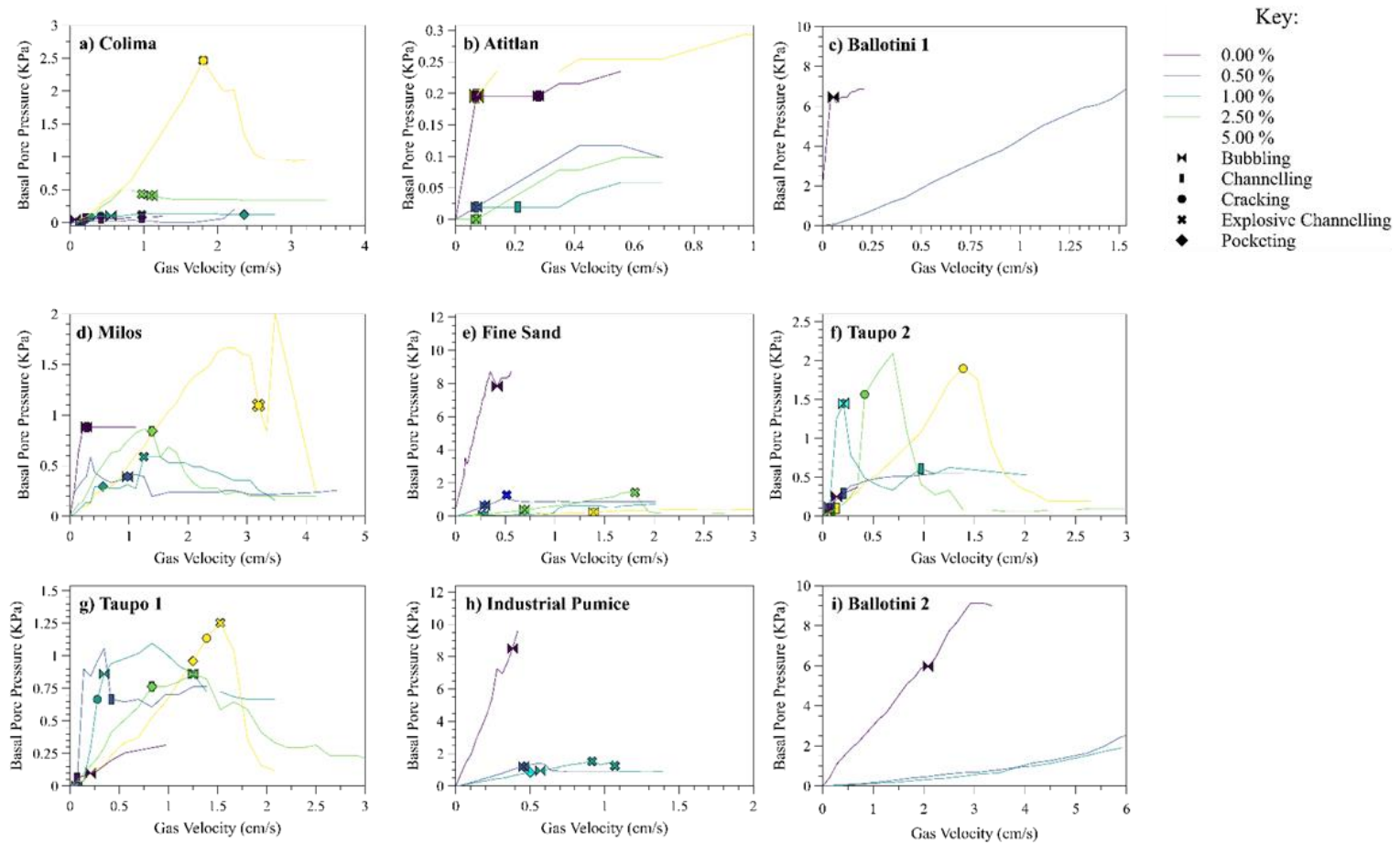


Figure 4.8. Fluidisation behaviours of pyroclastic and analogue materials at 0, 0.5, 1, 2.50 and 5 wt.% moisture addition a) Colima, b) Atitlan, c) Ballotini 1, d) Milos e) Fine Sand, f) Taupo 2, g) Taupo 1, h) Industrial Pumice i) Ballotini 2. Symbols show fluidisation behaviours of material. Data is presented in material mean size order. Fluidisation results from Tung 1 – 6 are in Supplementary Material 4D.

4.5.3.2 Analogue Materials

At 0.50 wt.% moisture (Fig. 4.8), no gas escape structures are observed in ballotini 1 and ballotini 2. Fine sand (Fig. 4.8e) and industrial pumice (Fig. 4.8h) both display bubbling (U_{mb} : 0.292, 0.458 cm/s respectively) in the upper deposit and channelling of the lower (Geldart Group A, B and C). At higher gas velocities, explosive channelling (0.514 cm/s) occurs in the fine sand but there is no significant change in pressure.

At 1.00 wt.% moisture, no gas escape was observed for ballotini 1 and ballotini 2 (Fig. 4.8c, i). Once material was dried by the fluidising gas, the ballotini deposit had stuck together as a “fused” package and had to be manually broken apart. No further fluidisation experiments were undertaken on the ballotini samples. Both the fine sand and industrial pumice exhibited pocketing and bubbling of dry material at 0.2778 and 0.5694 cm/s (Geldart Group A, B and C). At higher gas velocities, explosive channelling was observed in the industrial pumice. Explosive channelling at 1.069 cm/s released 0.33 kPa. Due to time constraints, fluidisation of industrial pumice at 2.5 and 5 wt.% were not completed.

At 2.50 wt.% moisture, fine sand (Fig. 4.8e) forms bubbling pockets at 0.69 cm/s and explosive channelling at 1.81 cm/s (releasing 0.69 kPa). Finally, at 5.00 wt.% moisture (Fig. 4.5b) fine sand shows pocketing and subsequent bubbling of the material (U_{mb} 1.39 cm/s) (Geldart Group C and A).

4.6 Discussion

In this discussion, we identify the key controls that influence the behaviours of pyroclastic material with increasing moisture content. We then discuss material recommendations for use in experimental modelling in dry and wet conditions in a flow and substrate.

4.6.1 Controls on the behaviour of pyroclastic material

To better constrain the controls on material behaviours in dry and wet conditions, we conducted principal component analysis (PCA) on AoR results and material characteristics (e.g., symmetry, sphericity, particle size mean, sorting, Sauter mean, geometric mean and fines content).

The results from the PCA analysis (Fig. 4.9; Supplementary Material 4E) show that SAoR and DAoR values at 0 wt.% moisture correlate to mean, fines content, sorting,

HR and CI. However, as we increase moisture from 0 to 0.50 wt.% the results become more positively correlated with sphericity, symmetry and Sauter mean and therefore more negatively with sorting and fines content. A further increase in moisture from 0.50 to 2.5 wt.% shows no correlation to any of the aforementioned variables.

These results are interpreted as reflecting the transition of the material from a non-capillary to a capillary state with the introduction of water. In the capillary state (Kim & Hwang, 2003; Kim & Sture, 2008) particles become semi-supported by capillary bonds. With no moisture, the AoR is dominated by material characteristics (fines and sorting) as there are no inter-capillary bonds present. At low moisture addition, the control becomes more correlated to physical particle characteristics (sphericity and symmetry). Finally, at the highest moisture values, we infer a transition due to changes in capillary bonds forming in interparticulate spaces, and thus behaviours are less controlled by material parameters (i.e., fines content, shape etc.).

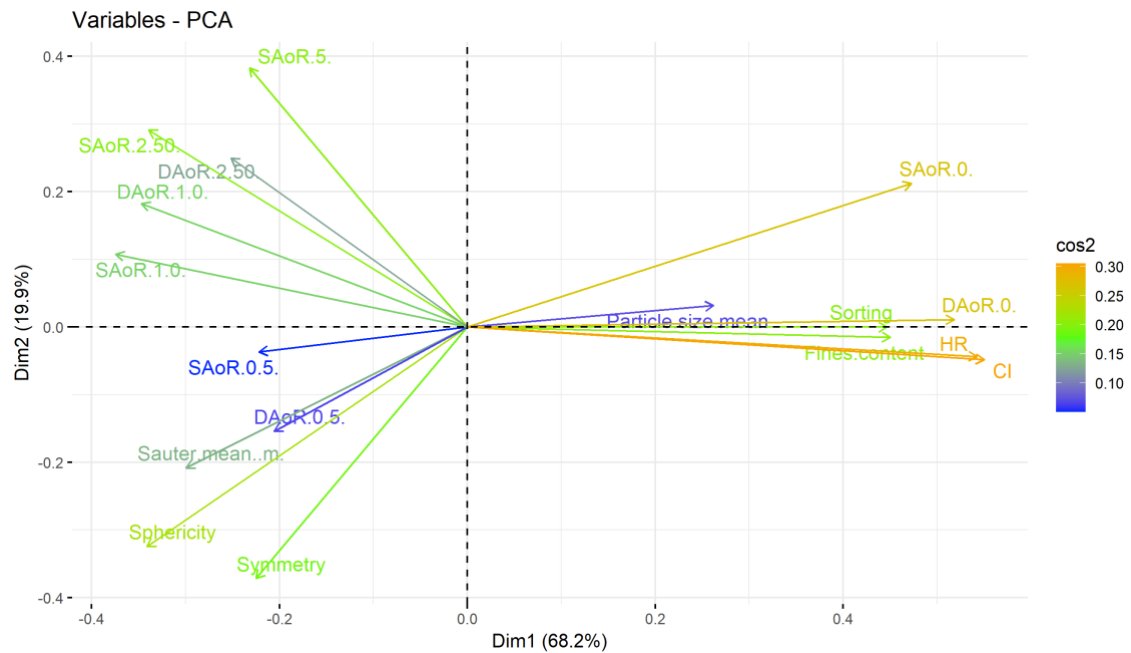


Figure 4.9. Loading plot from PCA analysis (Lê, Josse and Jussion, 2008; Kassambara and Mundt, 2020; R Core Team, 2023). Dim1 and Dim2 are the principal components and show percentages. Each variable used in the data set is showed as a vector. The direction of the vector indicates the correlation between the variable and the principal component, while the length of the vector represents the magnitude of the correlation (\cos^2). Vectors that group together or point in similar directions may indicate similarities or underlying relationships. Additional data can be found in Supplementary Material 4E.

4.6.2 The importance of the proportion of fines content

The presence of fines in a material influences its behaviour in both static and dynamic conditions, as well as in wet and dry environments, as demonstrated in the BTd (Fig. 4.2, 4.6), SAoR (Fig. 4.3, 4.7), DAoR (Fig. 4.3, 4.7), fluidisation (Fig. 4.5, 9a-i) tests

and PCA results (Fig. 4.9) (Supplementary Material 4B, 4D and 4E) . At 0 wt.% moisture, the angle of repose (both SAoR and DAoR) increases with mean size, sphericity, symmetry, Sauter mean and proportion of fines content (up to ~66 %). Note that the DAoR results are significantly higher than the SAoR results, this is attributed to boundary friction of the drum (Dury et al., 1998). At 84 % fines content, there is a clear divergence between SAoR (decreasing) and DAoR (increasing) values (Fig. 4.3b). Interestingly, at very high fines contents, pyroclastic material shows a decrease in flowability in a dynamic environment and an increase in flowability in a static environment (Fig. 4.3b, 4.7). This may indirectly influence the mechanical properties of a material, such as internal angle of friction and cohesion-related strength (Beakawi Al-Hashemi & Baghabra Al-Amoudi, 2018). For example, a material that has greater than 30 % volume of fines results in the stress forces being dominated by the fines fraction (Li et al., 2020; Breard et al., 2023).

In dry conditions, material with a low fines content can be expected to behave based on its physical particle characteristics such as size, sphericity, and symmetry (Abdullah & Geldart, 1999). With increasing sphericity of a particle, the angle of repose will decrease; and vice versa, with decreasing sphericity of a particle (i.e., increasing angularity), the angle of repose will increase (Beakawi Al-Hashemi & Baghabra Al-Amoudi, 2018). This is due to interparticle contacts, where angular particles increase jamming and interlocking connections (Beakawi Al-Hashemi & Baghabra Al-Amoudi, 2018). Our results somewhat agree with these observations as seen through the sphericity and symmetry values increasing in Figure 4.3c and d.

The addition of moisture to material with high fines content leads to a decrease in both SAoR (cornstarch, Colima, Atitlan, Taupo 2; Fig. 4.7) and DAoR (cornstarch Atitlan and Colima; Fig. 4.7) values. This may be due to friction between particles due to particle morphology characteristics and moisture-induced clumping of material. The fines material is more likely to form interlocking “clumps” of material in dry conditions or moisture-induced clumps when wet. In turn, both instances of clumping will increase the size of the material to form more spherical clumps, which are more likely to have greater translational and rotational velocities (Chen et al., 2019). Similarly, the presence of fines significantly increases the material surface area (Fig. 4.3e, f ; Huang et al., 2009) and the surface tension of free moisture cannot mix well in the fines-dominated mixture. This may result in the formation of liquid bridges which reduce the contact friction, resulting in a decrease of AoR values.

Bulk behaviour can significantly change with fines content (Beakawi Al-Hashemi & Baghabra Al-Amoudi, 2018). An increase in fines creates more interparticle contact points, which in turn can increase the packing of material (Breard et al., 2023). This is demonstrated in the BTd experiments where loose and tapped bulk densities increase with fines content and size (e.g., cornstarch, Colima, Atitlan; Supplementary Material 4B). This leads to better packing of material and thus poorer flowability. This also corresponds to what we observe in the DAoR experiments where an increase in fines content and a decrease in size results in higher DAoR values, and therefore a poorer flowability value (Fig. 4.2). These results highlight a clear relationship between fines content, particle size, loose/tapped behaviour and flowability.

4.6.3 Age, Composition and Environment Effects

Age, composition, and environment will all play a role in the decay or alteration of material (Nagasawa, 1978). Furthermore, post-deposition hydrothermal alteration over time may cause the alteration and decay of minerals into clay (Mirabella et al., 2005). Increasing clay content may result in changes in physical material properties (i.e., increase in cohesion, fines content, density etc.). We examined our results against composition and age of material to rule out any effect of age or composition on our results.

Our samples range from felsic (Taupo 1, 2 and Atitlan), intermediate (Milos) and mafic (Colima and Tung 1-6) in composition (Table. 4.2; Wilson, 1984; Hall et al., 2013; Kelfoun et al., 2009; Douillet et al., 2013; Eychenne et al., 2012; Zhou et al., 2020). The degree of magmatic evolution does not appear to be correlated with the changes in shear strength with increasing moisture. In this study, we have found no correlation between ages of samples to shear strength. For example, the Tungurahua (Tung 1-6) samples from 2006 showed significantly higher SAoR difference from 0 to 5 wt.% moisture (22-29° difference between 0 and 5 wt.% SAoR) in comparison to the more recent 2015 Colima samples (8° difference between 0 and 5 wt.% moisture SAoR). The oldest Taupo samples (235 A.D.) show a change of 17° (Taupo 1) and 18° SAoR (Taupo 2) from 0 – 5 wt.% moisture.

4.6.4 Implications for PDCs and their Deposits

Static and dynamic internal friction coefficient, as determined by the AoR values will play a critical role at different stages within a PDC system. For example, the static friction coefficient may play an important role in the initial movement, remobilisation

and entrainment of sediment from an overriding PDC. Once material is moving, dynamic friction will be the dominant force. However, in the case of the DAoR method used in these experiments, the angle of repose is high which is thought to be due to boundary friction of the drum.

4.6.4.1 Implications for deposits

In Walding et al. (2023) three types of gas escape structures were observed, dependent on moisture content. Type 1 (0 – 0.25 wt.% moisture) showed bubbling and channelling of material and relatively “good” fluidisation behaviours. Type 2 (0.50 – 5.00 wt.% moisture) resulted in bubbling, channelling, pocketing, a drying profile and explosive channelling. Type 3 (7.50 and 10 wt.% moisture) showed a bubbling drying profile, pocketing and cracking of the deposit (Fig. 4.4 a-d). These results showed that fluidisation and gas escape may be stalled or stopped by the presence of moisture (from 0.50 wt.%).

In this study, we observe the same gas escape structures as Walding et al. (2023), but sometimes at significantly lower moisture contents. Additionally, we describe a new behaviour, “diffusive cracking” (Fig. 4.4e; Supplementary material 4C). The present study expands on the types of behaviour of gas escape shown in Walding et al. (2023) and demonstrates that gas escape structures are highly variable with differing material characteristics, their geomechanical properties and moisture content.

Material behaviours differed greatly with varying presence of fines. At a high fines percentage (> 38 %) fluidisation behaviours behave more like the “high moisture” structures (i.e., explosive channelling, cracking) seen in Walding et al. (2023). This is due to the larger influence from Group C Geldart Group particles (Geldart, 1973). In dry conditions, Group C particles are dominated by interparticle forces and are known to demonstrate poor fluidisation behaviours of spouting, slugging, and channelling (Leturia et al., 2014). Materials moved through the different fluidisation stages described by Walding et al. (2023) with increasing moisture. However, the Atitlan material which comprises of 66 % fines showed no significant changes in fluidisation behaviour with increasing moisture. This may be due to having a large surface area, or the presence of H₂O-scavenging minerals. Further study would benefit from investigating the impact of varying chemical composition and H₂O scavenging in more detail.

4.6.4.2 Implications for secondary explosions

We show that secondary explosions may form from the cohesive nature of a dry high fines (%) material as well as with the introduction of moisture, expanding the findings of Walding et al. (2023). This behaviour is demonstrated in work completed by Gilbertson et al. (2020) where vertical changes in fine and coarse particle sizes resulted in secondary explosions. The cohesive nature of fine material creates an almost impermeable deposit therefore hindering gas release (Torres et al., 1996; Gilbertson et al., 2020) and subsequent pressure increase and release.

4.6.4.3 Implications for flow behaviour

We demonstrate an increase in cohesive behaviour and resulting shear strength with increasing fines content and moisture, consistent with the findings of Walding et al. (2023). However, at high volumes of fines (> 84 %), 0 wt.% moisture SAoR values decrease, therefore suggesting an increase in flowability. Breard et al. (2023) suggest that fines and packing behaviours can explain the relative long run-out distances of block and ash flows, as an increase in fines increases packing behaviour and elevates pore pressure within the flow. Our results support this finding, where with increasing fines %, flowability increases.

In Walding et al. (2023), we hypothesised that an increase in fines and moisture influences shear strength and therefore, higher moisture contents may reduce flowability and reduce the maximum runout distances of PDCs. However, at the maximum volume of water added (2.5 and 5 wt.%) in these experiments, material with a high fines content > 84 % showed a decrease in SAoR (cornstarch, Colima, Atitlan and Taupo 2) and DAoR (cornstarch, Colima) values, suggesting an increase in flowability.

The moisture content ranges used in these experiments are not high enough to mobilise the material as a slurry, therefore, the changes in flowability state are not due to the material becoming “laharic” or “saturated”. This may have implications for PDCs with a high proportion of fines in moisture influenced environments, such as phreatomagmatic or phreatic events (McPhie et al., 1990). In this work we only looked at the finer fractions of material, compared to the natural polydisperse nature of PDCs. Future work would benefit from investigating this behaviour at the bulk scale, or whether this behaviour is just indicative of a fine material. Furthermore, the use of a fluidised channel may show these behaviours better.

Our results from the D_{32} *SPHT and AoR data (Fig. 4.3e, f) show that fines-rich and irregular shaped mixtures will have low permeability, indicating that gas retention and

fluidisation may be increased (Breard et al., 2019). This is also supported by our fluidisation experiments, where finer material shows diffusive cracking (Fig. 4.4f) in comparison to bubbling (Fig. 4.4a, Supplementary Material 4C), suggesting that increased surface area is influencing frictional drag from the fluidising gas.

4.6.5 Material recommendations for experimental modelling

We have demonstrated that material behaviour is controlled by various properties which may have implications for PDCs and their deposits. Therefore, it is important to choose analogue material carefully, depending on the behaviour experimentalists are aiming to recreate. Here, we compare the material behaviours of pyroclastic samples with a range of analogue materials. We discuss the suitability of those materials for use in experiments conducted under both dry and wet conditions.

4.6.5.1 Dry experiments

4.6.5.1.1 For simulating a flow

Analogue material is often chosen based on its ability to fluidise in small laboratory experiments (Roche et al., 2010; Rowley et al., 2014; Smith et al., 2018). In this work we only investigate fluidised flow behaviour rather than free-falling from gravity. The particle size measurements suggest that all material should be able to exhibit good fluidisation behaviours, associated with Group A and B of Geldart's classification (Geldart, 1973). This is important because in analogue experiments it is important that the clogging of fine material in hoppers does not occur.

Due to the analogue materials used in these experiments having less polydispersity (e.g., size range, fines content, shape parameters) than the natural, pyroclastic material, it is thought that these will present better flowability and fluidisation results. As the size ranges of our analogue materials span the size ranges of the pyroclastic material, it is expected that finer particles (i.e., cornstarch) may behave in a similar manner to fine pyroclastic particles (e.g., our Atitlan or Colima sample). This is the same for the coarser material such as Tung 6 against ballotini 2.

For the dry AoR experiments, cornstarch, fine sand and industrial pumice fall into the range of all the pyroclastic material used (Table. 4.5). In the DAoR experiments, the dry values of analogue material lie in between 39 – 59° DAoR and for pyroclastic material range from 39 – 61° DAoR. However, both ballotini 1 and ballotini 2 show dramatically lower DAoR values of 13° to 32° for DAoR and therefore, generally do not fit too well when comparing to pyroclastic material in a dynamic testing environment (Table. 4.5).

The results of the fluidisation experiments completed demonstrate that U_{mf} is greater with increasing particle size mean and increasing density (Tung 5, Tung 6, ballotini 2). However, U_{mf} can also increase with decreasing mean particle size and with the proportion of fines content within the material. This results in more Group C behaviour (Geldart, 1973) of powders, where fluidisation begins to be inhibited by cohesive forces between finer particles. The results from the static (AoR and BTd) experiments can also be used to calculate the flowability of a material. The results from these static tests correlate well to what is observed in the fluidisation experiments. However, with increasing fines content the projected flowability from the static experiments does not match that of the fluidisation experiments. This is best shown in the behaviours of cornstarch, Atitlan, Taupo 2 and Colima where with increased fines content we see a decrease in SAoR values (Fig. 4.3b). Therefore, for material at high fines concentration it is important that we not only consider the use of AoR and BTd in determining flowability behaviours, but also how the material will perform in a fluidised environment.

For experiments where matching fluidisation behaviours is important, fine sand, ballotini and cornstarch show the closest match to the range of natural samples used in this study (Table. 4.5). However, it should be noted that although ballotini shows useful fluidisation behaviours in comparison to pyroclastic material, the BTd and AoR values are considerably lower in a dry environment. This is due to their high sphericity and smoothness, which will reduce contact friction between particles. For future experiments, the combination of different mixtures of these materials could potentially be used to simulate a full dynamic regime (i.e., turbulent to granular).

Although we have been careful to consider a range of pyroclastic options in these experiments, their natural variability means that different experiments may benefit from using different types of material. It should be noted that the practical considerations of using ballotini (i.e., being readily available, easy to characterize, does not deform, does not break) as well as its good fluidisation behaviour (Roche, 2012; Roche et al., 2004; Rowley et al., 2014; Smith et al., 2018) are of importance. Therefore, different experiments (i.e., such as fluidisation-based experiments) will benefit from different materials (i.e., good flowability results of ballotini). In the case of AoR experiments, ballotini shows approximately half the values of the pyroclastic material. Therefore, descriptions remain qualitative when exploring bedforms of flow deposits using

ballotini. A more quantitative bedform analysis will require materials with frictional behaviours similar to natural pyroclastic sediments.

Table 4.5. Dry pyroclastic material in comparison to analogue material for use in experiments. ‘X’ is where fluidisation behaviours were present. ‘-’ is where fluidisation behaviours were not present. ‘n/a’ symbolises experiments that did not take place.

Dry Experiments	Pyroclastic materials	Ballotini 1	Ballotini 2	Fine Sand	Cornstarch	Industrial pumice
HR	1.1-1.3	1.0	1.0	1.1	1.4	1.2
CI	6.6–24	3.3	0.0	8.6	27.1	18.3
SAoR	28-43	17.4	18.8	30	37	30
DAoR	39-61	32	32	39	59	41
Bubbling fluidisation	x	x	x	x	n/a	x
Channelling	x	-	-	-	n/a	-
Explosive channelling	-	-	-	-	n/a	-
Cracking	-	-	-	-	n/a	-

4.6.5.1.2 For use as a substrate for flume experiments

The strength or resistance of a material can be determined by its interparticulate forces (i.e., capillary, van der Waals or electrostatic) and the behaviour of the current (Andreotti et al., 2013; Pahtz et al 2020). Cohesive forces can cause fundamental material properties to change, resulting in variations in material strength (Pierrat & Caram, 1997; Kim & Sture, 2008; Andreotti et al., 2013; LaMarche et al., 2016; Chen et al., 2021). These forces, alongside the nonlocal effect of the current and force fluctuations, can determine a material’s ability to be eroded, deposited, or transported (Jop, 2015; Pahtz et al., 2020). In PDC modelling, investigating substrate and flow interaction is pivotal in our understanding of deposit architecture (Rowley et al., 2011; Lucchi et al., 2022; Brand et al., 2023). Here we explore the most replicable material for use in future experiments wishing to explore flows over erodible substrates (Table. 4.5).

When exploring the behaviour of material to be used in a substrate, the angle of repose can be a representation of the shear strength (Keaton, 2018; Breard et al., 2022; Dai et al., 2022). The shear strength is the ability for a material to withstand a shear stress, which directly correlates to the “resistance” of the material (Keaton, 2018). In dry granular material, SAoR tends to be governed by particle shape (Keaton, 2018; Beakawi

Al-Hashemi & Baghabra Al-Amoudi, 2018) and in our results we also see a strong influence from fines content (Fig. 4.3b). This is likely to be due to a range of packing at which particle jamming occurs. For example, with the increase in fine particles, jamming also increases. Furthermore, the temporal evolution of the strain rate, for instance, can have a strong impact on where jamming occurs. The materials that most closely match the range of the pyroclastic SAoR values are cornstarch, fine sand and industrial pumice (Table. 4.5). Ballotini 1 and 2 can be used but display lower AoR values. This is not a problem for substrate modelling but may mean that ballotini displays a lower static coefficient of friction and may be more likely to be moved under shearing conditions. Analogue material may be chosen based on the parameters to be investigated. For example, in substrate experiments, a finer material such as cornstarch or ballotini 1 may be adopted. In contrast, for experiments requiring a coarser or more angular material, fine sand, industrial pumice, or ballotini 2 would make a good analogue alternative.

4.6.5.2 Wet experiments

4.6.5.2.1 For simulating a flow

As moisture content increases, the cohesive behaviours and resulting shear strength of both pyroclastic and analogue material changes drastically, even with the addition of small weight percentages (> 0.50 wt.%). This heightened moisture can lead to a transition in flow characteristics, shifting from a state of free-flowing material (i.e., low HR, CI and AoR values) to that of a non-flowing material (Fig. 4.6). With increasing moisture added to the material, AoR, HR and CI values increase, representing poorer flowability. This is until ~ 80 % fines content where there is a decrease in AoR which indicates better flowability (Fig. 4.7). This is thought to be due to effects of interparticle lubrication or clumping of material. Cornstarch, fine sand and industrial pumice all sit well within the limits of AoR, HR and CI values of wet pyroclastic material used in this study (Table. 4.6). With increasing moisture, ballotini 1 and 2 display more similar results to the pyroclastic material and also sit within the wet pyroclastic material range (Fig. 4.7) (Table. 4.6).

Ballotini is one of the most commonly used analogue materials in experimental modelling due to its spherical properties and simple characterisation behaviours (Roche et al., 2004; Montserrat et al., 2012; Rowley et al., 2014; Smith et al., 2018, 2020; Table. 4.1). Ballotini glass beads are made of soda-lime glass and follow the Group A Geldart classification (Geldart, 1973) meaning that they are non-cohesive and display

homogeneous fluidisation behaviours (Smith et al., 2020). In dry conditions, our experiments also show this behaviour, however with the addition of moisture behaviours changed drastically. A key observation made from these experiments is the effect of wetting and quick drying of ballotini beads from very small moisture levels (> 0.50 wt.%). During the fluidisation experiments, it became evident that ballotini beads would “bind” together creating a strong lattice of the particles which had to be manually broken. This may be due to leaching of the coating on the ballotini or by salt-like precipitation occurring at the bonds between particles. Material in a nearly dry condition can experience greater strength due to the effect of suction (Ciantia et al., 2015) and interparticle friction factors can increase between 3.5 to 30 just by the wetting of material (Skinner, 1969). Liu et al. (2009) added small concentrations (0.3, 0.5, 0.6, 0.8 and 1.0 %) of a binder liquid (water) to ballotini and created compressed pellets of materials. It was noted that an increase in binder viscosity (from water to silicone oil) and a decrease in particle size increased the overall granule strength (Liu et al., 2009). However, this behaviour could also be due to lack of cleaning and contamination of the ballotini, as material from the supplier may be affected by contaminants on their surface. Ultimately, the origin of this ballotini behaviour is unknown. Nonetheless, the results from these experiments show that caution should be taken when a) using ballotini in the presence of moisture in quick-drying environments b) preparation and cleaning of ballotini before use to remove surface contaminants and c) if using ballotini within a moisture experiment, limit the wetting and drying of ballotini and complete experiments quickly to reduce this effect. Alternatively, this behaviour may also be utilized to take in-situ samples of material to look at internal structures.

For experiments in which moisture is being explored, fine sand and cornstarch are good substitutes and match the range of pyroclastic behaviour in wet conditions. Our recommendation is the use of fine sand because it shows similar fluidisation behaviours to the pyroclastic material. However, these materials may not adequately represent material with high fines content. Therefore, to better explore the role of fines content a combination of fine sand and cornstarch is recommended.

4.6.5.2.2 For use as a substrate for flume experiments

For substrate interaction experiments in wet environments, we again recommend fine sand and cornstarch. Ballotini 1 and 2 make strong analogues but should not be used in wet environments under quick drying (i.e., basal drying from gas flux) or left for a long period of time prior to use.

Table 4.6. Wet (0.5, 1, 2.5 wt.%) pyroclastic material in comparison to analogue material for use in experiments. ‘X’ is where fluidisation behaviours were present. ‘-’ is where fluidisation behaviours were not present. ‘n/a’ symbolises experiments that did not take place.

0.5, 1, 2.5 wt.% moisture experiments		Pyroclastic materials	Ballotini 1	Ballotini 2	Fine Sand	Cornstarch	Crushed pumice
HR	0.5	1.1 – 1.4	1.20	1.2	1.2	1.4	1.2
	1	1.0 – 1.5	1.5	1.1	1.2	1.4	1.8
	2.5	1.0 – 1.6	1.5	1.0	1.2	1.3	1.2
CI	0.5	9.1 - 29	16.7	14.29	14.6	28.4	18.7
	1	5.4 - 35	33.3	11.8	15.0	27.3	15.2
	2.5	11 - 36	34.2	3.23	15.1	25	17.2
SAoR (°)	0.5	23 – 38	54	50.7	33	34	28
	1	36 - 54	54.2	50.3	54	46	36
	2.5	32 – 48	55	53.4	45	37	30
DAoR (°)	0.5	45 – 68	66	50.5	59	59	46
	1	49 – 86	62	60	73	53	49
	2.5	50 - 90	56	62	78	55	53
Bubbling fluidisation	0.5	x	-	-	x	n/a	x
	1	x	-	-	x	n/a	x
	2.5	x	-	-	x	n/a	n/a
Diffusive Cracking	0.5	x	-	-	-	n/a	-
	1	x	-	-	-	n/a	-

	2.5	-	-	-	-	n/a	n/a
Channelling	0.5	x	-	-	-	n/a	-
	1	x	-	-	-	n/a	-
	2.5	x	-	-	-	n/a	n/a
Explosive Channelling	0.5	x	-	-	x	n/a	-
	1	x	-	-	-	n/a	x
	2.5	x	-	-	x	n/a	n/a
Pocketing	0.5	x	-	-	x	n/a	x
	1	x	-	-	x	n/a	x
	2.5	x	-	-	x	n/a	n/a

The materials used within these experiments cover a range of sizes and densities comparable to those of equivalent pyroclastic materials and exhibit similar flowability behaviours as demonstrated in the AoR and BTB results. In situations where pyroclastic material is limited or unsuitable for experimental modelling, it is essential to carefully select appropriate analogue materials. We recommend tailoring the choice of material to suit the specific experimental and scaling requirements, as there is no “one size fits all” material solution. By employing a series of static and dynamic experiments, we have investigated the optimal analogue materials for investigating PDC behaviour’s for both the deposit and current itself. Furthermore, we examine these behaviours under varying moisture conditions. Our findings indicate that particle size, shape, sorting, and fines content profoundly influence the static and dynamic behaviours of pyroclastic materials in both dry and wet conditions.

4.7 Conclusions

Modelling pyroclastic density currents (PDCs) is a challenging, yet essential element of hazard forecasting and assessment. The dynamics within these systems are difficult to understand and observe. PDCs exist as multiphase flow and are inferred to show behaviours of various rheology under different conditions. Furthermore, PDCs are unpredictable, and internal processes are often difficult to directly measure and can be obscured by a co-ignimbrite cloud. The use of analogue experiments are an important and attractive tool for investigating the internal dynamics of PDCs. Better understanding of the fundamental physics of PDCs will lead to deeper insights into the physical properties underlying these phenomena. In turn, this will lead to the better comprehensive integration of variables into numerical equations and computational models. Missing from our current understanding, is the comparison of a wide range of pyroclastic samples with well-known analogue materials in a range of environments (i.e., static, dynamic, wet and dry).

The use of analogue experiments are an important tool for investigating internal PDC dynamics. Previous analogue experiments have ensured the removal of moisture within a material to limit the impact of positive and negative pre-water and pore-air pressures. However, this does not reflect the reality of natural systems where moisture can be introduced into a PDC, such as where temperature and pressure allow the water phase to condense and form droplets. The addition of moisture can lead to fundamental changes in material properties resulting in significant impacts on geomechanical behaviours

(size, density, shear strength), fluidisation and flowability. For example, the rapid vaporisation of water into steam on PDC interaction with a wet substrate can lead to formation of a new gas source, increasing mobility and fluidisation.

Our findings explore the significant variations in behaviours of a suite of pyroclastic material under varying experimental conditions. The geomechanical properties of natural pyroclastic material are controlled by particle shape and size. Interestingly, the fines content (%) of a material has significant controls on angle of repose, fluidisation and flowability. Furthermore, the addition of moisture can greatly influence material behaviours in both static and dynamic environments and creates a package of material which is less likely to fluidise and flow. This work highlights the importance of validating the material choice used in modelling experiments, especially in wet conditions. Our findings not only enhance the fidelity of experimental models but also offer practical guidance and values for future research endeavours in this domain.

Supplementary Material for Chapter 4 can be found in Appendix B.

Supplementary Material 4A – Experimental methodology for BTd, SAoR and DAoR.

Supplementary Material 4B – Geomechanical data, error and uncertainty for BTd, SAoR and DAoR of all materials.

Supplementary Material 4C – Fluidisation videos of diffusive cracking.

Supplementary Material 4D – Fluidisation structures and profiles of Tung 1 – Tung 6

Supplementary Material 4E – PCA correlation plot, scree plot and Cos2 plot.

Chapter 5 : The influence of moisture on ash strength: implications for understanding volcanic stratigraphy.

5.1 Abstract

Ash layers within extensive pyroclastic density current (PDC) deposits can be important in understanding the evolution of explosive eruptions. If interpreted as ashfall deposits, they may be used to identify hiatus episodes and determine how many pyroclastic density currents were generated during an eruption. However, such layers, which often contain ash aggregates indicating the presence of moisture, may be variably deposited, preserved and eroded, and there has been little study of their characteristics. This paper investigates the geomechanical properties of ash layers through a comparison of field observations and experimental analysis. We present new field evidence of intriguing relationships between ash aggregate layers and overlying ignimbrite facies within the 273 ka Poris ignimbrite of Tenerife. We identify three types of interactions, each displaying distinct erosional and remobilisation behaviours associated with varying moisture conditions. To complement these field observations, we performed direct shear box, ring shear and drop tests under both low (1 wt.%) and high (> 15 wt.%) moisture conditions. We find that fine pyroclastic material increases yield strength with moisture compared to dry conditions. Furthermore, we see shear thickening behaviours in fine ash at high moisture content. These behaviours show how ash layers formed under low and high moisture conditions are more likely to be preserved than dry layers. This may lead to misunderstanding in flow unit interpretation and, therefore, assessments of eruption frequency. Furthermore, dry, loose ash material may promote flow bulking, increasing mobility, runout and flow velocities in PDCs.

5.2 Introduction

Pyroclastic density currents (PDCs) are a deadly volcanic hazard that can form during column lava dome collapse or lateral blast events (Fisher, 1979; Branney & Kokelaar, 2002) and pose a significant hazard to communities living around PDC-forming volcanoes (Auker et al., 2013; Lube et al., 2020). PDC activity can be short-lived (seconds to minutes) when associated with lava dome collapse, for example, or can be long-lived and sustained (hours to days) when associated with large-magnitude, caldera-forming

eruptions (Fisher, 1979; Branney & Kokelaar, 2002; Brown et al., 2003; Sulpizio et al., 2014; Lowe & Pittari., 2021).

The nature of PDC activity can be determined through visual observation (e.g., Cole et al., 1998) and field study of the resultant pyroclastic material, known as ignimbrite, deposited as these currents move across the landscape (e.g., Fisher, 1979). Analysis of ignimbrite stratigraphy has been vital in interpreting the evolution of historic PDC events (e.g., Sigurdsson, Carey & Espindola, 1984; Cas & Wright, 1987; Druitt et al., 1989; Wilson, 1993; Brown & Branney, 2004; Lucchi et al., 2018; Dowey & Williams, 2022), with stratigraphic data collection informing hazard planning strategies for future eruptions. Flow unit identification (i.e., how many PDCs formed within a single event) may form an essential part of this analysis (e.g., Silva Parejas et al., 2010; Brown & Branney, 2013; Douillet et al., 2013; Smith & Kokelaar, 2013; Cavazos-Álvarez et al., 2020; Dowey et al., 2024).

A flow unit is best defined as a stratigraphic package of ignimbrite that records the passage of an individual PDC (i.e., one flow unit = one PDC) (Sparks, 1976). In a model of progressive aggradation of ignimbrite material (Branney & Kokelaar, 2002), flow units are separated by evidence of hiatus, which may be represented by pumice or ash fallout layers, evidence of secondary reworking or soil horizons within an ignimbrite sequence (e.g., Sparks et al., 1973; Sparks & Walker, 1977; Wright & Walker, 1981; Sigurdsson & Carey, 1989; Branney & Kokelaar, 1992; Pittari et al., 2006; Brown & Branney, 2013; Cavazos-Álvarez & Carrasco-Núñez, 2020). Ash fall layers (Fig. 5.1) can become recorded in an ignimbrite succession during hiatuses in PDC activity either by deposition from the co-ignimbrite plume (i.e., the ash-laden cloud that lofts above a PDC, e.g., Brown & Branney, 2004) or from the eruption plume (Brown et al., 2003).

In significant, sustained eruptions, PDC activity can be unsteady through time, displaying phases of waxing and waning due to factors such as changing mass flux at source (Fig. 5.1) (Pittari et al., 2006; Báez et al., 2020; Charbonnier et al., 2023). Such unsteadiness can cause temporal changes in PDC mobility and run out, both longitudinally away from, and laterally around, a volcano (e.g., Williams et al., 2014) and may lead to variable preservation, erosion or remobilisation of key hiatus indicators such as ash fall layers (e.g., Dowey et al., 2024) (Fig. 5.2). Such factors can contribute to spatial complexity in the record of hiatus and, therefore, of flow units, leading to contradictory interpretations of eruption history at different locations (Dowey et al., 2024). Understanding the potential

for erosion or preservation of these distinct ash layers under various conditions is vital to understanding volcanic sequences, eruption evolution, and hazard identification.

5.2.1 Changes in variables: flow and deposit

Whether a PDC forms a deposit, erodes the substrate or bypasses an area depends on several factors. Eruption dynamics, such as mass flux and unsteadiness, can vary throughout the lifespan of the current (Bursik & Woods, 1996; Pittari et al., 2006; Rowley et al., 2023). Similarly, local environmental conditions play a crucial role in flow behaviours, including surface roughness and topography (Sparks et al., 1997; Brand et al., 2014). These factors influence the fundamental characteristics of the overriding current, such as thickness, particle concentration, pore pressure (Roche et al., 2013) and the resulting conditions at the flow boundary zone at the base of the PDC, which govern the depositional, erosional or bypassing regime (Brown & Branney, 2004; Branney & Kokelaar, 2002).

Under depositional or bypassing conditions, an ash layer is more likely to be preserved, whereas erosional conditions may lead to its removal (Brown & Branney, 2004). Erosion occurs where erosive forces exceed the resistive forces within the ash material, which include gravity, friction, tensile strength, compressive strength, cohesion and adhesion (Grabowski et al., 2011; Turowski et al., 2023). Several factors can influence these forces, such as particle size distribution (Alias et al., 2014), material composition, density, cement, local fractures, pore fraction, fines content (Jiang et al., 2015; Walding et al., 2024) and moisture content (Liu et al., 2022; Turowski et al., 2023; Walding et al., 2023, 2024). These properties collectively determine how individual particles react, interact and transfer forces throughout a granular pile (Turowski et al., 2023).

Moisture can be introduced into a PDC from various sources, including pre-eruptive groundwater conditions, surface water interaction and atmospheric humidity (Self & Sparks, 1978; Moyer & Swanson, 1987; Darteville et al., 2002; Cole et al., 2002; Hurwitz, 2003; Brown & Branney, 2013; Houghton et al., 2015; Pepin et al., 2017; Camuffo, 2019; Vecino et al., 2022; Shimizu et al., 2023). Furthermore, post-depositional factors like the extent and type of compaction (e.g., diagenesis) and additional water content (i.e., rainfall) will also contribute to the overall final strength of the ash material (Kim & Sture, 2008; Chen et al., 2021; Walding et al., 2023, 2024).

5.2.2 This work and aim

In this work, we investigate the controlling factors governing the strength of fine-grained pyroclastic materials to inform understanding of the fate of ash layer substrates during sustained PDC events. We analyse striking lithostratigraphic relationships observed in moist ash layers on Tenerife where moisture content is inferred by the presence of moisture-induced ash aggregations (Brown et al., 2010, 2012) and hypothesise that the preservation of ash layers depends on their strength, which can be controlled by moisture. The strength behaviours of various pyroclastic ash materials under different moisture conditions, ranging from 1 to 70 wt.%, have been investigated in laboratory tests to better understand these observations. This multidisciplinary work, which brings together volcanic stratigraphers and engineering geologists, aims to quantify the behaviour of volcanic ash in “dry” and “wet” shear environments. These relationships may have significant implications for the preservation or erosion of deposit architecture.

Flow unit formation in a sustained current: Ash hiatus layer

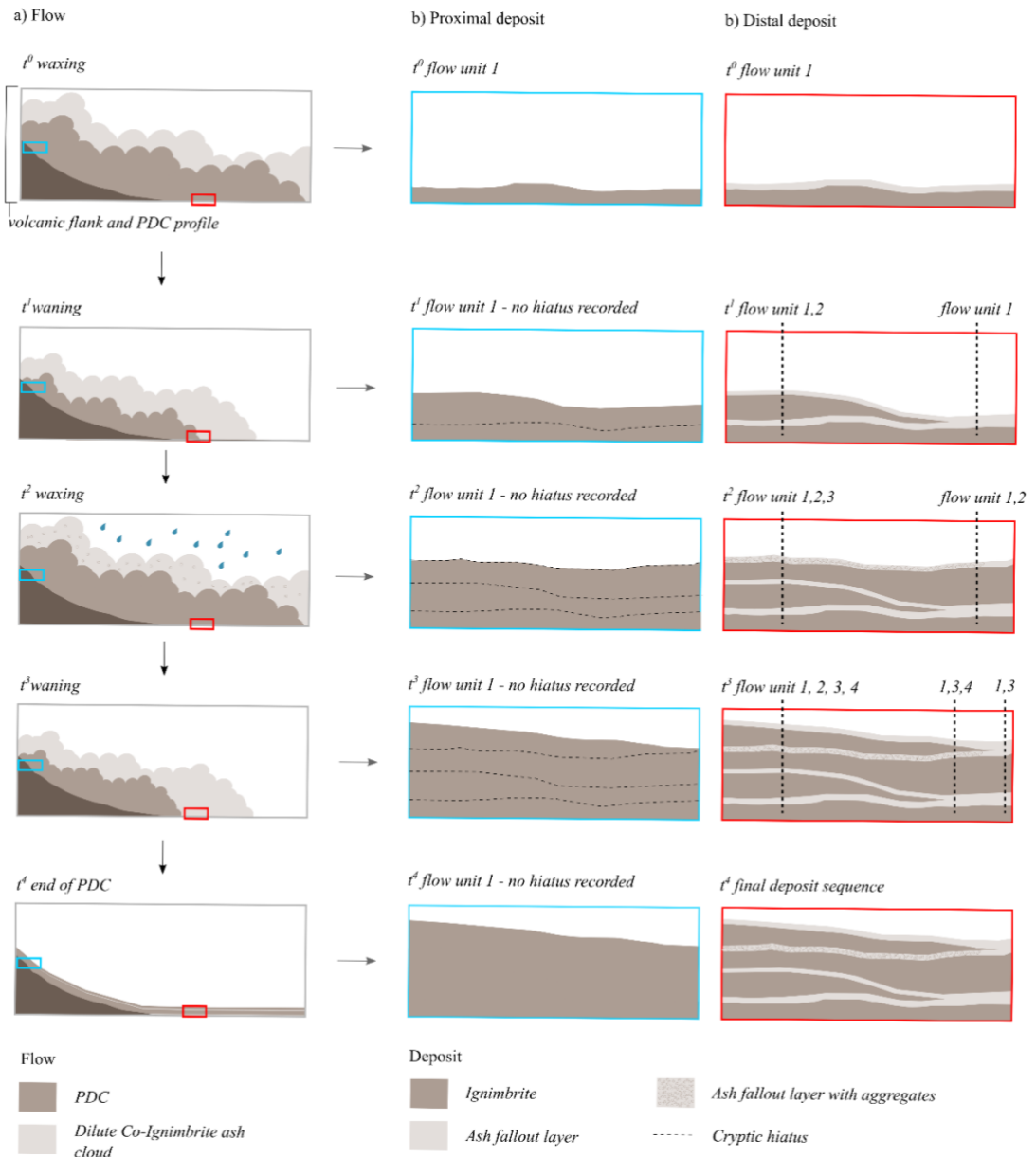


Figure 5.1. Conceptual model depicting how variable deposition of ash fallout layers in proximal and distal locations during unsteady PDC activity can complicate interpretations of flow units and eruption history. As a single PDC undergoes waxing and waning through time and, therefore, changes in run out through time (column a, t^0 - t^4), co-ignimbrite ash is deposited during episodes of local hiatus. Distally (column c), the final deposit may appear to have multiple ‘flow units’ (dashed line), but only one unsteady PDC was active throughout. Proximally (column b), no evidence of hiatus or ‘flow-units’ are evident (model based on field correlations presented in Dowey et al., 2024).

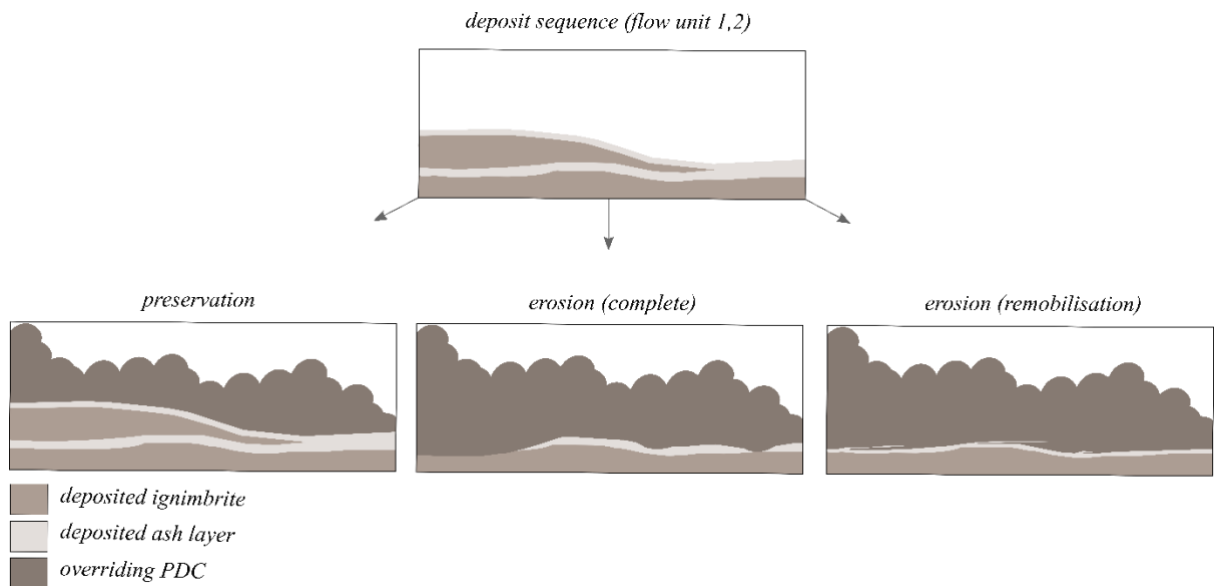


Figure 5.2. Illustration to show how ash layers recording hiatus in an ignimbrite succession may be (a) preserved, (b) eroded, or (c) remobilised by subsequent PDC activity, either due to waxing of a sustained unsteady current or by renewed activity following a complete cessation in PDC activity.

5.3 Terminology, Materials and Methods

5.3.1 Fieldwork Terminology

Volcanic ash (pyroclastic material with a particle diameter of < 2 mm, Cas & Wright, 1987) is a fine granular material, and the finest fractions can be considered a powder. Grainsize controls a variety of changes in the mechanics of how these materials behave, and for this work the more cohesive behaviour of fine powder materials is particularly relevant (Geldart, 1973).

Ash aggregates are clusters of volcanic ash particles formed via contact or interstitial forces. They can form due to electrostatic interaction and are found to be prevalent in moisture-influenced conditions (i.e., forming in the presence of rain or high-moisture environments) (Reimer, 1983; Gilbert & Lane, 1994; Schumacher & Schmincke, 1995; Brown et al., 2012; Telling et al., 2013; Diaz-Vecino et al., 2023). Ash aggregates have a higher terminal fall velocity than “dry” ash fallout, due to them being greater in size. They can be found in the ash fall deposits of co-ignimbrite clouds or from plume fallout that records hiatus between distinct episodes of PDC activity (Sparks et al., 1973; Sigurdsson & Carey, 1989; Brown & Branney, 2004; Pittari et al., 2006; Brown et al., 2010; Dowey et al., 2024).

In this study, we use the term “ash pellet” (AP1 in Brown et al., 2012 scheme) to refer to unstructured ash aggregates that are clast supported and “accretionary lapilli” (AP2 in Brown et al., 2012 scheme) to refer to structured, whole and fragmented ash aggregates that are matrix supported (Appendix C⁵, Supplementary Material 5A). On Tenerife, layers of unstructured ash pellets are interpreted to form within moist co-ignimbrite clouds, where ash begins to agglomerate as moisture condenses (Brown et al., 2010). Structured accretionary lapilli with multiple concentric layers have been interpreted to record vertical movement in a PDC system. For example, as accretionary lapilli are lofted and cycled in the thermally stratified area of a PDC, repeating layers of cohesive ash are accreted before lapilli return to relatively drier and hotter zones of the current (Brown et al., 2010). In the context of this work, ash pellets are moist on deposition, and accretionary lapilli are dry and brittle (as evidenced by fragmentation in some cases, Brown et al., 2010).

5.3.1.1 Fieldwork Stratigraphy and Lithofacies

Sedimentological analysis (logging, detailed imaging and sampling) of flow-unit ash layer marker beds and their contacts with overriding deposits was carried out in the Bandas del Sur region of Tenerife (March 2023). Lithostratigraphic features and physical relationships of selected ash layers of the 273 Ka Poris eruption, Tenerife, are reported. The outcrops are located in the Poris Quarry [GR: 2810696, 01627001] and Montana Magua [GR: 2811244, 01626702] (Fig. 5.3a.ii, 5.4a.iii, 5.5a.ii, 5.6a.ii). The stratigraphy in these locations has been worked on extensively by others (Edgar et al., 2002, 2007; Brown et al., 2003; Brown & Branney, 2004, 2013). The ash pellet layers investigated here are very-fine to fine-grained, buff-coloured ash and have been previously interpreted to record local hiatus in PDC activity (Brown & Branney, 2004, 2013). Where accretionary lapilli are present, this represents the lofting of pellets in the body of the PDC prior to deposition (Brown & Branney, 2004). Lithofacies analysis is based on the approach and descriptions of Branney and Kokelaar (2002), see Supplementary Material 5B.

⁵ All appendices for Chapter 5 are in Appendix C. Herein, this will be referred to as ‘Supplementary Material 5A, B, C’ etc...

5.3.2 Experimental Materials

Through direct shear, ring shear and drop test geomechanical experiments, the properties of a range of fine pyroclastic material at dry, low (1 wt.%) and high (> 15 wt.%) moisture content were explored.

5.3.2.1 Material Selection

The pyroclastic material studied in the field in Tenerife is lithified and could not be utilised as a loose granular material in laboratory work. Our experiments instead used a suite of fine pyroclastic-ash material from a range of volcanoes (Table. 5.1). Materials < 2 mm were used due to the size restrictions imposed by the shear equipment. The materials were chosen purposefully to span a range of particle sizes, sorting, particle ranges, fines content, composition and shape characteristics to explore the effect of these variables on moisture and shearing behaviours (Table. 5.2). The materials chosen have been previously described by Walding et al. (2023 and 2024). Cornstarch (5-340 µm) was also used as a comparative non-Newtonian synthetic material.

Table 5.1. Experimental material source location, chemical composition, formation mechanisms and the test completed in this work. DS – direct shear, RS – ring shear and DT – drop test. References detail material characteristics, collection and location.

Material	Composition	Formation	References	Test
Tung 1, 4, 5, 6 (Tungurahua, Ecuador)	Andesitic	2006 VEI 3 eruption. Sampled at different localities.	Hall et al. 2007; Kelfoun et al. 2009 ; Douillet et al. 2013; Eychenne et al. 2012	DS – Tung 1,4 and 5 DT – Tung 6
Atitlan 1 (Guatemala)	-	Volcán de San Pedro. Unstudied ignimbrite deposit GR: 14°40'55.24"N, 91°15'29.15"W	Rowley, P. <i>In comms</i> (2023)	DT
Atitlan 2 (Guatemala)	Andesitic	Los Chocoyos eruption (80.6 ka) of Atitlan Caldera. GR: 14°48'54.74"N, 91°12'27.37"W	Rowley, P. <i>In comms</i> (2023)	RS
Brown Tuff (Lipari, Italy)		La Fossa Caldera, 80-60 ka. GR: 38°28'46.5"N, 14°57'32.2"E		RS

Taupo 1 (New Zealand)	Rhyolitic	253 AD eruption. Sampled 17 km from vent.	Wilson (1985)	RS, DT
Taupo 2 (New Zealand)	Rhyolitic	232 AD eruption. Sampled 2-8 km from vent.	Wilson (1985)	DT
Colima (Mexico)	Andesitic	Volcán de Colima, México, 2015. GR: 19°43'92.22"N, - 103°61'47.05"W	Johnston, T. <i>In comms</i> (2023)	DS, DT
Cornstarch (synthetic material comparison)	Cornstarch	-	Walding et al., 2024	DT

Table 5.2 Material properties of both pyroclastic and cornstarch material. These include logarithmic particle size mean and particle size median, particle range, fines content (< 63 μm), and geometric mean (ϕ). The method of moments is employed for calculating Mean, Sorting, Sphericity, Symmetry, Skewness, and Kurtosis. The Sauter mean diameter is calculated following Breard et al. (2019). Material properties explored further in Walding et al., 2023; 2024. The table is ordered by particle size mean.

Material	Particle Size Mean (\bar{x}) \emptyset	Particle Size Median \emptyset	Particle Size Range (μm)	Fines Content (%)	Sorting Index (σ) \emptyset	Sorting (σ_G)	Sphericity	Symmetry	Skewness (Sk) \emptyset	Kurtosis (K) \emptyset	Sauter Mean (mm)	Geometric Mean (μm)
Cornstarch	4.8	4.8	5 - 340	96.2	0.6	Moderately Well Sorted	0.8	0.9	-0.3	4.3	0.02	35
Tung 1	3.8	3.7	2.5 -297.3	35.8	0.4	Well Sorted	0.8	0.9	1.9	17.0	0.06	73
Brown Tuff	3.6	3.4	1 - 1260	29.4	1.2	Poorly Sorted	0.8	0.9	0.5	3.9	0.05	85
Colima	3.5	3.6	10 - 1000	84.4	1.5	Poorly Sorted	0.7	0.9	-0.5	2.6	0.04	90
Atitlan 2	3.4	3.8	< 20 - 1780	40.6	1.5	Poorly Sorted	0.8	0.9	-0.9	3.2	0.02	92
Atitlan 1	2.8	3.1	2 - 2000	66.0	2.4	Very Poorly Sorted	0.8	0.9	0.1	2.0	0.02	97
Tung 4	2.7	2.7	20 - 650	0.2	0.3	Very well Sorted	0.8	0.9	0.1	8.5	0.01	154
Taupo 2	2.4	2.4	< 20 - 2000	52.2	1.0	Moderately Sorted	0.7	0.9	-0.5	4.1	0.04	196
Taupo 1	2.1	2.2	< 20 - 2000	38.9	1.2	Poorly Sorted	0.8	0.9	-0.5	3.3	0.04	235
Tung 5	1.5	1.6	10 - 1000	0.1	0.8	Moderately Sorted	0.8	0.9	- 0.1	2.5	0.02	347
Tung 6	0.8	0.8	10 - 1000	0.0	0.5	Well Sorted	0.8	0.9	0.6	8.3	0.03	557

5.3.2.2 Material Characteristics

Particle size analysis using a CAMSIZER X2 (University of Bristol) was completed to establish the shape and size characteristics of the dry material, with a maximum resolution of 0.8 μm per pixel. Particle size characteristics were measured before and after shear experiments to document physical changes, such as particle crushing.

Sphericity (SPHT) was calculated using:

$$SPHT = \frac{4\pi A_P}{P^2} \quad (5.1)$$

where P is the measured circumference of the particle, and A is the area covered by particle projection (see Table 5.2). An ideal sphere would record a value of 1 (Liu et al., 2015).

Symmetry, which describes the even distribution of the particle around the centre line, was calculated using:

$$\frac{1}{2} \left[1 + \min \left(\frac{r_1}{r_2} \right) \right] \quad (5.2)$$

where r_1 and r_2 are minimum and maximum particle radii (Buckland et al., 2021).

Symmetrical particles have a symmetry value of 1, and asymmetrical particles < 1 .

The particle size data were processed using GRADISTAT (Blott & Pye, 2001) to derive particle characteristics using the moments methods (Inman, 1952) to calculate logarithmic and geometric mean ($(\bar{x}) \Phi$), median ((Φ)), range (μm), sorting index ($(\sigma) \Phi$), sorting (σG), skewness ($(Sk) \Phi$), kurtosis ($(K) \Phi$), and the geometric mean (μm). Following the approach outlined in Breard et al. (2019), we calculated the D_{32} (mm) and fines content ($< 63 \mu\text{m}$, %) of the material. D_{32} values, also known as the surface-weighted mean diameter can characterise material fluidisation behaviour (Breard et al., 2019).

$$D_{32} (\text{mm}) = 2 - [\mu_{PSD}(\Phi) + \frac{\ln^2}{2} \sigma_{PSD}^2(\Phi)] \quad (5.3)$$

where μ_{PSD} and σ_{PSD} are the mean and standard deviation (Breard et al. 2019, in Φ units).

5.3.3 Experimental Methods

We describe material properties using peak and yield stress, bulk and shear modulus (Sheng et al., 2011; Donaldson et al., 2013; Keaton, 2018). Yield stress describes the point at which a material transitions from elastic to plastic behaviour. Elastic deformation describes reversible stretching or compression, where materials with higher elastic moduli are more resistant to deformation. Plastic deformation is irreversible, and the material will continue to deform until it fails at peak stress (i.e., the maximum stress before failure). Therefore, the yield stress measures a material's ability to withstand deformation without failing and, therefore, how less or more likely the material is to move. Similarly, bulk modulus describes the resistance of a material to changes in volume from hydrostatic stress (Donaldson et al., 2013), and shear modulus describes the resistance of a material to shear deformation (Keaton, 2018).

We investigated variation in yield strength, bulk and shear modulus using direct and ring shear apparatus at low (1 wt.%) and high moisture (> 15 wt.%) contents (Supplementary Material 5C). Variations were then explored using the bulk modulus of material at high moisture, with drop test experiments to explore further shear thickening (i.e., non-Newtonian) or shear thinning (i.e., Newtonian) behaviours (Supplementary Material 5C).

5.3.3.1 Direct Shear

Direct shear tests (Supplementary Material 5C, e.g., Niroumand, 2017) were performed to determine the shear strength of pyroclastic materials with the addition of moisture. These were completed using the direct shear apparatus (Faculty of Engineering, University of Bristol). Three experiments were undertaken on 200 g of various materials (Tung 1, Tung 4, Tung 5 and Colima) at 0, 0.25, 0.50, 1 and 5 wt.% moisture. Samples were dried at 80 °C for 24 hours before the experiments to ensure the removal of adsorbed moisture. Agglomerations were broken up by sieving before the addition of water. On addition of moisture, the samples were thoroughly mixed to ensure an even moisture distribution.

For each experiment, the material was loaded into the shear cell (60 × 60 mm) and consolidated for 20 minutes prior to shearing. The consolidation and shear tests were completed under a normal stress of 1, 14 and 27 kPa. These normal stress values were chosen to encompass a range of loads and to ensure behaviours were seen in a dry and wet (by adding moisture) state without generating pore pressure. The shear test was then completed at a 1 mm/min rate until peak shear was reached or the shear box length limited completion.

Experiments were also completed at 0.5 mm/min to ensure we were not seeing significant influence from pore pressure. The results from the 0.5 mm/min tests are reported in Supplementary Material 5H and show similar results to that of the 1 mm/min tests. Therefore, we can conclude that pore-pressure is not being generated by higher shear rates, so does not affect our results.

5.3.3.2 Ring Shear

A suite of fine pyroclastic material (< 1 mm) with varying moisture contents was tested in the Imperial College Ring Shear apparatus (Supplementary Material 5C, Bishop et al., 1971) at the University of Leeds, in order to inform interpretations of PDC behaviours made from stratigraphic relationships in Tenerife. Brown Tuff, Atitlan 2 and Taupo 1 (Table. 5.2) samples were used for ring shear testing to represent fine ash materials with high fines content. The samples were prepared as in the direct shear box tests.

The ring shear comprises two split confining rings with an outer diameter of 152.4 mm and an inner of 101.6 mm (Supplementary Material 5C). The depth of the sample area is 19 mm. Around 150-200 g of samples were used to run each experiment; variations in sample weight were due to changes in the density of the material and the required amount to fill the chamber. Each material was weighed before and after loading the shear chamber. The samples were sieved and sheared initially when dry (0 wt.% moisture). The initial set of experiments records the consolidation of the sample under a varying normal weight load. The second set of experiments records the shear behaviour of the samples. We then introduced water (0.5 and 1 wt.%) into the sample and repeated the experiment. Due to time constraints, higher moisture contents were not tested.

The ring shear tests were performed at constant normal stresses of 5, 10 and 20 kPa for each water addition. For each experiment, consolidation and shear measurements were recorded every 1s for the first hour, then every minute for an hour and finally every half-hour for the remainder of the experiment. Shearing was completed at a shear rate of 1.0 deg/min. The relative horizontal shear and vertical displacement were recorded, with the latter being measured through compaction or dilation of the material. It should be noted that the right proving ring sensor (Supplementary Material 5C) had fluctuating background noise that resulted in noisy results. This was reduced by using a moving average of the results.

The Mohr-Coulomb failure criterion describes the failure of materials where peak shear stress values are determined by cohesion and internal friction angle (Massoudi & Mehrabadi, 2001). Using the Mohr-Coulomb failure criterion on the normal stress and peak stress values, we determined friction angles (the ability of a material to withstand shear stress, therefore, higher resistance to erosion), cohesion and dilation (i.e., shear thickening) and compaction (i.e., shear thinning).

5.3.3.3 Drop Test

The drop test (Supplementary Material 5C, Crawford et al., 2013) was conducted on the Atitlan 1, Colima, Taupo 1, Taupo 2 and Tung 6 pyroclastic materials at varying states of high-water addition to explore the effects of shear thickening and thinning behaviours. Cornstarch and water (also named Oobleck), saturated at 75 wt.% moisture was used as a comparison sample to show explicit shear thickening behaviours.

A steel ball (20 mm diam, 7910 kg/m³) was dropped from a height of 270 mm onto loose material saturated at 0, 15, 25, 30, 40, 50, 60, 70 and 90 wt.% in a clear box (60 × 60 × 60 mm). Each experiment was completed three times. Video footage (700 fps), using a high-speed camera (Phantom VEO 440), recorded the steel ball hitting the sample. The footage was then analysed using ImageJ (Schindelin et al., 2012) to observe the nature of the interaction of the falling ball with the material deposit (i.e., the ball sinking through the deposit or the ball bouncing off the deposit). After each experiment, the ball penetration depth (i.e., how far the ball made it through the deposit) was measured to gain insight into the material's resistance under varying moisture.

5.4 Variations in ash layer strength on Tenerife

5.4.1 “Dry” ash layer contact

At the Montaña Magua location on Tenerife (Fig. 5.3a), two contacts between ash (T) and lapilli-tuff (LT) occur within the Cueva Honda member (< 0.90 m thick, distributed from La Caleta to Montaña Magua) of the Poris Formation (flow unit 3, member 7, Brown & Branney, 2004; Brown & Branney., 2013). A broad-scale context of this deposit can be found in Supplementary Material 5D. At this location, ash layers (T1 and T2) occur between lapilli-tuff

lithofacies (LT1, LT2, LT3). The contact between lapilli tuff (LT1) and tuff (T1) is typically clear and well-defined, whilst the upper contact between the tuff (T2) and lapilli tuff (LT3) is more graduated and diffuse, occasionally displaying grading. The ash layers (T1 and T2) are well sorted and normally graded into lapilli tuff. The second lapilli tuff layer (LT2, sandwiched between T1 and T2) contains pumice, lithics, and some eroded remnants of subrounded pumice clasts and shows no sign of ash aggregates (Fig. 5.3a).

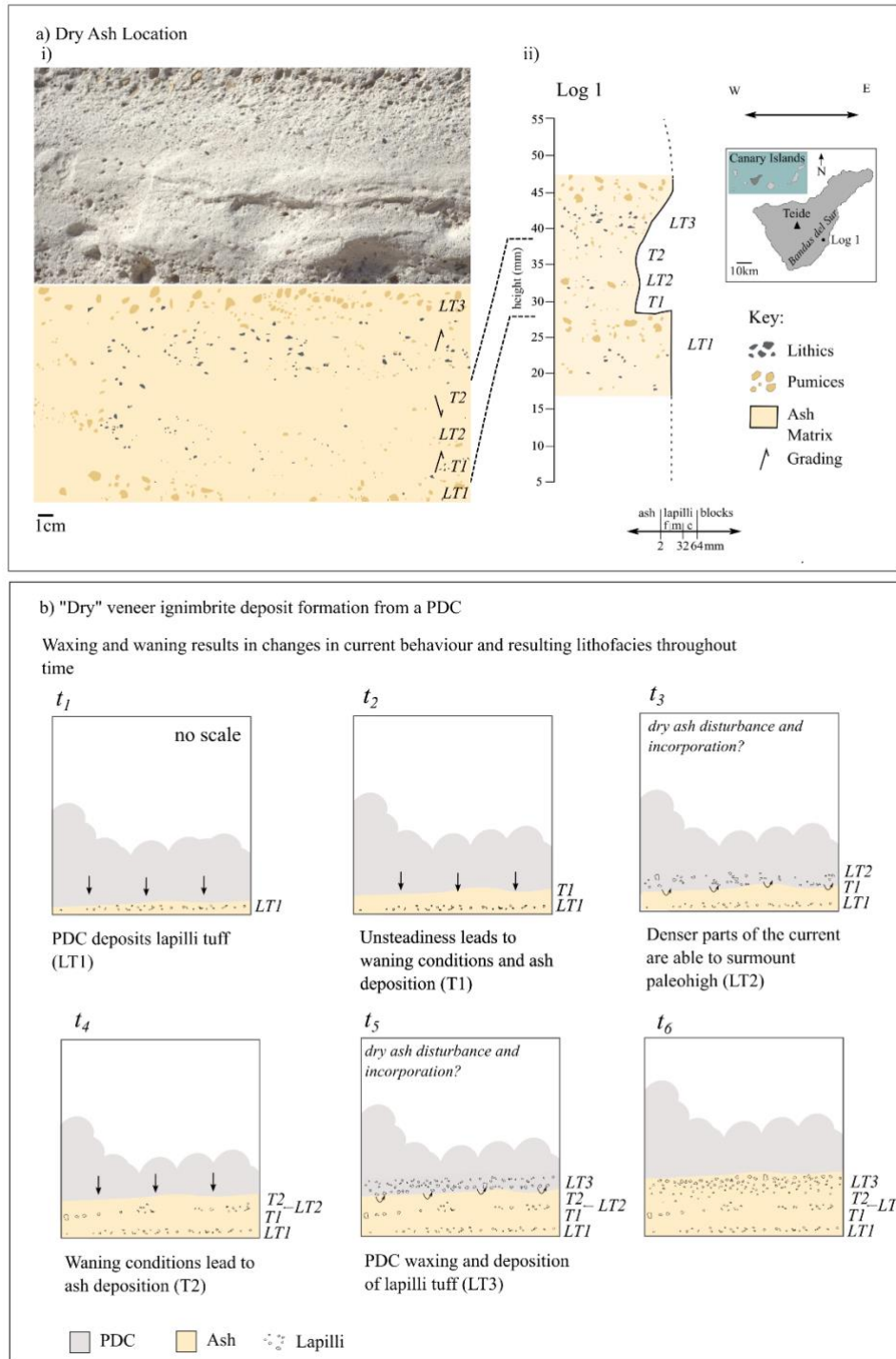


Figure 5.3. i) Ash-rich lapilli-tuff (LT1, LT2 and LT3) in contact with tuff (T1 & T2) within the Cueva Honda member of the Poris Formation at Montaña Magua. a. ii) Location map, log at GR: 2811282, 01626695, Supplementary Material 5D. See lithofacies terminology in Supplementary Material 5B. b. Interpretation of the formation of deposits shown in Log 1 through time (t) (see text for explanation).

5.4.1.1 Interpretation

This ash layer is interpreted to be an ignimbrite veneer, which is a thin ignimbrite layer deposited by dilute parts of a PDC that can surmount topographic palaeohighs (Branney & Kokelaar, 2002; Brown & Branney, 2004; flow unit 3, member 6, Brown & Branney, 2013). The lack of ash aggregates indicates formation in low-humidity or high-temperature environments with little external influence of moisture (such as precipitation or steam).

Transitions from lapilli tuff to ash, and then back to lapilli tuff, reflect unsteadiness in PDC dynamics (and therefore changes in flow boundary zone conditions) through time (*t1-t5*, Fig. 5.3b). Waxing or waning energy in the system may have led to the varying ability of denser parts of the current to surmount topography. The diffuse and graded nature of the contact, together with evidence that these ash layers were dry and likely loose on deposition, makes it seem likely that the ash layers were disturbed, remobilised and potentially incorporated into subsequent lapilli tuff layers as they were deposited (*t3 and t5*).

5.4.2 Sheared accretionary lapilli ash layer contact

Two subtle, cryptic contacts were identified at Montaña Magua, at different stratigraphic levels within the Magua Member (< 15 m thick, flow unit 3, Member 6 in Brown & Branney, 2004) of the Poris Formation (Fig. 5.4). At this location, the Magua Member consists of a fine-grained tuff containing scattered accretionary lapilli ranging from 3-30 mm in size (Brown & Branney, 2003, 2004; Brown et al., 2010). A broad-scale context of this deposit can be found in Supplementary Material 5E.

The first contact occurs between an accretionary lapilli-rich ash layer (mTacc in Fig. 5.4a. i) and a < 3 mm thick tuff layer above (T), which is then overlain by a diffusely stratified accretionary lapilli layer (dsTacc). In the lower aggregate-rich layer (mTacc), accretionary lapilli are mostly intact and unfragmented, however at the contact with the tuff, which is irregular with an undulating or stepped appearance (Fig. 5.4a. i), accretionary lapilli are sheared in-situ.

The overlying diffusely stratified accretionary lapilli facies (dsTacc) contains vertical transitions from increased to decreased accretionary lapilli concentrations. The second distinct contact, between this facies and massive lapilli tuff (mLT) above, is marked by a difference in lithic content (Fig. 5.4a. ii). In the diffusely stratified facies (dsTacc), accretionary lapilli are

mostly intact, although occasional angular accretionary lapilli fragments (< 20 mm) appear aligned with flow direction. In some areas, ash at the base of the massive lapilli facies (mLT) appears to be draped over whole accretionary lapilli, with no evidence of shear or erosion.

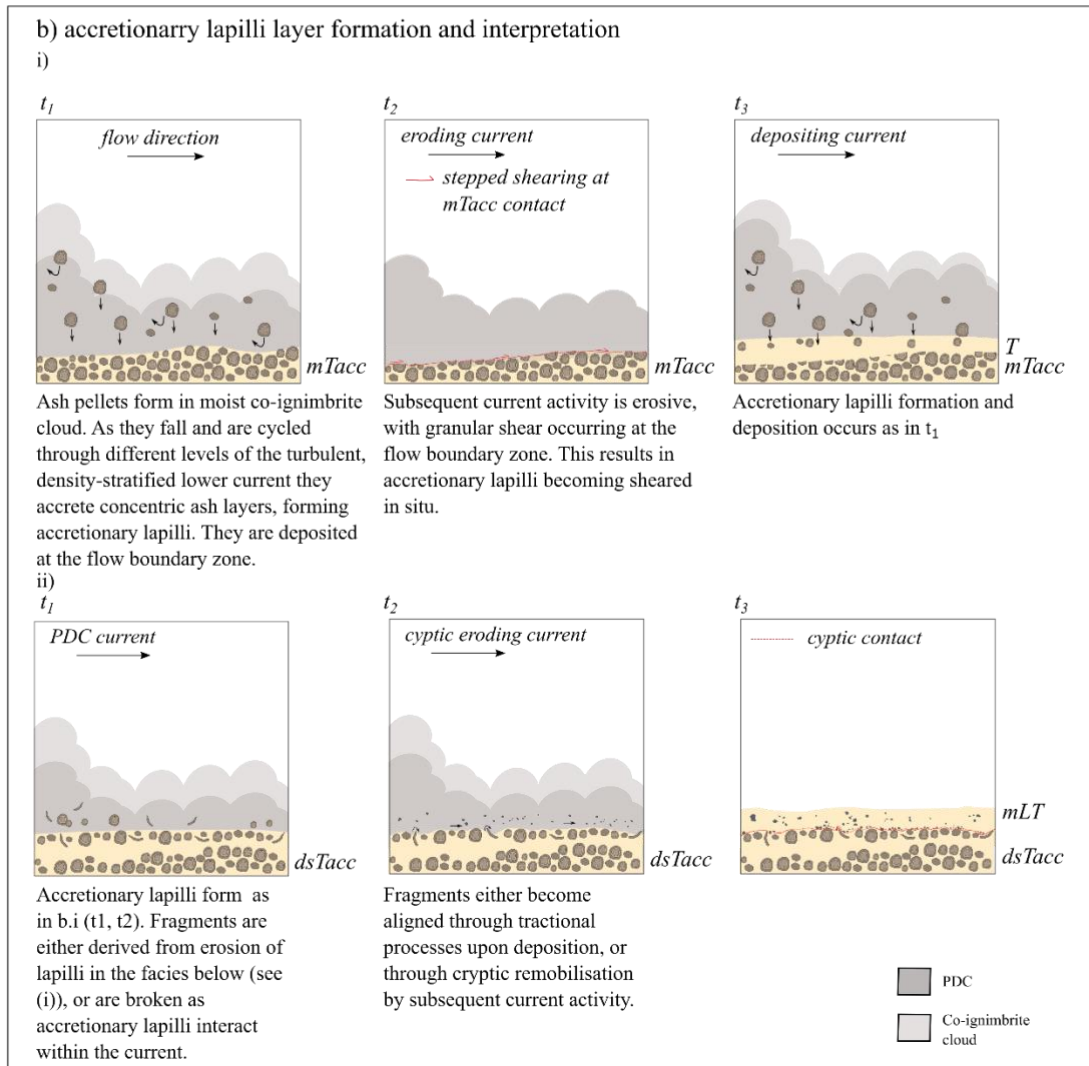
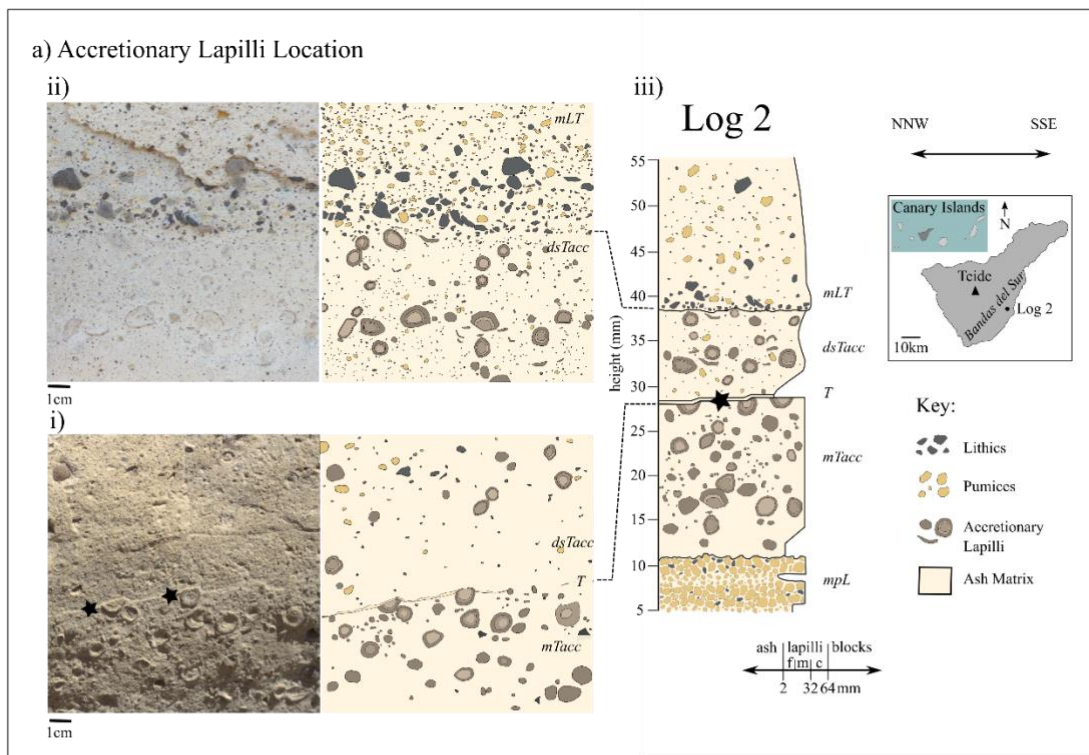


Figure 5.4. a. i) Accretionary lapilli layer (mTacc) in contact with overlying thin tuff (T) layer, observed in the Magua Member of the Poris Formation at Montaña Magua [GR: 2811244, 01626702]. Accretionary lapilli are sheared at the contact (star). a.ii) Diffuse stratified accretionary lapilli unit (dsTacc) in contact with overlying lapilli-tuff layer (mLT). Accretionary lapilli are fragmented at the contact. a. iii) Location map, log at GR: 2811244, 01626702, See Supplementary Material 5E. See lithofacies terminology in Supplementary Material 5B. 4b. Interpretation of formation of i) the lower contact (5.4. a. i) showing granular shear occurring at the flow boundary zone in log 2, and ii) the more cryptic upper contact shown in log 2 (see text for full explanation).

5.4.2.1 Interpretation

The lower contact between the accretionary lapilli (mTacc) and ash layer (T) is sharp and stepped and is interpreted to have formed through abrasion during low-impact granular shear in the lower regions of the current (Fig. 5b. i, Branney & Kokelaar, 2002; Brown et al., 2010). This observation is significant because layers rich in accretionary lapilli are thought to form during fluctuating current intensity (waxing and waning), perhaps making them unlikely to be fully cemented during the brief deposition period (Brown & Branney, 2010). However, in this example, the resistance of the accretionary lapilli to plucking from the substrate, the lack of disaggregation, and the planar erosion (shearing) through some of the lapilli suggest that both the accretionary lapilli (mTacc) and the ash (T) layer in which they were deposited had considerable strength. This strength during deposition has previously been attributed to the precipitation of salt or other minerals, which may have caused cementation of the ash (zeolite, Brown & Branney, 2004; Mueller et al., 2017), or from “baking” of the lapilli when moving through high-temperature areas of the PDC during lofting (Brown & Branney, 2004). A lack of fragmentation within the accretionary lapilli layer (mTacc) beneath the contact zone suggests that when the facies were deposited, the current was sufficiently dilute as to not induce breakage (Mueller et al., 2017).

The upper contact between the diffuse stratified accretionary lapilli (dsTacc) and lapilli tuff layer (mLT) contains fragmented accretionary lapilli with some directional fabric to them. This indicates that the current conditions were concentrated and sufficiently energetic to enable interactions and breakage (Mueller et al., 2017). This may be due to tractional processes during the deposition of the fragments, or through cryptic remobilisation by subsequent current activity. In addition to these fragmented lapilli, intact, non-sheared accretionary lapilli are also observed, protruding from the ash layer without signs of erosion from the overriding current (Fig. 5.4.ii).

5.4.3 “Wet” ash pellet layer contact

At the Poris Quarry, distinct layers of pellets are present that are associated with the Jurado Member of the Poris Formation (Brown & Branney, 2004); and a sequence containing ash pellet-rich tuff (pelT) is observed (Fig. 5.5a). A massive lapilli tuff facies (mLT1), characterized by a poorly-sorted lithic and pumice lapilli within an ash matrix, occurs in contact with a pellet-rich ash layer (pelT1). Another lapilli tuff layer (mLT2) occurs above this, in sharp contact with the pellet layer below with little evidence of erosion and is overlain by a second ash pellet layer (pelT2). All of these units are discontinuously preserved due to erosive contact with an overlying lithic-rich facies (lBr). This lithic breccia facies is observed cutting down into the sequence, with an undulous, scouring contact at its base (indicated by dashed red line in Fig. 5.5a. i), and in some places both pellet layers are completely absent. In one location (Feature A, Fig. 5.5a. i), a clump of the first pellet layer is seen to be detached and rotated from its original stratigraphic position within the lithic breccia facies. A broad-scale context of this deposit can be found in Supplementary Material 5F.

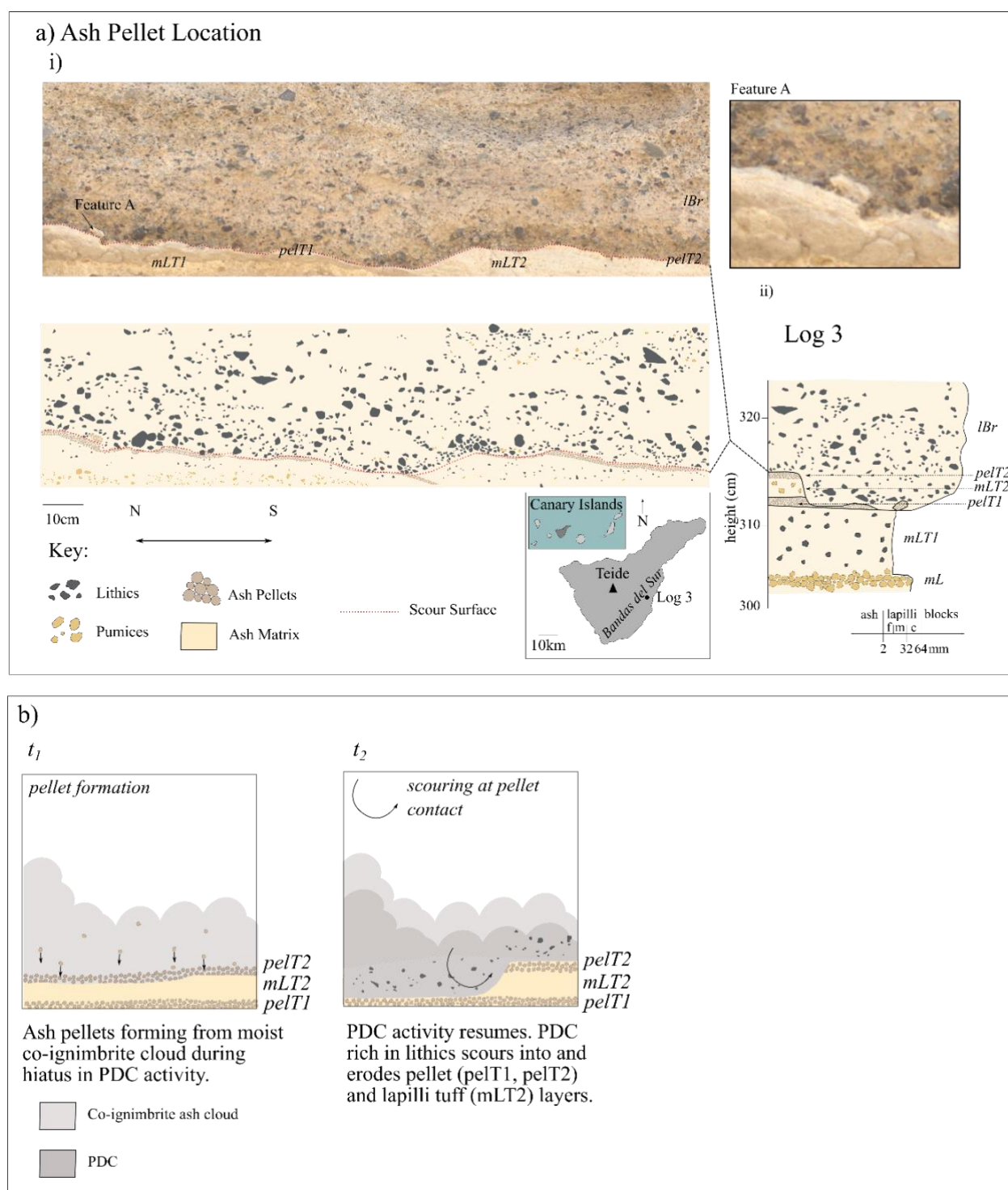


Figure 5.5. Ash pellet (pelT1 & 2) layers documenting an episode of PDC hiatus in this area. The ash pellet layers (pelT1 and 2) of the Jurado Member of the Poris ignimbrite (Brown & Branney, 2004) are in erosive scouring contact with the lithic breccia (lBr) facies above (red dashed line). i) Ash pellet contact (pelT1) is overlain by lapilli tuff (mLT2). Feature A indicates remobilisation. The second ash pellet layer (pelT2) is overlain (in erosive contact) by the lithic breccia unit (lBr). ii) Location map, log at GR: 2810693, 01627006, See Supplementary Material 5F. See lithofacies terminology in Supplementary Material 5B. Flow direction is north to south b) Interpretation panels showing (t_1) the formation of the ash pellet layers and (t_2) erosion of ash pellets and lapilli tuff by subsequent lithic-rich PDC activity (see interpretation text for full explanation).

5.4.3.1 Interpretation

The ash pellet layers (pelT1 and pelT2) at Poris Quarry represent direct fallout from a moist co-ignimbrite plume (Fig. 5.5b) (Brown & Branney, 2004, 2013; Brown et al., 2010), marking a hiatus in PDC activity. Unlike accretionary lapilli, ash pellets do not loft within the turbulent PDC, so their deposition signifies a temporary break in PDC activity in this area. Furthermore, the pellets identified in this area are considered moist on deposition due to the lack of internal laminations and evidence of amalgamation with surrounding pellets (Brown & Branney, 2004).

The lapilli tuff layer (mLT1) indicates PDC activity in the area followed by a hiatus ash pellet layer (pelT1). The second lapilli tuff layer (mLT2) indicates resuming PDC activity but is not seen to erode the underlying ash pellet layer (pelT1) (Fig. 5.5a. i). This facies are overlain by the second ash pellet layer (pelT2), marking further hiatus. Activity then resumes and a lithic-rich, erosive current scours into, remobilises (Feature A), and sometimes completely removes the underlying layers (Fig. 5.5, pelT1, mLT2 and pelT1). It is possible that, prior to the lithic-rich activity recorded here, other facies were deposited and completely removed from the record due to this erosion. However, lithic-rich facies have been linked to waxing current activity (as a result of events such as incremental caldera collapse) elsewhere in the Poris Formation (Brown et al., 2003; Smith & Kokelaar, 2013), and it seems sensible to infer that PDC activity resumed at this location following a period of hiatus due to current waxing, marked by increased lithics.

The nature of the relationship between the lithic breccia facies and the ash layers below is a strong indication that these lithics were responsible for the erosion (as opposed to the erosional surface marking an episode of scour and bypass onto which lithics from subsequent activity were deposited). Feature A (Fig. 5.5a) is particularly important. It shows the remobilisation of a portion of the pellet layer as a "rip-up clast," indicating a dynamic, shearing depositional environment at the interface between the lithic-rich current and the ash pellet (pelT1) layer. The ash pellet (pelT1) layer must have had an inherent strength to remain intact as a coherent package and to withstand shearing.

5.4.4 Ash layer remobilisation

A buff-coloured and fine-grained ash layer (T*) occurs in the Poris Quarry [GR: 2810696, 01627001]. It is observed between a lapilli tuff facies below (mLT) and a lithic breccia facies above (lBr) (the lithic-rich Tamadaya Member of Brown & Branney, 2004).

The ash layer (T*) is high in the sequence (~5 m above the ground), so the presence of ash aggregates could not be observed. However, a “*” notation is used here to indicate the high likelihood that this facies contains ash pellets or accretionary lapilli, due to its position at a similar stratigraphic level as other pellet layers in the sequence, and from descriptions in Brown and Branney (2004). The ash layer (~0.1 m thick and traced for ~2.5 m) is distinctive because it exhibits a zone of unique "peeling" and "lifting" in a hockey-stick shape. A broad-scale context of this deposit can be found in Supplementary Material 5G.

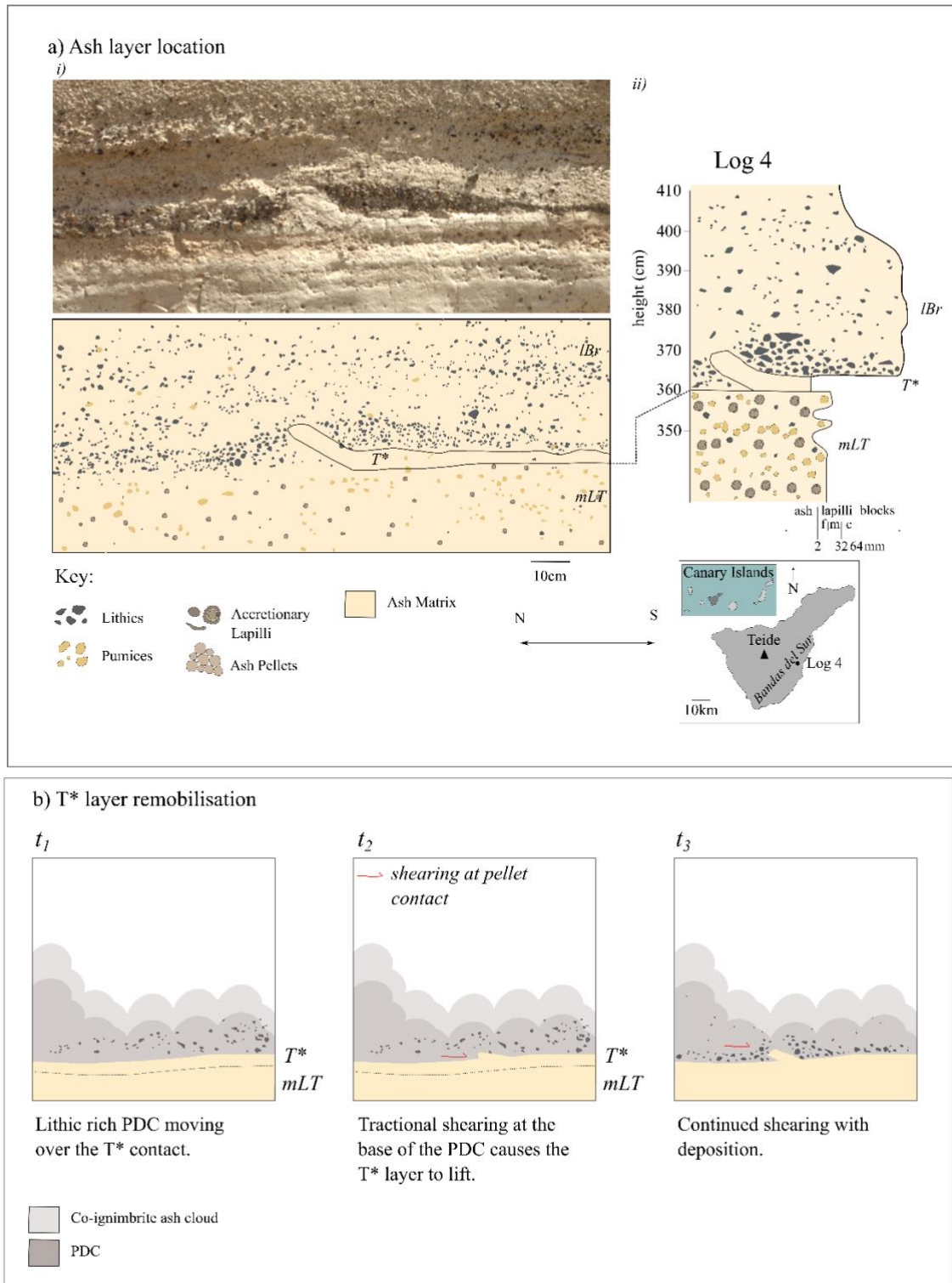


Figure 5.6. i) Ash layer (T*) in contact with overlying lithic-rich facies (lBr) in the Jurado and Tamadaya Member of the Poris Ignimbrite (Brown & Branney, 2004) at the Poris Quarry location. Note the ‘peeling up’ and lifting of the coherent zone of ash **ii)** Location map, log at GR: 2810696, 01627001, See Supplementary Material 5G. See lithofacies terminology in Supplementary Material 5B. Flow direction is north to south **b)** Interpretation panels showing the formation of this striking feature at the ash layer contact (see text for full explanation).

5.4.4.1 Interpretation

The ash layer (T*) is interpreted to record fallout from a moist co-ignimbrite plume during an episode of hiatus in main current activity (Fig. 5.6b. i; Brown & Branney, 2004), similar to the ash pellet layer described in section 5.4.3 (Fig. 5.5). The ‘hockey-stick’ structure (Fig. 5.6a) is interpreted to record remobilisation of coherent sections of the ash pellet layer due to shearing at the base of a subsequent PDC.

Field observations by Brown and Branney (2004) describe the pellet layers as traceable units, though they are often eroded by subsequent PDCs, leading to inconsistent preservation; this locality provides direct evidence of erosional processes in action. The high lithic content of the breccia (lBr) indicates waxing conditions and the influx of lithics at the source, such as that associated with incremental caldera collapse (Brown et al., 2003; Brown & Branney, 2004; Smith & Kokelaar, 2013). The interaction of this more concentrated, dense current with the underlying ash layer likely represents a significant change in shear and load behaviours at the flow boundary zone. Despite uncertainty in the nature of the aggregate content, this feature indicates the coherence of this ash layer.

5.4.5 Questions raised by the fieldwork

The field analysis presented here documents ash layers in various contact relationships. One layer, interpreted as ‘dry’ due to a lack of ash aggregates, shows no evidence of resistance to erosion by subsequent activity. Other ash layers, interpreted to have formed under either high or low moisture conditions by their ash aggregate content, are associated with intriguing shear relationships indicating resistance to erosion.

The preservation, or not, of these layers appears to be linked to their inherent strength, which we hypothesise is influenced by moisture content. This raises the question of how moisture influences the strength and, therefore, behaviour and preservation of an ash substrate during subsequent PDC activity. Improved understanding of this issue has implications for our interpretation of volcanic stratigraphy and hiatus layers, particularly for inferences of the number of PDCs formed during an eruption. In the following section, we investigate how moisture affects ash layer strength and vulnerability to erosion to gain a more comprehensive understanding of the dynamics and preservation of ash layers seen in PDC deposits.

5.5 Experimental results

Shear tests were completed to determine how the strength of material changes in dry (0 wt.%) and moist (> 0 wt.%) conditions. We hypothesise that the presence of moisture-induced ash aggregates may increase the yield strength of the material, thereby affecting its ability to be eroded or remobilised.

5.5.1 Direct shear box tests

Direct shear experiments were performed on four samples from 0 to 5 wt.% moisture. The peak stress was not reached during the duration of the experiments. Therefore, we completed the remaining experiments using the ring shear apparatus, employing finer sized material to better reflect the fine ash as seen in Tenerife. The results of the direct shear box are in Supplementary Material 5I.

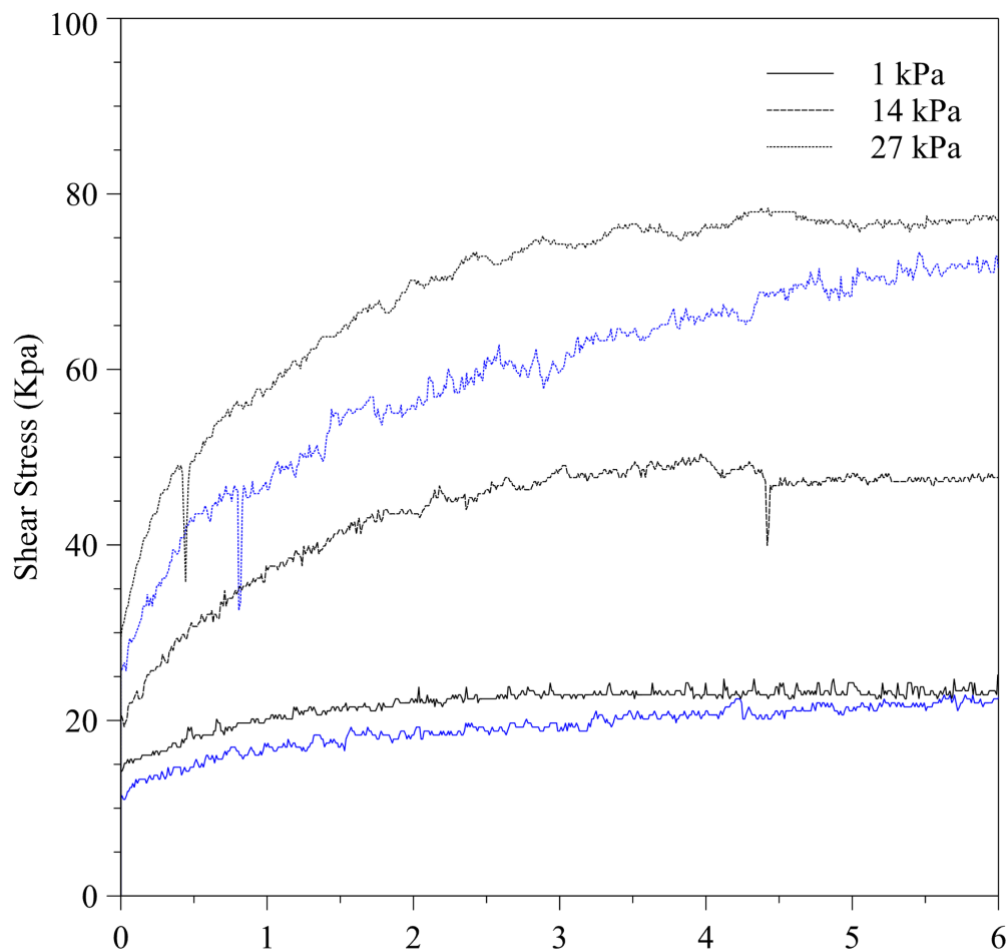


Figure 5.7. Direct shear box test of Tung 4 at 0 wt.% (black) and 1 wt.% (blue) moisture contents. Note that the yield stress was not reached. See Supplementary Material 5E.

5.5.2 Ring shear tests

The ring shear tests allow us to see the full extent of the shear profile, which was unable to be observed in the direct shear box. The ring shear tests were performed on three samples with 0 and 1 wt.% moisture content.

At 0 wt.% moisture (Fig. 5.8), Brown Tuff (mean size 3.55 ϕ , 29.35 % fines) and Taupo 1 (mean size 2.08 ϕ , 38.90 % fines) showed increasing peak shear stress with increasing normal stress (Table. 5.2). The peak shear stress was reached in a 5 – 20 mm shear distance, although it ran for much longer distances. Atitlan 2 (mean size 3.44 ϕ , 40.57 % fines) showed an unexplained decreasing peak stress with increasing normal stress (Table. 5.2, Fig. 5.8a).

At 1 wt.% moisture, Taupo 1 and Brown Tuff (Fig. 5.8b, c) again behave as expected, with peak stress increasing with normal stress. Similarly to the 0 wt.% moisture experiments, Atitlan 2 showed an unexplained decreasing peak stress with normal stress (Fig. 5.8a). The peak shear stress of all 1 wt.% moisture samples was reached in a shear distance of 5 – 10 mm.

Zones of elastic and plastic deformation separated by a region of yield have been identified (labelled B; Fig. 5.8). Our results show that at 0 wt.% moisture, the region of yielding is consistently reached in the first 16 mm of shearing across all normal stresses. The average linear displacement required to reach the yield increases with load and decreases with moisture addition.

For the Taupo 1 sample, the application of the Mohr-Coulomb failure shows an internal friction angle of 31° and cohesion value of 0.6 kPa for the dry (0 wt.% moisture) and an internal friction angle of 48° and cohesion value of 1.1 kPa for the 1 wt.% moisture conditions. Brown Tuff results show internal friction angles of 29° and 22° and a cohesion value of 0.56 and 0.42 kPa for 0 and 1 wt.% moisture, respectively. The decrease in values seen for the Brown Tuff may be due to pore-pressure generation. The application of the Mohr-Coulomb failure criterion to Atitlan 2 could not be confidently completed, as increasing normal stresses created negative internal friction and cohesion values. This indicates that another force may be present during the shearing of this material, such as pore-pressure build-up or particle crushing.

Throughout shearing, the results showed a decrease in vertical displacement (compaction) across most samples and moistures. Atitlan 2 is the only sample that shows a dilation (of 0.015 mm), which was recorded at the highest normal stress (20 kPa) at 0 wt.% moisture. However, with increasing shear distance, some granular material was lost through the gap between the two shearing rings (Supplementary Material 5C), and therefore, the equivalency of shear thinning and compaction was seen.

The ring shear results suggest relationships between the behaviour of the samples under varying moisture levels and normal stresses, highlighting the complexity of their mechanical response. However, Atitlan 2 does not show these relationships.

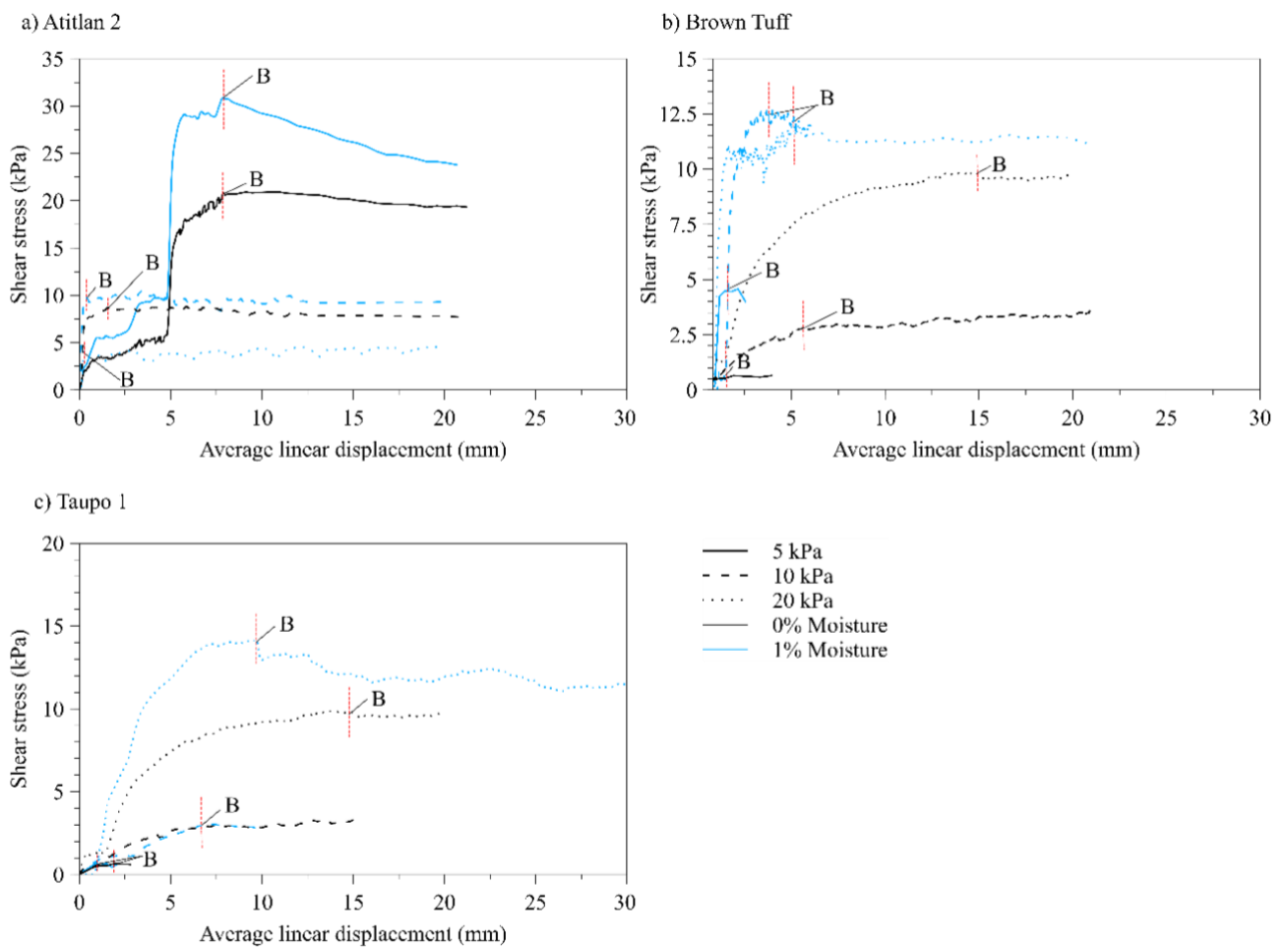


Figure 5.8. a) Atitlan 2, b) Brown Tuff and c) Taupo 1 shearing profiles of material at varying moisture contents (0 and 1 wt.%). B shows peak stress, and a dashed red line highlights the yield stress and separates areas of elastic response (left-hand side of the graph) and plastic hardening (right-hand side of the graph).

5.5.3 Particle size and shape analysis

Particle crushing over time may have resulted in fundamental changes in physical particle properties, leading to changes in the shear strength of the sample. To further investigate this effect, particle size and shape (sphericity and symmetry; Table. 5.4) analysis were completed before and after the ring shear experiments (Fig. 5.8).

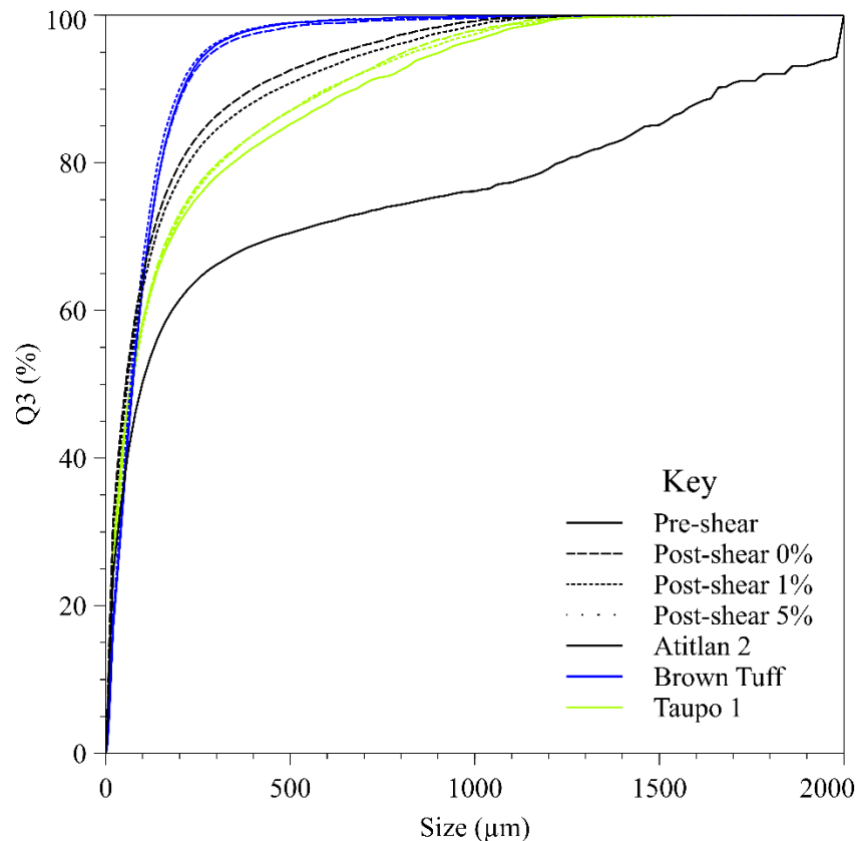


Figure 5.9. Particle size analysis of material before and after the ring shear experiments.

Interestingly, Atitlan 2 shows the most significant change in PSD following ring shear, becoming finer-grained after the experiments (Fig. 5.9). On analysis of the shape data, the mean sphericity and symmetry values after 0 and 1 wt.% shearing show a 1 % reduction (i.e., more angular and asymmetrical) compared to the un-sheared sample. These results indicate that particle crushing occurred in the Atitlan 2 sample during the experiments. This may have affected the geomechanical properties of the material and may be the cause of the reduced shear strength results for Atitlan 2. This is interesting and could be due to the composition of the material. Previous work by Walding et al. (2024) noted that the Atitlan sample in fluidisation experiments showed no significant change in gas escape morphologies with the addition of moisture. This suggests that perhaps the Atitlan material has H₂O scavenging minerals present

or has been hydrothermally altered, ultimately leading to the weakening of the particles, resulting in increased crushing of material. This observation would benefit from future work into the nature of hydrothermally altered ash material and moisture.

5.5.4 Drop Tests

Drop tests were carried out to determine whether the rheological properties of ash change at high moisture contents due to the effect known as “shear-thickening” (as seen in cornstarch material). We hypothesise that where ash pellet layers are preserved beneath lithic breccia lithofacies, the impact and shear from the large lithic blocks may induce shear thickening. The increased viscosity may increase the material's resistance and, therefore, develop a “protection” from the erosion of the dense granular current.

The drop test on cornstarch (96 % fine content) at 80 wt.% moisture demonstrated non-Newtonian and shear-thickening behaviour. The steel ball dropped at a speed of 0.16 cm/s, impacting the surface of the mixture and bouncing to a height of 0.55 cm (Supplementary Material 5J). The results for pyroclastic materials show that with sufficiently high wt.% moisture, Atitlan 1 (~ 40 wt.%, 66.03 % fine content), Colima (~ 25 wt.%, 84.39 % fine content), Taupo 1 (~ 50 wt.%, 38.9 % fine content), and Taupo 2 (~ 70 wt.%, 52.23 % fine content) all show evidence of shear thickening (i.e., a reducing ball penetration depth with increasing moisture and in some cases show the ball bouncing off the surface; Fig. 5.10, Supplementary Material 5F). At 50 wt.%, the ball bounced and reached a height of 0.6 cm for the Taupo 1 sample and ~0.6 cm for the 70 wt.% Taupo 2 sample (Supplementary Material 5J).

When moisture levels were increased above these percentages for each sample, the ball completely penetrated the saturated deposit with little resistance (Fig. 5.10d)

Shear thickening behaviours were associated only with some finer materials at a limited moisture range. Tung 6 (particle size mean 0.833 ϕ , 0.04 % fine content) did not show shear thickening in any experiment; at all moistures tested (30-40 wt.%), the ball moved straight through the material (Supplementary Material 5J).

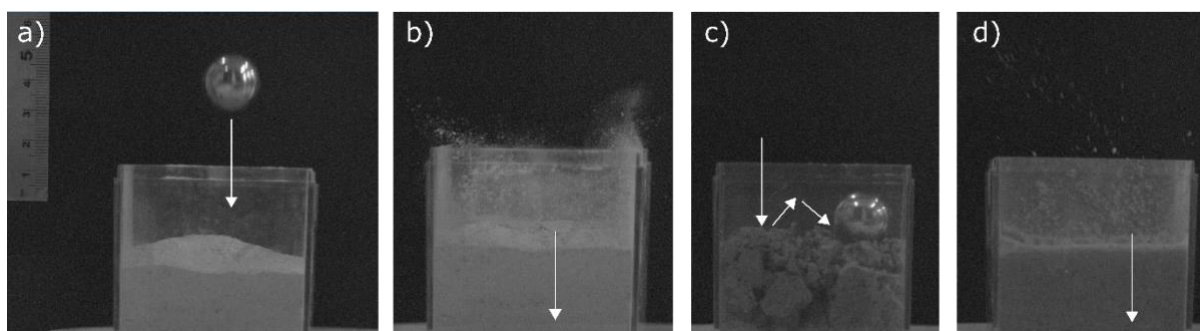


Figure 5.10. Drop test completed on Taupo 1 sample at b) 0 wt.% moisture, c) 50 wt.% moisture and d) 60 wt.%. Arrows show the movement of the ball from a) falling, b) and d) moving through the material and c) showing the bouncing movement of the ball on impact with the deposit. See Supplementary Material 5J.

These results demonstrate the ability of pyroclastic material to exhibit changes in strength at varying moisture ranges, dependent upon particle characteristics. The ball moves directly through all samples' at dry or low moisture contents under loose conditions (e.g., Fig. 5.10b). At high moisture levels (Atitlan 1, > 50 wt.%; Colima, > 30 wt.%; Taupo 1, > 60 wt.%; Taupo 2, > 80 wt.%), the material becomes a particle suspension, where the granular material is dominated by particle-fluid interactions (Sosio & Crosta, 2009) and the ball moves straight through the deposit (Fig. 5.10d). Some pyroclastic materials, as seen in Taupo 1 and 2, can show shear-thickening behaviour (Fig. 5.10c). This is not the case for Tung 6, probably due to its lack of fines content. When impacted or sheared, a shear-thickening material stiffens, which can result in resistance to deformation or penetration (as indicated in our results).

5.6 Discussion

5.6.1 Dry Deposit

The dry deposit environment is a baseline comparison since it represents a deposit not influenced by moisture (i.e., lacking accretionary lapilli or ash pellets). A dry ash substrate can form from ash fallout originating from an eruption plume, the fallout of a dry co-ignimbrite cloud or the deposition of a dilute PDC (e.g. Fig. 5.3a, 5.11). In such cases, the shear strength of the deposit are low. Variations in shear strength will be primarily influenced by particle packing, particle density and fine content (Roberts et al., 1998; Kimiaghali et al., 2016). Shear strength, and cohesion, will be affected by fines content and grain size, resulting in the formation of van der Waals or electrostatic forces between particles.

In the field, ash layers that were interpreted to be dry did not show sharp, upper contacts with overriding PDC deposits, nor did they display peeling features or any other features indicative of shear strength. The loose nature of recently deposited ash layers makes them vulnerable to

erosion by subsequent PDC activity. As a result, even when thin ash layers are deposited that could record a hiatus and delineate a flow unit (i.e., co-ignimbrite or plume fallout), their low preservation potential makes them unlikely to be recorded in volcanic stratigraphy – resulting in cryptic or missed layers (Fig. 5.11). Additionally, the erosion of the dry substrate may lead to entrainment and bulking of the overriding current, potentially increasing run-out distances and increasing the hazard risk (Bernard et al., 2014).

5.6.2 Moisture-affected deposits

The influence of moisture is inferred by the presence of accretionary lapilli and ash pellets. Ash pellets can form from a moist co-ignimbrite cloud or when raindrops interact with ash particles (Fig. 5.11, Brown et al., 2012; Diaz-Vecino et al., 2023). Consequently, resulting deposits may exhibit a range of moisture contents, from low to potentially saturated levels, either due to the presence of a high concentration of ash pellets or from direct rainfall on the aggrading deposits. Accretionary lapilli are formed by the lofting and cycling of ash pellets between hotter, lower areas and moister, cooler upper areas of a PDC, which leads to the accretion of thin concentric ash layers (Reimer, 1983; Schumacher & Schmincke, 1995; Brown et al., 2012; Diaz-Vecino et al., 2023). The final deposits are interpreted as being indicative of general low-moisture conditions. Given that PDCs are typically hot, it is unlikely that these deposits would be uniformly moist or saturated, leading instead to spatial variations in moisture content. Furthermore, the presence of water can facilitate salt and mineral precipitation at the particle boundaries, and so accretionary lapilli can be strong. However, energy exerted on them (i.e., from collision with other particles) can result in their fragmentation or complete disaggregation (Mueller et al., 2017).

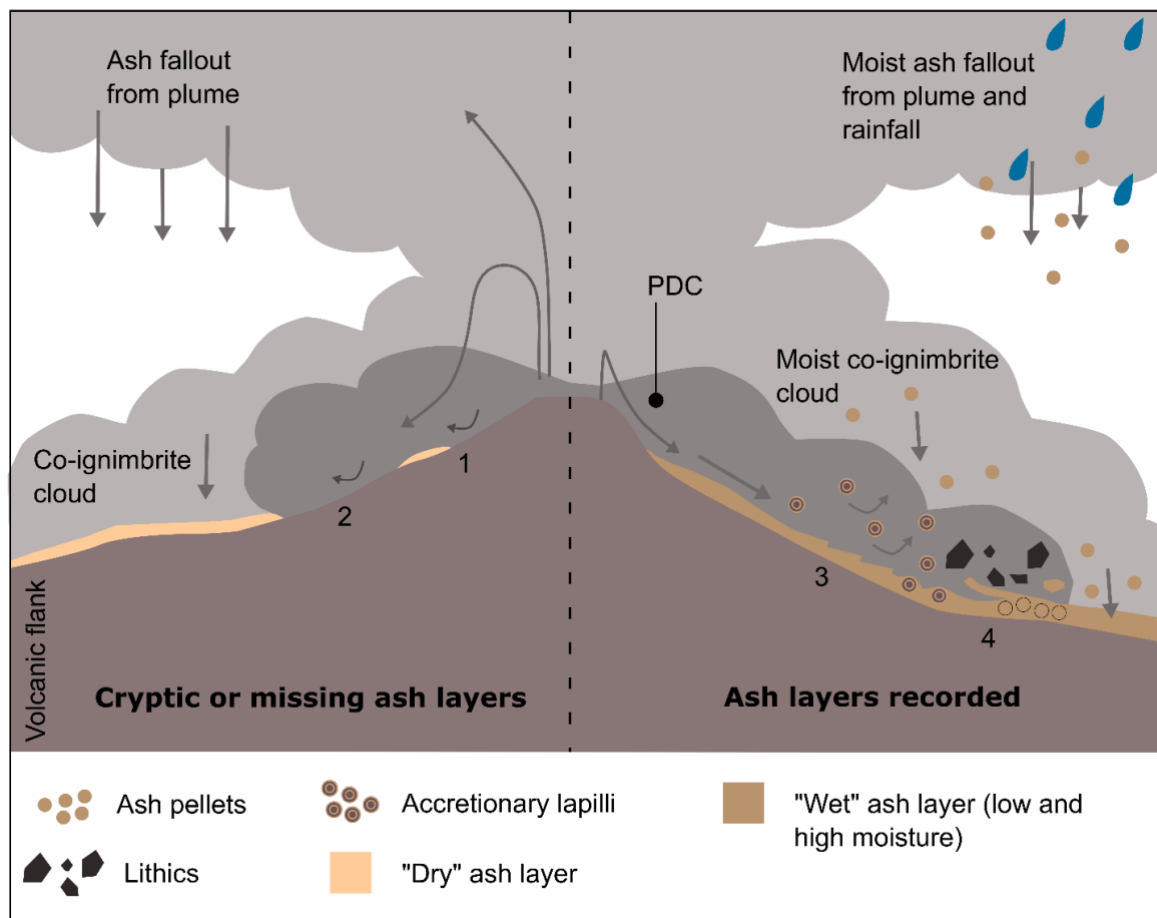


Figure 5.11. Schematic showing dry (left) and wet (right) ash layers forming from dry and moist plume fallout, co-ignimbrite fallout and dilute PDC deposition. At the dry locality, a subsequent PDC entrains (1) the loose ash material, possibly leading to bulking (2) in the current. The final deposit shows a cryptic or missing ash layer. In the wet scenario, moisture in the substrate is inferred by the presence of accretionary lapilli and ash pellets, which lead to an overall more cohesive deposit of greater shear strength (3). Furthermore, where lithics are present (4), high moisture substrates can experience shear thickening. This results in the preservation of “wet” ash layers, which are recorded.

In the field, ash layers rich in accretionary lapilli sometimes displayed stepped erosive contacts, where the contact sheared through them, or more diffuse contacts, where the contact wrapped around protruding accretionary lapilli. For the accretionary lapilli to be sheared through, they and the surrounding unconsolidated ash must possess similar sufficient inherent strength to resist disaggregation and erosion despite having only recently formed. Additionally, the presence of protruding accretionary lapilli that were not plucked out by the overriding current suggests that the lapilli are strong (Fig. 5.11). Laboratory experiments with low moisture conditions support these field observations, where moisture increase from 0 to 1

wt.% in pyroclastic material increases the yield strength and, therefore, resistance to shear (Fig. 5.11).

In contrast, ash pellet layers often formed sharp contacts with overlying lithic-rich deposits and, in some cases, were seen to be ‘lifted’, ‘peeled up’ or incorporated as clasts, indicating a greater shear strength within the deposit, allowing for coherent remobilisation of these layers. These features are reminiscent of deformed laminations and rip-up clasts of mud layers seen within turbidite sequences. Such features occur in turbidite sequences when cohesive sediments, like clay, bind together and are subsequently eroded and transported (Allen, 1984; Li et al., 2017; Yang et al., 2024).

The erosion of mud-rich sediments requires a critical shear stress to initiate substrate erosion (Chen et al., 2021). Particle size plays a crucial role in influencing a material’s erosional potential; for example, clay-rich materials exhibit greater cohesion compared to sand-dominated, granular materials. In addition, experimental studies have demonstrated that cohesive sediments erode as aggregates under low bed shear stresses or as ‘clasts’ of material under higher shear stresses (Sanford & Maa, 2001; Le Hir et al., 2011; Chen et al., 2018; 2021, and references therein).

The results from the shear experiments (Fig. 5.8b, c) show that increasing moisture (1 wt.%) led to an increase in the yield strength. The elastic limit is reached in less time than the dry material in the 1 wt.% substrates (Brown Tuff and Taupo 1). This indicates that the 1 wt.% material is deforming over shorter periods of time, but with more yield strength required to do so than material at lower moisture content. The separation between plastic and elastic deformation may also explain the remobilisation structures seen, for example, the elastic deformation (i.e., connected to the base and being “peeled” up) of the feature in Figure 5.7 and the more plastic deformation (i.e., the brittle separation from the underlying substrate) of feature A in Figure 5.6. Furthermore, at high moisture contents (25 – 70 wt.%), the drop tests revealed that a ball will impact and bounce off a deposit, resulting in less penetration. This reveals compelling evidence of shear thickening in a high-moisture pyroclastic material, leading to the dynamic preservation of high-moisture layers in high-stress environments. This behaviour, commonly seen in dense suspensions of solid particles, illustrates the complex rheological response of ash deposits, which can transition from flowing at low shear rates (as determined by the shear experiments) to solid-like resistance at higher shear stresses (drop

tests). In volcanic successions, this process may explain the resistance of thin ash pellet layers to erosion by more significant, caldera-forming deposits, such as lithic breccia.

5.6.3 Implications for interpreting PDC stratigraphy and hazard

This work demonstrates the influence of moisture on the preservation of ash layers that can be important marker horizons (Fig. 5.1) and finds that ash layers formed in low or high moisture conditions are more likely to be preserved than those formed in dry conditions (Fig. 5.11).

These findings have important implications for interpreting ash layers in volcanoclastic sequences, which can record episodes of PDC hiatus and delineate flow units. A lack of understanding of the preservation potential of an ash layer could lead to an overestimation or underestimation of the number of flow units in a deposit, relevant to interpretations of the location of PDC hazard through time. Furthermore, understanding the likelihood of erosion and incorporation of a fine-grained ash substrate into a PDC is non-trivial; the entrainment of dry, loose material can promote flow bulking of PDCs, resulting in increased flow mobility, higher velocities and extended runout distances (Iverson, 2012; Bernard et al., 2014).

Future research should focus on understanding deposit variability in order to determine how natural changes in the substrate affect entrainment, thereby contributing to current bulking and the removal of key deposit layers. Additionally, further investigation into the rheological behaviour of pyroclastic materials under varying moisture and shear conditions would provide a more precise understanding of shear thickening behaviour. This is important in understanding the erosion processes that might lead to flow-bulking and associated modifications to flow hazard. Finally, when reassessing past deposits and conducting future studies, it will be crucial to consider the role of cohesion in layer preservation and incorporate this factor into stratigraphic field interpretations.

Supplementary Material for Chapter 5 can be found in Appendix C.

Supplementary Material 5A – accretionary lapilli and ash pellet descriptions of Brown et al. (2010, 2012) and the descriptions used in this work.

Supplementary Material 5B – Lithofacies name, descriptions and interpretation of formation.

Supplementary Material 5C – Schematic figure showing the configuration and set-up of direct shear box, ring shear and drop tests.

Supplementary Material 5D – Broad-scale context of the “dry” deposit.

Supplementary Material 5E – Broad-scale context of the accretionary lapilli ash layer deposit.
Supplementary Material 5F – Broad-scale context of the “wet” ash pellet deposit.
Supplementary Material 5G – Broad-scale context of the remobilised deposit.
Supplementary Material 5H – Direct shear results at 0.5 mm/min and 1 mm/min experiments.
Supplementary Material 5I – Direct shear peak values and Mohr-Coulomb analysis.
Supplementary Material 5J – Drop test results.

Chapter 6 : Capturing shear instabilities, pulses and current behaviours at the flow boundary zone of granular currents.

6.1 Abstract

Understanding granular currents through analogue models enhances our knowledge of their dynamics and resulting deposits. Sedimentary features formed are crucial in reconstructing erosional and depositional behaviours at the current-substrate boundary. Both current dynamics (such as mass flux and unsteadiness) and substrate strength (cohesion, friction, density) can have fundamental controls on these behaviours. This study employs analogue flume experiments to observe interactions between a fluidised current and a stationary substrate. Use of gelatine has enabled the final deposit to be set and sectioned into longitudinal slices, allowing the internal 3D observation of features formed. Sedimentary features representing shearing, erosion, and remobilisation of the substrate have been identified using image and video analysis techniques. The influence of substrate apparent cohesion, introduced through 2.5 wt.% addition of moisture, has also been investigated to determine its effect on current-substrate interactions. Complex stepped flame-like features formed in dry conditions (0 wt.% moisture), driven by current unsteadiness and pulsatory behaviour. In contrast, the addition of moisture into the substrate suppresses erosion and remobilisation, resulting in the formation of discrete clumps of cohesive material and less intricate flame-like features. The findings show that increased cohesion in the substrate reduces erosion and remobilisation of material. This study applies the features observed to gain insight into current-substrate interactions in pyroclastic density currents, demonstrating the critical role of substrate strength and cohesion in our understanding of depositional and erosional models, which impacts our knowledge of stratigraphic patterns and deposits.

6.2 Introduction

Granular currents consist of discrete, solid particles that primarily interact through contact forces within an ambient fluid (i.e., a multiphase current; Jaeger, Nagel et al., 1996; Campbell, 2006; Delannay et al., 2017; Estep & Dufek, 2012). In dense granular currents, the dominant forces arise from interparticle contacts (i.e., collisional or frictional forces), which are subsequently transferred between particles and to surrounding interfaces such as substrates or walls (Roche et al., 2013; Crosta et al., 2017; Delannay et al., 2017; Artoni et

al., 2018; Liu et al., 2023). A granular material's ability to behave as a fluid or solid depends on external variations such as surface shear, fluidisation, or vibration (Geldart, 1973; Corwin et al., 2005; Campbell, 2006; Behringer & Chakraborty, 2019). Fluidisation is a process by which a granular material transitions to a more fluid state through the movement of fluid (Cocco and Chew, 2023). These complex factors in granular currents result in an unsteady, non-uniform and non-linear current (Dartevelle, 2004).

In industrial contexts, understanding material behaviours is essential for optimizing manufacturing, bulk handling, and material transport (Mirsha et al., 2020; Liu et al., 2020). In geophysical contexts, granular materials manifest in complex currents, such as turbidity currents, landslides, debris currents, avalanches and pyroclastic currents and their dynamics and impacts are governed by particulate fluid dynamics (Valentine, 1987; Nishimura & Ito, 1997; Gladstone & Sparks, 2002; Iverson, 2012; Baas et al., 2016; Delannay et al., 2017; Gauer & Issler, 2004; Zrelak et al., 2020).

6.2.1 Current–substrate interaction and erosion

Interaction between a granular current and a substrate has been observed in the field through features like scour marks, rip-up clasts, flame-like features and impact marks (Mutti & Nilson, 1981; Allen, 1982; Sparks et al., 1997; Calder et al., 2000; Goldfarb et al., 2002; Le Friant et al., 2004; Eggenhuisen et al., 2011; Iverson, 2012; Talling et al., 2013; Douillet et al., 2015, 2018; Pollock et al., 2016, 2019; Shanmugam, 2017; Delannay et al., 2017; Zrelak et al., 2020; Lucchi et al., 2022, Chapter 5 in this thesis). These features can directly result from forces and processes occurring at the current-substrate boundary (i.e., the flow-boundary zone in PDC systems; Branney & Kokelaar, 2002) or by post-depositional behaviours such as compaction (Prentice, 1956; Kelling & Walton, 1957; Allen, 1982; Valentine et al., 1989; Douillet et al., 2015).

Particles in the substrate will move once they exceed the erosion threshold, marking a point where particle motion begins or where they are eroded, and this critical value can change as a result of substrate and current parameters (Valyrakis et al., 2010; Agudo et al., 2014, 2017; Artoni et al., 2018; Xu et al., 2019; Pahtz et al., 2020). It is important however to recognise that even when shear stress remains below the critical shear stress, material can still be transported through traction, saltation and suspension (Baas et al., 2016; Pahtz et al., 2020). This has implications for the prediction of current behaviours at this boundary and subsequent deposit architecture. For example, a loose or weak substrate can be eroded by an

over-riding current, resulting in increased sediment load – a process known as “bulking” (Iverson, 2012). This can result in enhanced current mobility, extended runout distances, and increased hazard potential of the current (Gauer & Issler, 2004; Hungr & Evans, 2004; Mangeney et al., 2007, 2010; Doyle et al., 2011; Iverson, 2012; Dufrense, 2012; McCoy et al., 2013; Roche et al., 2013; Edwards et al., 2021).

6.2.1.1 Substrate strength

Understanding how currents interact with underlying substrates is crucial for predicting and constraining the current behaviour at the time of deposition. Previous work has explored the propagation of granular currents over soft, loose, hard, dense, rough, smooth, horizontal, sloped, thin and thick substrates (Parker et al., 1987; Rowley et al., 2011; Dufrense, 2012; Verhagen et al., 2013; Baas et al., 2016; Nogueira et al., 2013; Douillet et al., 2015; Sequeiros et al., 2018; Baghalian & Ghodsian, 2020; Breard et al., 2020; Chou et al., 2023). These parameters can all significantly influence forces and behaviours and the substrate-current interface.

In turbidity currents, the presence of clay-induced cohesion within a substrate has been shown to result in changes in erosional, by-passing, and depositional behaviours (Verhagen et al., 2013; Baas et al., 2016). However, other geophysical currents very rarely have considered the presence of cohesion in a substrate and the resulting effects on current dynamics and substrate features. The presence of moisture in a granular substrate can induce capillary bridges to form between grains, resulting in an overall increased yield strength of the material (Pierret & Caram, 1997; Kim & Sture, 2008, Chapter 5 in this thesis). In pyroclastic density currents, factors such as the overall condition of the substrate, and more specifically, the presence of moisture within it, as well as its interaction with the overriding current, have been largely neglected. If similar to turbidity current systems, the current-substrate boundary will be influenced by the substrate characteristics as well as variations in topography or current behaviours (e.g., such as mass flux, velocity, and unsteadiness).

6.2.1.2 Unsteadiness in currents and generation of pulses

Unsteadiness in currents can arise from fluctuating source conditions, such as shifts in mass flux, or from spontaneous variations within the current itself (Fig. 6.1; Smith & Kokelaar, 2013; Williams et al., 2014; Risica et al., 2022; Charbonnier et al., 2023; Dowey et al., 2024; Rowley et al., 2024) resulting in changes in current velocities and concentration.

Additionally, unsteadiness can lead to the formation and propagation of pulses within the

current (Iverson, 1997; Sulpizio & Dellino, 2008; Rowley et al., 2024). Unsteadiness and uniformity within the current are thought to be the key to controlling depositional or erosional processes at the current-substrate boundary (Branney & Kokelaar, 2002).

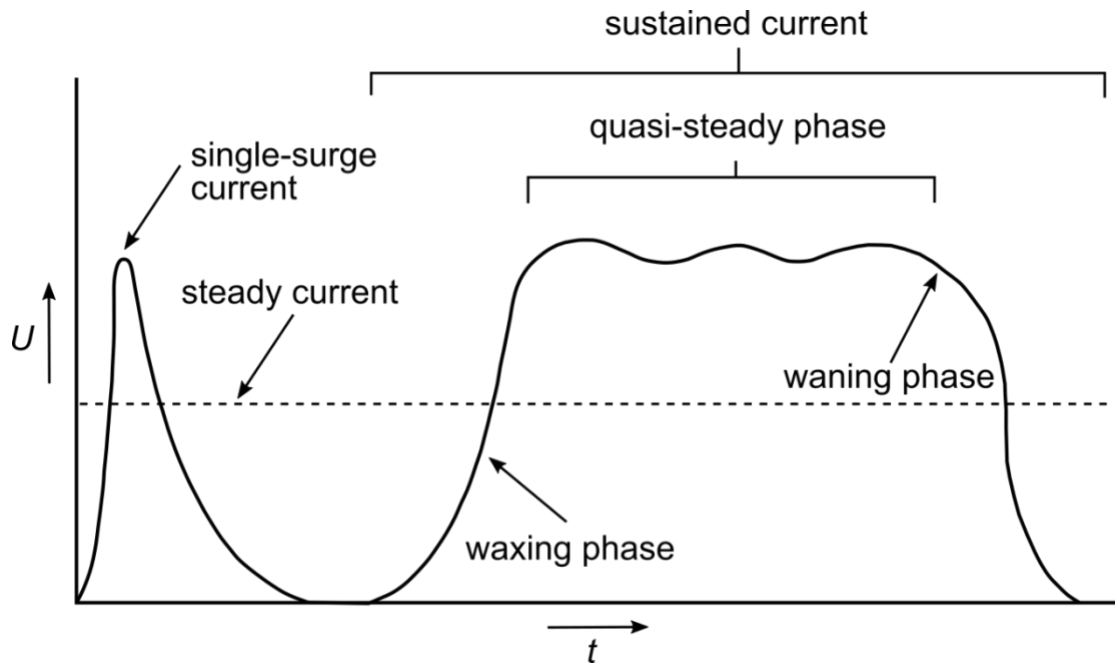


Figure 6.1. Unsteadiness in a sustained, long-lived current. In the quasi-steady phase, material pulses (i.e., an increase in velocity) can form. U is a change in current parameter (e.g., velocity, concentration) and t is time.

Connecting natural sedimentary features observed in the field (e.g., scour marks, remobilisation structures) directly to current behaviours is challenging due to the often hazardous and unpredictable nature of currents, which limits the potential of in-situ measurements. Furthermore, numerical models are limited by the lack of existing physical understanding of the processes at the current-substrate boundary. Analogue models can provide unique insight into these processes.

6.2.2 Understanding current-substrate interaction through analogue modelling

Analogue models are valuable tools for studying geophysical currents as they enable natural processes to be simulated using a wide range of parameters in controlled, scaled environments. The ability to manipulate specific parameters, such as size, moisture, density, shape, and temperature, enables a more detailed examination of the factors that control these processes, which is particularly useful in complex systems, such as multiphase granular currents (Iverson, 1997; Dellino et al., 2007, 2010; Roche et al., 2008; Rowley et al., 2014; Lube et al., 2015; Breard & Lube, 2017; Smith et al., 2018, 2020; Lube et al., 2020; Walding et al., 2022; Noviandi et al., 2022).

Analogue models have limitations, particularly regarding the data resolution they can provide. It can be challenging to capture fine-scale processes at the small scale, especially in dynamic systems where current behaviours, sediment transport and erosion-deposition processes occur rapidly and have complex interactions. Moreover, any observation of the current and substrate can only be made through sidewall image and video analysis or by bulk sampling of the final deposit (Dufrense, 2012; Roche et al., 2013; Baas et al., 2016; Louge et al., 2015; Brosch & Lube, 2020; Smith et al., 2020), hence, potentially missing key longitudinal and lateral variations of sedimentary formed structures.

Gelatine has been widely used in analogue experiments to explore the deformation of 3D stratigraphic packages in response to fault propagation, magmatic emplacements, and large-scale tectonic processes (Hyndman & Alt, 1987; Agarwal & Agrawal, 2002; Kennedy et al., 2004; Kavanagh et al., 2006, 2013; Shea & Wyk de Vries, 2008; Di Giuseppe et al., 2009; Kervyn et al., 2009; Corbi et al., 2011, 2013; Kobchenko et al., 2014; Jara et al., 2015; Lee et al., 2016; Jagger and McClay, 2016; Reber et al., 2020; Dooley & Hudec, 2020; Massaro et al., 2022; Zwaan et al., 2022). Gelatine can be useful, as during the curing process it transitions from a liquid to a gel-like state. It is readily available, dries transparently, and, if left, will dry to a solid state. Rowley et al. (2011) adapted the use of gelatine to see the internal structure of a deposit resulting from repeated granular currents interacting with their aggraded deposits and a substrate. Sectioning and slicing the deposit revealed interesting internal structures generated by shear interaction between the over-riding current and loose aggraded deposit and pre-existing substrate, useable as indicators for current behaviour at the flow boundary zone (e.g., Kelvin-Helmholtz-like instabilities, Rowley et al., 2011). This method presents an opportunity to observe and analyse the deposits formed from sidewall to flume centre and longitudinally parallel to the current thalweg.

6.2.3 Aims

This work explores the impact of moisture on the behaviour of an unsteady fluidised granular current with a static, loose substrate. The gelatine sectioning methodology is used to explore longitudinal (current-parallel) complexities in the deposit to gain a better understanding of behaviours at the current-substrate boundary. Specifically, this work aims to characterise erosional features formed at the current-substrate boundary and how these features vary and change with an increase in moisture in the substrate.

6.3 Methods and material preparation

This work investigates the interaction between a fluidised granular current and a static substrate by preserving the 3D deposit in a gelatine-water mixture and sectioning it longitudinally. Two flume experiments were completed where gas-fluidised currents were allowed to propagate over substrates that were either dry (0 wt.% moisture) or wet (2.5 wt.% moisture), and all other conditions throughout the experiment were held consistent.

6.3.1 Flume set-up

The flume used is a 3 m long 0.15 m wide apparatus (Rowley et al., 2014; Smith et al., 2018; Walding, 2022) with a porous base that allows gas fluidisation of granular currents. In these experiments, flume angle was maintained at 15° (Fig. 6.2). Three 1 m chambers supply gas to the base of the flume, which allows gas flux to be individually controlled along the length (Fig. 6.2).

In the experiments presented here, the first chamber was supplied with a gas flux of 75 l/min. The second and third chambers were lined with vinyl plastic and cling film and filled with the substrate material. The flume base in the second two chambers was dropped 10 mm relative to the first metre, allowing 10 mm of substrate to be laid. This resulted in the current experiencing a topographically flat contact between the first metre (solid flume base) and the second two (loose substrate) (Fig. 6.2).

To lay the substrate (Fig. 6.2), 10 kg batches of dyed material were mixed (with or without moisture) and sieved evenly into chambers 2 and 3. Care was taken to carefully level the substrate to ensure a flat surface overall.

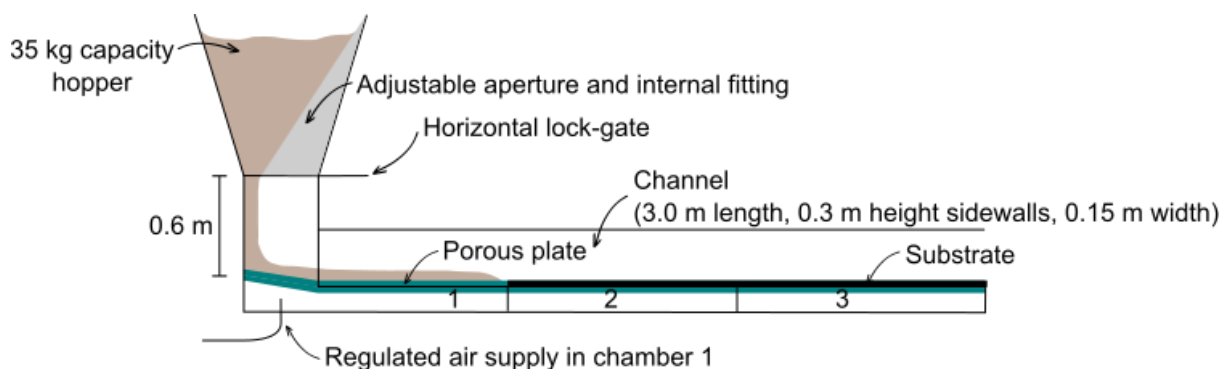


Figure 6.2. Experimental flume set-up as outlined in and adapted from Rowley et al, (2014) showing the porous plate (green) and substrate (black). The experiments recorded in this work utilise the first chamber to supply a gas flux to the material. Chambers 2 and 3 hold the unfluidised loose substrate.

6.3.2 Materials

Ballotini was used for both the current and the substrate in the experiments (Appendix D⁷, Supplementary Material 6A) due to its excellent fluidisation properties and good analogue behaviours (Walding et al., 2024). All ballotini were dried in an oven at 80° for 24 hours and then sieved before use.

For the current, 6 kg of ballotini was loaded into the hopper (Fig. 6.2). For the substrate, ballotini were dyed in different colours using acrylic paint (see detailed methodology in Supplementary Material 6B) so interactions could be picked out clearly. Where moisture was added to the substrate, water was mixed into the sample by weight percentage and shaken thoroughly to ensure a homogeneous mixture.

6.3.3 Setting and Sectioning

A methodology was developed to set and section the deposit (which included substrate, and materials emplaced by the current) to view internal structures within it following the experiments. This technique was adapted from methods used by tectonic sandbox modelling groups (Agarwal & Agrawal, 2002; Kennedy et al., 2004; Shea & Wyk de Vries, 2008; Jara et al., 2015; Jagger and McClay, 2016; Dooley & Hudec, 2020; Massaro et al., 2022; Zwaan et al., 2022) and from work by Rowley et al. (2011).

To set the deposit, a sand mixture and blue paper towels were gently placed on top of the deposit to dampen the effect of the gelatine pouring and protect the upper surface. A gelatine and hot water mixture (1:5) was poured over the deposit and left to set for ~12 hours prior to sectioning. Rowley (2010) provides a detailed overview of this methodology.

Once set, the deposit was sectioned laterally (perpendicular to current direction) into easily handled 0.1 - 0.2 m (± 0.01 m) long blocks labelled A-E (Fig. 6.3a), where A is the 1.0 m mark at the beginning of the substrate, and D/E are the more distal sections that represent the extent of the current runout. These blocks were then sliced longitudinally using wire (parallel to current direction) where slice 1 is the section towards the right-hand flume wall, 3 is the flume centre, and 2 is in between the two (Fig. 6.3b). High-resolution photographs of each

⁷ All appendices for Chapter 6 are in Appendix D. Herein, material will be referred to as 'Supplementary Material 6A, B, C' etc...

slice were taken, allowing the stitching of slices to create complete longitudinal sections of the deposit.

6.3.4 Data collection and analysis

The cameras used during the experiments were placed facing the flume wall. A high-speed camera (Phantom v 9.1, 500 FPS, 1632 x 1200 resolution) was placed at the base of the flume and loose substrate boundary (0.70 – 1.30 m), and a DSLR with video capabilities (Canon EOS 700D, 50 FPS, 1280 x 720 pixels) was positioned to show the whole length of the flume. Before the runs, photos of the substrate were taken, and during the runs, videos were recorded of the current and substrate. After the experiments were completed, photos of the final deposit (current and substrate) were taken prior to excavation.

ImageJ software (Schneider et al., 2012) was used to calculate the current and pulse velocities and thickness from the high-speed video. For the sectioned deposit, software was used to trace the contact between the substrate and material emplaced by the current. Each feature was measured from scaled image analysis and categorised.

Throughout the results and the discussion, the deposit is referenced by flume run (e.g., Flume Run 1), blocks (e.g., A-E) and slice number (e.g., 1, 2 and 3) as represented in the schematic image (Fig. 6.3c).

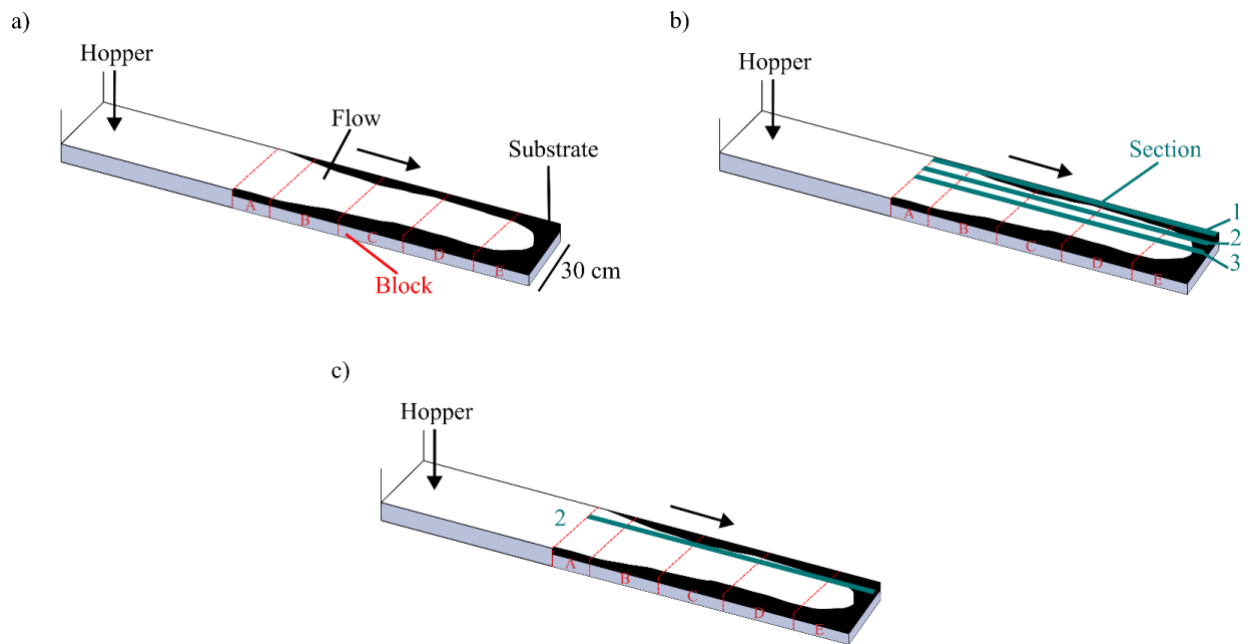
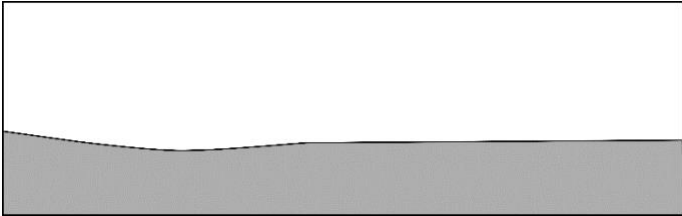
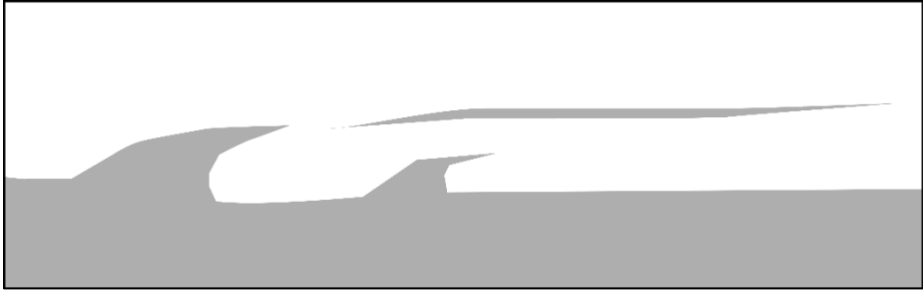


Figure 6.3. a) Block divisions within the flume (A-E). The arrow shows the current direction, and the dashed red lines show the partitioning of deposit blocks at a distance away from the hopper. b) The lateral division of slices (1, 2 and 3) in shaded dark aquamarine, and c) illustrates the schematic used throughout this work to indicate the position within the flume.

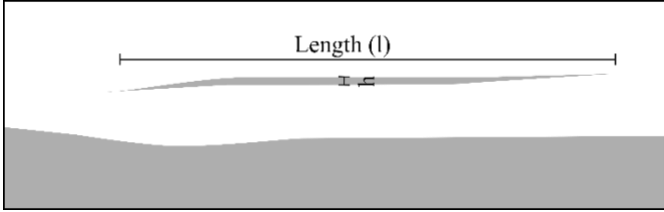
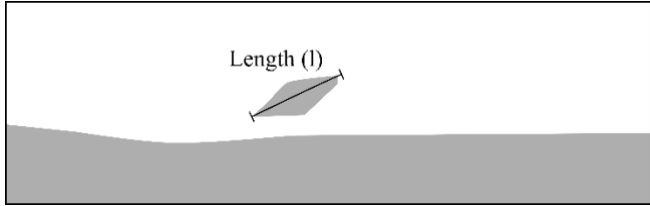
6.3.5 Deposit architecture classification

During analysis of the sectioned deposits, sedimentary features were observed at the contact between substrate and material emplaced by the current. To understand the formation of these features and what they may tell us about current-substrate dynamics, the features were categorised based on their morphology, contact relationships, and concentration of entrained material from the substrate into the current (Table 6.1).

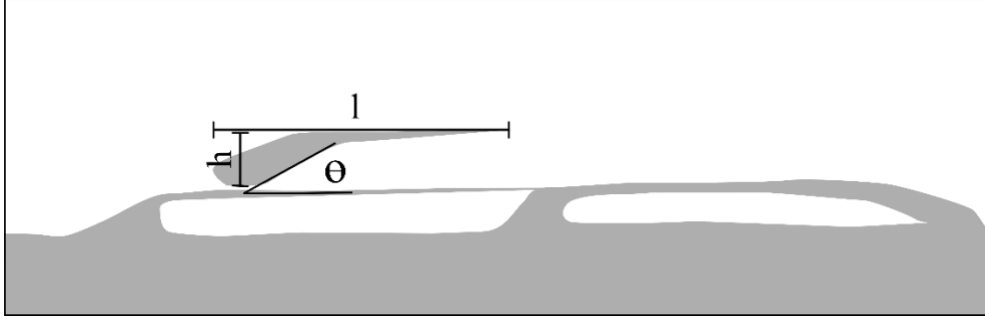
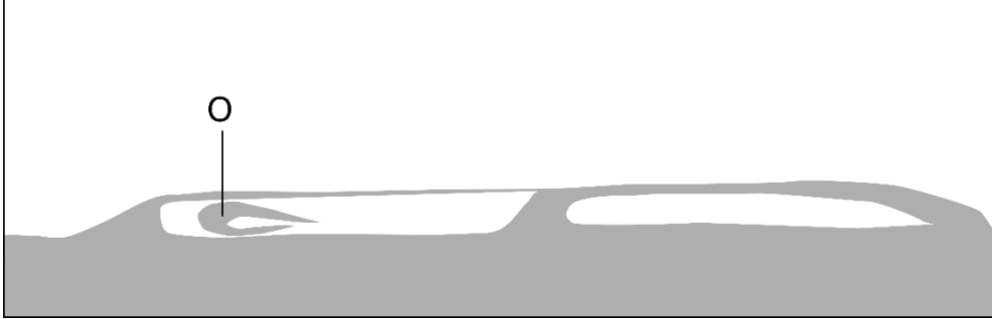
Table 6.1. Sedimentary features observed in this work, their characteristics and descriptions and how they have been measured in this work.

Substrate descriptions				
Name	Key code	Description	Quantification	Schematic illustrations of features and relevant measurements
Flat	Fl	Area of substrate that is planar and shows no features.	No features are present.	
Undulating	Un	Undulating topography with clear peaks and troughs and a clear area of remobilisation of the substrate. Often containing large flame-like features and stringers.	Features are present in the substrate.	
Features				

Flame-like	F	Flame-like structures that taper out towards flow direction. Show clear shearing of material.	<p>Tracing out of material. Aspect ratio measured as length/height. Angle (θ) measured from underlying feature or substrate. In some cases the angle pinches down-flume and therefore a negative angle value is recorded (angle at the right of the diagram)</p>
------------	---	---	--

Stringers	Str	Often low concentrated areas of particles which have no connection to the substrate and appear to be “floating” within the deposit.	Tracing out of material. Angle and length measurements.	
Clump	CL	An accumulation of particles.	A clast is classified as having a maximum particle length of > 0.2 mm.	
Feature descriptions				
High concentration	HC	Areas of a high particle population (eroded particles) than the surrounding area.	The mean grey value (mgv) is used to determine where the material is at maximum concentration (mgv = 31.5). The average mgv of 119 is used to distinguish between areas of high concentration	

			and areas of low concentration.	
Low concentration	LC	Areas of a particle population which are less than the surrounding area.	The mean grey value (mgv) is used to determine where the material is at its lowest concentration (mgv = 158). The average mgv of 119 is used to distinguish between areas of high concentration and areas of low concentration.	
Connected	C	Reworked material that was part of the substrate, that has now moved but is still connected to the substrate.	Tracing out of the material.	

Disconnected	D	Material that was part of the substrate but has now moved and is no longer connected to the substrate.	Tracing out of the material.	
Vortical	O	Dispersive shape of granular material substrate which are disconnected to the substrate and are elongate and vortical in nature.	Tracing out of the material. Dimension measurements.	

When categorising sedimentary features, flat portions of the current-substrate contact without features (F1) and undulating areas that show features (Un) are first identified. Individual features are initially categorised by physical distinctions (e.g., flame-like, stringers, and clumps), then by whether they contain high or low concentrations of entrained material (LC vs HC), whether they are still connected to or disconnected from the substrate contact (C vs D), and finally, whether their shape is vortical (O) (Table 6.1). Each feature can have multiple descriptive characteristics (i.e., LC-C). Analysis of the occurrence of these features in dry and moist substrate environments is presented in the following sections. A feature graph for each block shows the frequency of the features observed. Any additional quantitative data is also recorded (i.e., angle of features, aspect ratio; Table 6.1).

The methods of Pollock et al. (2019) are adopted to measure flame-like structures, where measurements are calculated from their length and height to determine aspect ratio (length/height). Following Pollock et al. (2019), our flame-like features are described as having a trunk and an arm (see flame-like features, Table 6.1). The trunk is the beginning of the feature, where it protrudes from the substrate, and the arm is the flame that extends downstream from the trunk. In some areas, flame-like features form on top of each other or laterally move into each other. Where flame-like features merge into one another, the termination of aspect ratio measurements is at the end of the arm in the next flame-like feature trunk (see flame-like features, Table 6.1). A similar method is used for measuring the aspect ratio of stringers; stringer length is measured where the stringer starts and ends, and stringer thickness is measured at the thickest point of the stringer (see stringers, Table 6.1).

6.4 Results

6.4.1 Comparison of current mobility and pulses over substrate conditions of 0 wt.% and 2.5 wt.% moisture

Results for the experimental granular currents show that their runout distance decreases when emplaced over a moist substrate compared with a dry substrate (Fig. 6.4). Specifically, the overall runout distance was 1.89 m over the dry substrate (0 wt.% moisture) and 1.67 m over the moist substrate (2.5 wt.% moisture). Interestingly, the velocity of the current front was not uniform as the current propagated down the flume during experiments (Fig. 6.4). This is indicative of unsteadiness in the current, observed as a pulse that propagates through the current. Pulses that form spontaneously behind the current front can be observed and followed from initiation to the point where they either increase in velocity and eventually overtake the current front (0 wt.%: Pulse 1) or where they lose velocity and halt at the distal end of the current where deposition has occurred (2.5 wt.%: Pulse 1).

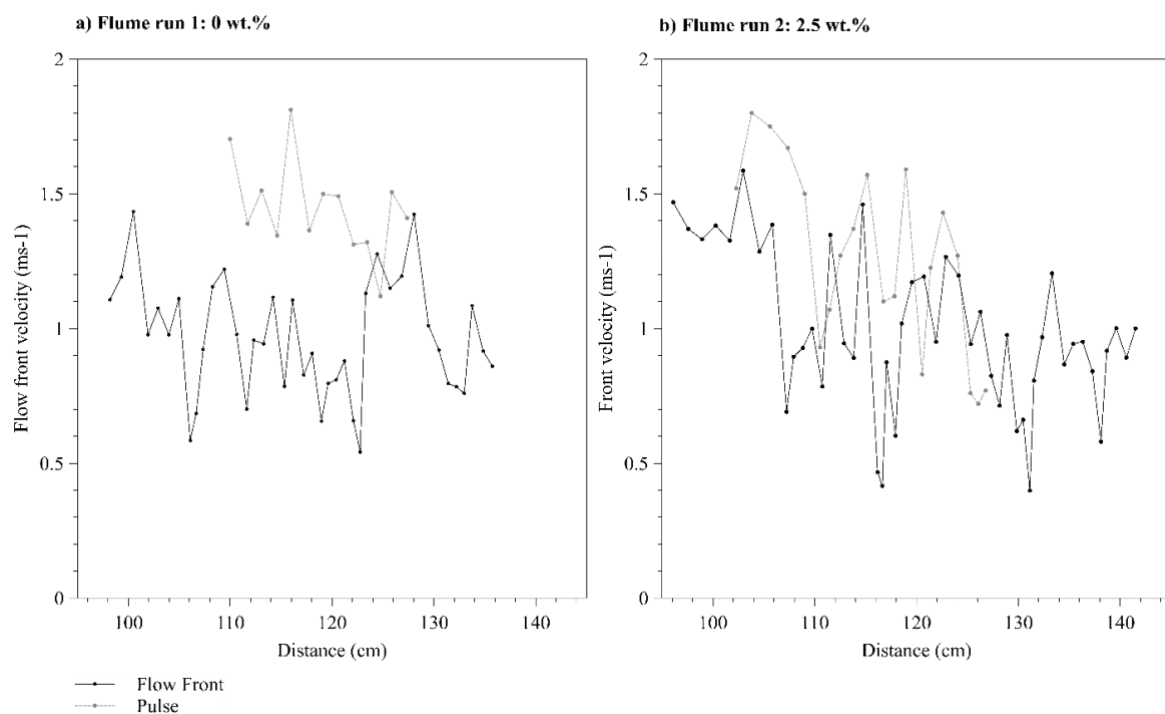


Figure 6.4. a) Flume run 1 (0 wt.% moisture substrate) and b) flume run 2 (2.5 wt.% moisture substrate) current front velocity (m/s) against distance (cm). The velocities of the pulse front are recorded (dashed line) and end where they meet the current front, can no longer be traced or where current motion ceases completely.

6.4.2 Sedimentary features observed in a substrate of 0 wt.% moisture

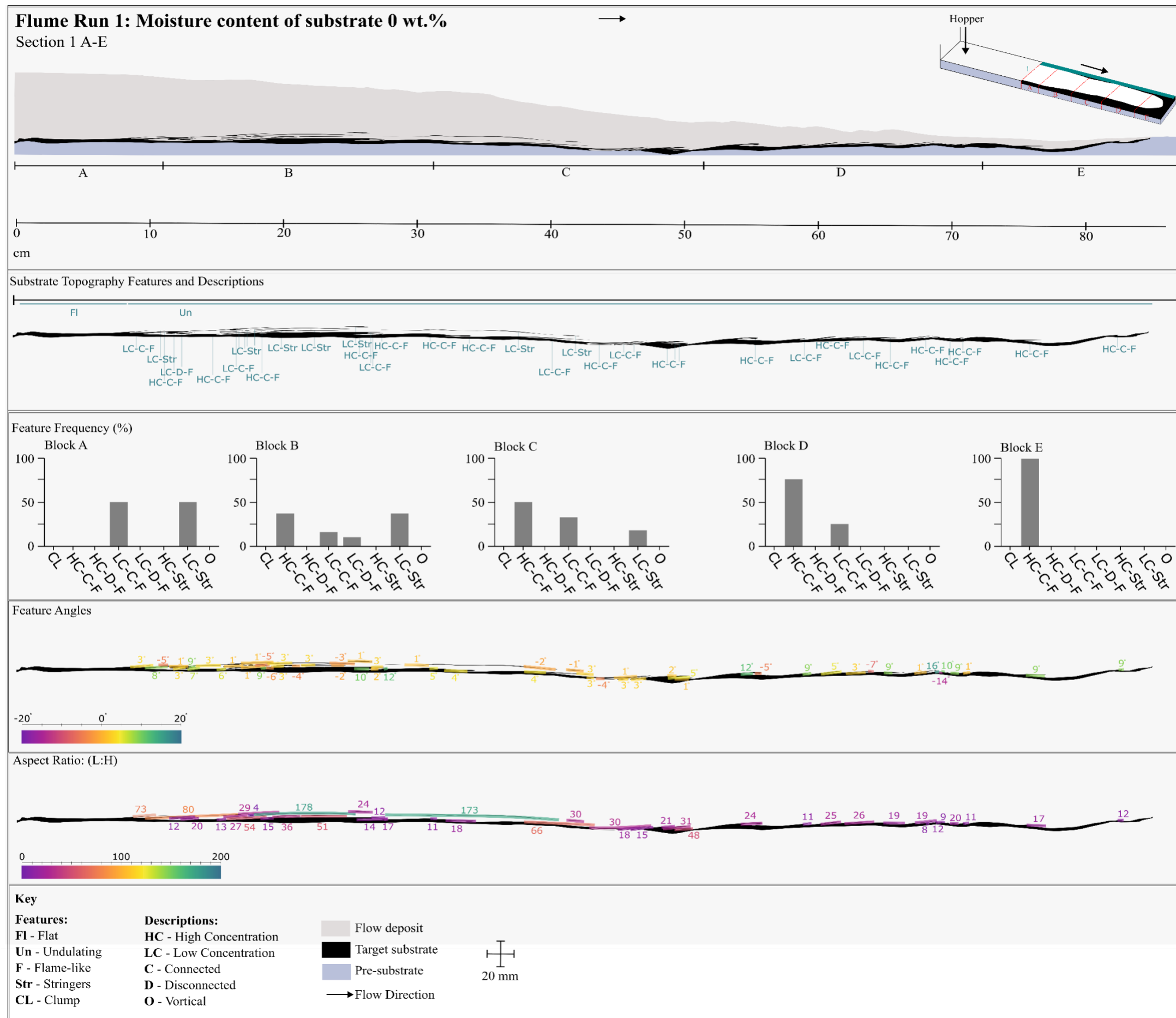
Here Sections 1, 2 and 3 are analysed. The first block of the sections (A, Fig. 6.5, Supplementary Material 6C) often shows a sharp contact with no features present, ranging from lengths of 9.5 cm in Section 1 and 16 cm in Section 3 (Fig. 6.5, Supplementary Material

6C). Features are then observed to form on an undulating contact between the substrate and the current. This is not the case for section 2, which shows features present from the beginning of the substrate to the end of the deposit (1.5 to 76 cm). The features consist of low-angle flame-like and stringer features (Fig. 6.5, Supplementary Material 6C).

In Section 1 (Fig. 6.5), features begin at 9.5 cm. These features are predominantly low concentrated flames and stringers which become less frequent and more concentrated down flume (9.5 to 80 cm). The aspect ratio for flame-like features and stringers becomes shorter with distance down the flume. For example, the longest aspect ratio is 178 at 10 cm distance and the shortest is 8 at 70 cm distance. The feature angles become steeper with distance down the flume. From 9.50 to 48 cm distance, angles range from -6° (where the flame-like feature pinches down-flume, see Table 6.1) to 12° ; from 48 to 80 cm distance, angles range from -14° to 16° (Fig. 6.5).

In Section 2 (Supplementary Material 6C), flame-like features and stringers across the flume are both low and high concentrated. The longest aspect ratio of features is 133 at 32 cm and the lowest is 4 at 10.8 cm. The features initially steeply angled (-14° and 10° at 1.5 – 6.4 cm) but then become less steep where stringers and stacked features are present (1° to 5° at 15.4 – 56.3 cm). In the distal part of the deposit (59.8 to 74.5 cm) the feature angles are steepest (16°).

In Section 3 (Supplementary Material 6C), features begin at 16 cm. Initially, they are low and high concentrated and become less frequent and overall low concentrated at the end of the deposit (72.4 – 86 cm). The longest aspect ratio features are seen from 16.4 to 54 cm (maximum 81) and the shortest at 70 cm (2). Feature angles range from -13° to 13° and are generally steeper in the distal part of the deposit (64.4 – 86.1 cm).



6.4.3 Sedimentary features observed in a substrate of 2.5 wt.% moisture

Across all sections (1, 2 and 3) the contact between the substrate and the current deposit is sharp, with often no features present (Table 6.1). In section 1 (Fig. 6.6), the contact shows an undulating shear plane with small topographic depressions. In contrast, in sections 2 and 3, the contact has been planarly sheared and these small topographic depressions are no longer seen (Supplementary Material 6D). In Section 1 (Fig. 6.6), features form from 35.7 to 68.2 cm and consist of steeply angled (16.3° - 45.6°), low aspect ratio (1 – 6.6), low and high concentrated flames. Clumps of substrate material were seen transported in the overriding current from 44.5 to 54.3 cm and range from 0.6 to 1.6 mm in length. Similarly, in section 2 (Supplementary Material 6E), features formed from 7.6 to 62.1 cm are steep (12.8° – 30°) and show a low aspect ratio down-flume (7.5 to 1.7). Clumps are 0.1 to 0.24 mm in size (located at 57.2 – 61.3 cm). In Section 3, flame-like and stringer features formed from 6.4 – 43.5 cm get steeper (7.6° to 32.9°) and show lower aspect ratios (16.5 to 1) down-flume. The clump in this section is 0.2 mm in size (Supplementary Material 6E).

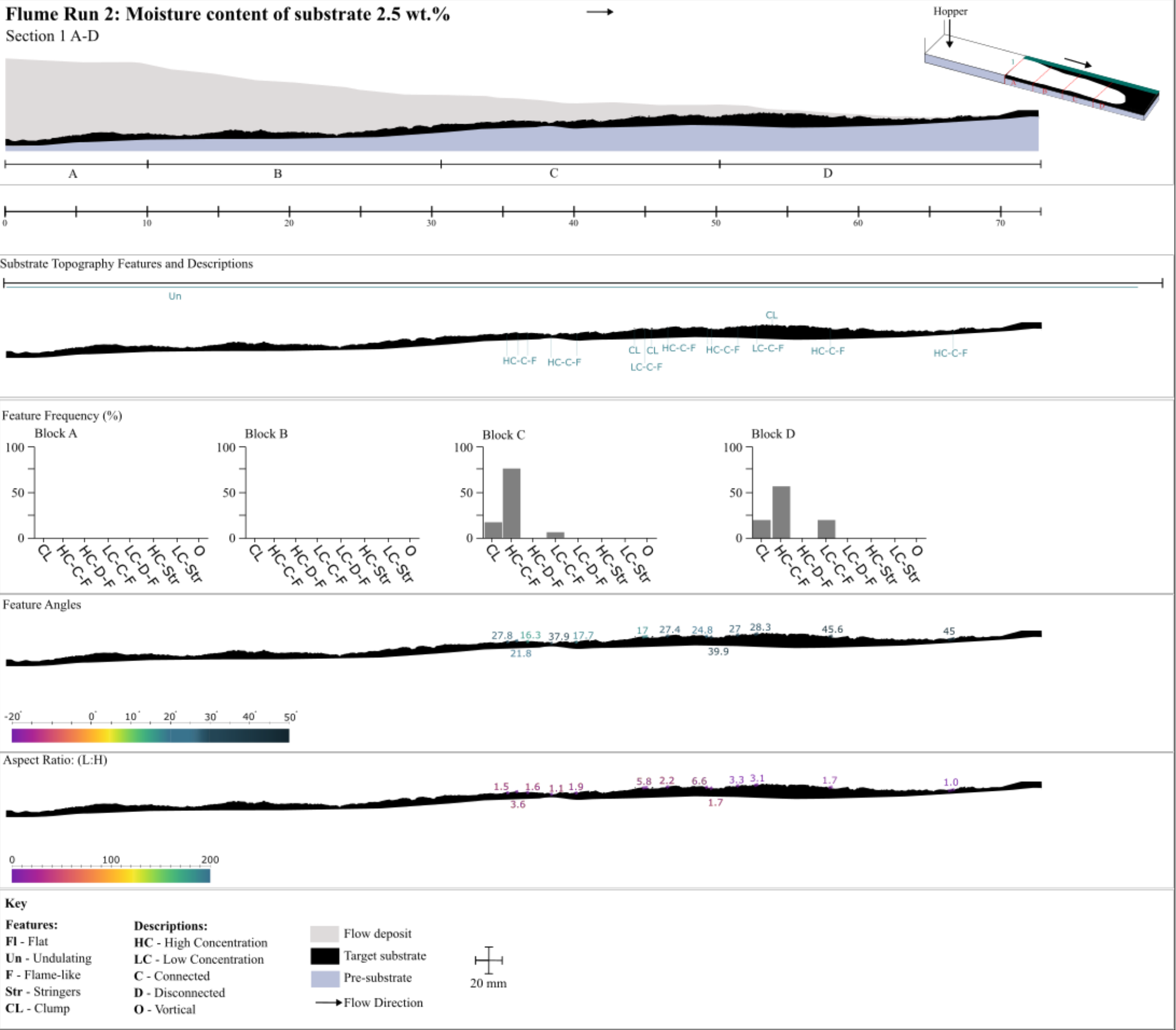


Figure 6.6. Panel of Flume Run 2, Section 1, A-E. The substrate had a moisture addition of 2.5 wt.%. A is proximal (i.e., where the substrate starts), and E is distal (i.e., down-flume where the substrate ends and the run out of the current stops). Feature type, frequency, angle and aspect ratio are described. Feature classification and descriptions can be found in Table 6.1. Panel sections 2 and 3 for Flume Run 2 can be found in Supplementary Material 6E. Current videos can be found in Supplementary Material 6F.

6.4.4 Sedimentary feature interpretation

Sedimentary features commonly form as a result of a complex interplay between current and substrate, leading to changes in erosion or deposition. Erosion may completely remove material at the current-substrate boundary but can also leave behind unique features. These sedimentary features can then be used to interpret the processes that formed them, such as depositional process, paleocurrent or current conditions (e.g., velocity, shear stress at the current-substrate boundary). For example, in geophysical gravity-driven currents, erosion can be recorded as rip-up clasts in turbidity currents and flame-like features in pyroclastic density currents (Douillet et al., 2015, 2018; Pollock et al., 2019; Lucchi et al., 2022). Both current and substrate behaviours are important in understanding the generation of features and can be used as key events of current reconstruction. In this work, flame-like features and stringers are interpreted as forming from the remobilisation of loosely packed substrate material from cross-flume shearing of the current. Clump features are interpreted as forming from shear-resistant, cohesive packages of material being remobilised from cross-flume shearing of the current.

6.4.5 Multi-stepped feature formation at the current-substrate boundary

The experiments presented in this work generated unsteady currents, characterised by changes in velocity and pulsatory behaviours (Fig. 6.5). Here, current-substrate interaction is discussed through the concept of the flow-boundary zone (Branney & Kokelaar, 2002). The flow boundary zone (FBZ) marks a transitional region from static substrate, a mobile entrained substrate and the mobile current (Branney & Kokelaar, 1992, 2002). Therefore, current behaviour, such as unsteadiness, will be reflected during material deposition of the FBZ as well as the features formed, typically behind the head of the current (e.g., Mangeney et al., 2010; Rowley et al., 2011; Roche et al., 2013; Farin et al., 2014; Pollock et al., 2019).

In the dry (0 wt.%) substrate, unique, multi-stepped shear features are formed (Flume run 1: section 1, 10.5 – 51.1 cm; section 2, 16.4 – 75.0 cm; section 3, 17.6 – 56.2 cm, Fig. 6.5, Supplementary Material 6C). Multi-stage shearing episodes are interpreted to result from unsteadiness and pulses in the flow, which manifest as high velocity, thick pulses (i.e., a change in energy in the system) within a sustained current. These episodes are hypothesized to represent vertically migrating and shearing processes, interpreted as deposition formed from unsteady deposition within a stepped FBZ (Fig. 6.4) (Supplementary Material 6G).

Two locations of the deposit showing stepped features have been identified, and remobilisation events have been described for each one. Additionally, current thickness (± 0.1 cm) and velocity have been recorded at each area of deposition to better constrain the controls and behaviours of the multi-stepped feature formation, as hypothesised above.

6.4.5.1 Multi-stepped feature: 1

Multi-stepped feature 1 occurred in Flume run 1, Section 2 at 17 – 22.5 cm from the start of the substrate (Fig. 6.7). These multi-stepped structures are composed of multiple flame-like features, with secondary flame-like features forming on the arms (Table. 6.1, Fig. 6.7). The stepped formations have been sequenced by identifying which one formed first, followed by those that formed subsequently. These are referred to here as remobilisation events 1, 2, 3, etc... (R1, R2, R3 in Fig. 6.7a). Current thickness measurements were taken at 17 cm and measured incrementally until the current began to deposit its material.

Firstly, a flame structure (R1) forms at the substrate contact. This is thought to be due to initial current propagation (Fig. 6.7b, black line and Fig. 6.7c). R2 forms next and presumably erodes R1 material. This second remobilisation event is thought to coincide with the arrival of the pulse and subsequent thickening of the current (Fig. 6.7b, dashed line and Fig. 6.7c peak in current thickness). Finally, R3 forms small flame-like features on the arms of R2. Although there are no additional detected pulses in the current, the clear fluctuations in current thickness (Fig. 6.7c, at 0.18s, 0.30s and 0.37s) suggest that ongoing pulses may be present as a result of continued unsteadiness within the current that are not visible by the techniques used in this study.

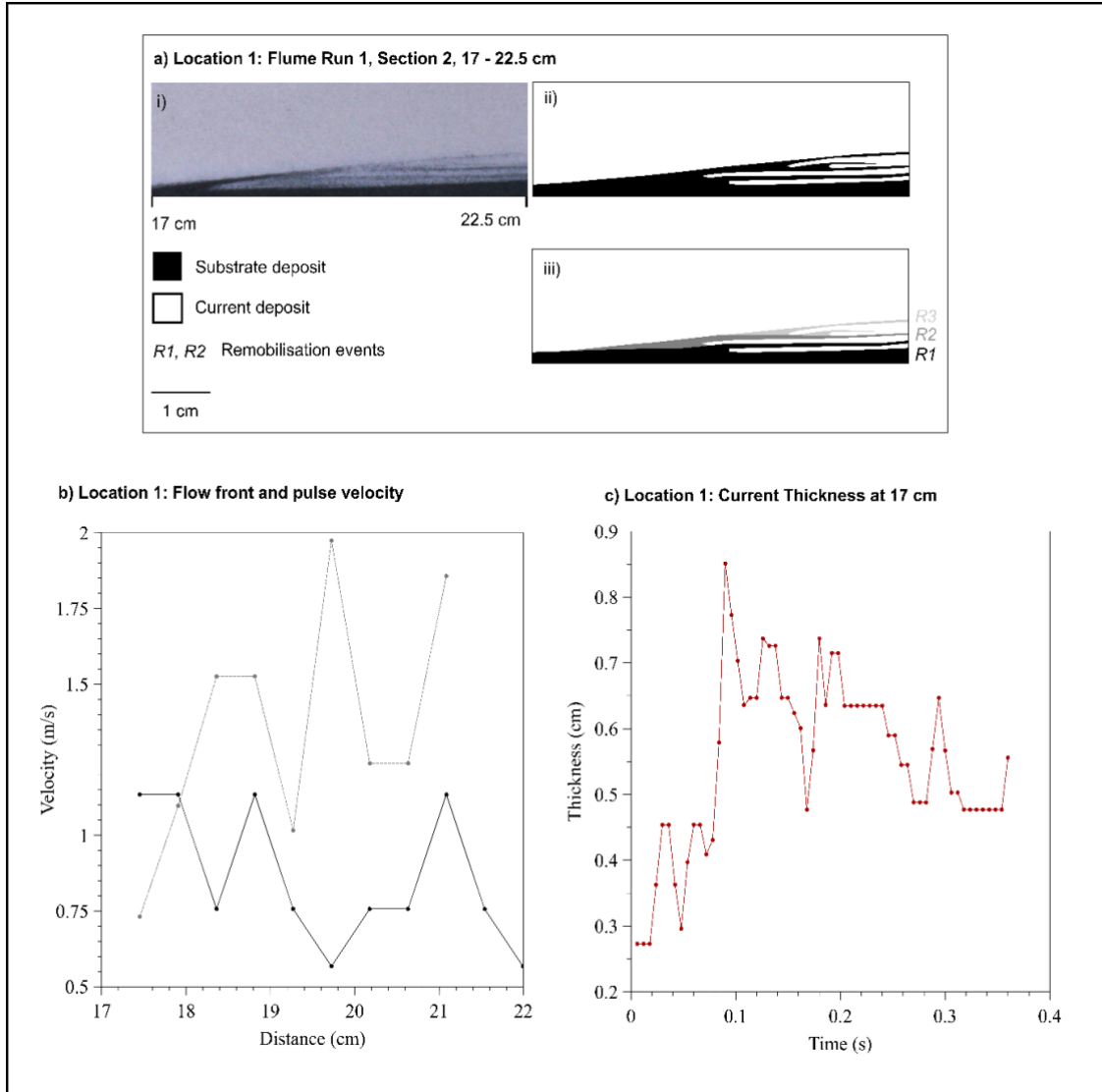


Figure 6.7. a) Remobilisation events sequenced from the deposit in Flume run 1, Section 2 from 17 to 22.5 cm (a.i – a.iii) b) Flow front (solid black line) and pulse (dashed grey line) velocity from 17 – 22 cm and c) Current thickness through time at 17 (± 1.0) cm.

6.4.5.2 Multi-stepped feature : 2

The multi-stepped feature 2 is located in Flume Run 1, section 2 from 69 – 72 cm from the start of the substrate (Fig. 6.8). Similarly to feature 1, flame-like features are formed on top of previous flame-like features giving them a “stepped” appearance (Table. 6.1, Fig. 6.8).

Sequencing the remobilisation events revealed three distinct phases. Firstly, R1 forms a high-concentrated flame-like structure, which is thought to be due to the current flow front moving and eroding through the area (Fig. 6.8b). R2 forms next and remobilises earlier substrate material and presumably some R1 material. This location is thought to coincide with the increase in current thickness at 0.07s, which cannot be identified as a visible pulse in the

current (Fig. 6.8c). Finally, R3 shows a low-concentrated flame-like feature that forms on the arm of R2 and is thought to be due to the arrival of the pulse (Fig. 6.8b) and subsequent thickening of the current at 0.25s (Fig. 6.8c). The break in current thickness from $\sim 0.113 - 0.24$ s represents a time when the flow front deposited prior to the arrival of the pulse.

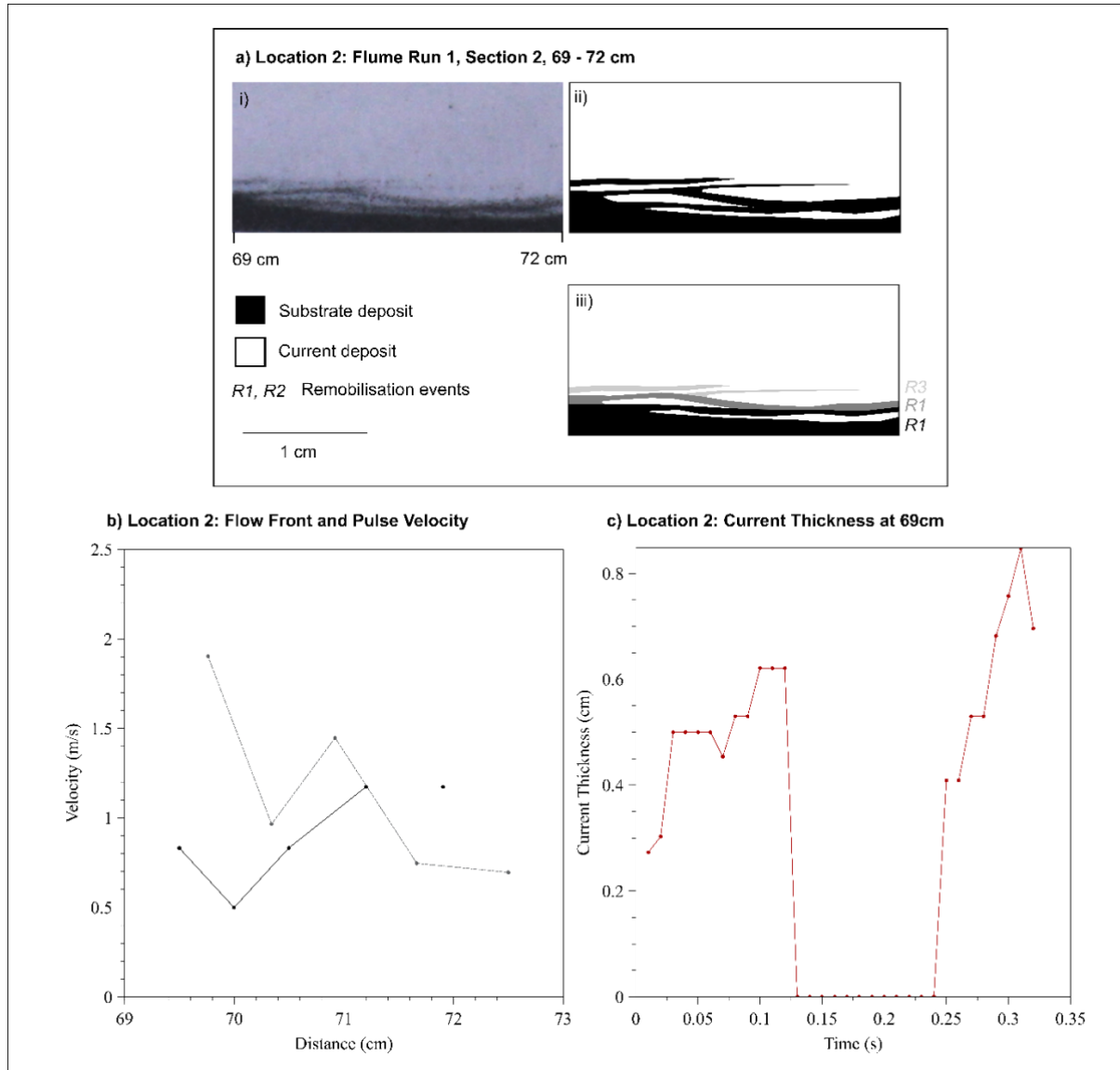


Figure 6.8. a) Remobilisation events sequenced from the deposit in Flume Run 1, Section 2 from 69 to 72 cm (a.i – a.iii) b) Flow front (solid black line) and pulse (dashed grey line) velocity from 69 – 72 cm and c) Current thickness through time at 69 (± 1.0) cm.

6.4.5.3 Multi-stepped model of formation

The interpretation of the multi-stepped flame features (Fig. 6.7 and 6.8) is that the front of the current formed the initial structure (R1), and then subsequent pulses in the current formed the second structure (R2, remobilised from the R1 material). At this point in time, the depth of shearing is vertically higher due to the aggrading deposit, so the migrating shear zone has stepped vertically (Fig. 6.9). The final remobilisation event (R3) is seen to form on top of the R2 feature. No additional pulses are identified, however, the inherent unsteadiness of the current is believed to continue throughout the duration of the experiment. Therefore, this may lead to additional unseen pulses, or changes in energy throughout the current, resulting in the formation of R3. With this data, it is concluded that multi-stepped features are formed from a rapid step-wise current boundary migration (Fig. 6.9).

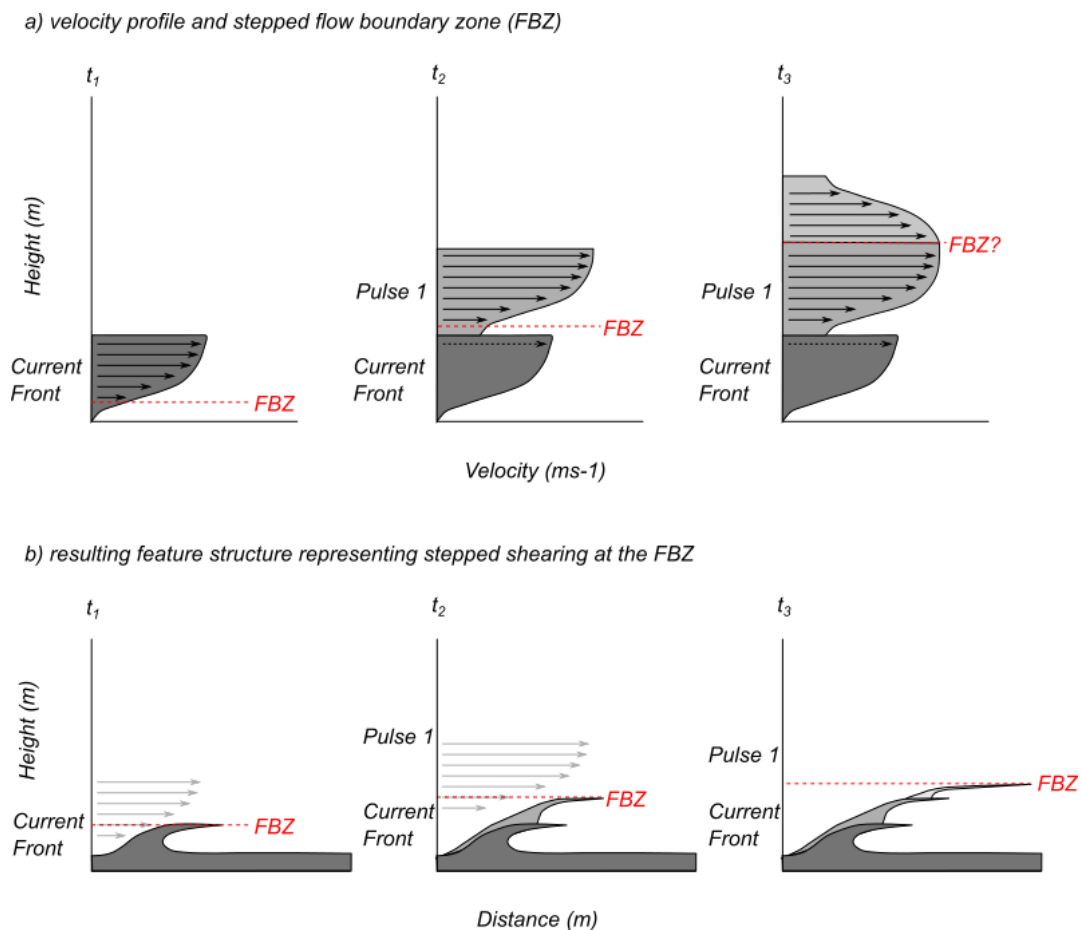


Figure 6.9. Conceptual model showing the stepped flow boundary zone caused by unsteady, multiphase shearing episodes. Pulses are "energetic episodes" such as an increase in velocity in the current. a) Velocity profile and the stepped flow boundary zone, b) Resulting feature formation which represents stepped shearing at the flow boundary zone. t_1 , t_2 and t_3 are different points in time. At t_3 , velocity is thought to be sustained, unsteady or to decrease as the final current deposition takes place. The current velocity profiles are based on Smith et al. (2023).

6.4.6 Extent of Remobilisation

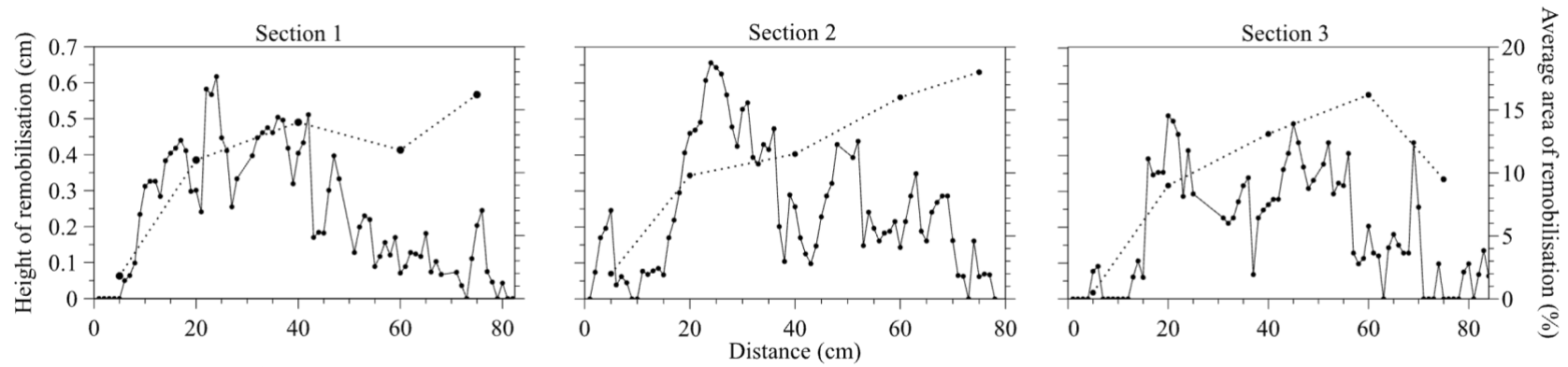
Sedimentary features that clearly recorded interaction with the substrate (by colour difference) are interpreted as remobilisation features. The height of remobilisation was measured from the top of the substrate to the top of the largest feature at 10 mm intervals across the flume. The average height of each block was calculated, and the percentage of remobilisation within the whole of the overall deposit was calculated (Fig. 6.10).

At 0 wt.% substrate moisture, the height affected by remobilisation within the deposit decreases along the length of the flume (solid line, Fig. 6.10a). The height of remobilisation is low from 0 to 15 cm and then peaks in the middle of the down-current blocks (20 to 30 cm). This is thought to be due to initial substrate erosion, where fewer features are formed (Fig. 6.5) before depositing them as the current loses energy down-flume (30 – 80 cm).

In sections 1 and 2 (Fig. 6.10a), the area of remobilisation (dotted line (%), Fig. 6.10) increases with distance along the flume. This is due to the current deposit thinning out in distal areas but still forming features, resulting in a relative increase in the area of remobilisation.

The 2.5 wt.% results show that the height of features fluctuates with no systematic change across the flume (Fig. 6.10b). This is due to the lack of stepped or elongated features within the deposit (Fig. 6.6). Instead, the features are predominantly isolated clumps and small flame-like features. The area of remobilisation (%) increases with distance down-flume in sections 1 and 2 and, similarly to the dry substrate, this is thought to be due to current deposit thinning whilst still forming features of the same height (Fig. 6.10b). In section 3, the area of remobilisation increases and then decreases to 0 % in the final block (50 – 70 cm). The height of the current is so thin here, due to it being the maximum extent of the current, that no remobilisation occurred.

a) Flume run 1: 0 wt.% substrate



b) Flume run 2: 2.5 wt.% substrate

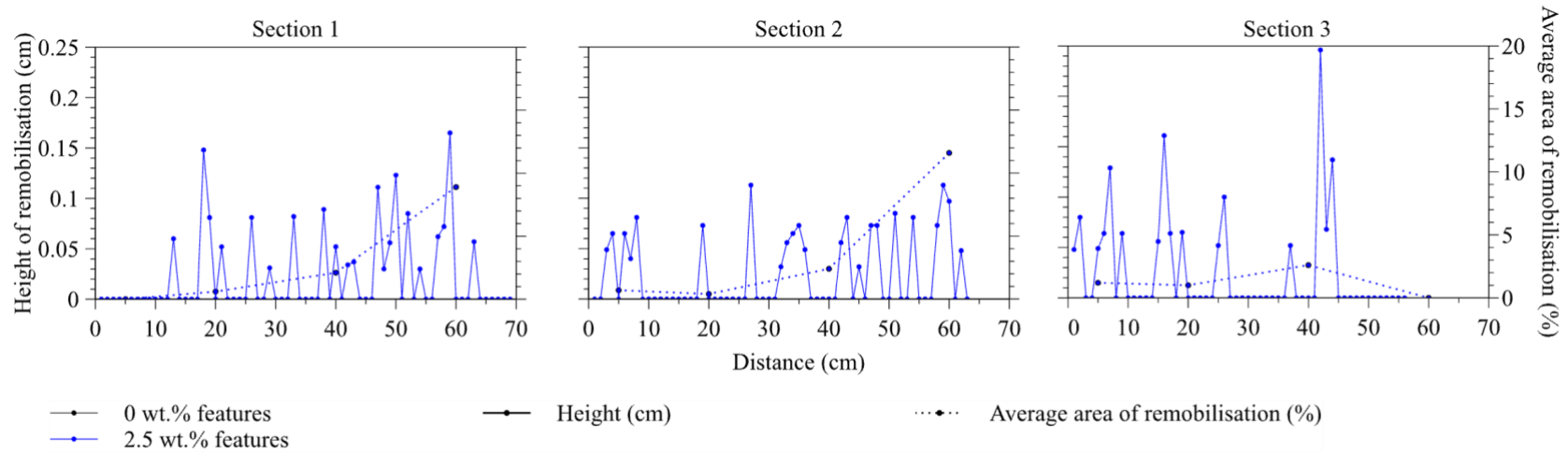


Figure 6.10. Remobilisation height of features (from the top of the substrate to the top of the highest feature) and average remobilisation are (%) against down-flume distance (m) for a) flume run 1 at 0 wt.% substrate and b) flume run 2 at 2.5 wt.% substrate. Section q Section 1 is at the side wall, section 3 is at the flume centreline, and Section 2 is the divisor between the two.

6.5 Discussion

This discussion first identifies the key factors controlling the formation of stepped multiphase sedimentary features in dry (0 wt.% moisture) substrate conditions, as shown in Figure 6.5 (Supplementary Material 6C). Analysis of these features seeks to better understand the role of velocity, pulses and shear behaviours at the flow boundary zone. The discussion then focuses on how changes in substrate moisture affect current mobility, substrate strength and the formation of sedimentary features. Finally, these findings are applied to real-world applications of geophysical currents, specifically in understanding the implications for stratigraphy generated by pyroclastic density current (PDC) deposits.

6.5.1 Dry shear structures and multi-stepped shearing

Stepped features have formed from current-induced erosion and the remobilisation of substrate material. In this section, we use Equation 6.1 from Rowley et al. (2011), as adapted from Kundu and Cohen (2004), to calculate basal velocity at the current-substrate interface. This equation determines the critical threshold required for the formation of instability features at the boundary between two materials (i.e., a current and a substrate). Using the lengths of the features, the basal velocity can be derived at the time of deposition, which in turn provides insight into the characteristics of the flow boundary zone. Following the methodology of Pollock et al. (2019), the length of the recumbent flame features is used instead of wavelength:

$$v_1 - v_2 \geq \sqrt{\frac{g\lambda}{2\pi} \left(\frac{\phi_2}{\phi_1} - \frac{\phi_1}{\phi_2} \right)} \quad (6.1)$$

where λ is the length of the features in the deposit used to calculate basal velocity at the shearing boundary (i.e., behind the current front); ϕ_1 is the bulk density of particles in the fluidised current (1439 kg/m³); and ϕ_2 is the bulk density of particles within the substrate (1677 kg/m³). The velocities of the current and substrate are v_1 and v_2 , respectively. As Rowley et al. (2011) suggested, a substrate velocity of 0 m/s (v_2) is assumed. Using Equation 6.1, the minimum basal velocity at the shearing boundary is calculated to be 0.04 to 0.29 m/s for instability features 0.003 to 0.18 (± 0.01) m in length.

6.5.2 Multi-stepped feature formation

Pulses within granular currents can be observed in small- and large-scale analogue experiments (Iverson, 1997; Smith et al., 2018; Rowley et al., 2024). Based on the interpretation of features identified in the deposit sections (Fig. 6.7 and 6.8) and the thickness and velocity profiles, it is determined that flow front erosion and pulses within the current generate multi-stepped features from a rapidly migrating progressive aggradation “step-wise” FBZ (Branney & Kokelaar, 2002). Additionally, the continuation of stepped features in this work that are not seen to be related to flow front erosion or pulses suggest that continuous growth of features may occur during the emplacement of sustained, unsteady currents. The use of coloured, dry substrates permitted the observation of feature formation and preservation.

6.5.3 The effect of adding moisture to the substrate

Moisture was introduced to the substrate to observe the effect of substrate properties (capillary cohesion) on current mobility and feature formation. Previous work (Pierrat & Caram, 1997; Kim & Sture, 2008; Andreotti et al., 2013; LaMarche et al., 2016; Chen et al., 2021; Chapters 3 – 5 in this thesis) demonstrates that moisture affects material strength through interparticulate capillary bonds. Therefore, a loose erodible substrate may have additional coherent strength associated with it when moisture is added (e.g., flames and stringers vs clumps in this work). A drier material is then expected to display increased erosion and remobilisation, an increased volume and a higher run-out distance (Mangeney et al., 2010; Dufrense, 2012; Crosta et al., 2017; Liu et al., 2023).

6.5.3.1 Current mobility

The experimental current travelled a shorter distance over the moist (2.5 wt.% moisture) substrate compared to the dry (0 wt.% moisture) substrate. The decrease in runout distance is attributed to the presence of capillary bonds forming in-between particles in the substrate, which would increase the surface tension of the substrate (Pierrat & Carram, 1997; Mohseni, 2008). The increased surface tension could lead to greater basal friction experienced by the current, potentially explaining the reduced runout distance. Despite the increased run-out distance in the dry (0 wt.% moisture) substrate, the moist (2.5 wt.% substrate) flow front velocity overall shows a faster velocity (1.6 m/s). This is thought to be due to potential initial by-passing of the current over the wet substrate before surface tension effects take place and results in the deposition of the material.

6.5.3.2 Substrate strength

Increasing moisture in the substrate reduces the frequency, height, and length of the features. This is due to the presence of liquid bridges between particles, which increases capillary cohesion and hydrostatic forces (Kim & Hwang, 2003; Kim & Sture, 2008). These forces enhance the substrate's yield strength, making it more resistant to erosion and remobilisation (Walding et al., 2024). Using Equation 6.1, the length of the shearing features was used to calculate basal velocity at the shearing boundary. At 2.5 wt.% moisture conditions, the minimum velocity for instability structures ($0.001 - 0.177 \pm 0.01$ m) to form ranges from 0.02 to 0.1 m/s. This is unexpectedly lower than the values obtained in the dry (0 wt.%) experiments. One possible explanation is the difficulty in accurately measuring flame structures due to their small and often indistinct appearance at higher moisture levels. Alternatively, this may reflect a limitation of Equation 6.1 which may accurately describe elongate flame structures, but, is less applicable where flame structures are ambiguous. In such cases, alternate models such as those used for clast rip-up features, may produce more representative results.

Moisture added to the substrate will also increase the bulk density of that substrate, which may make it more resistant to remobilisation. In order to test the relative control of density, a model was created using Equation 6.1 to test the basal velocity of the granular currents over dry (0 % model, Fig. 6.11) and moist (2.5 % model, Fig. 6.11) substrates, where the density of the moist substrate is $\phi_{2\text{wet}} = 1754 \text{ kg/m}^3$ for a range of simulated shear features of wavelengths from 0-10 cm at 0.1 cm intervals.

Figure 6.11 compares the modelled feature lengths against the modelled velocities. It shows that higher velocities are required to create the same-sized feature wavelengths in a moist substrate than in a dry substrate (Fig. 6.11, blue line and black solid line). Video analysis of the flume experiments completed in this work (Fig. 6.4) were used to calculate minimum and maximum flow front velocities of 0.05 – 0.14 and 0.04 - 0.16 m/s for 0 wt.% and 2.5 wt.% experiments, respectively.

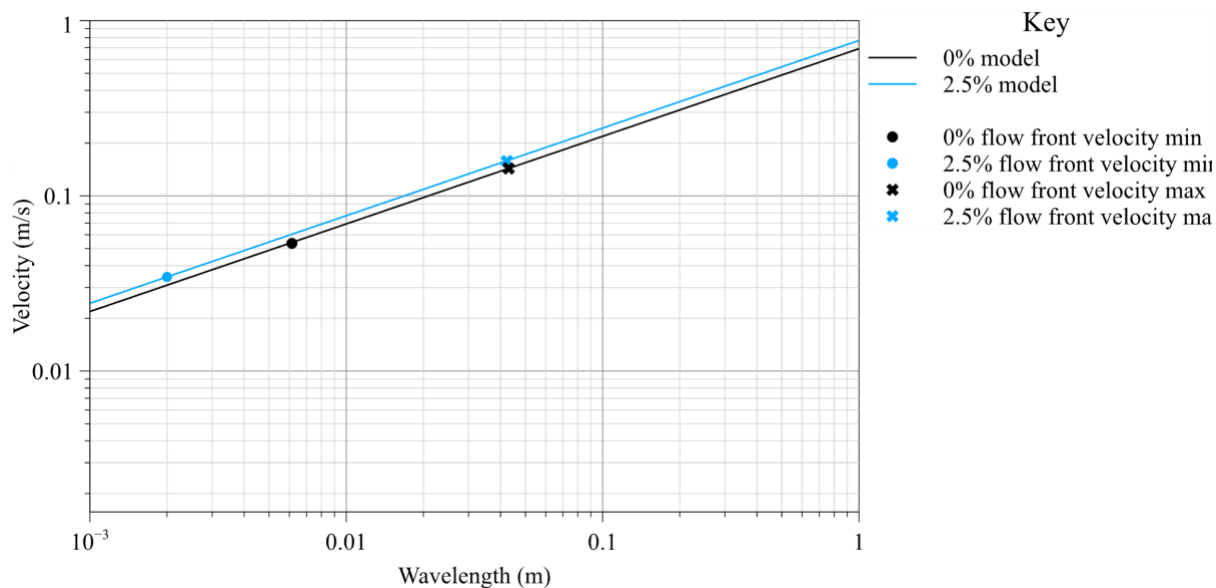


Figure 6.11. Modelled basal shear velocities for currents over dry (0 % model) and wet (2.5 % model) substrates. Simulated features have lengths that range from 0 to 1 m at 0.001 m intervals. Flow front velocities from the flume experiments (min and max for 0 wt.% (black) and 2.5 wt.% (blue) are plotted to show the modelled minimum and maximum wavelengths formed at these velocities.

Using the 0 wt.% flow front velocities calculated from our experiments on the model (black circles and crosses) shows that at 0 wt.% moisture, feature lengths should vary from 0.006 to 0.043 m (Fig. 6.11). Comparing these values to our measured experimental results in the flume sections (0 wt.%: 0.003 – 0.181 (± 0.01) mm) shows that the minimum 0 wt.% feature length falls within the predicted range of the dry model curve. However, our measured maximum dry lengths are significantly higher than what is modelled. This is believed to be caused by the sustained and pulsed current interaction with the dry substrate, which creates a stepped profile as it moves through the current – a feature that is not represented in this model.

Using the flow front velocities calculated from the 2.5 wt.% experiment on the model (blue circles and crosses) shows that at 2.5 wt.%, feature lengths should vary from 0.002 – 0.042 (± 0.01) m in length (Fig. 6.11). However, the modelled lengths are significantly higher from what is observed in the experimental sections (2.5 wt.%: 0.001 – 0.017 m). Firstly, in the 2.5 wt.% sections, long or stepped flame-like features are not present (mainly clumps and small flames). Therefore, this model, which assumes that substrate density controls feature formation, does not explain the experimental observations. Thus, it is likely that capillary-related cohesion, which increases substrate strength, has a control on current-substrate interaction and the formation of the shear features. The absence of the multi-stepped features

in the 2.5 wt.% substrate does not mean that the stepped vertical migration was not taking place (Fig. 6.9) but was merely not recorded in the final stratigraphy.

Experiments in Chapter 5 demonstrated that an increase from 0 to 1 wt.% moisture leads to an increase in yield stress of natural pyroclastic material, increasing the resistance to shear. The model has revealed that moisture is a significant control in substrate-current interaction and influences substrate erosion behaviours.

6.5.4 Application to geophysical flows

Geophysical flows (i.e., debris flows, snow avalanches, pyroclastic density currents) can act erosively when passing over a substrate (Mangeney et al., 2010; Roche et al., 2013 and references therein). Material erosion can be induced by a change in the gradient, the thickness of the beds, the nature of the substrate or by the overriding current dynamics (Branney & Kokelaar, 2002; Jain & Kothiyari, 2009; Mangeney et al., 2010; Baas et al., 2016; Edwards et al., 2021; de Haas et al., 2022) (Section 6.3). As material from a substrate is eroded, it can be entrained and incorporated into the current. This increases the volume of the flow (McCoy et al., 2012), which in turn affects current behaviours (Mangeney et al., 2010) and leads to the reworking of stratigraphic packages (Rowley et al., 2011).

In this work, features can be observed due to the contrast between the substrate and current (e.g., dyed ballotini) and the relatively short-lived, thin experimental currents produced. However, in natural geophysical currents, features may not be observed due to homogeneity between the substrate and the current, waxing or waning in the current, or due to continuous and longer-lived shearing, leading to their thinning and eventual removal (Pollock et al., 2019). Nonetheless, this work has captured unique processes at the current-substrate boundary, potentially having significant implications for our understanding of fluidised currents over dry and moist substrates. Here, the implications of this work for pyroclastic density currents (PDCs) are explored.

6.5.4.1 Implications for Pyroclastic Density Currents

In Chapter 5, a hypothesis was proposed that the preservation of ash layers in volcanic stratigraphic sequences (such as the markers of PDC hiatus) depends upon the material strength, which is shown to be controlled by moisture. Moisture can be introduced into a PDC through pre-eruptive conditions (Wilson et al., 1986; Morrissey & Mastin, 2000), atmospheric conditions (Diaz Vecino et al., 2023), bodies of water (Cole et al., 1998, 2002; Darteville et al., 2002), saturated substrates (Wilson, 1980; Brown & Branney, 2013) and

vegetation. Ash- and moisture-rich deposits (e.g., the presence of accretionary lapilli or ash pellets; Brown et al., 2010), can mark critical delineating stratigraphy, such as hiatus layers in flow units. These hiatus layers are essential stratigraphic units for reconstructing eruption activity and are crucial for developing a complete record of PDC frequency and the sequences of stratigraphic events (Dowey et al., 2024).

The experiments completed within this work use analogue flume models to simulate these processes, albeit on a small scale. Results have shown that moisture in the substrate can reduce current runout, erosion, and remobilisation. Consequently, this also leads to the inhibition of more complex feature formation as capillary cohesion reduces substrate erosion and remobilisation. This relationship has identified that moisture is a primary control on current velocity and deposition and supports the hypothesis of moisture-affected layer preservation described in Chapter 5.

In dry substrates, flame features are elongated and stepped, resulting from the sustained current and subsequent pulses. This work has enabled the “mapping” of these stepped features, alongside flow thickness and velocity data. This highlights how energy changes within the current manifesting as pulses, are important in controlling erosional and depositional processes at the FBZ.

6.5.4.2 Implications for the flow boundary zone

The granular currents in this work are envisaged to have deposited as per the granular flow FBZ model, where clast concentration and interaction are high, with intense shearing at the FBZ (Branney & Kokelaar, 1992, 2002) (Fig. 6.12a). However, the model by Branney and Kokelaar (2002) considers a substrate formed from an aggrading, depositional current and neglects the consideration of a pre-eruptive (i.e., a PDC moving over an old lava deposit, for example) or syn-eruptive formed substrate (i.e., an ash fall, or ash pellet substrate formed during a brief hiatus in PDC activity).

Where the substrate and overriding current are the same or similar (e.g., the substrate and current are both ballotini in this work), the concentration profile of the material (Fig 6.12a) will be the difference between the loose substrate and the fluidised current. However, this work has shown that the presence of moisture in the substrate can create a sharp rheological boundary by increasing the shear strength of the substrate. Therefore, when current conditions are kept the same (such as Flume Run 1 and 2 in this work), any changes at the

FBZ will be a result of the substrate (“dry” versus “wet”) and not only should concentration and velocity be considered in FBZs (Fig 6.12), but also the substrate conditions. For instance, if we take a granular-flow dominated FBZ with a dry, loose substrate, there will be a sharp rheological interface and a gradual decrease in velocity near the bed (Fig. 6.12a). Here, variations at the FBZ may result in the percolation of smaller clasts and the upper and lower areas of the FBZ will be similar in nature (Branney & Kokelaar, 2002). Furthermore, in unsteady conditions, this may lead to the upward or downward migration of the FBZ over time (Fig. 6.12a), where downward migration is considered erosion and upward migration deposition. If the same scenario is repeated but the substrate is changed by adding moisture, the FBZ is restricted by the strength of the substrate, therefore perhaps inhibiting the downwards (erosional) movement of the FBZ (Fig. 6.12b).

In both dry and moist scenarios, the FBZ is influenced by basal shear, concentration and rheology of both the current and the underlying material. This work highlights the importance of substrate in the FBZ model, in inhibiting erosion or deposition, which has previously been neglected in the literature. In volcanic stratigraphy, this may result in the removal or preservation of important hiatus layers in flow units. Changes in the FBZ will result in changes in lithofacies, for example, the formation or not of sedimentary features as observed in the experiments over different substrates, resulting in a misinterpretation of the current conditions at the time of deposition. This work demonstrates that whether a gas-fluidised current deposits, by-passes or erodes is controlled by an interplay between substrate shear stress and current conditions (Fig. 6.13), similar to that understood for turbidity current-substrate interactions (Jain & Kothyari, 2009; Verhagen et al., 2013; Baas et al., 2016). For erosion to occur in a dry substrate environment, the basal shear stress of the gas-fluidised currents needs to exceed the critical shear stress of the substrate (Fig 6.13a, dashed line). Simply, where it exceeds the critical shear stress, the material is eroded (Fig 6.13a) and where it does not exceed the critical shear stress, the material is deposited (Fig 6.13a). It is important however to recognise that erosion and deposition have specific thresholds. Even when shear stress remains below the critical shear stress, material can still be transported through traction, saltation and suspension (Pahtz et al., 2020). Where these forces are balanced (i.e., not eroding nor depositing) then by-passing is likely to occur (Fig 6.13a). A moist, coherent or lithified substrate will increase the gradient of the relationship (Fig 6.13b, dashed line), where larger forces in the current are required to overcome the critical shear

stress. This results in erosion being suppressed at the equivalent current conditions and more potential for by-passing of the current (Fig 6.13b).

By-passing of a current exists between erosion and deposition, where the shear stress of the currents are not of a value that can either deposit or erode. By-passing in PDCs is seen where slopes are steep, and dynamic material cannot settle past its natural angle of repose (as in Scott et al., 1996; Edwards et al., 2019). However, by-passing on shallow slopes (3° , Brown & Branney, 2004) has been seen in large ignimbrite sequences, resulting in ~ 20 km of by-passed material. Our work demonstrates that an erosional current may not be able to erode underlying substrates, depending on substrate strength. In stratigraphic sequences this may result in a “wet” substrate being preserved or thinned (through by-passing or resistance to

erosion). This has large implications for the interpretation of eruption frequency and volume, which are critical factors in the assessment of volcanic hazards.

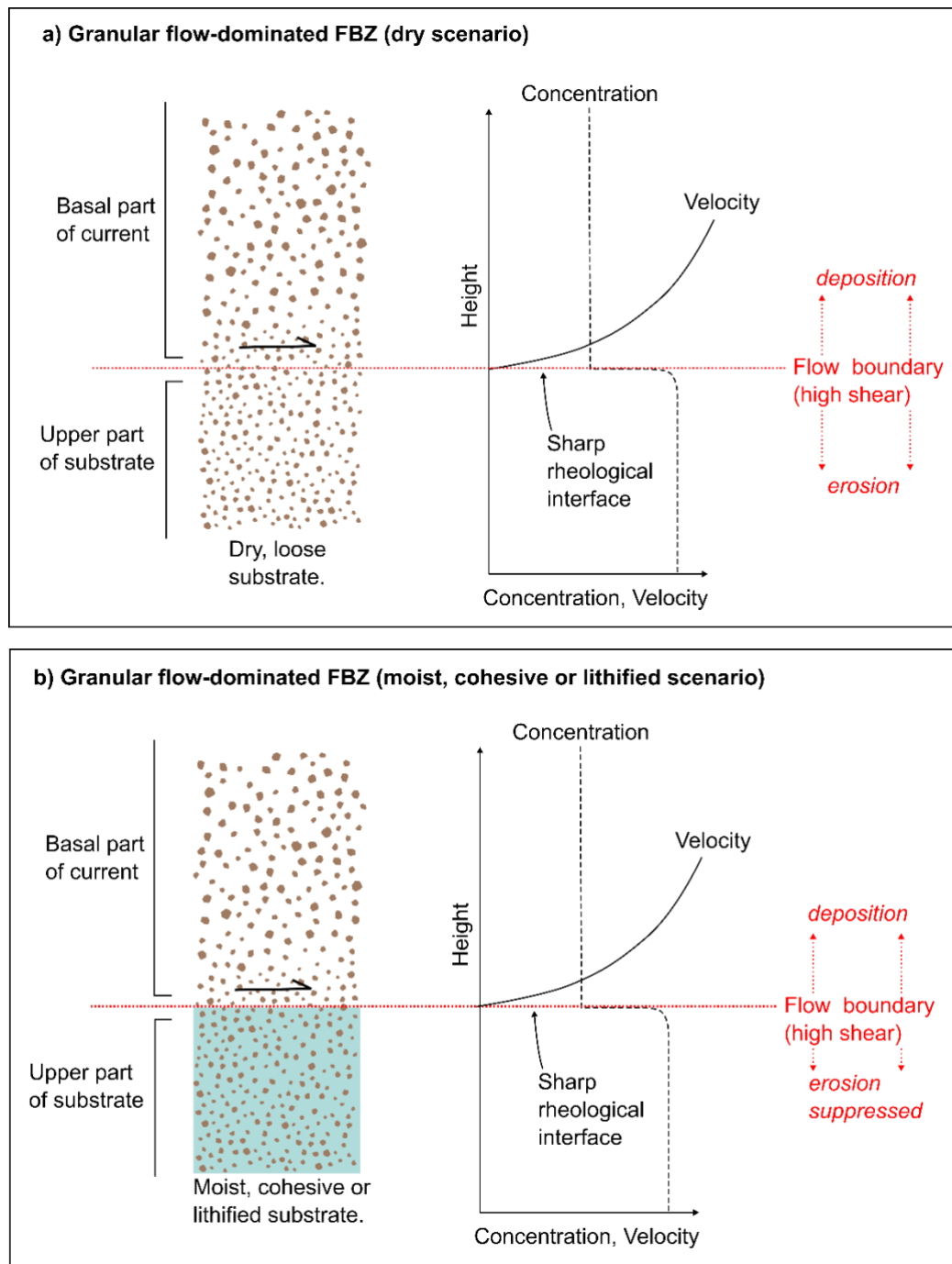


Figure 6.12. Schematics of a) a dry, loose substrate from Branney and Kokelaar (2002) and a b) moist, cohesive or lithified substrate from this work, with indicative concentration and velocity profiles. The FBZ (red dashed line) can migrate vertically, reflecting erosion and deposition at the current-substrate boundary. In b) erosion into the underlying substrate is suppressed due to the associated shear strength of the substrate.

Although this work focuses on the effect of moisture, this model can be used as a proxy for a variety of substrate variations that may be present (i.e., pre-eruptive substrates (lithified

pyroclastic material, lava deposits, saturated sand) or syn-eruptive substrates (welded deposit, ash-, pumice-, pellet-fall layers). The use of analogue models has helped to uncover these key processes and missing details that are currently absent in the flow-boundary zone paradigm of PDCs (Branney & Kokelaar, 1992, 2002). Future work should use field studies alongside analogue and numerical models to better constrain these behaviours to enhance understanding of PDC dynamics and resulting stratigraphic deposits.

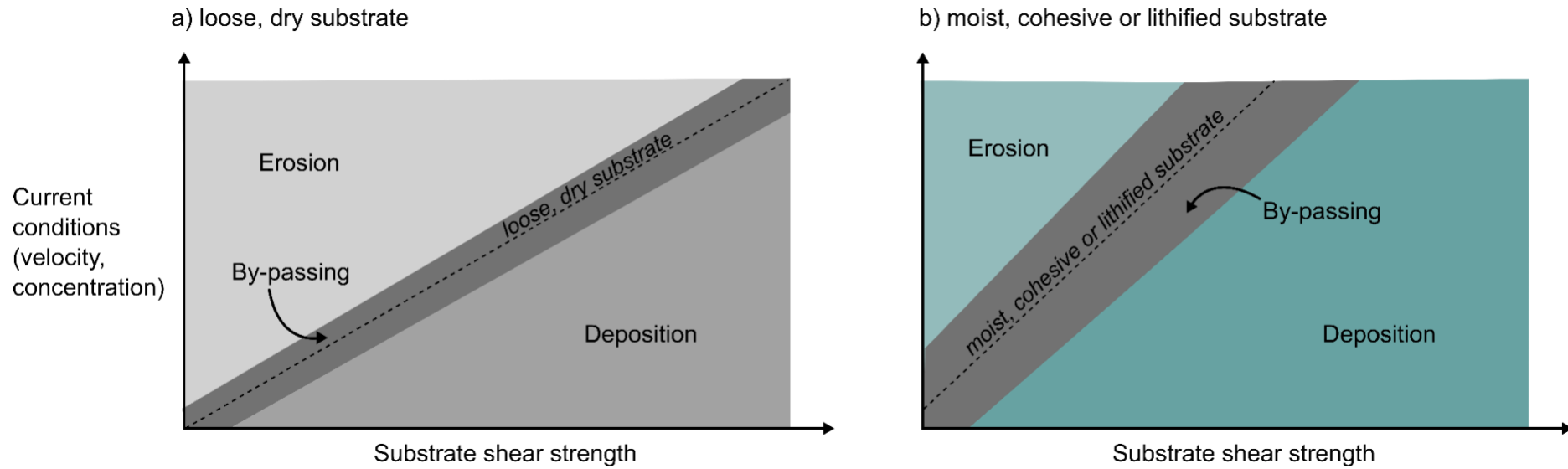


Figure 6.13. The control of critical shear stress on erosion and deposition by a current in a) loose dry conditions and in b) moist, cohesive or lithified substrate.

Supplementary Material for Chapter 6 can be found in Appendix D.

Supplementary Material 6A – Particle size analysis method and material properties of ballotini material.

Supplementary Material 6B – Methodology for dyeing ballotini.

Supplementary Material 6C – Flume Run 1 (0 wt.% substrate) a) section 2 and b) section 3.

Supplementary Material 6D – Current-substrate contact at a) the flume side-wall and b) flume center.

Supplementary Material 6E – Flume Run 2 (2.5 wt.% substrate) a) section 2 and b) section 3.

Supplementary Material 6F – Videos of Flume Run 1 and 2.

Supplementary Material 6G – Flume Run 1 pulse initiation, propagation and overtaking of flow front.

Chapter 7 Discussion and Conclusions

This thesis aimed to determine the influence of moisture on pyroclastic density current (PDC) dynamics and deposits to improve understanding of volcanic stratigraphy. It explored how the presence of moisture on a suite of pyroclastic and analogue materials fundamentally impacts their dynamic (i.e., in-motion) and static (i.e., stationary deposit) behaviours, drawing on experimental and field approaches.

The results show that increasing moisture content decreases flowability and fluidisation of pyroclastic materials during dynamic experiments, which changes flowability properties from “excellent” to “poor” under these conditions (**Chapter 3, Chapter 4**). Additionally, moisture increases the overall yield stress and shear strength of pyroclastic materials to varying degrees, which may impact the strength profiles of wet pyroclastic deposits (**Chapter 5**). This has implications for the erosion or preservation potential of hiatus layers in flow-unit stratigraphy (**Chapter 5**) and the transport and remobilisation of material (**Chapter 6**).

This discussion chapter draws upon results from **Chapters 3 to 6** to answer the thesis research questions posed in **Chapter 1**, which have implications for pyroclastic material behaviours (RQ1), stratigraphic architecture (RQ2, RQ3, RQ4) and flow dynamics (RQ5) :

RQ1: What controls the behaviour of dry and wet pyroclastic material in both static and dynamic environments?

RQ2: How does moisture and material type affect deposit heterogeneity and architecture?

RQ3: What influences the preservation or erosion of substrate materials; particularly those that may mark PDC hiatus?

RQ4: How do changes in moisture result in substrate entrainment or remobilisation within a flow?

RQ5: How do changes in moisture within the substrate affect flow dynamics (i.e., velocity, run-out, mobility)?

The broader implications of these findings are then considered, along with suggestions for areas of future research.

7.1 Implications for the behaviour of wet and dry pyroclastic materials

Chapters 3, 4, and 5 data show how moisture affects the static friction coefficient, shear strength, angle of internal friction, density, minimum fluidisation velocity, and yield strength of a pyroclastic material. Here, I collate the results and discuss the main controls that govern these behaviours in static and dynamic conditions with and without moisture, answering research question 1: *What controls the behaviour of dry and wet pyroclastic material in both static and dynamic environments?*

7.1.1 Static environments

In a static environment, behaviours of granular material, such as pyroclastic material, are strongly influenced by particle characteristics (particle size, shape, fines) as well as moisture content (i.e., capillary cohesion). These factors play a critical role in determining the material's shear strength and internal friction angle, which can be determined by shear stress experiments and static angle of repose (SAoR). Shear strength is an important parameter in understanding the strength of a deposit, resistance to external forces and resistance to the movement of particles.

For dry pyroclastic material (0 wt.% moisture), the friction coefficient and shear strength of pyroclastic material have been found to be strongly correlated to particle shape and fines content (Fig. 4.3, 4.9, 5.8). These characteristics contribute to increased packing and density (Fig. 7.1); which both contribute to an increase in shear strength (Kwan & Huen, 2014; Vahidi-Nia et al., 2020). This relationship is further supported by the principal component analysis (PCA) results in *Chapter 4*, where dry pyroclastic material behaviours were correlated to particle size mean, sorting, fines content and density (HR and CI). In this dry state, the dominant interparticle forces will be van der Waals.

The incorporation of moisture results in an increased angle of internal friction for some materials, with the most significant change observed in high fine-content material (Fig. 4.7, *Chapter 4*). In *Chapter 5*, the experiments showed that peak shear stress increased by increasing normal stress and moisture content in some materials. Drop experiments from *Chapter 5* showed that at certain moisture contents (~25 to 70 wt.% moisture addition), a material with a small mean particle size and high fine content would result in shear thickening behaviours when subjected to a sudden impact. This results in the stiffening of the material to deformation and may be of noteworthy importance for material strength.

Results from the PCA analysis in **Chapter 4** (Fig. 4.9) showed that, at 0.5 wt.% moisture content, the controls on wet pyroclastic material geomechanical behaviour were correlated with particle sphericity, symmetry, and Sauter mean diameter. Additionally, the PCA results showed that increasing moisture from 0.5 to 2.5 wt.% resulted in particle behaviours being controlled by the formation of capillary bonds and, therefore, being less correlated with particle characteristics such as shape and size.

The fine ash fraction of a pyroclastic material is predominantly asymmetrical and angular (Fig. 4.3) and in the presence of heterogeneous particle mixtures (e.g., sorting) will result in increased packing density of the material, resulting in a reduced void ratio (i.e., “how tightly packed the material is”; Chen et al., 2016). Studies have explored the control of packing density on shear strength and have shown, similarly to this study, that fines concentration increases shear strength due to packing density (Kwan & Huen, 2014; Vahidi-Nia et al., 2020). Interestingly, in studies completed by Vahidi-Nia et al. (2020), an increase in packing density increases shear strength and the material's dilation (maximum dilatancy is seen at 85 % packing density). This finding may provide an explanation as to why shear thickening behaviour is seen at different moisture levels between samples and why some samples do not show an increased shear stress at high fines content (FC). For example, in Chapter 3, increased shear stress with the addition of moisture was observed in Taupo 1 (38.9 % FC), Taupo 2 (52.2 % FC) and Brown Tuff (29.3 % FC) but not in the Atitlan samples, which also had a high fines content (66.0 and 40.6 %). If we compare the sorting values of these materials (i.e., the packing density), we can see that both Atitlan samples display a higher sorting index than the other samples (Atitlan 1 = 2.4, Atitlan 2 = 1.5, Brown Tuff = 1.2, Taupo 1 = 1.2, Taupo 2 = 1.0), which may be why no increase in shear stress is observed. Where moisture is added, the finer ash particles will fill voids between larger particles, facilitating the formation of capillary bridges between fine and coarse particles. However, these interparticle capillary bridges may be negatively affected at high fine concentrations, where a significant increase in surface area would essentially “thin out” capillary bridges so much that any forces between particles would be negligible (seen in the decreasing SAoR values with the addition of moisture, at > 52 % fines in Fig. 4.7). The results from **Chapters**

3, 4 and 5 demonstrate how fine content and moisture are crucial in enhancing the cohesion of pyroclastic material and, therefore, being the **main controls on material strength**.

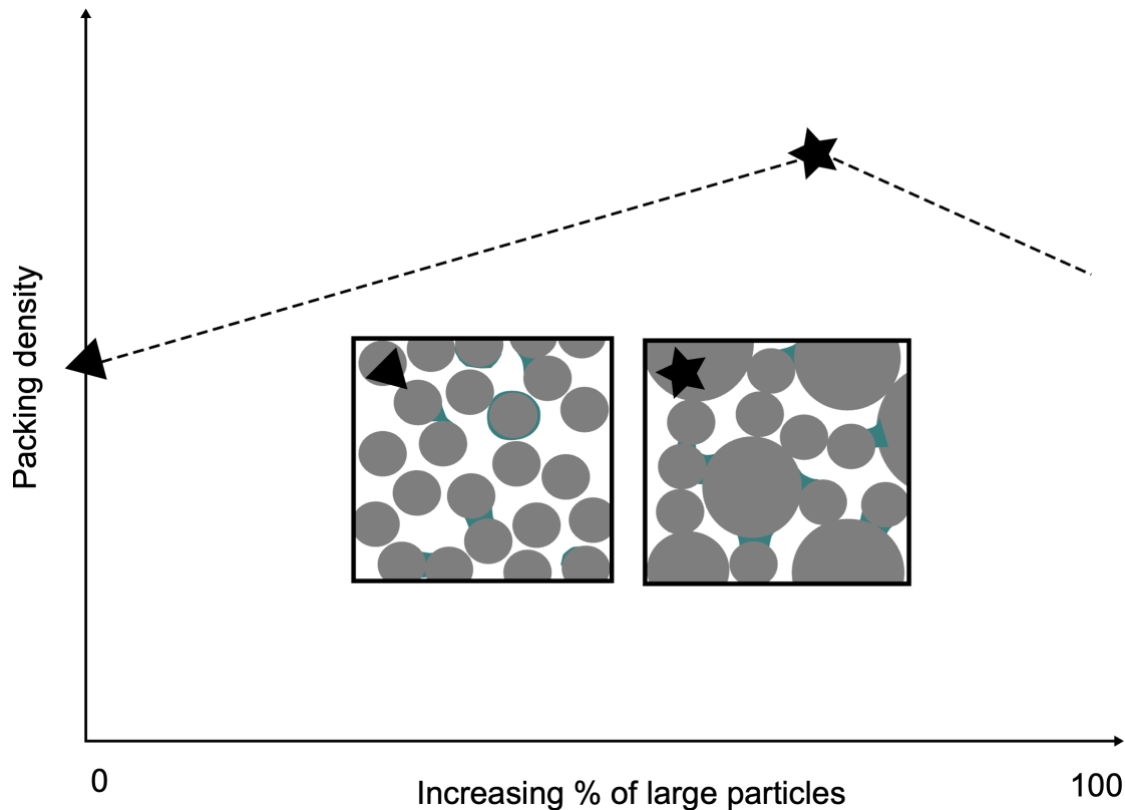


Figure 7.1. Schematic showing the maximum packing density of pyroclastic material with increasing percentage of large particles with small volumes of moisture, as inferred in this work (adapted from Shakor et al., 2022)

7.1.2 Dynamic environments

In a dynamic environment, the behaviour of granular materials is influenced not only by particle characteristics and moisture content but also by external forces like gas flux, which drives fluidisation, an important feature in pyroclastic density currents. Experimental techniques such as bulk tapped density (BTD) and dynamic angle of repose (DAoR) can be used to assess a material's “flowability” (i.e., how easily the material will flow). Additionally, fluidisation experiments, where an upward flow of gas supports granular particles, can provide valuable insights into how easily the material transitions into a fluid-like state. This can determine the fluidisation behaviour of the material and allow a better understanding of the fluidisation of material in dynamic conditions.

In dry (**0 wt.% moisture**) **dynamic environments**, flowability and fluidisation are controlled by geometric mean particle size and fines content (*Chapters 3 and 4*). Flowability is determined from the Hausner Ratio (HR) and Carr's Index (CI), where the HR determines the packing of material, and the CI measures the strength and compressibility of a material

(Moondra et al., 2018). HR and CI values demonstrate that the poorer flowability is consistent with an increase in fines content ($> 52\%$, Fig. 4.2). Pyroclastic materials with the best flowability properties are those with low fine content and high sorting values (Fig. 4.2, Table. 4.2). This is consistent with the DAoR results, where small mean particle size and fine content control the dynamic friction coefficient (Fig. 4.3). In the fluidisation experiments, the minimum fluidisation velocity depends on the material's particle size and fines content; in dry conditions, this leads to heterogeneous channelling of coarser material in the lower deposit and bubbling of the finer material in the upper. Materials with the highest fine content (section 4.4.4) exhibited “diffusive cracking”, which is due to the strong interparticulate van der Waals forces forming between particles (Geldart, 1973).

The **addition of moisture** results in significantly different material behaviours. HR and CI values demonstrate that adding moisture to pyroclastic material leads to poorer flowability (Fig. 4.6). Moisture increase results in an increase in DAoR, but this is dependent on up to $\sim 40\%$ fines (Fig. 4.7). Similarly to the dry, static environments (section 7.1.1), this behaviour may be attributed to the material's packing density. At high fines contents, the formation of capillary bonds between particles is negligible due to the increased surface area. The fluidisation experiments show that higher gas velocities are required to fluidise material in wet conditions and in the presence of materials with a high fines content (Table. 4.2). The fluidisation behaviours exhibited by the fines-rich materials are similar to those seen in the “high moisture experiments” but at significantly lower moisture levels and gas velocities (Fig. 4.2). This, however, is not the case for the Atitlan sample, where, under all moisture conditions, there is no significant change in fluidisation behaviour. This is considered to be due to the significantly higher fines content (66.03%) and sorting parameter (2.42) (Table. 4.2), which has completely removed any significant capillary bonds being formed.

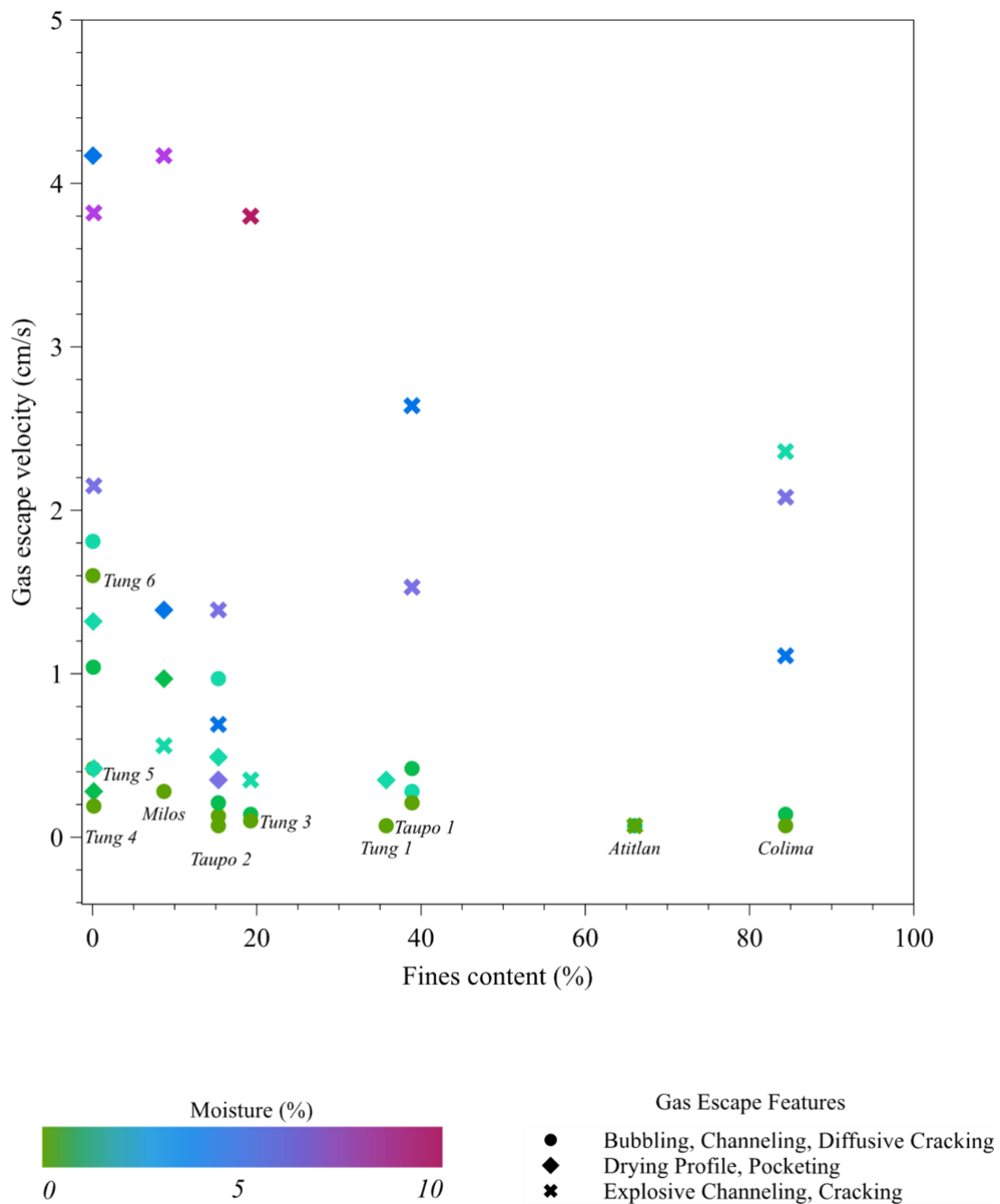


Figure 7.2. Maximum gas escape velocity against fines content for the samples analysed in Chapters 3 and 4. Samples exhibiting “easier” fluidisation behaviours, such as bubbling, channelling and diffusive cracking are shown as circles, those exhibiting “intermediate” behaviours, such as drying profiles and pocketing as shown as diamonds and those exhibiting “difficult” behaviours such as explosive channelling and racking are shown as crosses. Colours show different moisture additions from 0 (green) to 10 (pink).

7.2 Implications for ignimbrite stratigraphic architecture

7.2.1 Deposit heterogeneity

Here, the results from Chapters 3, 4 and 5 answer research question 2: *How does moisture and material type affect deposit heterogeneity and architecture?* Firstly, the role of moisture on individual lithofacies is explored before expanding to the wider implications for deposit architecture.

Lithofacies are characterised in a deposit by their variations in particle arrangements and characteristics. They can be used to gain insight into the conditions at the flow boundary zone during the time of deposition (Branney & Kokelaar, 2002). **Chapters 3** and **4** investigated how moisture and particle characteristics affected the presence of gas escape structures (see sections 3.4.2 and 4.4.4) in a fluidised package of material (Fig. 4.4). Gas escape structures form from a fluid-escape flow boundary zone during deposition from degassing vegetation, lithics, and charcoal, from interaction with a wet substrate or emplacement over a fluidised substrate (Pacheco-Hoyos et al., 2020). Examples in the field have shown elutriated pipes as being elongated pipes (Pacheco-Hoyos et al., 2020) and more rarely have been described as “pods” in Wilson (1980). This work highlights how gas escape structure lithofacies (pip, section 2.5) can vary at different moisture additions (Fig. 4.4) and may explain the variety of shapes of these structures in the field, where all other conditions remain the same.

Moreover, as the underlying material dries through fluidisation, a cohesive cap of wet material can form above the dry deposit. Continued gas influx increases pressure, eventually leading to explosive channelling and cracking (Fig. 4.5). This observation has implications for forming moisture-induced secondary explosive craters (Fig. 3.8), which erupt and change the final architecture of a PDC deposit.

A better understanding of PDC lithofacies is essential for the interpretation of flow behaviours during deposition. This study highlights how variations in lithofacies and moisture contribute to deposit heterogeneity, which is influenced by flow processes (i.e., defluidising deposit and gas movement) and particle characteristics (particle size, shape, density, etc...). Notably, moisture can impact gas escape during the defluidisation and drying of pyroclastic deposits, leading to the preservation of different gas escape structures in the ignimbrite record, which can provide further insights into depositional conditions.

7.2.2 Erosion, preservation and remobilisation

Erosional and remobilisation processes are seen throughout this work, in Chapter 5, in natural field examples, and in Chapter 6, through the use of analogue modelling. The results from all chapters answer research questions 3 and 4: *What influences the preservation or erosion of substrate materials, particularly those that may mark PDC hiatus?* and *how do changes in moisture result in substrate entrainment or remobilisation within a flow?*

The ability of a deposit to erode or not is controlled by current velocity, basal shear stress, and substrate strength (Baas et al., 2016). In Tenerife (Fig. 5.3), an ash layer interpreted to have formed from a dilute PDC shows diffuse, graded contact with the overlying deposit. It was inferred in this work (section 5.4.1.1) that these ash layers were dry, suggesting that they were likely disturbed, remobilised and incorporated into the subsequent layers during deposition. Flume experiments (chapter 6, section 6.4.2) showed that in a dry environment, the material is loose and is able to be incorporated and transported into the flow, showing unique and complex instability features being formed (Fig. 6.5). These multi-stepped features have been shown to form from erosion, subsequent entrainment, and deposition through a rapid upward migration of the flow boundary zone (Fig. 6.9). The dry material substrate is considered to have no additional cohesive strength associated with it. Therefore, any strength of the substrate is likely to be a result of van der Waals forces or variations in fines content and packing density (section 7.1.1).

Throughout this work, the addition of moisture to a material has been shown to change its strength (Chapters 3-6). Therefore, the strength of a substrate must be considered in assessing a moist layer's erosional or remobilisation potential. Investigations using the experimental flume showed that the addition of 2.5 wt.% moisture in the substrate resulted in the shortening of flame features, a sharper sheared contact and the formation of cohesive clumps being remobilised in the overriding currents (Fig. 6.6). This is a direct result of capillary-related strength in the deposit, causing the erosive capacity of the current to be limited (i.e., the downward-moving FBZ is inhibited by the substrate shear strength) and enhancing the preservation of moist layers. In Tenerife, remarkably similar features to the clumps and sheared contacts were observed between high moisture pellet and low moisture accretionary layers (Fig. 7.3, Fig. 5.5 - Feature A).

a) Field localities



b) Experimental examples



Sheared stepped deposit in Flume Run 3 (2.5% substrate, Section 4, Block C.).



1 cm
Clumping and remobilisation of substrate in Flume Run 3 (2.5% substrate), Section 1, Block E.

Figure 7.3. a) Field localities in the Poris ignimbrite in Tenerife showing moist layers of accretionary lapilli (upper left picture) and pellets (lower left picture). For more detail see sections 5.4.2 and 5.4.3. b) Experimental examples completed in Chapter 6, Section 6.4.3 showing shearing (top right) of a cohesive deposit and remobilisation of cohesive clumps (bottom right).

Additionally, in Tenerife, distinct ash pellet layers were seen as “peeling” and, in some cases, showed sharp contacts with overriding lithic-rich facies. In Chapter 6, this was inferred as the shear thickening behaviour of the material, supported by laboratory experiments demonstrating the ability of wet pyroclastic material to exhibit shear thickening properties at high moisture contents (Fig. 5.10). Evidence of these features was not seen in the flume experiments, but this may be due to the relatively low-density contrast between current and substrate and insufficient “impact” forces required to initiate this behaviour. Future work would benefit from further exploration into the rheological changes of wet pyroclastic material under varying shearing rates to better constrain the behaviours of shear thickening in these environments.

The presence of drying profiles was observed to move through fluidised packages of material and varying water additions (Fig. 4.4). This created lateral and vertical variations in moisture and, therefore, variations in strength (see section 7.1.1). If we consider applying the drying profiles to a natural deposit, it can be inferred that an overriding current would be subject to the varying strength profiles in the deposit. This may aid in local erosion – perhaps initiating large scoured surfaces that are present in ignimbrite deposits. This can result in the complete

entrainment and remobilisation of dry ash fall-out layers, which often mark a hiatus in pyroclastic density current activity in dry environments (i.e., dry ash fall). The addition of moisture to the substrate increases the material's strength and, consequently, its shear resistance. Therefore, substrates with moisture in (i.e., aggregate fall layers) are more likely to be preserved. As a result, moisture-rich hiatus layers are more resistant to entrainment and remobilisation by subsequent PDC events and have a preferential preservation potential.

7.3 Implications for flow dynamics

Features formed at the flow boundary zone can provide a unique insight into current behaviours (i.e., velocity) at the time of deposition. In this work, features (e.g., flame-like structures) observed at the flow boundary zone (*Chapter 6*) have been used to gain insight into current conditions during the time of their formation and deposition in both dry and wet conditions, answering research question 5: *How do changes in moisture within the substrate affect flow dynamics (i.e., velocity, run-out, mobility)?*

The current run-out distance from flume experiments completed in this work decreased with the addition of moisture to the substrate (0 wt.%: 1.89 m, 2.5 wt.%: 1.67 m). Interestingly, in the sectioned deposits of *Chapter 6*, stepped features are observed to form in a dry substrate (Fig. 6.5, 6.9), which are interpreted to reflect a migrating, stepped flow boundary zone due to flow pulses and a sustained current. These features are not seen in natural examples, but this is inferred to be due to larger time scales within natural currents, or perhaps, these features are preserved but are indistinguishable from the surrounding material (due to the homogeneity of an eruption in a waxing and waning current or from intense mixing and incorporation of the underlying material into the overriding current deposit). The addition of 2.5 wt.% moisture to the substrate led to the formation of shorter, lower aspect ratio flame-like features and clumps.

Using the length of the flame-like features in both experimental runs allowed the calculation of current basal shear velocity for the formation of the features. In the proposed model (Fig. 6.11), wet conditions required a higher basal shear velocity to form the features in the deposit than in dry, loose conditions.). This is thought to be due to increased basal shear strength in the wet substrate. However, it should be noted that the experimental currents in this work are cold. The addition of high temperatures, as observed in some natural PDCs, may induce “sediment flashing”, where the rapid vaporization of moisture from a wet substrate creates an

upward gas flux and promotes mobility of the current (Wilson, 1980; Branney & Kokelaar, 2002; Brown & Branney, 2013).

7.4 Wider Implications and Future Work

This research has generated a comprehensive dataset from experimental models that enhances our understanding of analogue and pyroclastic materials in dry and moist conditions. The insights gained from this data have the potential to meaningfully advance our knowledge of ignimbrite stratigraphy. This data will lead to a better understanding of the ignimbrite stratigraphic record and inferred behaviours of PDCs, which offers valuable contributions to hazard modelling for risk mitigation. Moreover, this study has provided new insights into the role of moisture in PDC systems, addressing key gaps in our knowledge. These findings are informed by and linked to some broader issues, which are discussed below.

7.4.1 Re-thinking flow units

A flow unit identifies a unit of stratigraphic ignimbrite material used to record the passage of an individual PDC. For example, one flow unit is equal to one PDC moving through that area at that time (Sparks, 1976). Flow units can be delineated by evidence of hiatus, such as pumice-fall and ash-fall layers, clear erosional scours, or compositional variations (Branney & Kokelaar, 2002). Flow unit packages are important to understand as they show the frequency of PDCs during an eruption. However, the “problem” in flow unit stratigraphy is that it does not account for unsteadiness in one individual PDC (Dowey et al., 2024). In sustained eruptions, lateral changes in current runout will wax and wane through time (e.g., increase or decrease in a certain parameter, Williams et al., 2014; Branney & Kokelaar, 2002). Depending on the exposure of the stratigraphic material in the field, a contradictory number of flow units may be seen in proximal and distal locations (Fig. 7.4, Dowey et al., 2024). *Chapters 3 to 6* within this thesis have investigated the control of moisture on ash-rich layers in dry and moist conditions and how the shear strength of material can ultimately result in the preservation, or not, of these key hiatus layers (section 7.1.1). However, a range of parameters will ultimately significantly impact the resulting preservation of hiatus layers. For example, variations in both the substrate (particle size, shape, density, packing, time, thickness) and the current (mass flux and unsteadiness) will all lead to changes at the flow boundary zone, determining whether or not that layer is removed.

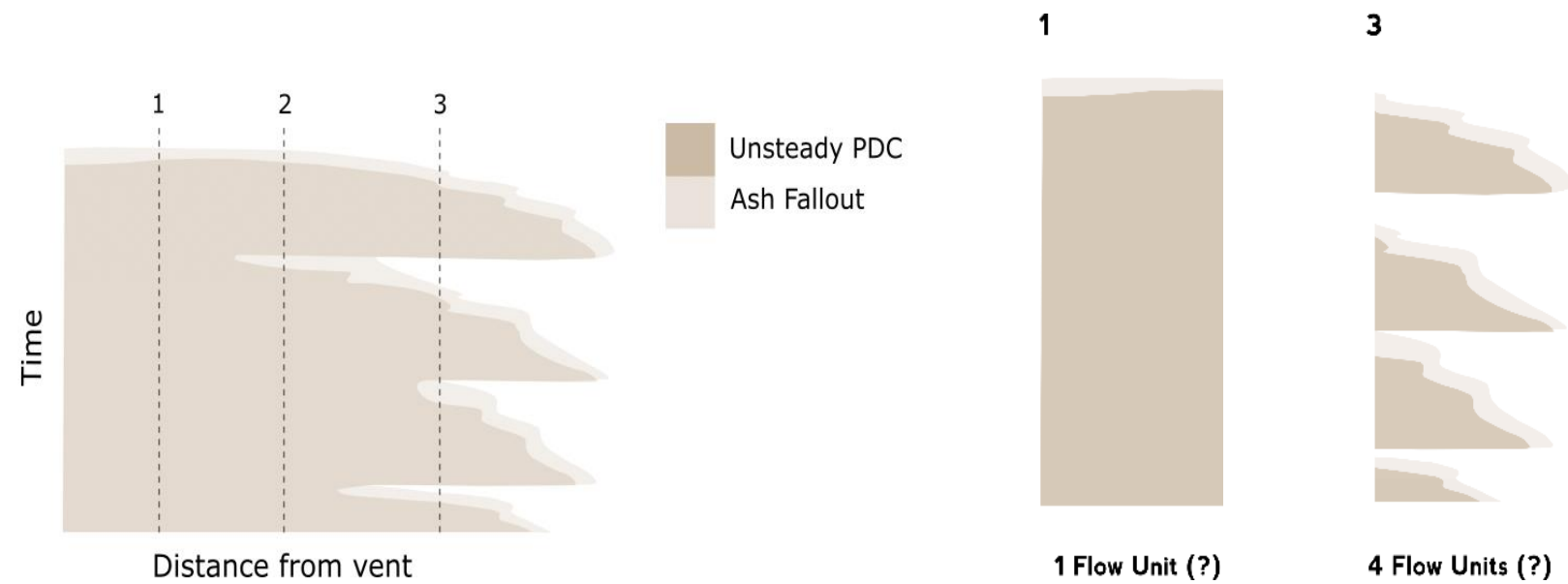


Figure 7.4. Schematic image showing a PDC through time and the resulting flow units that can be interpreted at different locations (1, 2, 3) from the vent. At location 1, one flow unit is recorded. At location 2, two flow units are recorded, and at location 3, four flow units are recorded. Figure adapted from Dowey et al. (2024)

Implications for interpreting flow units

The work in this thesis demonstrated strength variations in pyroclastic material due to moisture and fines. When combined with the issue of waxing and waning currents, as raised in Dowey et al. (2024), this raises the question: *Can we reliably use flow units as accurate PDC frequency recorders?* Somewhat. Flow unit boundaries can only be used as accurate PDC frequency recorders when it is shown, for certain, that the flow has stopped. However, they do not account for changes in any of the aforementioned variables (such as dry or wet conditions, etc.) or *uniformity and unsteadiness* throughout time and space (e.g., waxing and waning in the current). Therefore, it is likely that flow unit estimates (e.g., number of units in pyroclastic sequence) are being severely underestimated in ignimbrite sequences.

7.4.2 Rethinking the flow boundary zone model

The flow boundary zone (FBZ) model describes the aggrading area of the current, which encompasses the uppermost part of a substrate and the lower portion of the current. Changes in current behaviour (i.e., velocity, unsteadiness, concentration) will be reflected by changes at the FBZ (Branney & Kokelaar, 1992, 2002). Through the processes of progressive aggradation, material aggrades (deposits) upwards, and unique characteristics at that location (lithofacies) are a product of the FBZ. Branney and Kokelaar (1992, 2002) pioneered this model by applying it to PDC dynamics. There are four intergradational members, which include: 1) direct fallout, 2) traction, 3) granular and 4) fluid-escape dominated FBZs (see Section 2.5). Importantly, these members capture the FBZ over an aggrading current. That is a PDC in motion is depositing through time, and the location of deposition creates the sharp rheological interfaces referred to in the model (Fig. 7.5 a-e).

Chapter 6 explored the granular flow FBZ model in dry and moist conditions (Fig. 7.5 a, b). In dry, loose, environments, the FBZ is free to move upward and downward depending on the current controls (e.g., velocity or concentration). However, the presence of a moist, coherent substrate creates a sharp rheological boundary. This moisture-induced strength means that the downward movement of the FBZ is now limited to the strength and capacity of the substrate. Here, I explore two other end-members (traction shear and fluid escape dominated) of the FBZ model and apply the same theory of the presence of a more shear-resistant substrate. Fall-out dominated FBZ is not explored as these are not erosional processes and are not discussed further.

The tractional-dominated FBZ in Branney and Kokelaar (2002) shows a sharp interface between the (dry, loose) substrate and the current. Particle concentrations are low, and interactions are dominated by fluid turbulence. Shearing causes saltation, lifting, dragging, sliding and rolling of particles before deposition, and turbulence can lead to selective entrainment and segregation. The resulting deposits are “pyroclastic surge” type deposits which form bedforms, stratified and cross-stratified deposits. The concentration profile will remain unchanged; however, the velocity profile will exhibit a velocity of zero at the moist, shear-resistant static bed and will increase upward into the overriding traction layer (Fig. 7.5d). The presence of moisture in the substrate will cause more rapid deposition from moist adherence, and therefore, this may result in bedforms or stratified deposits not being recorded. Additionally, if the current cannot overcome the strength of the substrate, then erosion and entrainment will be suppressed.

The fluid escape-dominated FBZ, as described by Branney and Kokelaar (2002), shows no sharp rheological interface between the depositing substrate and the basal part of the current. Here, shear is low and depositing particles maintain an upward movement of gas, which supports the particles within the lower current. The deposition of particles will be due to particle interlocking from a degassing deposit (Fig. 7.5 e). Again, if the substrate is changed (moist, cohesive, lithified), a sharp rheological interface will be formed and erosion suppressed (Fig. 7.5 f).

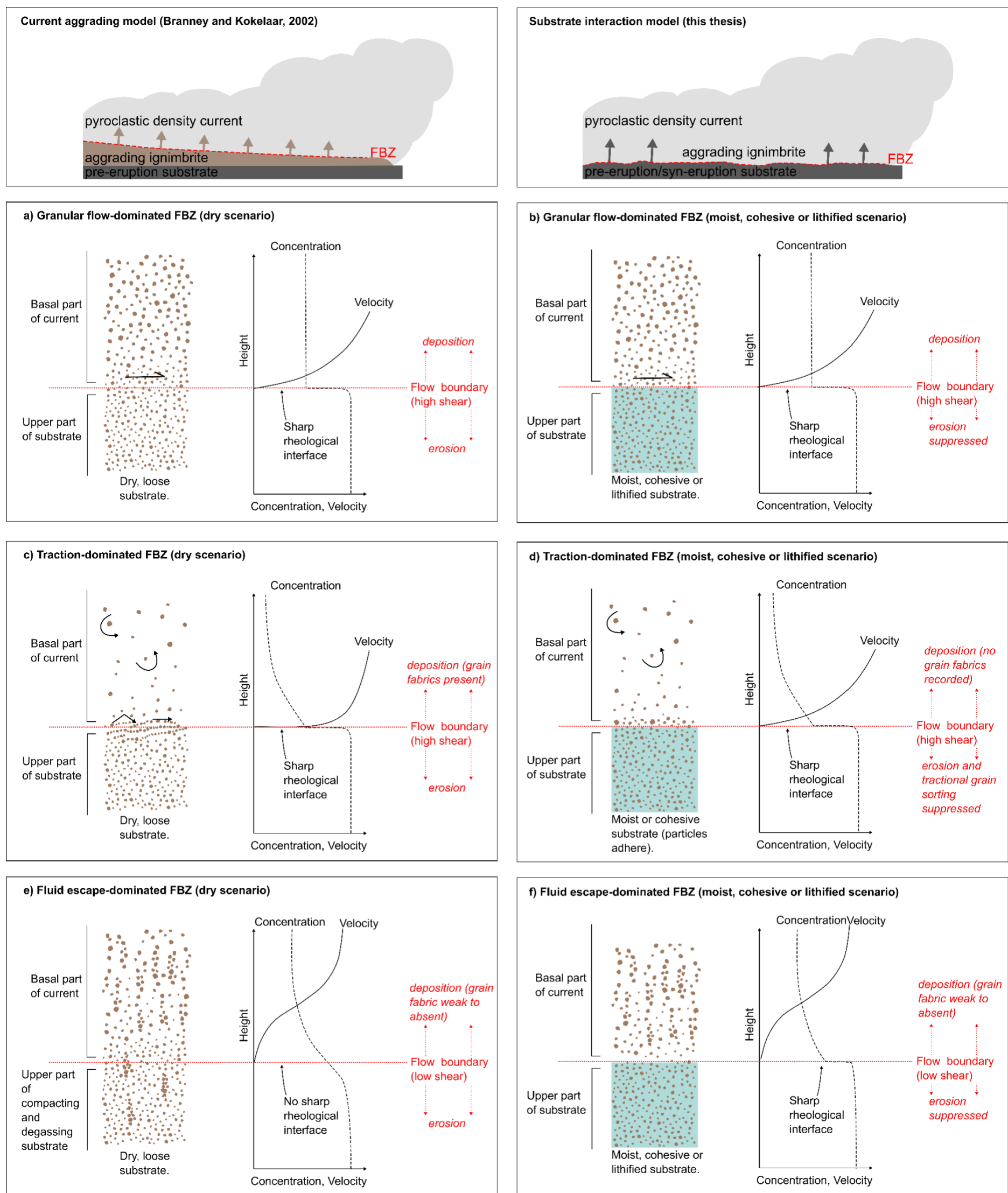


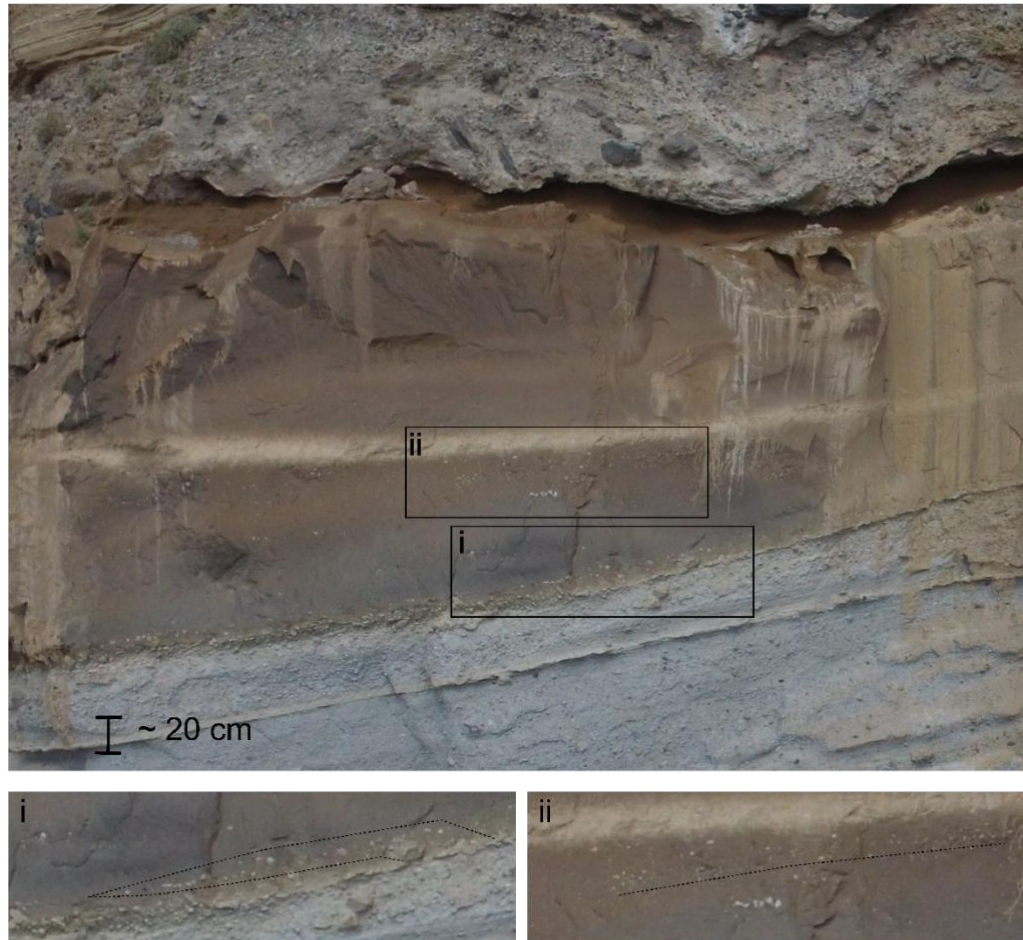
Figure 7.5. Comparison of the FBZ as presented in Branney and Kokelaar (2002) and interpreted in this thesis. a) granular flow-dominated FBZ with schematic concentration and velocity profiles with a dry, loose substrate and a b) moist, cohesive or lithified substrate from this work. c) a traction dominated FBZ with schematic concentration and velocity profiles with a dry, loose substrate and a d) moist and cohesive substrate, e) a fluid escape dominated FBZ with schematic concentration and velocity profiles with a dry, loose substrate and a f) moist, cohesive or lithified substrate. The FBZ (red dashed line) can migrate vertically, reflecting erosion and deposition at the current-substrate boundary.

Although this work has focused on moisture-induced strength, this can apply to pre-eruptive substrate strength (i.e., lithified rock, large changes in surface roughness, density, particle packing, vegetation) and syn-eruptive substrate strength (i.e., variations in welding, cohesion, coherence which are ongoing during a PDC eruption). Moisture may lead to adherence of particles to the substrate, suppressing fabric grains being formed (Fig. 7.5b), but the same behaviour will not be applicable to where a substrate has been lithified, for example. This process has confirmed the need to reassess FBZs to encompass both the substrate and the current. Additionally, although here I have discussed these three FBZ models in detail, it should be noted that these are gradational into each other and will naturally shift into one another depending on current and substrate behaviour at that point in time.

7.4.3 Understanding PDCs in time and space

Chapter 6 enabled a unique perspective into visualising substrate entrainment and remobilisation down flume in experimental currents. Further analysis of this work could use the slices of current and substrate material to gain a complete 3D architectural analysis of the features formed. Additionally, exploring different parameters could be used to identify behaviours of denser, coarser, more saturated material. Additional fieldwork was undertaken in Lipari, exploring the remobilisation of a pumice fall layer by the Brown Tuff PDC deposit (Lucchi et al., 2022). Compared to the fieldwork in Tenerife, the pumice fall layer is coarser and less dense. In addition to the work in this thesis, additional flume sectioning experiments were completed using a coarser ballotini as the substrate material (380 – 1460 μm , Table. 4.4). A 6 kg hopper load of ballotini (20 -655 μm , Table. 4.4) was used, and the runout was 1.59 m. The sectioned analysis of these deposits showed flame-like features forming at the current-substrate boundary (Fig. 7.6b). For Section 3 (the flume centre), the features were located at 0 to 47 cm distance down-flume and showed a maximum 0.03 cm height of remobilisation. The pumice flame-like features in the field were found to reach a height of 10 cm, and pumice stringers reached a height of 30 cm into the overriding PDC deposit (Fig. 7.6a). This begins to validate the features in the field and highlights the effectiveness of this method used to observe these features.

a)



b)

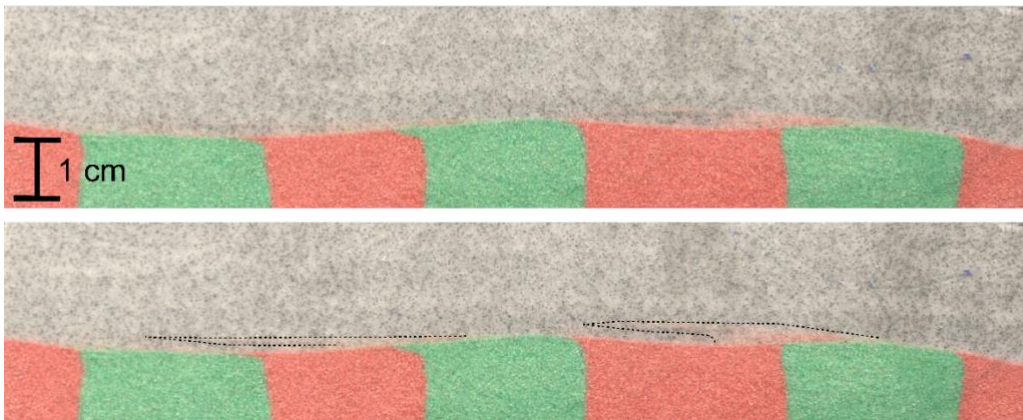


Figure 7.6. a) field images from the Brown Tuff PDC deposit in Lipari, Italy, overriding a pumice fall layer. In the boxes, i) shows stringer features and ii) shows flame-like features remobilised from the underlying pumice fall. The current direction is from right to left. b) Additional flume experiments completed as part of this work. The substrate is dry and loose (0 wt.% moisture) and has been remobilised by the current to form flame-like features in the deposit (dashed lines). The current direction is left to right.

7.4.3.1 Effect of the sidewall in flume modelling

The ability to section the current from the sidewall to the centre allows the discussion of the effect of a sidewall in experimental modelling. Rowley et al. (2011) completed

repeated current-release flume experiments and sectioned the final deposit to reveal features at the current-substrate interface. The features formed showed different degrees of deformation from the sidewall to the flume centre, suggesting that the sidewall was suppressing the current at the boundary and a longer current was occurring in the flume centre. Here, the sidewall effect was measured to be 50 mm within the flume edge.

Experimental studies by Roche et al. (2010), Rowley et al. (2014) and Smith et al. (2018, 2020) completed a similar flume set-up and analogue to the ones described in this work and used a fluidised current. A fluidised current may result in increased pore pressure and, therefore, a decrease in friction against the sidewall (Gilbertson et al., 2008). The flume width is also increased to reduce the effects of the sidewall (Rowley et al., 2011; Girolami et al., 2008). In previous studies (Roche et al., 2010; Rowley et al., 2014), a flume channel width of 10 cm was used. In experiments completed by Girolami et al. (2008), Smith et al. (2018, 2020), and this thesis, a flume channel width of 15 cm is used.

Here, I re-examine the Flume Run 1, Section 1 and 3 slices from Chapter 6 to determine and compare the effect of the sidewall. In Section 1 (Fig. 6.5), features (flame-like, stringers) form from 9.5 to 80 cm down-flume. The height of remobilisation reaches a maximum height of 0.62 cm at 24 cm and a minimum of 0.06 cm at 80 cm (Fig. 6.10). In Section 3 (Supplementary Material 6C), features (flame-like, stringers) form from 16 to 86 cm down-flume, and the height of remobilisation reaches a maximum of 0.51 cm at 20 cm and a minimum of 0.05 cm at 83 cm (Fig. 6.10).

In video and image analysis of the current and deposit, the current is initially channelled along the flume centre, and this is where the maximum run-out is recorded. This would explain the later onset and reduced height of substrate remobilisation, where the current has undergone longer periods of shearing. Additionally, the side-wall where the substrate lies has been modified in these experiments to enable gelatine setting (by the addition of clingfilm and plastic vinyl). Therefore, the sidewall view of the final features is distorted and may be subject to additional frictional sidewall forces during formation.

Considering these factors, the results suggest that the sidewall has been reduced from previous sectioning experiments (Rowley et al., 2011) as a result of fluidising the

current and increasing the flume width. It can be determined that sidewall effects, if present, are taking place < 10 mm from the flume edge.

7.4.4 Secondary hazard generation

Secondary PDCs can form from the remobilisation of previously deposited material due to ongoing volcanic activity (such as magma movement) or by the failure of volcanic material on slopes (Traglia et al., 2024). The results from *Chapters 3, 4* and *5* bring new insights into the role that particle characteristics and moisture content may play in these processes.

One of the key findings of the results in this work suggests that a volcanic flank composed of material with a high percentage of fines will have a steeper dynamic angle of repose, and, therefore, be more resistant to remobilisation and the generation of secondary PDCs. In this sense, there seems to be a “sweet spot” for flank stability, which allows material to form on steeper slopes without collapse. However, the stability of the flanks is not definite. Under certain circumstances and conditions, a relatively “stable” deposit can become potentially hazardous. For example, as discussed in *Chapter 3*, the presence of a cooler or more shear-resistant substrate on top of a still-hot deposit could trigger secondary eruptions, initiating another PDC event.

Moisture content of the deposit material will also play a crucial role in the stability of the loose material on volcanic flanks. With a small amount of moisture, cohesion and strength increases (*Chapter 3, 4, 5*), resulting in further stability of the deposit. However, if the deposit then becomes over-saturated, as shown in *Chapter 5*, interparticulate friction will reduce, initiating lahars. The interplay between particle characteristics and moisture content reveals the subtle controls that influence deposit failure on volcanic flanks.

7.4.5 Flow migration, entrainment and bulking

In *Chapter 3*, the formation of an uneven drying profile ultimately leads to lateral and vertical changes in the strength of the deposit. Additionally, lateral variation in substrate moisture can be influenced by the formation of moist layers (pellet fall-out) or through interaction with pre-existing substrates (saturated sand deposits, for example). As observed in *Chapter 6*, the influence of moisture within the substrate will influence the erosional potential of the current. So, if a dry and moist substrate were laid next to each other, it can be assumed that the current would preferentially erode the weaker, less

resistant “dry” deposit. This may, therefore, influence the shifting of the main body of the current, resulting in thalweg migration. A similar dynamic is seen in fluvial processes, where shifting in the main channel can lead to lateral thalweg migration into riverbanks. Similarly to the theory within this work, the erosional processes at the riverbanks can be controlled by the presence of shear strength (Li et al., 2020).

In PDCs, thalweg migration is thought to occur readily and rapidly throughout time, but variations in topography can constrict the current (Branney & Kokelaar, 2002; Williams et al., 2014; Doronzo et al., 2014). Furthermore, in large ignimbrite sheets or fans, the unsteady nature of PDCs may result in multiple converging or diverging thalwegs. Mapping and understanding these features is complex, especially in large ignimbrite fans, but it could give an insight into ignimbrite architecture and current behaviours. The results from this work suggest that if a substrate is cohesive, then erosion and incision into an underlying substrate may be more constrained into a deeper channel – creating a relatively channelised PDC. Moreover, changes in substrate strength may cause diversion or splaying of thalwegs where preferential erosion of the substrate occur. In comparison, a dry and loose substrate may increase substrate entrainment and subsequent bulking of the material – potentially creating PDCs with higher mobility and longer run-out distances. This has not been explored in this work; however, the results from *Chapter 6* have shown that in the dry (0 wt.% substrate), the run-out distance was 0.22 m longer, and the final deposit displayed significantly higher areas of remobilisation.

7.4.6 What about altered ash?

Hydrothermal and weathering processes can alter the mineralogical, chemical, and physical changes of pyroclastic material and rocks (Pola et al., 2012; Heap et al., 2022). Changes in temperature, water solution, particle composition, pH, and particle size can cause different phases of alteration of pyroclastic ash, resulting in the formation of “clayey ash” that can contain zeolite, smectite, illite and kaolinite minerals (de la Fuente et al., 2000; Quintero et al., 2024). The presence of these minerals in pyroclastic ash may result in water adsorption (e.g., clay swelling, or the formation of a water layer on the surface of these particles (Hatch et al., 2012). In dry conditions, concentrations of clay may result in an increase in shear strength of a pyroclastic ash (Supandi et al., 2019). However, the presence of moisture in a clay-bearing material can lead to a significant reduction in tensile strength (Lu et al., 2024). In a pyroclastic substrate, this may result in plastic deformation and also rheological changes in both the current and

substrate. This has implications for substrate architecture, similar to what has been recorded in this work, and more widely for hazard initiation in hydrothermally altered volcanic areas, such as the remobilisation of pyroclastic material into secondary PDC on volcanic flanks. Future work would benefit from better exploring the behaviour of moisture in hydrothermally altered ash material and the presence of fine clay particles.

7.4.7 Cold, wet PDCs: Limitations and future work

PDCs can become cold, wet and unpredictable from the introduction of moisture (McPhie et al., 1990; Druitt, 2014; Lube et al., 2020). The 1888 Ontake phreatic eruption produced low-temperature ($< 100\text{ }^{\circ}\text{C}$) PDCs that reached a maximum of 6 km from the crater (Yamamoto et al., 1999). Many casualties were fatally burned by the effects of the PDCs, and 461 people died. People were reported to be covered in “wet” ash; interestingly, although buildings and trees were inundated, there was no evidence of burning (Fujinawa et al., 2008). Vesicles in the material matrix, soft-state deformation structures and high-angle deposition of ash suggested that the current was moist and wet (Fujinawa et al., 2008). This is due to a high percentage of water vapour within the flow condensing into droplets. Fujinawa et al. (2008) hypothesized that the phase change from vapour to droplets may have also resulted in a loss of current momentum.

The work in this thesis has highlighted how the incorporation of moisture can result in poor flowability behaviours and rheological changes in pyroclastic material (*Chapters 3, 4 and 5*), which may be fundamental to a better understanding of PDC internal dynamics. Contradictory to the behaviours observed in our results, work by Shimizu et al. (2023) showed that the runout distances from wet phreatomagmatic eruptions increase compared to “dry” magmatic eruptions. This is thought to be due to the vaporisation of water, causing the upward movement of steam, which supports prolonged runout (Dufek et al., 2007; Roche et al., 2021). However, this work only conducted experiments at room temperature, where moisture was incorporated as water, not vapour. Therefore, a limitation of this work is the lack of understanding of the effect of dynamic water phase regimes within these systems. For example, what are the intricate relationships between water, temperature and pressure within a current? How can the presence of capillary bonds affect changes in particle clustering and resulting changes in turbulence, sedimentation and deposition of material?

Future work would benefit from a better understanding of these interactions and resulting particle flow dynamics. This should focus on water phase changes, from liquid to vapour, under varying temperature and pressure conditions. Detailed numerical simulations or physical experiments should also be utilised to analyse thermodynamic and rheological behaviours and interactions.

7.5 Conclusions

This thesis has determined the impact of moisture on the properties of pyroclastic material, examining its effect on both static and dynamic behaviours and its implications for pyroclastic architecture and stratigraphy. Through a combination of fieldwork, experimental analogue modelling and geomechanical testing, this research has investigated how moisture influences the strength of pyroclastic material. This has implications for how important current hiatus layers, or moisture-rich or depleted-layers, may be preserved or not in volcanic records.

A more precise understanding of ignimbrite material's erosional and preservational potential will contribute to more accurate definition, interpretation and understanding of stratigraphic sequences. This research has contributed to a new understanding of the influence of moisture on PDCs, which will allow for improved assessments of PDC architecture and initiate future research that can be incorporated into numerical and hazard models.

References

- Abdullah, E. C., & Geldart, D. (1999). The use of bulk density measurements as flowability indicators. *Powder Technology*, 102(2), 151-165. [https://doi.org/10.1016/S0032-5910\(98\)00208-3](https://doi.org/10.1016/S0032-5910(98)00208-3)
- Agarwal, K. K., & Agrawal, G. K. (2002). Analogue sandbox models of thrust wedges with variable basal frictions. *Gondwana Research*, 5(3), 641-647. [https://doi.org/10.1016/S1342-937X\(05\)70635-3](https://doi.org/10.1016/S1342-937X(05)70635-3)
- Agudo, J. R., Dasilva, S., & Wierschem, A. (2014). How do neighbors affect incipient particle motion in laminar shear flow? *Physics of Fluids*, 26(5), 053303. <https://doi.org/10.1063/1.4874604>
- Agudo, J. R., Illigmann, C., Luzi, G., Laukart, A., Delgado, A., & Wierschem, A. (2017). Shear-induced incipient motion of a single sphere on uniform substrates at low particle Reynolds numbers. *Journal of Fluid Mechanics*, 825, 284-314. <https://doi.org/10.1017/jfm.2017.370>
- Alias, R., Kasa, A., & Taha, M. R. (2014). Particle size effect on shear strength of granular materials in direct shear test. *Journal of Civil and Environmental Engineering*, 8(11), 1048-1051.
- Alidibirov, M., & Dingwell, D. B. (2000). Three fragmentation mechanisms for highly viscous magma under rapid decompression. *Journal of Volcanology and Geothermal Research*, 100(1-4), 413-421. [https://doi.org/10.1016/S0377-0273\(00\)00149-9](https://doi.org/10.1016/S0377-0273(00)00149-9)
- Allen, J. (1984). *Sedimentary structures: Their character and physical basis* (Vol. 2). Amsterdam: Elsevier.
- Allen, J. R. L. (1982). *Sedimentary structures, their character and physical basis* (Vol. 2). Developments in Sedimentology 30B. Elsevier.
- Amidon, G. E., Meyer, P. J., & Mudie, D. M. (2017). Particle, powder, and compact characterization. In *Developing Solid Oral Dosage Forms* (pp. 271-293). Elsevier. <https://doi.org/10.1016/B978-0-12-802447-8.00010-8>
- Andreotti, B., Forterre, Y. and Pouliquen, O. (2013). *Granular Media Between Fluid and Solid*. Cambridge University Press, Cambridge.
- Andrews, B. J. (2014). Dispersal and air entrainment in unconfined dilute pyroclastic density currents. *Bulletin of Volcanology*, 76, 852. Available at: <https://link.springer.com/article/10.1007/s00445-014-0852-4>
- Andrews, B. J. (2019). Recognizing unsteadiness in the transport systems of dilute pyroclastic density currents. *Bulletin of Volcanology*, 81, 5. <https://doi.org/10.1007/s00445-018-1266-5>
- Andrews, B., & Manga, M. (2011). Effects of topography on pyroclastic density current runout and formation of coignimbrites. *Geology*, 39, 1099-1102.

- Aravena, A., Chupin, L., Dubois, T., & Roche, O. (2021). The influence of gas pore pressure in dense granular flows: Numerical simulations versus experiments and implications for pyroclastic density currents. *Bulletin of Volcanology*, 83, 10. <https://doi.org/10.1007/s00445-021-01507-7>
- Aravena, Á., Cioni, R., De'michieli Vitturi, M., & Neri, A. (2018). Conduit stability effects on intensity and steadiness of explosive eruptions. *Scientific Reports*, 8(1). <https://doi.org/10.1038/s41598-018-22539-8>
- Artoni, R., Soligo, A., Paul, J. M., & Richard, P. (2018). Shear localization and wall friction in confined dense granular flows. *Journal of Fluid Mechanics*, 849, 395-418. <https://doi.org/10.1017/jfm.2018.407>
- Auker, M. R., Sparks, R. S. J., Siebert, L., Croweller, H. S., & Ewert, J. (2013). A statistical analysis of the global historical volcanic fatalities record. *Journal of Applied Volcanology*, 2, 2. <https://doi.org/10.1186/2191-5040-2-2>
- Autin-Erickson, A., Büttner, R., Dellino, P., Ort, M. H., & Zimanowski, B. (2008). Phreatomagmatic explosions of rhyolitic magma: Experimental and field evidence. *Journal of Geophysical Research: Solid Earth*, 113(11). <https://doi.org/10.1029/2008JB005731>
- Baas, J. H., & Best, J. L. (2002). Turbulence modulation in clay-rich sediment-laden flows and some implications for sediment deposition. *Journal of Sedimentary Research*, 72(3), 336-340. <https://doi.org/10.1306/120601720336>
- Baas, J. H., Best, J. L., Peakall, J., & Wang, M. (2009). A phase diagram for turbulent, transitional, and laminar clay suspension flows. *Journal of Sedimentary Research*, 79(4), 162–183. <https://doi.org/10.2110/jsr.2009.025>
- Baas, J. H., McCaffrey, W. D., Haughton, P. D. W., & Thorne, J. A. (2011). The effect of packing density on the properties of sedimentary deposits: A comparative study of fine-grained sediments and natural sedimentary rocks. *Sedimentology*, 58, 1094-1109.
- Baas, J.H., Manica, R., Puhl, E. & de Oliveira Borges, A.L. (2016) Thresholds of intrabed flow and other interactions of turbidity currents with soft muddy substrates. *Sedimentology*, 63, 2002–2036. doi: 10.1111/sed.12292
- Baas, J.H., McCaffrey, W.D., Haughton, P.D.W. & Choux, C. (2005) Coupling between suspended sediment distribution and turbulence structure in a laboratory turbidity current. *Journal of Geophysical Research*, 110. doi: 10.1029/2004JC002668
- Baas, J.H., Tracey, N.D. & Peakall, J. (2021) Sole marks reveal deep-marine depositional processes and environment: Implications for flow transformation and hybrid-event-bed models. *Journal of Sedimentary Research*, 91, 986–1009. doi: 10.2110/jsr.2020.104

- Baghalian, S., & Ghodsian, M. (2020). Experimental study on the effects of artificial bed roughness on turbidity currents over abrupt bed slope change. *International Journal of Sediment Research*, 35(3), 256–268. <https://doi.org/10.1016/j.ijsrc.2019.12.004>
- Baker, M. L., & Baas, J. H. (2020). Mixed sand–mud bedforms produced by transient turbulent flows in the fringe of submarine fans: Indicators of flow transformation. *Sedimentology*, 67(5), 2645–2671. <https://doi.org/10.1111/sed.12714>
- Baker, M. L., Baas, J. H., Malarkey, J., Jacinto, R. S., Craig, M. J., Kane, I. A., & Barker, S. (2017). The effect of clay type on the properties of cohesive sediment gravity flows and their deposits. *Journal of Sedimentary Research*, 87(11), 1176–1195. <https://doi.org/10.2110/jsr.2017.63>
- Barclay, J., Johnstone, J.E., Matthews A.J. (2006). Meteorological monitoring of an active volcano: Implications for eruption prediction, *Journal of Volcanology and Geothermal Research*, 150(4), 339–358, <https://doi.org/10.1016/j.jvolgeores.2005.07.020>.
- Belousov, A., Voight, B., & Belousova, M. (2007). Directed blasts and blast-generated pyroclastic density currents: A comparison of the Bezymianny 1956, Mount St Helens 1980, and Soufrière Hills, Montserrat 1997 eruptions and deposits. *Bulletin of Volcanology*, 69(7), 701–740. <https://doi.org/10.1007/s00445-006-0109-y>
- Benage, M. C., Dufek, J., & Mothes, P. A. (2016). Quantifying entrainment in pyroclastic density currents from the Tungurahua eruption, Ecuador: Integrating field proxies with numerical simulations. *Geophysical Research Letters*, 43(13), 6932–6941. <https://doi.org/10.1002/2016GL069527>
- Bernard, J., Kelfoun, K., Le Pennec, J. L., et al. (2014). Pyroclastic flow erosion and bulking processes: Comparing field-based vs. modeling results at Tungurahua volcano, Ecuador. *Bulletin of Volcanology*, 76, 858. <https://doi.org/10.1007/s00445-014-0858-y>
- Bishop, A. W., Green, G. E., Garga, V. K., Andresen, A., & Brown, J. D. (1971). A new ring shear apparatus and its application to the measurement of residual strength. *Geotechnique*, 21(4), 273–328. <https://doi.org/10.1680/geot.1971.21.4.273>
- Blott, S. J., & Pye, K. (2001). GRADISTAT: A grain size distribution and statistics package for the analysis of unconsolidated sediments. *Earth Surface Processes and Landforms*, 26, 1237–1248. <https://doi.org/10.1002/esp.261>
- Brand, B. D., Mackaman-Lofland, C., Pollock, N. M., Bendaña, S., Dawson, B., & Wichgers, P. (2014). Dynamics of pyroclastic density currents: Conditions that promote substrate erosion and self-channelization—Mount St Helens, Washington (USA). *Journal of Volcanology and Geothermal Research*, 276, 189–214. <https://doi.org/10.1016/j.jvolgeores.2014.01.007>

- Brand, B. D., Pollock, N., Vallance, J. W., et al. (2023). Advances in our understanding of pyroclastic current behavior from the 1980 eruption sequence of Mount St. Helens volcano (Washington), USA. *Bulletin of Volcanology*, 85, 24. <https://doi.org/10.1007/s00445-022-01617-w>
- Branney, M. J., & Kokelaar, B. P. (1992). A reappraisal of ignimbrite emplacement: Progressive aggradation and changes from particulate to non-particulate flow during emplacement of high-grade ignimbrite. *Bulletin of Volcanology*, 54(6), 504–520. <https://doi.org/10.1007/BF00301396>
- Branney, M. J., & Kokelaar, B. P. (1997). Giant bed from a sustained catastrophic density current flowing over topography: Acatlán ignimbrite, Mexico. *Geology*, 25(2), 115–118. [https://doi.org/10.1130/0091-7613\(1997\)025%3C0115%3E2.3.CO;2](https://doi.org/10.1130/0091-7613(1997)025%3C0115%3E2.3.CO;2)
- Branney, M. J., & Kokelaar, B. P. (2002). Pyroclastic density currents and the sedimentation of ignimbrites. Geological Society, London. <https://doi.org/10.1144/GSL.MEM.2003.027>
- Breard, E. C. P., & Lube, G. (2017). Inside pyroclastic density currents – Uncovering the enigmatic flow structure and transport behaviour in large-scale experiments. *Earth and Planetary Science Letters*, 458, 22–36. <https://doi.org/10.1016/j.epsl.2016.10.016>
- Breard, E. C. P., Dufek, J., & Lube, G. (2017). Enhanced mobility in concentrated pyroclastic density currents: An examination of a self-fluidization mechanism. *Geophysical Research Letters*, 45. <https://doi.org/10.1002/2017GL075759>
- Breard, E. C. P., Dufek, J., Charbonnier, S., Gueugneau, V., Giachetti, T., & Walsh, B. (2023). The fragmentation-induced fluidisation of pyroclastic density currents. *Nature Communications*, 14(1), 2079. <https://doi.org/10.1038/s41467-023-37867-1>
- Breard, E. C. P., Dufek, J., Fullard, L., & Carrara, A. (2020). The basal friction coefficient of granular flows with and without excess pore pressure: Implications for pyroclastic density currents, water-rich debris flows, and rock and submarine avalanches. *Journal of Geophysical Research: Solid Earth*, 125. <https://doi.org/10.1029/2020JB020203>
- Breard, E. C. P., Fullard, L., Dufek, J., Tennenbaum, M., Fernandez Nieves, A., & Dietiker, J. F. (2022). Investigating the rheology of fluidized and non-fluidized gas-particle beds: Implications for the dynamics of geophysical flows and substrate entrainment. *Granular Matter*, 24(1), 34. <https://doi.org/10.1007/s10035-021-01192-5>
- Breard, E. C. P., Jones, J. R., Fullard, L., Lube, G., Davies, C., & Dufek, J. (2019). The permeability of volcanic mixtures—implications for pyroclastic currents. *Journal of Geophysical Research: Solid Earth*, 124(2), 1343–1360. <https://doi.org/10.1029/2018JB016544>
- Breard, E. C. P., Lube, G., Jones, J. R., Dufek, J., Cronin, S. J., Valentine, G. A., & Moebis, A. (2016). Coupling of turbulent and non-turbulent flow regimes within pyroclastic density currents. *Nature Geoscience*, 9(10), 767–771. <https://doi.org/10.1038/ngeo2794>

- Brosch, E., & Lube, G. (2020). Spatiotemporal sediment transport and deposition processes in experimental dilute pyroclastic density currents. *Journal of Volcanology and Geothermal Research*, 401, 106946. <https://doi.org/10.1016/j.jvolgeores.2020.106946>
- Brosch, E., Lube, G., Cerminara, M., et al. (2021). Destructiveness of pyroclastic surges controlled by turbulent fluctuations. *Nature Communications*, 12, 7306. <https://doi.org/10.1038/s41467-021-27517-9>
- Brown, R. J., & Branney, M. J. (2004). Bypassing and diachronous deposition from density currents: Evidence from a giant regressive bed form in the Poris ignimbrite, Tenerife, Canary Islands. *Geology*, 32(5), 445–448. <https://doi.org/10.1130/G20188.1>
- Brown, R. J., & Branney, M. J. (2013). Internal flow variations and diachronous sedimentation within extensive, sustained, density-stratified pyroclastic density currents flowing down gentle slopes, as revealed by the internal architectures of ignimbrites on Tenerife. *Bulletin of Volcanology*, 75(7), 1–24. <https://doi.org/10.1007/s00445-013-0727-0>
- Brown, R. J., Barry, T. L., Branney, M. J., Pringle, M. S., & Bryan, S. E. (2003). The Quaternary pyroclastic succession of southeast Tenerife, Canary Islands: Explosive eruptions, related caldera subsidence, and sector collapse. *Geological Magazine*, 140(3), 265–288. <https://doi.org/10.1017/S0016756802007252>
- Brown, R. J., Bonadonna, C., & Durant, A. J. (2012). A review of volcanic ash aggregation. *Physics and Chemistry of the Earth, Parts A/B/C*, 45-46, 65–78. <https://doi.org/10.1016/j.pce.2011.11.001>
- Brown, R. J., Branney, M. J., Maher, C., & Dávila-Harris, P. (2010). Origin of accretionary lapilli within ground-hugging density currents: Evidence from pyroclastic couplets on Tenerife. *Geological Society of America Bulletin*, 122(1-2), 305–320. <https://doi.org/10.1130/B26449.1>
- Buckland, H. M., Saxby, J., Roche, M., Meredith, P., Rust, A. C., Cashman, K. V., & Engwell, S. L. (2021). Measuring the size of non-spherical particles and the implications for grain size analysis in volcanology. *Journal of Volcanology and Geothermal Research*, 415, 107257. <https://doi.org/10.1016/j.jvolgeores.2021.107257>
- Burgisser, A., & Bergantz, G. W. (2002). Reconciling pyroclastic flow and surge: The multiphase physics of pyroclastic density currents. *Earth and Planetary Science Letters*, 202(2), 405–418. [https://doi.org/10.1016/S0012-821X\(02\)00789-6](https://doi.org/10.1016/S0012-821X(02)00789-6)
- Burgisser, A., Bergantz, G. W., & Breidenthal, R. E. (2005). Addressing complexity in laboratory experiments: The scaling of dilute multiphase flows in magmatic systems. *Journal of Volcanology and Geothermal Research*, 141(3–4), 245–265. <https://doi.org/10.1016/j.jvolgeores.2004.11.001>
- Bursik, M., & Woods, A. (1996). The dynamics and thermodynamics of large ash flows. *Bulletin of Volcanology*, 58, 175–193. <https://doi.org/10.1007/s004450050134>

- Buttner, R., Dellino, P., & Zimanowski, B. (1999). Identifying magma-water interaction from the surface features of ash particles. *Nature*, *401*, 688–690.
- Calder, E. S., Sparks, R. S. J., & Gardeweg, M. C. (2000). Erosion, transport, and segregation of pumice and lithic clasts in pyroclastic flows inferred from ignimbrite at Lascar Volcano, Chile. *Journal of Volcanology and Geothermal Research*, *104*(1–4), 201–235.
- Campbell, C. S. (2006). Granular material flows – An overview. *Powder Technology*, *162*, 208–229. <https://doi.org/10.1016/j.powtec.2005.12.008>
- Camuffo, D. (2019). Theoretical grounds for humidity. In *Microclimate for Cultural Heritage* (pp. 43–59). Amsterdam: Elsevier. <https://doi.org/10.1016/B978-0-444-64106-9.00003-1>
- Cas, R. A. F., & Wright, J. V. (1987). *Volcanic successions modern and ancient*. <https://doi.org/10.1007/978-94-009-3167-1>
- Cas, R. A. F., & Wright, J. V. (1988). Modern pyroclastic fall deposits and their eruptions. In *Volcanic Successions Modern and Ancient* (pp. 161–182). Dordrecht: Springer. https://doi.org/10.1007/978-94-009-3167-1_6
- Cas, R. A., & Wright, J. V. (1991). Subaqueous pyroclastic flows and ignimbrites: An assessment. *Bulletin of Volcanology*, *53*(5), 357–380. <https://doi.org/10.1007/BF00280227>
- Cavazos-Álvarez, J. A. C., & Carrasco-Núñez, G. (2019). Anatomy of the Xáltipan ignimbrite at Los Humeros Volcanic Complex; the largest eruption of the Trans-Mexican Volcanic Belt. *Journal of Volcanology and Geothermal Research*, *106755*. <https://doi.org/10.1016/j.jvolgeores.2019.106755>
- Cavazos-Álvarez, J. A., Carrasco-Núñez, G., Dávila-Harris, P., et al. (2020). Facies variations and permeability of ignimbrites in active geothermal systems; case study of the Xáltipan ignimbrite at Los Humeros Volcanic Complex. *Journal of South American Earth Sciences*, *104*, 102810. <https://doi.org/10.1016/j.jsames.2020.102810>
- Charbonnier, S. J., Garin, F., Rodríguez, L. A., et al. (2023). Unraveling the dynamics and hazards of the June 3rd, 2018, pyroclastic density currents at Fuego volcano (Guatemala). *Journal of Volcanology and Geothermal Research*, *436*, 107791. <https://doi.org/10.1016/j.jvolgeores.2023.107791>
- Chédeville, C., & Roche, O. (2014). Auto-fluidization of pyroclastic flows propagating on rough substrates as shown by laboratory experiments. *Journal of Geophysical Research: Solid Earth*, *119*, 1764–1776. <https://doi.org/10.1002/2013JB010554>
- Chédeville, C., & Roche, O. (2015). Influence of slope angle on pore pressure generation and kinematics of pyroclastic flows: Insights from laboratory experiments. *Bulletin of Volcanology*, *77*(11), 96. <https://doi.org/10.1007/s00445-015-0981-4>

- Chédeville, C., & Roche, O. (2018). Auto-fluidization of collapsing beds of fine particles: Implications for the emplacement of pyroclastic flows. *Journal of Volcanology and Geothermal Research*, 368, 91–99. <https://doi.org/10.1016/j.jvolgeores.2018.11.007>
- Chen, D., Melville, B., Zheng, J., et al. (2021). Pickup rate of non-cohesive sediments in low-velocity flows. *Journal of Hydraulic Research*, 60(1), 125–135. <https://doi.org/10.1080/00221686.2020.1871430>
- Chen, D., Wang, Y., Melville, B., Huang, H., & Zhang, W. (2018). Unified formula for critical shear stress for erosion of sand, mud, and sand-mud mixtures. *Journal of Hydraulic Engineering*, 144(8). [https://doi.org/10.1061/\(ASCE\)HY.1943-7900.0001489](https://doi.org/10.1061/(ASCE)HY.1943-7900.0001489)
- Chen, D., Zheng, J., Zhang, C., et al. (2021). Critical shear stress for erosion of sand-mud mixtures and pure mud. *Frontiers in Marine Science*, 8, 713. <https://doi.org/10.3389/fmars.2021.713039>
- Chen, J., Gao, R., & Liu, Y. (2019). Numerical study of particle morphology effect on the angle of repose for coarse assemblies using DEM. *Advances in Materials Science and Engineering*, 2019. <https://doi.org/10.1155/2019/8095267>
- Chen, J., Kwan, A., Ng, P., & Li, L. (2016). Packing density improvement through addition of limestone fines, superfine cement and condensed silica fume. *Journal of Materials Science & Chemical Engineering*, 4(7), 29-36. <https://doi.org/10.4236/msce.2016.47005>
- Chigira, M., & Yokoyama, O. (2005). Weathering profile of non-welded ignimbrite and the water infiltration behavior within it in relation to the generation of shallow landslides. *Engineering Geology*, 78(3–4), 187–207. <https://doi.org/10.1016/j.enggeo.2004.12.008>
- Chou, S. H., Yang, S. J., & Hsiau, S. S. (2023). Investigation on the erosion and deposition process of granular collapse flow on an erodible inclined plane. *Powder Technology*, 414, 118086. <https://doi.org/10.1016/j.powtec.2022.118086>
- Ciantia, M. O., Castellanza, R., Crosta, G. B., & Hueckel, T. (2015). Effects of mineral suspension and dissolution on strength and compressibility of soft carbonate rocks. *Engineering Geology*, 184, 1–18. <https://doi.org/10.1016/j.enggeo.2014.10.024>
- Cioni, R., Gurioli, L., Lanza, R., & Zanella, E. (2004). Temperature of the A.D. 79 pyroclastic density current deposits (Vesuvius, Italy). *Journal of Geophysical Research*, 109(B02207). <https://doi.org/10.1029/2002JB002251>
- Cioni, R., Pistolesi, M., & Rosi, M. (2015). Plinian and subplinian eruptions. In *The Encyclopedia of Volcanoes* (2nd ed., pp. 519–535). Academic Press.
- Clark, J.D. & Stanbrook, D.A. (2001) Formation of large-scale shear structures during deposition from high-density turbidity currents, Grès d'Annot Formation, South-East France. In: McCaffrey, W., Kneller, B. & Peakall, J. (eds) Particulate Gravity Currents. doi: 10.1002/9781444304275.ch16

- Cocco, R., & Chew, J. W. (2023). 50 years of Geldart classification. *Powder Technology*, 428, 0032-5910. <https://doi.org/10.1016/j.powtec.2023.118861>
- Cocco, R., Reddy, S. B., & Knowlton, K. T. (2014). Back to basics: Introduction to fluidization. *Chemical Engineering Progress*. Available at: www.aiche.org/cep. Accessed 2 October 2024.
- Cole, P. D., Calder, E. S., Druitt, T. H., Hoblitt, R., Robertson, R., Sparks, R. S. J., & Young, S. R. (1998). Pyroclastic flows generated by gravitational instability of the 1996–97 Lava Dome of Soufriere Hills Volcano, Montserrat. *Geophysical Research Letters*, 25(18), 3425–3428. <https://doi.org/10.1029/98GL01510>
- Cole, P. D., Calder, E. S., Sparks, R. S. J., Clarke, A. B., Druitt, T. H., Young, S. R., Herd, R. A., Harford, C. L., & Norton, G. E. (2002). Deposits from dome collapse and fountain-collapse pyroclastic flows at Soufriere Hills Volcano, Montserrat. *Geological Society*, 21, 231–262. <https://doi.org/10.1144/GSL.MEM.2002.021.01.11>
- Colombier, M., Mueller, S. B., Kueppers, U., Scheu, B., Delmelle, P., Cimorelli, C., Cronin, S. J., Brown, R. J., Tost, M., & Dingwell, D. B. (2019). Diversity of soluble salt concentrations on volcanic ash aggregates from a variety of eruption types and deposits. *Bulletin of Volcanology*, 81(7). <https://doi.org/10.1007/s00445-019-1302-0>
- Connolly, B. J., Loth, E., & Smith, C. F. (2020). Shape and drag of irregular angular particles and test dust. *Powder Technology*, 363, 275–285. <https://doi.org/10.1016/j.powtec.2019.12.045>
- Corbi, F., Funiciello, F., Faccenna, C., Ranalli, G., & Heuret, A. (2011). Seismic variability of subduction thrust faults: Insights from laboratory models. *Journal of Geophysical Research: Solid Earth*, 116(B6).
- Corbi, F., Funiciello, F., Moroni, M., Dinther, Y., Mai, P., Dalguer, L., & Faccenna, C. (2013). The seismic cycle at subduction thrusts: 1. Insights from laboratory models. *Journal of Geophysical Research: Solid Earth*, 118, 1483–1501. <https://doi.org/10.1029/2012JB009481>
- Corwin, E., Jaeger, H., & Nagel, S. (2005). Structural signature of jamming in granular media. *Nature*, 435, 1075–1078. <https://doi.org/10.1038/nature03698>
- Costa, A., Folch, A., & Macedonio, G. (2010). A model for wet aggregation of ash particles in volcanic plumes and clouds: 1. Theoretical formulation. *Journal of Geophysical Research: Solid Earth*, 115(9). <https://doi.org/10.1029/2009JB007175>
- Crawford, N. C., Popp, L. B., Johns, K. E., Caire, L. M., Peterson, B. N., & Liberatore, N. W. (2013). Shear thickening of corn starch suspensions: Does concentration matter? *Journal of Colloid and Interface Science*, 396, 83–89. <https://doi.org/10.1016/j.jcis.2013.01.024>

- Crosta, G. B., De Blasio, F. V., De Caro, M., et al. (2017). Modes of propagation and deposition of granular flows onto an erodible substrate: Experimental, analytical, and numerical study. *Landslides*, 14, 47–68. <https://doi.org/10.1007/s10346-016-0697-3>
- Cunningham, A. (1964). Notes on carbonised wood and leaf fragments occurring in Taupo pumice in the vicinity of the Kaweka Range. *New Zealand Journal of Botany*, 2(2), 107–119. <https://doi.org/10.1080/0028825X.1964.10428700>
- Daag, A., & Westen, C. J. (1996). Cartographic modelling of erosion in pyroclastic flow deposits of Mount Pinatubo, Philippines. *ITC Journal*, 2, 110–124.
- Darteville, S. (2004) Numerical modeling of geophysical granular flows: 1. A comprehensive approach to granular rheologies and geophysical multiphase flows. *Geochemistry, Geophysics, Geosystems*, 5. doi: 10.1029/2003GC000636
- Darteville, S. (2005) Comprehensive approaches to multiphase flows in geophysics – Application to non-isothermal, nonhomogeneous, unsteady, large-scale, turbulent dusty clouds I. Hydrodynamic and thermodynamic RANS and LES models. Los Alamos National Laboratory.
- Darteville, S., Ernst, G. G. J., Stix, J., & Bernard, A. (2002). Origin of the Mount Pinatubo climactic eruption cloud: Implications for volcanic hazards and atmospheric impacts. *Geology*, 30(7), 663–666. [https://doi.org/10.1130/0091-7613\(2002\)030](https://doi.org/10.1130/0091-7613(2002)030)
- Darteville, S., Rose, W., Stix, J., Kelfoun, K., & Vallance, J. (2004). Numerical modelling of geophysical granular flow: 2. Computer simulation of Plinian clouds and pyroclastic flows and surges. *Geochemistry, Geophysics, Geosystems*, 5(8). <https://doi.org/10.1029/2003GC000637>
- de Haas, T., McARDell, B. W., Nijland, W., Åberg, A. S., Hirschberg, J., & Huguenin, P. (2022). Flow and bed conditions jointly control debris-flow erosion and bulking. *Geophysical Research Letters*, 49. <https://doi.org/10.1029/2021GL097611>
- Deb, P. K., Abed, S. N., Jaber, A. M. Y., & Tekade, R. K. (2018). Particulate level properties and its implications on product performance and processing. In *Dosage Form Design Parameters* (pp. 155–220). <https://doi.org/10.1016/B978-0-12-814421-3.00005-1>
- Delannay, R., Valance, A., Mangeney, A., Roche, O., & Richard, P. (2017). Granular and particle-laden flows: From laboratory experiments to field observations. *Journal of Physics D: Applied Physics*, 50(5), 05300. <https://doi.org/10.1088/1361-6463/50/5/05300>
- Delenne, J., Richefeu, V., & Radjaï, F. (2013). Capillary states of granular materials in the funicular state. *AIP Conference Proceedings*. <https://doi.org/10.1063/1.4812108>
- Dellino, P. et al. (2005) ‘The analysis of the influence of pumice shape on its terminal velocity’, *Geophysical Research Letters*, 32. doi: 10.1029/2005GL023954.

- Dellino, P., & La Volpe, L. (1996). Image processing analysis in reconstructing fragmentation and transportation mechanisms of pyroclastic deposits: The case of Monte Pilato-Rocche Rosse eruptions, Lipari (Aeolian Islands, Italy). *Journal of Volcanology and Geothermal Research*, 71(1), 13–29. [https://doi.org/10.1016/0377-0273\(95\)00062-3](https://doi.org/10.1016/0377-0273(95)00062-3)
- Dellino, P., & Volpe, L. L. (1995). Fragmentation versus transportation mechanisms in the pyroclastic sequence of Monte Pilato-Rocche Rosse (Lipari, Italy). *Journal of Volcanology and Geothermal Research*, 64.
- Dellino, P., Büttner, R., Dioguardi, F., Doronzo, D. M., La Volpe, L., Mele, D., Sonder, I., Sulpizio, R., & Zimanowski, B. (2010). Experimental evidence links volcanic particle characteristics to pyroclastic flow hazard. *Earth and Planetary Science Letters*, 295(1–2), 314–320. <https://doi.org/10.1016/j.epsl.2010.04.022>
- Dellino, P., Dioguardi, F., Doronzo, D.M. & Mele, D. (2019) The entrainment rate of non-Boussinesq hazardous geophysical gas-particle flows: An experimental model with application to pyroclastic density currents. *Geophysical Research Letters*, 46, 12851–12861. doi: 10.1029/2019GL084776
- Dellino, P., Dioguardi, F., Isaia, R., Sulpizio, R., & Male, D. (2021). The impact of pyroclastic density currents duration on humans: The case of the AD 79 eruption of Vesuvius. *Scientific Reports*, 11, 4959. <https://doi.org/10.1038/s41598-021-84456-7>
- Dellino, P., Zimanowski, B., Büttner, R., Volpe, L. L., & Mele, D. (2007). Large-scale experiments on the mechanics of pyroclastic flows: Design, engineering, and first results. *Journal of Geophysical Research*, 112. <https://doi.org/10.1029/2006JB004313>
- Di Giuseppe, E., Funicello, F., Corbi, F., Ranalli, G., & Mojoli, G. (2009). Gelatins as rock analogs: A systematic study of their rheological and physical properties. *Tectonophysics*, 473(3–4), 391–403.
- Díaz-Vecino, C., Rossi, E., Pollastri, S., et al. (2023). Insights into the sticking probability of volcanic ash particles from laboratory experiments. *Scientific Reports*, 13, 21188. <https://doi.org/10.1038/s41598-023-47712-6>
- Dioguardi, F., Mele, D., Dellino, P., & Dürig, T. (2017). The terminal velocity of volcanic particles with shape obtained from 3D X-ray microtomography. *Journal of Volcanology and Geothermal Research*, 329, 41–53. <https://doi.org/10.1016/j.jvolgeores.2016.11.013>
- Donaldson, E. C., Alam, W., & Begum, N. (2013). Rock mechanics of fracturing. In E. C. Donaldson, W. Alam, & N. Begum (Eds.), *Hydraulic Fracturing Explained* (pp. 47–76). Gulf Publishing Company. <https://doi.org/10.1016/B978-1-933762-40-1.50012-X>
- Dooley, T. P., & Hudec, M. R. (2020). Extension and inversion of salt-bearing rift systems. *Solid Earth*, 11, 1187–1204. <https://doi.org/10.5194/se-11-1187-2020>

- Doronzo, D. M., & Dellino, P. (2014). Pyroclastic density currents and local topography as seen with the conveyer model. *Journal of Volcanology and Geothermal Research*, 278-279, 25-39.
<https://doi.org/10.1016/j.jvolgeores.2014.03.012>
- Douillet, G. A., Bernard, B., Bouysson, M., Chaffaut, Q., Dingwell, D. B., Gegg, L., & Witting, P. (2018). Pyroclastic dune bedforms: Macroscale structures and lateral variations. Examples from the 2006 pyroclastic currents at Tungurahua (Ecuador). *Sedimentology*, 66(5), 1531–1559.
<https://doi.org/10.1111/sed.12542>
- Douillet, G. A., et al. (2019). Pyroclastic dune bedforms: Macroscale structures and lateral variations. Examples from the 2006 pyroclastic currents at Tungurahua (Ecuador). *Sedimentology*, 66(5), 1531–1559. <https://doi.org/10.1111/sed.12542>
- Douillet, G. A., Pacheco, D. A., Kueppers, U., Letort, J., Tsang-Hin-Sun, È., Bustillos, J., Hall, M., Ramon, P., & Dingwell, D. B. (2013). Dune bedforms produced by dilute pyroclastic density currents from the August 2006 eruption of Tungurahua volcano, Ecuador. *Bulletin of Volcanology*, 75, 762.
<https://doi.org/10.1007/s00445-013-0762-x>
- Douillet, G. A., Taisne, B., Tsang-Hin-Sun, È., Müller, S. K., Kueppers, U., et al. (2015). Syn-eruptive, soft-sediment deformation of deposits from dilute pyroclastic density current: Triggers from granular shear, dynamic pore pressure, ballistic impacts, and shock waves. *Physics and Chemistry of the Earth, Part A: Solid Earth and Geodesy*, 6(2), 553–572. <https://doi.org/10.5194/se-6-553-2015>
- Douillet, G. A., Tsang-Hin-Sun, È., Kueppers, U., et al. (2013). Sedimentology and geomorphology of the deposits from the August 2006 pyroclastic density currents at Tungurahua volcano, Ecuador. *Bulletin of Volcanology*, 75, 765. <https://doi.org/10.1007/s00445-013-0765-7>
- Douillet, G., Chaffaut, Q., Schlunegger, F., Kueppers, U., & Dingwell, D. (2018). Shark-fins: Overturned patterns linked to shear instabilities at the flow-bed boundary. Examples from the deposits of the 2006 pyroclastic currents at Tungurahua volcano (Ecuador). <https://doi.org/10.31223/OSF.IO/E8APK>
- Dowey, N. J., Brown, R. J., & Kokelaar, B. P. (2024). Counting currents: Resolving contradictory records of eruption history created by unsteady pyroclastic density current dynamics. *EarthArXiv*.
<https://doi.org/10.31223/X5W42M>
- Dowey, N., & Williams, R. (2022). Simultaneous fall and flow during pyroclastic eruptions: A novel proximal hybrid facies. *Geology*, 50(10), 1187–1191. <https://doi.org/10.1130/G50169.1>
- Doyle, E. E., Cronin, S. J., & Thouret, J. C. (2011). Defining conditions for bulking and debulking in lahars. *Geological Society of America Bulletin*, 123(7-8), 1234–1246.
- Doyle, E. E., Hogg, A. J., Mader, H. M., & Sparks, R. S. J. (2010). A two-layer model for the evolution and propagation of dense and dilute regions of pyroclastic currents. *Journal of Volcanology and Geothermal Research*, 190(3–4), 365–378. <https://doi.org/10.1016/j.jvolgeores.2009.12.004>
- Druitt, T. H. (1998). Pyroclastic density currents. *Geological Society of London Special Publications*. Retrieved from <http://sp.lyellcollection.org/>

- Druitt, T. H. (2014). New insights into the initiation and venting of the Bronze-Age eruption of Santorini (Greece), from component analysis. *Bulletin of Volcanology*, 76(2), 794. <https://doi.org/10.1007/s00445-014-0794-x>
- Druitt, T. H., & Bacon, C. R. (1986). Lithic breccia and ignimbrite erupted during the collapse of Crater Lake Caldera, Oregon. *Journal of Volcanology and Geothermal Research*, 29(1–4), 1–32. [https://doi.org/10.1016/0377-0273\(86\)90038-7](https://doi.org/10.1016/0377-0273(86)90038-7)
- Druitt, T. H., Avard, G., Bruni, G., & Lettieri, P. (2007). Gas retention in fine-grained pyroclastic flow materials at high temperatures. *Bulletin of Volcanology*, 69, 881–901. <https://doi.org/10.1007/s00445-007-0116-7>
- Druitt, T. H., Bruni, G., Lettieri, P., & Yates, J. G. (2004). The fluidization behaviour of ignimbrite at high temperature and with mechanical agitation. *Geophysical Research Letters*, 31, L02604. <https://doi.org/10.1029/2003GL018593>
- Druitt, T. H., Mellors, R. A., Pyle, D. M., & Sparks, R. S. J. (1989). Explosive volcanism on Santorini, Greece. *Geological Magazine*, 126(2), 95. <https://doi.org/10.1017/S0016756800006270>
- Duane, W. J., Pepin, N. C., Losleben, M. L., & Hardy, D. R. (2008). General characteristics of temperature and humidity variability on Kilimanjaro, Tanzania. *Arctic, Antarctic, and Alpine Research*, 40(2), 323–334. <https://doi.org/10.1657/1523-0430>
- Dufek, J. (2016). The fluid mechanics of pyroclastic density currents. *Annual Review of Fluid Mechanics*, 48, 459–485. <https://doi.org/10.1146/annurev-fluid-122414-034252>
- Dufek, J., & Manga, M. (2008). In situ production of ash in pyroclastic flows. *Journal of Geophysical Research: Solid Earth*, 113(B9). <https://doi.org/10.1029/2007JB005555>
- Dufek, J., Manga, M., & Patel, A. (2012). Granular disruption during explosive volcanic eruptions. *Nature Geoscience*, 5(8), 561–564. <https://doi.org/10.1038/ngeo1524>
- Dufek, J., Manga, M., & Staedter, M. (2007). Littoral blasts: Pumice-water heat transfer and the conditions for steam explosions when pyroclastic flows enter the ocean. *Journal of Geophysical Research*, 112. <https://doi.org/10.1029/2006JB004910>
- Dufresne, A. (2012). Granular flow experiments on the interaction with stationary runout path materials and comparison to rock avalanche events. *Earth Surface Processes and Landforms*, 37, 1527–1541. <https://doi.org/10.1002/esp.3296>
- Dury, C., Ristow, G., Moss, J., & Nakagawa, M. (1998). Boundary effects on the angle of repose in rotating cylinders. *Physical Review*, 57(4491). <https://doi.org/10.1103/PhysRevE.57.4491>

Dyer, K. R., & Manning, A. J. (1999). Observation of the size, settling velocity and effective density of flocs, and their fractal dimensions. *Journal of Sea Research*, 41, 203–213.

Eames, I. & Gilbertson, M.A. (2000) Aerated granular flow over a horizontal rigid surface. *Journal of Fluid Mechanics*, 424, 169–195. doi: 10.1017/S0022112000001920

Edgar, C. J., Wolff, J. A., Nichols, H. J., et al. (2002). A complex Quaternary ignimbrite-forming phonolitic eruption: The Poris Member of the Diego Hernández Formation (Tenerife, Canary Islands). *Journal of Volcanology and Geothermal Research*, 118(1–2), 99–130. [https://doi.org/10.1016/S0377-0273\(02\)00252-4](https://doi.org/10.1016/S0377-0273(02)00252-4)

Edgar, C. J., Wolff, J. A., Olin, P. H., et al. (2007). The late Quaternary Diego Hernandez Formation, Tenerife: Volcanology of a complex cycle of voluminous explosive phonolitic eruptions. *Journal of Volcanology and Geothermal Research*, 160(1–2), 59–85. <https://doi.org/10.1016/j.jvolgeores.2006.06.001>

Edwards, A. N., Russell, A. S., Johnson, C. G., & Gray, J. M. N. T. (2019). Frictional hysteresis and particle deposition in granular free-surface flows. *Journal of Fluid Mechanics*, 875, 1058–1095. <https://doi.org/10.1017/jfm.2019.1061>

Edwards, A. N., Viroulet, S., Johnson, C. G., & Gray, J. M. N. T. (2021). Erosion-deposition dynamics and long-distance propagation of granular avalanches. *Journal of Fluid Mechanics*, 915. <https://doi.org/10.1017/jfm.2021.34>

Efford, J. T., Bylsma, R. J., Clarkson, B. D., Pittari, A., Mauriohooho, K., & Moon, V. G. (2014a). Vegetation dieback as a proxy for temperature within a wet pyroclastic density current: A novel experiment and observations from the 6th of August 2012 Tongariro eruption. *Journal of Volcanology and Geothermal Research*, 286, 367–372. <https://doi.org/10.1016/j.jvolgeores.2014.05.016>

Efford, J. T., Bylsma, R. J., Clarkson, B. D., Pittari, A., Mauriohooho, K., & Moon, V. G. (2014b). Vegetation dieback as a proxy for temperature within a wet pyroclastic density current: A novel experiment and observations from the 6th of August 2012 Tongariro eruption. *Journal of Volcanology and Geothermal Research*, 286, 367–372. <https://doi.org/10.1016/j.jvolgeores.2014.05.016>

Eggenhuisen, J. T., McCaffrey, W. D., Houghton, P. D. W., & Butler, R. W. H. (2011). Shallow erosion beneath turbidity currents and its impact on the architectural development of turbidite sheet systems. *Sedimentology*, 58, 936–959. <https://doi.org/10.1111/j.1365-3091.2010.01190.x>

Estep, J., & Dufek, J. (2012). Substrate effects from force chain dynamics in dense granular flows. *Journal of Geophysical Research*, 117, F01028. <https://doi.org/10.1029/2011JF002125>

Eychenne, J., Pennec, J. L. L., Troncoso, L., Gouhier, M., & Nedelec, J. M. (2012). Causes and consequences of bimodal grain-size distribution of tephra fall deposited during the August 2006

Tungurahua eruption (Ecuador). *Bulletin of Volcanology*, 74(1), 187–205. <https://doi.org/10.1007/s00445-011-0517-5>

Farin, M., Mangeney, A., & Roche, O. (2014). Fundamental changes of granular flow dynamics, deposition, and erosion processes at high slope angles: Insights from laboratory experiments. *Journal of Geophysical Research: Earth Surface*, 119, 504–532. <https://doi.org/10.1002/2013JF002750>

Fisher, R. V. (1966). Rocks composed of volcanic fragments and their classification. *Earth-Science Reviews*, 1(4), 287–298. [https://doi.org/10.1016/0012-8252\(66\)90001-6](https://doi.org/10.1016/0012-8252(66)90001-6)

Fisher, R. V. (1979). Models for pyroclastic surges and pyroclastic flows. *Journal of Volcanology and Geothermal Research*, 6(3–4), 305–318. [https://doi.org/10.1016/0377-0273\(79\)90008-8](https://doi.org/10.1016/0377-0273(79)90008-8)

Fisher, R. V., & Schmincke, H. U. (1984). Pyroclastic flow deposits. In *Pyroclastic Rocks* (pp. 186–230). Berlin, Heidelberg: Springer. https://doi.org/10.1007/978-3-642-74864-6_8

Freundt, A. (2003). Entrance of hot pyroclastic flows into the sea: Experimental observations. *Bulletin of Volcanology*, 65, 144–164. <https://doi.org/10.1007/s00445-002-0250-1>

Kueppers, U., Putz, C., Spieler, O., & Dingwell, D. B. (2012). Abrasion in pyroclastic density currents: Insights from tumbling experiments. *Physics and Chemistry of the Earth, Parts A/B/C*, 45–46, 33–39. <https://doi.org/10.1016/j.pce.2011.09.002>

Fujinawa, A., Ban, M., Ohba, T., Kontani, K., & Miura, K. (2008). Characterization of low-temperature pyroclastic surges that occurred in the northeastern Japan arc during the late 19th century. *Journal of Volcanology and Geothermal Research*, 178(1), 113–130. <https://doi.org/10.1016/j.jvolgeores.2008.05.002>

Fullmer, W. D., & Hrenya, C. M. (2017). The clustering instability in rapid granular and gas-solid flows. In *Annual Review of Fluid Mechanics* (Vol. 49, pp. 485–510). Annual Reviews Inc. <https://doi.org/10.1146/annurev-fluid-010816-060028>

Gauer, P., & Issler, D. (2004). Possible erosion mechanisms in snow avalanches. *Annals of Glaciology*, 38, 384–392. <https://doi.org/10.3189/172756404781815068>

Gauthier, T. D. (2001). Detecting trends using Spearman's rank correlation coefficient. *Environmental Forensics*, 2(4), 359–362. <https://doi.org/10.1080/713848278>

Geldart, D. (1973). Types of gas fluidization. *Powder Technology*, 7, 285–292. [https://doi.org/10.1016/0032-5910\(73\)80037-3](https://doi.org/10.1016/0032-5910(73)80037-3)

Gilbert, J. S., & Lane, S. J. (1994). The origin of accretionary lapilli. *Bulletin of Volcanology*, 56, 398–411. <https://doi.org/10.1007/BF00326465>

Gilbertson, M. A. (2019). Estimation of the minimum fluidisation velocities in well-mixed bi-disperse fluidised beds. *Powder Technology*, 346, 433–440. <https://doi.org/10.1016/j.powtec.2019.02.019>

- Gilbertson, M. A., Taylor, A., Mitchell, S., & Rust, A. C. (2020). A fluidisation mechanism for secondary hydroeruptions in pyroclastic flow deposits. *Frontiers in Earth Science*, 8. <https://doi.org/10.3389/feart.2020.00324>
- Gilbertson, M.A., Jessop, D.E. & Hogg, A.J. (2008) The effects of gas flow on granular currents. *Philosophical Transactions of the Royal Society A*, 366, 2191–2203. doi: 10.1098/rsta.2007.0021
- Girolami, L., Druitt, T. H., & Roche, O. (2015). Towards a quantitative understanding of pyroclastic flows: Effects of expansion on the dynamics of laboratory fluidized granular flows. *Journal of Volcanology and Geothermal Research*, 296, 31–39. <https://doi.org/10.1016/j.jvolgeores.2015.03.008>
- Girolami, L., Druitt, T., Roche, O., & Khrabrykh, Z. V. (2008). Propagation and hindered settling of laboratory ash flows. *Journal of Geophysical Research*, 113, B02202. <https://doi.org/10.1029/2007JB005074>
- Gladstone, C., & Sparks, R. S. J. (2002). The significance of grain-size breaks in turbidites and pyroclastic density current deposits. *Journal of Sedimentary Research*, 72(1), 182–191. <https://doi.org/10.1306/041801720182>
- Goldfarb, D., Glasser, B., & Shinbrot, T. (2002). Shear instabilities in granular flows. *Nature*, 415, 302–305. <https://doi.org/10.1038/415302a>
- Gorle, A. P., & Chopade, S. S. (2020). Lquisolid technology: Preparation, characterization, and applications. *Journal of Drug Delivery and Therapeutics*, 10(3-s), 295–307. <https://doi.org/10.22270/jddt.v10i3-s.4067>
- Grabowski, R. C., Droppo, I. G., & Wharton, G. (2011). Erodibility of cohesive sediment: The importance of sediment properties. *Earth Science Reviews*, 105, 101–120. <https://doi.org/10.1016/j.earscirev.2011.01.008>
- Groen, J. C., Kooijman, W., van Belzen, D., Meesters, G. M. H., Schütz, D., Aschl, T., & Verolme, P. (2020). Real-time in-situ rheological assessment of sticky point temperature and humidity of powdered products. *KONA Powder and Particle Journal*, 37, 176–186. <https://doi.org/10.14356/kona.2020006>
- Hall, M. L., Steele, A. L., Mothes, P. A., & Ruiz, M. C. (2013). Pyroclastic density currents (PDC) of the 16–17 August 2006 eruptions of Tungurahua volcano, Ecuador: Geophysical registry and characteristics. *Journal of Volcanology and Geothermal Research*, 265, 78–93. <https://doi.org/10.1016/j.jvolgeores.2013.08.011>
- Hall, M., Mothes, P., Ramon, P., Arellano, S., Barba, D., & Palacios, P. (2007). Dense pyroclastic flows of the 16–17 August 2006 eruption of Tungurahua Volcano, Ecuador. *AGU Spring Meeting Abstracts*.
- Han, M., Zhou, Y., & Zhu, J. (2020). Improvement on flowability and fluidization of Group C particles after nanoparticle modification. *Powder Technology*, 365, 208–214. <https://doi.org/10.1016/j.powtec.2019.07.026>

- Hartmann, D. L. (2016). *Global physical climatology* (Vol. 103). Newnes.
- Hatch, C.D., Wiese, J.S., Crane, C.C., Harris, K.J., Kloss, H.G. & Baltrusaitis, J. (2012) Water adsorption on clay minerals as a function of relative humidity: Application of BET and Freundlich adsorption models. *Langmuir*, 28(3), 1790–1803. doi: 10.1021/la2042873
- Hausner, H. H. (1981). Powder characteristics and their effect on powder processing. *Powder Technology*, 30(1), 3–8. [https://doi.org/10.1016/0032-5910\(81\)85021-8](https://doi.org/10.1016/0032-5910(81)85021-8)
- Hofstra, M., Hodgson, D.M., Peakall, J. & Flint, S.S. (2015) Giant scour-fills in ancient channel-lobe transition zones: Formative processes and depositional architecture. *Sedimentology*, 329, 98–114. doi: 10.1016/j.sedgeo.2015.09.004
- Houghton, B., White, J. D. L., & Van Eaton, A. R. (2015). Phreatomagmatic and related eruption styles. In H. Sigurdsson, B. Houghton, H. Rymer, J. Stix, & S. McNutt (Eds.), *The Encyclopedia of Volcanoes* (pp. 537–552). Elsevier. <https://doi.org/10.1016/B978-0-12-385938-9.00030-4>
- Huang, Q., Zhang, H., & Zhu, J. (2009). Experimental study on fluidization of fine powders in rotating drums with various wall friction and baffled rotating drums. *Chemical Engineering Science*, 64(9), 2234–2244. <https://doi.org/10.1016/j.ces.2009.01.047>
- Hudspith, V. A., Scott, A. C., Wilson, C. J. N., & Collinson, M. E. (2010). Charring of woods by volcanic processes: An example from the Taupo ignimbrite, New Zealand. *Palaeogeography, Palaeoclimatology, Palaeoecology*, 291(1–2), 40–51. <https://doi.org/10.1016/j.palaeo.2009.06.036>
- Hungr, O., & Evans, S. G. (2004). Entrainment of debris in rock avalanches: An analysis of a long run-out mechanism. *Geological Society of America Bulletin*, 116, 1240–1252. <https://doi.org/10.1130/B25362.1>
- Hurwitz, S. (2003). Groundwater flow, heat transport, and water table position within volcanic edifices: Implications for volcanic processes in the Cascade Range. *Journal of Geophysical Research*, 108(B12). <https://doi.org/10.1029/2003jb002565>
- Hyndman, D. W., & Alt, D. (1987). Radial dikes, laccoliths, and gelatin models. *The Journal of Geology*, 95(6), 763–774.
- Inman, D. L. (1952). Measures for describing the size distribution of sediments. *Journal of Sedimentary Research*, 22, 125–145. <https://doi.org/10.1306/D42694DB-2B26-11D7-8648000102C1865D>
- Israelachvili, J.. (2011). *Intermolecular and Surface Forces*, 3rd Edition.
- Iverson, R. M. (1997). The physics of debris flows. *Reviews of Geophysics*, 35(3), 245–296. <https://doi.org/10.1029/97RG00426>

- Iverson, R. M. (2012). Elementary theory of bed-sediment entrainment by debris flows and avalanches. *Journal of Geophysical Research: Earth Surface*, 117(F3), F03006. <https://doi.org/10.1029/2011JF002189>
- Jaeger, H. M., Nagel, S. R., & Behringer, R. P. (1996). The physics of granular materials. *Physics Today*, 49(4), 32–38. <https://doi.org/10.1063/1.881494>
- Jagger, L. J., & McClay, K. (2016). Analogue modelling of inverted domino-style basement fault systems. *Basin Research*, 30, 363–381. <https://doi.org/10.1111/bre.12224>
- Jain, R. K., & Kothiyari, U. C. (2009). Cohesion influences on erosion and bed load transport. *Water Resources Research*, 45. <https://doi.org/10.1029/2008WR007044>
- James, M. R., Gilbert, J. S., & Lane, S. J. (2002). Experimental investigation of volcanic particle aggregation in the absence of a liquid phase. *Journal of Geophysical Research: Solid Earth*, 107(B9), ECV 4-1-ECV 4-13. <https://doi.org/10.1029/2001jb000950>
- James, M. R., Lane, S. J., & Gilbert, J. S. (2000). Volcanic plume electrification: Experimental investigation of a fracture-charging mechanism. *Journal of Geophysical Research: Solid Earth*, 105(B7), 16641–16649. <https://doi.org/10.1029/2000jb900068>
- James, M. R., Lane, S. J., & Gilbert, J. S. (2003). Density, construction, and drag coefficient of electrostatic volcanic ash aggregates. *Journal of Geophysical Research: Solid Earth*, 108(B9). <https://doi.org/10.1029/2002jb002011>
- Jara, P., Likerman, J., Winocur, D., Ghiglione, M. C., Cristallini, E. O., Pinto, L., & Charrier, R. (2015). Role of basin width variation in tectonic inversion: Insight from analogue modelling and implications for the tectonic inversion of the Abanico Basin, 32°–34° S, Central Andes. *Geological Society Special Publications*, 399, 83–107. <https://doi.org/10.1144/SP399.7>
- Jia, X., & Williams, R. A. (2001). A packing algorithm for particles of arbitrary shapes. *Powder Technology*, 120(3), 175–186. [https://doi.org/10.1016/S0032-5910\(01\)00268-6](https://doi.org/10.1016/S0032-5910(01)00268-6)
- Jiang, X., Cui, P., & Ge, Y. (2015). Effects of fines on the strength characteristics of mixtures. *Engineering Geology*, 198, 78–86. <https://doi.org/10.1016/j.enggeo.2015.09.011>
- Jop, P. (2015). Rheological properties of dense granular flows. *Comptes Rendus Physique*, 16(1), 62–72. <https://doi.org/10.1016/j.crhy.2014.12.001>
- Kaminski, E., & Jaupart, C. (1998). The size distribution of pyroclasts and the fragmentation sequence in explosive volcanic eruptions. *Journal of Geophysical Research: Solid Earth*, 103(B12), 29759–29779. <https://doi.org/10.1029/98jb02795>

- Kassambara, A., & Mundt, F. (2020). *Factoextra: Extract and visualize the results of multivariate data analyses*. Retrieved from <https://cran.r-project.org/web/packages/factoextra/index.html> (Accessed: 2 October 2024).
- Kavanagh, J. L., Engwell, S. L., & Martin, S. A. (2018). A review of laboratory and numerical modelling in volcanology. *Solid Earth*, 9, 531–571. <https://doi.org/10.5194/se-9-531-2018>
- Kavanagh, J. L., Menand, T., & Daniels, K. A. (2013). Gelatine as a crustal analogue: Determining elastic properties for modelling magmatic intrusions. *Tectonophysics*, 582, 101–111. <https://doi.org/10.1016/j.tecto.2012.09.032>
- Kavanagh, J. L., Menand, T., & Sparks, R. S. J. (2006). An experimental investigation of sill formation and propagation in layered elastic media. *Earth and Planetary Science Letters*, 245(3–4), 799–813. <https://doi.org/10.1016/j.epsl.2006.03.025>
- Keating, G. N. (2005). The role of water in cooling ignimbrites. *Journal of Volcanology and Geothermal Research*, 142(1–2), 145–171. <https://doi.org/10.1016/j.jvolgeores.2004.10.019>
- Keaton, J. R. (2018). Angle of internal friction. In P. T. Bobrowsky & B. Marker (Eds.), *Encyclopedia of engineering geology*. Encyclopedia of Earth Sciences Series. Springer, Cham. https://doi.org/10.1007/978-3-319-73568-9_1
- Kelfoun, K. (2017). A two-layer depth-averaged model for both the dilute and the concentrated parts of pyroclastic currents. *Journal of Geophysical Research: Solid Earth*, 122(6), 4293–4311. <https://doi.org/10.1002/2017JB013981>
- Kelfoun, K., & Gueugneau, V. (2022). A unifying model for pyroclastic surge genesis and pyroclastic flow fluidization. *Geophysical Research Letters*, 49, e2021GL096517. <https://doi.org/10.1029/2021GL096517>
- Kelfoun, K., Samaniego, P., Palacios, P., & Barba, D. (2009). Testing the suitability of frictional behaviour for pyroclastic flow simulation by comparison with a well-constrained eruption at Tungurahua volcano (Ecuador). *Bulletin of Volcanology*, 71, 1057–1075. <https://doi.org/10.1007/s00445-009-0286-6>
- Kelling, G., & Walton, E. K. (1957). Load-cast structures: Their relationship to upper-surface structures and their mode of formation. *Geological Magazine*, 94(6), 481–490. <https://doi.org/10.1017/S0016756800070175>
- Kennedy, B., Stix, J., Vallance, J. W., Lavallée, Y., & Longpré, M.-A. (2004). Controls on caldera structure: Results from analogue sandbox modeling. *GSA Bulletin*, 116(5–6), 515–524. <https://doi.org/10.1130/B25228.1>
- Kervyn, M., Ernst, G. G. J., van Wyk de Vries, B., Mathieu, L., & Jacobs, P. (2009). Volcano load control on dyke propagation and vent distribution: Insights from analogue modeling. *Journal of Geophysical Research: Solid Earth*, 114(B3). <https://doi.org/10.1029/2008JB005925>

- Kim, T. H., & Hwang, C. (2003). Modelling of tensile strength on moist granular earth material at low water content. *Engineering Geology*, 69(3–4), 233–244. [https://doi.org/10.1016/S0013-7952\(02\)00284-3](https://doi.org/10.1016/S0013-7952(02)00284-3)
- Kim, T. H., & Sture, S. (2008). Capillary-induced tensile strength in unsaturated sands. *Canadian Geotechnical Journal*, 45(5), 726–737. <https://doi.org/10.1139/T08-017>
- Kimiaghalam, N., Clark, S. P., & Ahmari, H. (2016). An experimental study on the effects of physical, mechanical, and electrochemical properties of natural cohesive soils on critical shear stress and erosion rate. *International Journal of Sediment Research*, 31, 1–15. <https://doi.org/10.1016/j.ijsrc.2015.01.001>
- Kobchenko, M., Hafver, A., Jettstuen, E., Renard, F., Galland, O., Jamtveit, B., Meakin, P., & Dysthe, D. K. (2014). Evolution of a fracture network in an elastic medium with internal fluid generation and expulsion. *Physical Review E*, 90(5), 052801. <https://doi.org/10.1103/PhysRevE.90.052801>
- Koos, E. (2014). Capillary suspensions: Particle networks formed through the capillary force. *Current Opinion in Colloid & Interface Science*, 19(6), 575–584. <https://doi.org/10.1016/j.cocis.2014.10.004>
- Kubo Hutchison, A., & Dufek, J. (2021). Generation of overspill pyroclastic density currents in sinuous channels. *Journal of Geophysical Research: Solid Earth*, 126(10), e2021JB022442. <https://doi.org/10.1029/2021JB022442>
- Kundu, P. K., & Cohen, I. M. (2004). *Fluid mechanics*. Elsevier Academic Press.
- Kwan, A. K. H., Ng, P. L., & Huen, K. Y. (2014). Effects of fines content on packing density of fine aggregate in concrete. *Construction and Building Materials*, 61, 270–277. <https://doi.org/10.1016/j.conbuildmat.2014.03.022>
- Lam, D., & Nakagawa, M. (1993). Packing of particles (Part 2): Effect of extra pore volume on packing density of mixtures of monosized spheres. *Journal of the Ceramic Society of Japan*, 101(11), 1234–1238. <https://doi.org/10.2109/jcersj.101.1234>
- LaMarche, C. Q., Miller, A. W., Liu, P., & Hrenya, C. (2016). Linking microscale predictions of capillary forces to macro-scale fluidization experiments in humid environments. *AIChE Journal*, 62(10), 3585–3597. <https://doi.org/10.1002/aic.15281>
- Lane, S. J., Gilbert, J. S., & Hilton, M. (1993). *The aerodynamic behaviour of volcanic aggregates* (Vol. 55). Springer-Verlag.
- Le Friant, A., Harford, C. L., Deplus, C., Boudon, G., Sparks, R. S. J., Herd, R. A., & Komorowski, J. C. (2004). Geomorphological evolution of Montserrat (West Indies): Importance of flank collapse and erosional processes. *Journal of the Geological Society*, 161(1), 147–160. <https://doi.org/10.1144/0016-764903-001>
- Le Hir, P., Cayocca, F., & Waeles, B. (2011). Dynamics of sand and mud mixtures: A multiprocess-based modelling strategy. *Continental Shelf Research*, 31, 135–149. <https://doi.org/10.1016/j.csr.2010.12.009>

- Lê, S., Josse, J., & Husson, F. (2008). FactoMineR: A package for multivariate analysis. *Journal of Statistical Software*, 25(1), 1–18. <https://doi.org/10.18637/jss.v025.i01>
- Lee, S., Reber, J. E., Hayman, N. W., & Wheeler, M. F. (2016). Investigation of wing crack formation with a combined phase-field and experimental approach. *Geophysical Research Letters*, 43, 7946–7952. <https://doi.org/10.1002/2016GL069979>
- Lesti, C., Porreca, M., Giordano, G., et al. (2011). High-temperature emplacement of the Cerro Galán and Toconquis Group ignimbrites (Puna plateau, NW Argentina) determined by TRM analyses. *Bulletin of Volcanology*, 73, 1535–1565. <https://doi.org/10.1007/s00445-011-0536-2>
- Leturia, M., Benali, M., Lagarde, S., Ronga, I., & Saleh, K. (2014). Characterization of flow properties of cohesive powders: A comparative study of traditional and new testing methods. *Powder Technology*, 253, 406–423. <https://doi.org/10.1016/j.powtec.2013.11.045>
- Li, J., Zhang, Y. & Ji, Q. (2020) Lateral migration in a wandering reach of the Middle Yellow River in response to different boundary conditions. *Applied Sciences*, 10(15), 5229. doi: 10.3390/app10155229
- Li, S., Li, S., Shan, X., Gong, C., & Yu, X. (2017). Classification, formation, and transport mechanisms of mud clasts. *International Geology Review*, 59, 1609–1620. <https://doi.org/10.1080/00206814.2017.1287014>
- Li, W. C., Deng, G., Liang, X. Q., Sun, X. X., Wang, S. W., & Lee, L. M. (2020). Effects of stress state and fine fraction on stress transmission in internally unstable granular mixtures investigated via discrete element method. *Powder Technology*, 367, 659–670. <https://doi.org/10.1016/j.powtec.2020.04.024>
- Lipman, P. W. (2019). When ignimbrite meets water: Mega scale gas-escape structures formed during welding. *Geology*, 47(1), 63–66. <https://doi.org/10.1130/G45772.1>
- Liu, E. J., Cashman, K. V., & Rust, A. C. (2015). Optimising shape analysis to quantify volcanic ash morphology. *GeoResJ*, 8, 14–30. <https://doi.org/10.1016/j.grj.2015.09.001>
- Liu, H., Wang, C., Wu, D., Liu, X., & Zhang, Z. (2022). Deformation and critical dynamic stress for compacted volcanic ash subjected to monotonic and dynamic loads. *Construction and Building Materials*, 358. <https://doi.org/10.1016/j.conbuildmat.2022.129454>
- Liu, H., Zhao, X., Frattini, P., Crosta, G. B., De Blasio, F. V., Wan, Y., & Zhu, X. (2023). Mobility and erosion of granular flows travelling on an erodible substrate: Insights from small-scale flume experiments. *Engineering Geology*, 326, 107316. <https://doi.org/10.1016/j.enggeo.2023.107316>
- Liu, L. X., Smith, R., & Litster, J. D. (2009). Wet granule breakage in a breakage only high-heat mixer: Effect of formulation properties on breakage behaviour. *Powder Technology*, 189(2), 158–164. <https://doi.org/10.1016/j.powtec.2008.04.029>
- Lorenz, V. (1987). Phreatomagmatism and its relevance. In *Chemical Geology* (Vol. 62)

Louati, H., Oulahna, D., & de Ryck, A. (2015). Apparent friction and cohesion of a partially wet granular material in steady-state shear. *Powder Technology*, 278, 65–71.
<https://doi.org/10.1016/j.powtec.2015.03.011>

Louge, M., Valance, A., Lancelot, P., Delannay, R., & Artières, O. (2015). Granular flows on a dissipative base. *Physical Review E*, 92, 022204. <https://doi.org/10.1103/PhysRevE.92.022204>

Lowe, D. J., & Pittari, A. (2021). The Taupō eruption sequence of AD 232 ± 10 in Aotearoa New Zealand: A retrospection. *Journal of Geography*, 130, 117–141.
<https://doi.org/10.5026/jgeography.130.117>

Lu, H., Cao, J., Guo, X., Gong, X., & Luo, C. (2020). Evaluation of powder tensile strength by compression, shear and fluidization modules of the powder rheometer. *Chemical Engineering Research and Design*, 160, 1–10. <https://doi.org/10.1016/j.cherd.2020.05.026>

Lu, H., Guo, X., Jin, Y., & Gong, X. (2018). Effect of moisture on flowability of pulverized coal. *Chemical Engineering Research and Design*, 133, 326–334. <https://doi.org/10.1016/j.cherd.2018.03.023>

Lu, M., Diao, Q.F., Zheng, Y.Y., Yin, Z.Y. & Dai, Z. (2024) Influence of water on tensile behavior of illite through the molecular dynamics method. *International Journal of Geomechanics*, 24(4). doi: 10.1061/IJGNAI.GMENG-8999

Lube, G., Breard, E. C. P., Cronin, S. J., & Jones, J. (2015). Synthesizing large-scale pyroclastic flows: Experimental design, scaling, and first results from PELE. *Journal of Geophysical Research: Solid Earth*, 120, 1487–1502. <https://doi.org/10.1002/2014JB011666>.

Lube, G., Breard, E. C., Esposti-Ongaro, T., Dufek, J., & Brand, B. (2020). Multiphase flow behaviour and hazard prediction of pyroclastic density currents. *Nature Reviews Earth & Environment*, 1(7), 348–365. <https://doi.org/10.1038/s43017-020-0064-8>

Lube, G., Breard, E.C., Jones, J., Fullard, L., Dufek, J., Cronin, S.J. and Wang, T. (2019) ‘Generation of air lubrication within pyroclastic density currents’, *Nature Geoscience*, 12(5), pp. 381–386. doi: 10.1038/s41561-019-0338-2.

Lucchi, F., Francalanci, L., De Astis, G., Tranne, C. A., Braschi, E., & Klaver, M. (2018). Geological evidence for recurrent collapse-driven phreatomagmatic pyroclastic density currents in the Holocene activity of Stromboli volcano, Italy. *Journal of Volcanology and Geothermal Research*.
<https://doi.org/10.1016/j.jvolgeores.2018.10>.

Lucchi, F., Sulpizio, R., Meschiari, S., Tranne, C. A., Albert, P. G., Mele, D., & Dellino, P. (2022). Sedimentological analysis of ash-rich pyroclastic density currents, with special emphasis on sin-depositional erosion and clast incorporation: The Brown Tuff eruptions (Vulcano, Italy). *Sedimentary Geology*, 427, 106040. <https://doi.org/10.1016/j.sedgeo.2021.106040>

- Ludwig, B., Millington-Smith, D., Dattani, R., Adair, J. H., Posatko, E. P., Mawby, L. M., Ward, S. K., & Sills, C. A. (2020). Evaluation of the hydrodynamic behaviour of powders of varying cohesivity in a fluidized bed using the FT4 Powder Rheometer®. *Powder Technology*, 371, 106–114. <https://doi.org/10.1016/j.powtec.2020.05.042>.
- Ma, Y., Evans, T. M., Phillips, N., & Cunningham, N. (2019). Modelling the effect of moisture on the flowability of a granular material. *Meccanica*, 54(4–5), 667–681. <https://doi.org/10.1007/s11012-018-0901-8>.
- Macri, D., Chirone, R., Salehi, H., Sofia, D., Materazzi, M., Barletta, D., Lettieri, P., & Poletto, M. (2020). Characterization of the bulk flow properties of industrial powders from shear tests. *Processes*, 8(5), Article 540. <https://doi.org/10.3390/PR8050540>
- Manga, M., Patel, A., & Dufek, J. (2011). Rounding of pumice clasts during transport: Field measurements and laboratory studies. *Bulletin of Volcanology*, 73(3), 321–333. <https://doi.org/10.1007/s00445-010-0411-6>
- Mangeney, A., Roche, O., Hungr, O., Mangold, N., Faccanoni, G., & Lucas, A. (2010). Erosion and mobility in granular collapse over sloping beds. *Journal of Geophysical Research*, 115, F02004. <https://doi.org/10.1029/2009JF001462>
- Mangeney, A., Tsimring, L. S., Volfson, D., Aranson, I. S., & Bouchut, F. (2007). Avalanche mobility induced by the presence of an erodible bed and associated entrainment. *Geophysical Research Letters*, 34, L22401. <https://doi.org/10.1029/2007GL031348>
- Manville, V., Segschneider, B., & White, J. D. L. (2002). Hydrodynamic behaviour of Taupo 1800a pumice: Implications for the sedimentology of remobilized pyroclasts. *Sedimentology*, 49(5), 955–976. <https://doi.org/10.1046/j.1365-3091.2002.00485.x>
- Marr, J. G., Harff, P. A., Shanmugam, G., & Parker, G. (2001). Experiments on subaqueous sandy gravity flows: The role of clay and water content in flow dynamics and depositional structures. *GSA Bulletin*, 113(11), 1377–1391. http://pubs.geoscienceworld.org/gsa/gsabulletin/article-pdf/113/11/1377/3384482/i0016-7606_113_11_1377.pdf
- Marschalko, R. (1970) The origin of disturbed structures in Carpathian turbidites. *Sedimentology*, 4, 5–18. doi: 10.1016/0037-0738(70)90002-3
- Massaro, L., Adam, J., Jonade, E., & Yamada, Y. (2022). New granular rock-analogue materials for simulation of multi-scale fault and fracture processes. *Geological Magazine*, 159(11-12), 2036–2059. <https://doi.org/10.1017/S0016756821001321>
- Massoudi, M., & Mehrabadi, M. M. (2001). A continuum model for granular materials: Considering dilatancy and the Mohr-Coulomb criterion. *Acta Mechanica*, 152(1-2), 121–138. <https://doi.org/10.1007/BF01176949>

- Matthews, A. J., Barclay, J., & Johnstone, J. E. (2009). The fast response of volcano-seismic activity to intense precipitation: Triggering of primary volcanic activity by rainfall at Soufrière Hills Volcano, Montserrat. *Journal of Volcanology and Geothermal Research*, 184(3–4), 405–415.
<https://doi.org/10.1016/j.jvolgeores.2009.05.010>
- McClelland, E., & Druitt, T. (1989). Palaeomagnetic estimates of emplacement temperatures of pyroclastic deposits on Santorini, Greece. *Bulletin of Volcanology*, 51, 16–27.
<https://doi.org/10.1007/BF01086758>
- McCoy, S. W., Kean, J. W., Coe, J. A., Tucker, G. E., Staley, D. M., & Wasklewicz, T. A. (2012). Sediment entrainment by debris flows: In situ measurements from the headwaters of a steep catchment. *Journal of Geophysical Research: Earth Surface*, 117(3). <https://doi.org/10.1029/2011JF002278>
- McCoy, S. W., Tucker, G. E., Kean, J. W., & Coe, J. A. (2013). Field measurement of basal forces generated by erosive debris flows. *Journal of Geophysical Research: Earth Surface*, 118, 589–602.
<https://doi.org/10.1002/jgrf.20041>
- McNutt, S. R., & Williams, E. R. (2010). Volcanic lightning: Global observations and constraints on source mechanisms. *Bulletin of Volcanology*, 72(10), 1153–1167. <https://doi.org/10.1007/s00445-010-0393-4>
- McPhie, J., Walker, G. P., & Christiansen, R. L. (1990). Phreatomagmatic and phreatic fall and surge deposits from explosions at Kilauea volcano, Hawaii, 1790 AD: Keanakakoi Ash Member. *Bulletin of Volcanology*, 52, 334–354. <https://doi.org/10.1007/BF00302047>
- McTaggart, K. C. (1960). The mobility of nuees ardentes. *American Journal of Science*, 258, 368–382.
- Meiburg, E. & Kneller, B. (2010) Turbidity Currents and Their Deposits. *Annual Review of Fluid Mechanics*, 42, 135–156. doi: 10.1146/annurev-fluid-121108-145618
- Mirabella, A., Egli, M., Raimondi, S., & Giaccai, D. (2005). Origin of clay minerals in soils on pyroclastic deposits in the island of Lipari (Italy). *Clays and Clay Minerals*, 53(4), 409–421.
<https://doi.org/10.1346/CCMN.2005.0530409>
- Mishra, I., Liu, P., Shetty, A., & Hrenya, C. M. (2020). On the use of a powder rheometer to probe defluidization of cohesive particles. *Chemical Engineering Science*, 214, 115422.
<https://doi.org/10.1016/j.ces.2019.115422>
- Mohseni, K. (2008). Surface tension, capillarity and contact angle. In D. Li (Ed.), *Encyclopedia of Microfluidics and Nanofluidics* (pp. 1507). Springer. https://doi.org/10.1007/978-0-387-48998-8_1507
- Moitra, P., Sonder, I., & Valentine, G. A. (2020). The role of external water on rapid cooling and fragmentation of magma. *Earth and Planetary Science Letters*, 537, 116194.
<https://doi.org/10.1016/j.epsl.2020.116194>

- Montanari, D., Agostini, A., Bonini, M., Corti, G., & Ventisette, C. D. (2017). The use of empirical methods for testing granular materials in analogue modelling. *Materials*, 10(6), 635. <https://doi.org/10.3390/ma10060635>
- Montserrat, S., Tamburrino, A., Roche, O., & Niño, Y. (2012). Pore fluid pressure diffusion in defluidizing granular columns. *Journal of Geophysical Research: Earth Surface*, 117(F2). <https://doi.org/10.1029/2011JF002164>
- Moondra, S., Maheshwari, R., Tanja, N., Tekade, M., & Tekadle, R. K. (2018). Bulk level properties and its role in formulation development and processing. In *Dosage Form Design Parameters* (pp. 221–256). Elsevier. <https://doi.org/10.1016/B978-0-12-814421-3.00006-3>
- Morrissey, M. M. & Mastin, L. G., (2000). *Encyclopedia of Volcanoes* (pp. 463). Academic Press.
- Morrissey, M. M., & Mastin, L. G. (2000). Moisture in pyroclastic density currents. *Journal of Volcanology and Geothermal Research*. [https://doi.org/10.1016/S0377-0273\(00\)00103-7](https://doi.org/10.1016/S0377-0273(00)00103-7)
- Moyer, T. C., & Swanson, D. A. (1987). Secondary hydroeruptions in pyroclastic-flow deposits: Examples from Mount St. Helens. *Journal of Volcanology and Geothermal Research*, 32(3), 299–319. [https://doi.org/10.1016/0377-0273\(87\)90081-3](https://doi.org/10.1016/0377-0273(87)90081-3)
- Mueller, S. B., Kueppers, U., Ametsbichler, J., Cimarelli, C., Merrison, J. P., Poret, M., Wadsworth, F. B., & Dingwell, D. B. (2017). Stability of volcanic ash aggregates and break-up processes. *Scientific Reports*, 7, 7440. <https://doi.org/10.1038/s41598-017-07927-w>
- Mueller, S. B., Kueppers, U., Ayris, P. M., Jacob, M., & Dingwell, D. B. (2016). Experimental volcanic ash aggregation: Internal structuring of accretionary lapilli and the role of liquid bonding. *Earth and Planetary Science Letters*, 433, 232–240. <https://doi.org/10.1016/j.epsl.2015.11.007>
- Mueller, S. B., Kueppers, U., Huber, M. S., Hess, K. U., Poesges, G., Ruthensteiner, B., & Dingwell, D. B. (2018). Aggregation in particle-rich environments: A textural study of examples from volcanic eruptions, meteorite impacts, and fluidized bed processing. *Bulletin of Volcanology*, 80(4). <https://doi.org/10.1007/s00445-018-1207-3>
- Mueller, S. B., Lane, S. J., & Kueppers, U. (2015). Lab-scale ash production by abrasion and collision experiments of porous volcanic samples. *Journal of Volcanology and Geothermal Research*.
- Mutti, E., & Nilsen, T. H. (1981). Significance of intraformational rip-up clasts in deep-sea fan deposits. *Abstracts International Association of Sedimentology*, 117-119.
- Nagasawa, K. (1978). Weathering of volcanic ash and other pyroclastic materials. In *Developments in Sedimentology* (Vol. 26, pp. 105-125). Elsevier. [https://doi.org/10.1016/S0070-4571\(08\)70683-6](https://doi.org/10.1016/S0070-4571(08)70683-6)

- Naismith, A., Armijos, M.T., Barrios Escobar, E.A., Chigna, W. & Watson, I.M. (2020) Fireside tales: Understanding experiences of previous eruptions and factors influencing the decision to evacuate from activity of Volcán de Fuego. *Volcanica*, 3(2), 205–226. doi: 10.30909/vol.03.02.205226
- Nemeth, K., Martin, U., & Harangi, S. (2001). Miocene phreatomagmatic volcanism at Tihany (Pannonian Basin, Hungary). *Journal of Volcanology and Geothermal Research*, 111, 111–135. [https://doi.org/10.1016/S0377-0273\(01\)00206-6](https://doi.org/10.1016/S0377-0273(01)00206-6)
- Niroumand, H. (2017). Chapter 3 - Research methodology. In H. Niroumand, *Soil Reinforcement for Anchor Plates and Uplift Response* (pp. 67–96). Butterworth-Heinemann.
- Nishimura, K., & Ito, Y. (1997). Velocity distribution in snow avalanches. *Journal of Geophysical Research: Solid Earth*, 102(B12), 27297–27303. <https://doi.org/10.1029/97JB02258>
- Nogueira, H. I. S., Adduce, C., Alves, E., & Franca, M. J. (2013). Analysis of lock-exchange gravity currents over smooth and rough beds. *Journal of Hydraulic Research*, 51(4), 417–431. <https://doi.org/10.1080/00221686.2013.798363>
- Noviandi, R., Gomi, T., Kharismalatri, H. S., Sidle, R. C., Ritonga, R. P., & Shiraki, K. (2022). The mobility of landslides in pumice: Insights from a flume experiment. *Water*, 14(19), 3083. <https://doi.org/10.3390/w14193083>
- Ongaro, T. E., Barsotti, S., Neri, A., & Salvetti, M. V. (2011). Large-eddy simulation of pyroclastic density currents. In M. Salvetti, B. Geurts, J. Meyers, & P. Sagaut (Eds.), *Quality and Reliability of Large-Eddy Simulations II* (pp. 15). https://doi.org/10.1007/978-94-007-0231-8_15
- Ongaro, T. E., Clarke, A. B., Voight, B., Neri, A., & Widiwijayanti, C. (2012). Multiphase flow dynamics of pyroclastic density currents during the May 18, 1980 lateral blast of Mount St. Helens. *Journal of Geophysical Research: Solid Earth*, 117(B6). <https://doi.org/10.1029/2011JB009081>
- Ongaro, T. E., Neri, A., Todesco, M., et al. (2002). Pyroclastic flow hazard assessment at Vesuvius (Italy) by using numerical modelling. II. Analysis of flow variables. *Bulletin of Volcanology*, 64, 178–191. <https://doi.org/10.1007/s00445-001-0190-1>
- Osman, S., Thomas, M., Crummy, J., et al. (2022). Investigation of geomechanical properties of tephra relevant to roof loading for application in vulnerability analyses. *Journal of Applied Volcanology*, 11(9). <https://doi.org/10.1186/s13617-022-00121-2>
- Pacheco-Hoyos, J. G., Aguirre-Díaz, G. J., & Dávila-Harris, P. (2020). Elutriation pipes in ignimbrites: An analysis of concepts based on the Huichapan Ignimbrite, Mexico. *Journal of Volcanology and Geothermal Research*, 403, 107026. <https://doi.org/10.1016/j.jvolgeores.2020.107026>
- Pähtz, T., Clark, A. H., Valyrakis, M., & Durán, O. (2020). The physics of sediment transport initiation, cessation, and entrainment across aeolian and fluvial environments. *Reviews of Geophysics*, 58, e2019RG000679. <https://doi.org/10.1029/2019RG000679>

- Palladino, D. M., & Valentine, G. A. (1995). Coarse-tail vertical and lateral grading in pyroclastic flow deposits of the Lateral Volcanic Complex (Vulsini, central Italy): Origin and implications for flow dynamics. *Journal of Volcanology and Geothermal Research*, 69(3–4), 343–364.
[https://doi.org/10.1016/0377-0273\(95\)00036-4](https://doi.org/10.1016/0377-0273(95)00036-4)
- Pardo, N., Cronin, S. J., Németh, K., Brenna, M., Schipper, C. I., Breard, E., & Wallace, C. (2014). Perils in distinguishing phreatic from phreatomagmatic ash; insights into the eruption mechanisms of the 6 August 2012 Mt. Tongariro eruption, New Zealand. *Journal of Volcanology and Geothermal Research*, 286, 397–414. <https://doi.org/10.1016/j.jvolgeores.2014.05.001>
- Parker, G., Garcia, M., Fukushima, Y., & Yu, W. (1987). Experiments on turbidity currents over an erodible bed. *Journal of Hydraulic Research*, 25(1), 123–147.
<https://doi.org/10.1080/00221688709499292>
- Pensa, A., Giordano, G., Corrado, S., & Petrone, P. P. (2023). A new hazard scenario at Vesuvius: Deadly thermal impact of detached ash cloud surges in 79 CE at Herculaneum. *Scientific Reports*, 13, 5622.
<https://doi.org/10.1038/s41598-023-32623-3>
- Pepin, N. C., Pike, G., Schaefer, M., Boston, C. M., & Lovell, H. (2017). A comparison of simultaneous temperature and humidity observations from the SW and NE slopes of Kilimanjaro: The role of slope aspect and differential land-cover in controlling mountain climate. *Global and Planetary Change*, 157, 244–258. <https://doi.org/10.1016/j.gloplacha.2017.08.006>
- Pierrat, P., & Caram, H. S. (1997). Tensile strength of wet granular materials. *Powder Technology*, 97(2), 83–93. [https://doi.org/10.1016/S0032-5910\(96\)03179-8](https://doi.org/10.1016/S0032-5910(96)03179-8)
- Pittari, A., Cas, R. A. F., Edgar, C. J., Nichols, H. J., Wolff, J. A., & Martí, J. (2006). The influence of palaeotopography on facies architecture and pyroclastic flow processes of a lithic-rich ignimbrite in a high gradient setting: The Abrigo Ignimbrite, Tenerife, Canary Islands. *Journal of Volcanology and Geothermal Research*, 152(3–4), 273–315. <https://doi.org/10.1016/j.jvolgeores.2005.10.007>
- Pola, A., Crosta, G., Fusi, N., Barberini, V. & Norini, G. (2012) Influence of alteration on physical properties of volcanic rocks. *Tectonophysics*, 566–567, 67–86. doi: 10.1016/j.tecto.2012.07.017
- Pollock, N. M., Brand, B. D., & Roche, O. (2016). The controls and consequences of substrate entrainment by pyroclastic density currents at Mount St Helens, Washington (USA). *Journal of Volcanology and Geothermal Research*, 325, 135–147. <https://doi.org/10.1016/j.jvolgeores.2016.08.005>
- Pollock, N. M., Brand, B. D., Rowley, P. J., et al. (2019). Inferring pyroclastic density current flow conditions using syn-depositional sedimentary structures. *Bulletin of Volcanology*, 81, 46.
<https://doi.org/10.1007/s00445-019-1303-z>

- Prentice, J. E. (1956). The interpretation of flow-markings and load-casts. *Geological Magazine*, 93(5), 393–400. <https://doi.org/10.1017/S0016756800066838>
- R Core Team. (2023). *R: A language and environment for statistical computing*. R Foundation for Statistical Computing, Vienna, Austria. <https://www.R-project.org/>
- R Package Version 1.0.7. <https://CRAN.R-project.org/package=factoextra>
- Reber, J. E., Cooke, M. L., & Dooley, T. P. (2020). What model material to use? A review on rock analogs for structural geology and tectonics. *Earth-Science Reviews*, 202, 103107. <https://doi.org/10.1016/j.earscirev.2020.103107>
- Reimer, T. O. (1983). Accretionary lapilli in volcanic ash falls: Physical factors governing their formation. In *Coated grains* (pp. 56–68). Springer Berlin Heidelberg.
- Riehle, J. R., Miller, T. F., & Bailey, R. A. (1995). Cooling, degassing, and compaction of rhyolitic ash flow tufts: A computational model.
- Rios, M. (2006). Developments in powder flow testing. *Pharmaceutical Technology*, 30(2), 38–49.
- Ripp, M., & Ripperger, S. (2010). Influence of temperature on the flow properties of bulk solids. *Chemical Engineering Science*, 65(13), 4007–4013. <https://doi.org/10.1016/j.ces.2010.03.046>
- Risica, G., Rosi, M., Pistolesi, M., Speranza, F., & Branney, M. J. (2022). Deposit-derived block-and-ash flows: The hazard posed by perched temporary tephra accumulations on volcanoes; 2018 Fuego disaster, Guatemala. *Journal of Geophysical Research: Solid Earth*, 127, e2021JB023699. <https://doi.org/10.1029/2021JB023699>
- Roberts, J., Jepsen, R., Gotthard, D., & Lick, W. (1998). Effects of particle size and bulk density on erosion of quartz particles. *Journal of Hydraulic Engineering*, 124(12), 1261–1267. [https://doi.org/10.1061/\(ASCE\)0733-9429\(1998\)124:12\(1261\)](https://doi.org/10.1061/(ASCE)0733-9429(1998)124:12(1261))
- Roche, O., Gilbertson, M., Phillips, J. C., & Sparks, R. S. J. (2002). Experiments on deaerating granular flows and implications for pyroclastic flow mobility. *Geophysical Research Letters*, 29(16). <https://doi.org/10.1029/2002GL014819>
- Roche, O. (2012). Depositional processes and gas pore pressure in pyroclastic flows: An experimental perspective. *Bulletin of Volcanology*, 74, 1807–1820. <https://doi.org/10.1007/s00445-012-0639-4>
- Roche, O., Azzaoui, N., & Guillin, A. (2021). Discharge rate of explosive volcanic eruption controls runout distance of pyroclastic density currents. *Earth and Planetary Science Letters*, 568, 117017. <https://doi.org/10.1016/j.epsl.2021.117017>
- Roche, O., Druitt, T. H., & Cas, R. A. F. (2001). Experimental aqueous fluidization of ignimbrite. *Journal of Volcanology and Geothermal Research*, 112(1–4), 267–280. [https://doi.org/10.1016/S0377-0273\(01\)00246-3](https://doi.org/10.1016/S0377-0273(01)00246-3)

- Roche, O., Gilbertson, M. A., Phillips, J. C., & Sparks, R. S. J. (2004). Experimental study of gas-fluidized granular flows with implications for pyroclastic flow emplacement. *Journal of Geophysical Research: Solid Earth*, 109(B10). <https://doi.org/10.1029/2003JB002916>
- Roche, O., Montserrat, S., Niño, Y., & Tamburrino, A. (2008). Experimental observations of water-like behavior of initially fluidized, dam break granular flows and their relevance for the propagation of ash-rich pyroclastic flows. *Journal of Geophysical Research*, 113, B12203. <https://doi.org/10.1029/2008JB005664>
- Roche, O., Montserrat, S., Niño, Y., & Tamburrino, A. (2010). Pore fluid pressure and internal kinematics of gravitational laboratory air-particle flows: Insights into the emplacement dynamics of pyroclastic flows. *Journal of Geophysical Research: Solid Earth*, 115(B9). <https://doi.org/10.1029/2009JB007133>
- Roche, O., Niño, Y., Mangeney, A., Brand, B., Pollock, N., & Valentine, G. A. (2013). Dynamic pore-pressure variations induce substrate erosion by pyroclastic flows. *Geology*, 41(10), 1107–1110. <https://doi.org/10.1130/G34668.1>
- Rodriguez-Sedano, L. A., Sarocchi, D., Sulpizio, R., Borselli, L., Campos, G., & Moreno Chavez, G. (2016). Influence of particle density on flow behavior and deposit architecture of concentrated pyroclastic density currents over a break in slope: Insights from laboratory experiments. *Journal of Volcanology and Geothermal Research*, 328, 178–186. <https://doi.org/10.1016/j.jvolgeores.2016.10.017>
- Rose, W. I., & Durant, A. J. (2009). Fine ash content of explosive eruptions. *Journal of Volcanology and Geothermal Research*, 186(1–2), 32–39. <https://doi.org/10.1016/j.jvolgeores.2009.01.010>
- Rossano, S., Mastrolorenzo, G. & De Natale, G. (2004) Numerical simulation of pyroclastic density currents on Campi Flegrei topography: A tool for statistical hazard estimation. *Journal of Volcanology and Geothermal Research*, 132(1), 1–14. doi: 10.1016/S0377-0273
- Rossi, E., Bagheri, G., Beckett, F., & Bonadonna, C. (2021). The fate of volcanic ash: Premature or delayed sedimentation? *Nature Communications*, 12(1). <https://doi.org/10.1038/s41467-021-21568-8>
- Rowley, P. (2010). Analogue modelling of pyroclastic density current deposition (PhD thesis, Royal Holloway, University of London). Available at: http://royalholloway.academia.edu/PeteRowley/Papers/159481/Analogue_modelling_of_pyroclastic_density_current_deposition
- Rowley, P. J., Kokelaar, P., Menzies, M., & Waltham, D. (2011). Shear-derived mixing in dense granular flows. *Journal of Sedimentary Research*, 81(12), 874–884. <https://doi.org/10.2110/jsr.2011.72>
- Rowley, P. J., Roche, O., Druitt, T. H., et al. (2014). Experimental study of dense pyroclastic density currents using sustained, gas-fluidized granular flows. *Bulletin of Volcanology*, 76, 855. <https://doi.org/10.1007/s00445-014-0855-1>

- Rowley, P., Williams, R., Johnson, M., Johnston, T., Dowey, N., Parsons, D., Provost, A., Roche, O., Smith, G., & Walding, N. (2023). Spontaneous unsteadiness and sorting in pyroclastic density currents and their deposits. <https://doi.org/10.31223/X51M32>
- Rowley, P., Roche, O., Druitt, T. & Cas, Raymond. (2014). Experimental study of dense pyroclastic density currents using sustained, gas-fluidized granular flows. *Bulletin of Volcanology*, 76, 855-868. 10.1007/s00445-014-0855-1.
- Sahoo, S., Tiwari, D. K., Panda, D., & Kundu, B. (2022). Eruption cycles of Mount Etna triggered by seasonal climatic rainfall. *Journal of Geodynamics*, 149. <https://doi.org/10.1016/j.jog.2021.101896>
- Salatino, P., Bareschino, P., Marzocchella, A., & Petrosino, P. (2024). Fluidization in pyroclastic flows. *Powder Technology*, 439. <https://doi.org/10.1016/j.powtec.2024.119685>
- Sanford, L., & Maa, J. P. Y. (2001). A unified erosion formulation for fine sediments. *Marine Geology*, 179(1–2), 9–23. [https://doi.org/10.1016/S0025-3227\(01\)00201-8](https://doi.org/10.1016/S0025-3227(01)00201-8)
- Scharff, L., Hort, M., & Varley, N. R. (2019). First in-situ observation of a moving natural pyroclastic density current using Doppler radar. *Scientific Reports*, 9, 7386. <https://doi.org/10.1038/s41598-019-43620-w>
- Schindelin, J., Arganda-Carreras, I., Frise, E., Kaynig, V., Longair, M., Pietzsch, T., et al. (2012). Fiji: An open-source platform for biological-image analysis. *Nature Methods*, 9(7), 676–682. <https://doi.org/10.1038/nmeth.2019>
- Schneider, C. A., Rasband, W. S., & Eliceiri, K. W. (2012). NIH Image to ImageJ: 25 years of image analysis. *Nature Methods*, 9, 671–675. <https://doi.org/10.1038/nmeth.2089>
- Schumacher, R., & Schmincke, H.-U. (1991). Internal structure and occurrence of accretionary lapilli: A case study at Laacher See volcano. *Bulletin of Volcanology*, 53.
- Schumacher, R., & Schmincke, H.-U. (1995). Models for the origin of accretionary lapilli. *Bulletin of Volcanology*, 56, 626–639. <https://doi.org/10.1007/BF00301467>
- Scott, A. C., & Glasspool, I. J. (2005). Charcoal reflectance as a proxy for the emplacement temperature of pyroclastic flow deposits. *Geology*, 33(7), 589–592. <https://doi.org/10.1130/G21474.1>
- Scott, A. C., Sparks, R. S. J., Bull, I. D., Knicker, H., & Evershed, R. P. (2008). Temperature proxy data and their significance for the understanding of pyroclastic density currents. *Geology*, 36(2), 143–146. <https://doi.org/10.1130/G24439A.1>
- Scott, W. E., Hoblitt, R. P., Torres, R. C., Self, S., Martinez, M. L., & Nillos, T. J. (1996). Pyroclastic flows of the June 15, 1991, climactic eruption of Mount Pinatubo. In C. G. Newhall & S. Punongbayan (Eds.), *Fire and mud: eruptions of Pinatubo, Philippines* (pp. 545–570). Philippine Institute for Volcanology and Seismology, Quezon City, and University of Washington Press, Seattle.

- Self, S., & Sparks, R. S. J. (1978). Characteristics of widespread pyroclastic deposits formed by the interaction of silicic magma and water. *Bulletin of Volcanology*, 41, 196–212.
<https://doi.org/10.1007/BF02597223>
- Sequeiros, O. E., Mosquera, R. L., & Pedocchi, F. (2018). Internal structure of a self-accelerating turbidity current. *Journal of Geophysical Research: Oceans*, 123, 6260–6276.
<https://doi.org/10.1029/2018JC014061>
- Shakor, P., Chu, S. H., Puzatova, A., & Dini, E. (2022). Review of binder jetting 3D printing in the construction industry. *Progress in Additive Manufacturing*, 7. <https://doi.org/10.1007/s40964-021-00252-9>
- Shang, X. Y., Zhao, K., Qian, W. X., Zhu, Q. Y., & Zhou, G. Q. (2020). On the calculation of van der Waals force between clay particles. *Minerals*, 10(11), 1–15. <https://doi.org/10.3390/min10110993>
- Shanmugam, G. (2017). Global case studies of soft-sediment deformation structures (SSDS): Definitions, classifications, advances, origins, and problems. *Journal of Palaeogeography*, 6(4), 251–320.
<https://doi.org/10.1016/j.jop.2017.06.004>
- Shea, T., & van Wyk de Vries, B. (2008). Structural analysis and analogue modeling of the kinematics and dynamics of rockslide avalanches. *Geosphere*, 4(4), 657–686. <https://doi.org/10.1130/GES00131.1>
- Sheng, D., Zhou, A., & Fredlund, D. G. (2011). Shear strength criteria for unsaturated soils. *Geotechnical and Geological Engineering*, 29, 145–159. <https://doi.org/10.1007/s10706-009-9276-x>
- Shimizu, H. A., Koyaguchi, T., & Suzuki, Y. J. (2019). The run-out distance of large-scale pyroclastic density currents: A two-layer depth-averaged model. *Journal of Volcanology and Geothermal Research*, 381, 168–184. <https://doi.org/10.1016/j.jvolgeores.2019.03.013>
- Shimizu, H. A., Koyaguchi, T., & Suzuki, Y. J. (2023). Dynamics and deposits of pyroclastic density currents in magmatic and phreatomagmatic eruptions revealed by a two-layer depth-averaged model. *Geophysical Research Letters*, 50(16), 616. <https://doi.org/10.1029/2023GL104616>
- Sigurdsson, H., & Carey, S. (1989). Plinian and co-ignimbrite tephra fall from the 1815 Tambora eruption. *Bulletin of Volcanology*, 51(4), 243–270. <https://doi.org/10.1007/BF01073515>
- Sigurdsson, H., Carey, S. N., & Espindola, J. M. (1984). The 1982 eruptions of El Chichón Volcano, Mexico: Stratigraphy of pyroclastic deposits. *Journal of Volcanology and Geothermal Research*, 23(1–2), 11–37. [https://doi.org/10.1016/0377-0273\(84\)90055-6](https://doi.org/10.1016/0377-0273(84)90055-6)
- Silva Parejas, C., Druitt, T. H., Robin, C., et al. (2010). The Holocene Pucón eruption of Volcán Villarrica, Chile: Deposit architecture and eruption chronology. *Bulletin of Volcanology*, 72, 677–692.
<https://doi.org/10.1007/s00445-010-0348-9>

- Skinner, A. E. (1969). A note on the influence of interparticle friction on the shearing strength of a random assembly of spherical particles. *Géotechnique*, 19(1), 150–157.
<https://doi.org/10.1680/geot.1969.19.1.150>
- Smith, G. M., Williams, R., Rowley, P. J., et al. (2018). Investigation of variable aeration of monodisperse mixtures: Implications for pyroclastic density currents. *Bulletin of Volcanology*, 80, 67.
<https://doi.org/10.1007/s00445-018-1241-1>
- Smith, G., Rowley, P., Williams, R., et al. (2020). A bedform phase diagram for dense granular currents. *Nature Communications*, 11, 2873. <https://doi.org/10.1038/s41467-020-16657-z>
- Smith, G., Williams, R., & Rowley, P. (2023). Characterising the flow-boundary zone in fluidised granular currents.
- Smith, N. J., & Kokelaar, B. P. (2013). Proximal record of the 273 ka Poris caldera-forming eruption, Las Cañadas, Tenerife. *Bulletin of Volcanology*, 75, 768. <https://doi.org/10.1007/s00445-013-0768-4>
- Smith, R. L. (1960). Ash flows. *Geological Society of America Bulletin*, 71(6), 795.
[https://doi.org/10.1130/0016-7606\(1960\)71\[795\]2.0.co;2](https://doi.org/10.1130/0016-7606(1960)71[795]2.0.co;2)
- Sosio, R., & Crosta, G. (2009). Rheology of concentrated granular suspensions and possible implications for debris flow modelling. *Water Resources Research*, 45(3). <https://doi.org/10.1029/2008WR006920>
- Sparks RSJ, Walker GPL (1977) The significance of vitric-enriched air-fall ashes associated with crystal-enriched ignimbrites. *J Volcanol Geotherm Res* 2(4):329–341. [https://doi.org/10.1016/0377-0273\(77\)90019-1](https://doi.org/10.1016/0377-0273(77)90019-1)
- Sparks, R. S. J. (1976). Grain size variations in ignimbrites and implications for the transport of pyroclastic flows. *Sedimentology*, 23(2), 147–188. <https://doi.org/10.1111/j.1365-3091.1976.tb00045.x>
- Sparks, R. S. J. (1978). Gas release rates from pyroclastic flows: An assessment of the role of fluidisation in their emplacement. *Bulletin of Volcanology*, 41(1), 1–9. <https://doi.org/10.1007/BF02597679>
- Sparks, R. S. J., & Wilson, C. J. N. (1990). The Minoan deposits: A review of their characteristics and interpretation. In D. A. Hardy (Ed.), *Thera and the World III*. The Thera Foundation Aegean.
- Sparks, R. S. J., Self, S., & Walker, G. P. L. (1973). Products of ignimbrite eruptions. *Geology*, 1(3), 115–118. [https://doi.org/10.1130/0091-7613\(1973\)12.0.CO;2](https://doi.org/10.1130/0091-7613(1973)12.0.CO;2)
- Sparks, R., Gardeweg, M., Calder, E., et al. (1997). Erosion by pyroclastic flows on Lascar Volcano, Chile. *Bulletin of Volcanology*, 58, 557–565. <https://doi.org/10.1007/s004450050162>
- Sparks, R. (2003). Dynamics of magma degassing. Geological Society, London, Special Publications. 213. 5-22. 10.1144/GSL.SP.2003.213.01.02.

- Spieler, O., Kennedy, B., Kueppers, U., Dingwell, D. B., Scheu, B., & Taddeucci, J. (2004). The fragmentation threshold of pyroclastic rocks. *Earth and Planetary Science Letters*, 226(1–2), 139–148. <https://doi.org/10.1016/j.epsl.2004.07.016>
- Sulpizio, R. (2005). Lithofacies and lithofacies architecture analyses in the study of pyroclastic density current deposits. *Acta Vulcanologica: Journal of the National Volcanic Group of Italy*, 17(1/2), 1000–1015.
- Sulpizio, R., & Dellino, P. (2008). Chapter 2: Sedimentology, depositional mechanisms and pulsating behaviour of pyroclastic density currents. In *Developments in Volcanology*, 10, 57–96. [https://doi.org/10.1016/S1871-644X\(07\)00002-2](https://doi.org/10.1016/S1871-644X(07)00002-2)
- Sulpizio, R., Dellino, P., Doronzo, D. M., & Sarocchi, D. (2014). Pyroclastic density currents: State of the art and perspectives. *Journal of Volcanology and Geothermal Research*, 283, 36–65. <https://doi.org/10.1016/j.jvolgeores.2014.06.014>
- Supandi, Zakaria, Z., Sukiyah, E. & Sudradjat, A. (2019) The influence of kaolinite-illite toward mechanical properties of claystone. *Open Geosciences*, 11, 440–446. doi: 10.1515/geo-2019-0035
- Talling, P. J., Paull, C. K., & Piper, D. J. W. (2013). How are subaqueous sediment density flows triggered, what is their internal structure and how does it evolve? Direct observations from monitoring of active flows. *Earth-Science Reviews*, 125, 244–287. <https://doi.org/10.1016/j.earscirev.2013.07.005>
- Telling, J., Dufek, J., & Shaikh, A. (2013). Ash aggregation in explosive volcanic eruptions. *Geophysical Research Letters*, 40(10), 2355–2360. <https://doi.org/10.1002/grl.50376>
- The United States Pharmacopeial Convention. (2015). Bulk density and tapped density of powders - US Pharmacopeia (USP), (616) Bulk Density and Tapped Density of Powders. Available at: https://www.usp.org/sites/default/files/usp/document/harmonization/gen-chapter/bulk_density.pdf (Accessed: 02 June 2023).
- Torres, R. C., Self, S., & Martinez, M. M. L. (1996). Secondary pyroclastic flows from the June 15, 1991, ignimbrite of Mount Pinatubo. In C. G. Newhall & R. S. Punongbayan (Eds.), *Fire and mud: Eruptions and lahars of Mount Pinatubo, Philippines* (pp. 625–678). Seattle: University of Washington Press.
- Turowski, J. M., Pruß, G., Voigtländer, A., Ludwig, A., Landgraf, A., Kober, F., and Bonnelye, A.: Geotechnical controls on erodibility in fluvial impact erosion, *Earth Surf. Dynam.*, 11, 979–994, <https://doi.org/10.5194/esurf-11-979-2023>, 2023.
- Vahidi-Nia, F., Bayesteh, H., & Khodaparast, M. (2020). Effect of initial packing density, stress level and particle size ratio on the behavior of binary granular material: A micromechanical approach. *Granular Matter*, 22, 68. <https://doi.org/10.1007/s10035-020-01036-8>

- Vale, A. B., Jenkins, L. T., Phillips, J. C., Rust, A. C., Hogg, A. J., Kilgour, G., & Seward, A. (2024). Heat transfer in pyroclastic density current-ice interactions: Insights from experimental and numerical simulations. *Journal of Geophysical Research: Solid Earth*, 129(6).
<https://doi.org/10.1029/2024JB029321>
- Valentine, G.A., & Wohletz, K.H. (1989). Numerical models of Plinian eruption columns and pyroclastic flows. *Journal of Geophysical Research*, 94, 1867-1887.
- Valentine, G. A. (2020). Initiation of dilute and concentrated pyroclastic currents from collapsing mixtures and origin of their proximal deposits. *Bulletin of Volcanology*, 82, 20.
<https://doi.org/10.1007/s00445-020-1366-x>
- Valentine, G. A. (1987). Stratified flow in pyroclastic surges. *Bulletin of Volcanology*, 49, 616–630.
<https://doi.org/10.1007/BF01079967>
- Valentine, G. A. (1998). Damage to structures by pyroclastic flows and surges, inferred from nuclear weapons effects. *Journal of Volcanology and Geothermal Research*, 87.
- Valentine, G. A., Buesch, D. C., & Fisher, R. V. (1989). Basal layered deposits of the Peach Springs Tuff, northwestern Arizona, USA. *Bulletin of Volcanology*, 51, 395–414. <https://doi.org/10.1007/BF01079967>
- Valentine, G., & Sweeney, M. (2018). Compressible flow phenomena at inception of lateral density currents fed by collapsing gas-particle mixtures. *Journal of Geophysical Research: Solid Earth*, 123(2), 1286–1302. <https://doi.org/10.1002/2017JB015129>
- Valverde, J. M., & Soria-Hoyo, C. (2015). Vibration-induced dynamical weakening of pyroclastic flows: Insights from rotating drum experiments. *Journal of Geophysical Research: Solid Earth*, 120(9), 6182–6190. <https://doi.org/10.1002/2015JB012317>
- Valyrakis, M., Diplas, P., Dancey, C. L., Greer, K., & Celik, A. O. (2010). Role of instantaneous force magnitude and duration on particle entrainment. *Journal of Geophysical Research: Earth Surface*, 115(F2). <https://doi.org/10.1029/2010JF001721>
- Van Eaton, A. R., & Wilson, C. J. N. (2012). What is the role of pyroclastic density currents in volcanic ash aggregation? Perspectives from a phreatoplinian eruption deposit, New Zealand. In *AGU Fall Meeting Abstracts* (Vol. 2012: V41B-2789). <https://doi.org/10.2012AGUFM.V41B2789V>
- Van Eaton, A. R., & Wilson, C. J. N. (2013). The nature, origins and distribution of ash aggregates in a large-scale wet eruption deposit: Oruanui, New Zealand. *Journal of Volcanology and Geothermal Research*, 250, 129–154. <https://doi.org/10.1016/j.jvolgeores.2012.10.016>
- van Westen, C. J., & Daag, A. S. (2005). Analysing the relation between rainfall characteristics and lahar activity at Mount Pinatubo, Philippines. *Earth Surface Processes and Landforms*, 30(13), 1663–1674.
<https://doi.org/10.1002/esp.1225>

- Vecino, M. C. D., Rossi, E., Freret-Logeril, V., Fries, A., Gabellini, P., Lemus, J., Pollastri, S., Poulidis, A. P., Iguchi, M., & Bonadonna, C. (2022). Aerodynamic characteristics and genesis of aggregates at Sakurajima Volcano, Japan. *Scientific Reports*, 14. <https://doi.org/10.1038/s41598-022-05854-z>
- Verhagen, I. T. E., Baas, J. H., Jacinto, R. S., et al. (2013). A first classification scheme of flow-bed interaction for clay-laden density currents and soft substrates. *Ocean Dynamics*, 63, 385–397. <https://doi.org/10.1007/s10236-013-0602-8>
- Walder, J. S. (2000a). Pyroclast/snow interactions and thermally driven slurry formation. Part 1: Theory for monodisperse grain beds. Retrieved from <http://link.springer.de/link/service/>
- Walder, J. S. (2000b). Pyroclast/snow interactions and thermally driven slurry formation. Part 2: Experiments and theoretical extension to polydisperse tephra (Vol. 62). Springer-Verlag. Retrieved from <http://link.springer.de/link/service/>
- Walding, N. (2022). Exploring pyroclastic density currents with analogue models. *Nature Reviews Earth and Environment*, 3(8), 499. <https://doi.org/10.1038/s43017-022-00365-0>
- Walding, N., Williams, R., Rowley, P., et al. (2023). Cohesional behaviours in pyroclastic material and the implications for deposit architecture. *Bulletin of Volcanology*, 85, 67. <https://doi.org/10.1007/s00445-023-01682-9>
- Walding, N., Williams, R., Rowley, P., et al. (in press). Behaviours of pyroclastic and analogue materials in dry and wet environments for use in experimental modelling of pyroclastic density currents. *Volcanica*. Accepted on 27/09/24.
- Walker, G. P. L. (1981). Generation and dispersal of fine ash and dust by volcanic eruptions. In *Journal of Volcanology and Geothermal Research* (Vol. 11). [https://doi.org/10.1016/0377-0273\(81\)90080-3](https://doi.org/10.1016/0377-0273(81)90080-3)
- Weit, A., Roche, O., Dubois, T., & Manga, M. (2019). Maximum solid phase concentration in geophysical turbulent gas-particle flows: Insights from laboratory experiments. *Geophysical Research Letters*, 46(12), 6388–6396. <https://doi.org/10.1029/2019GL082658>
- Whelley, P. L., Jay, J., Calder, E. S., Pritchard, M. E., Cassidy, N. J., Alcaraz, S., & Pavez, A. (2012). Post-depositional fracturing and subsidence of pumice flow deposits: Lascar Volcano, Chile. *Bulletin of Volcanology*, 74(2), 511–531. <https://doi.org/10.1007/s00445-011-0545-1>
- Wibowo, H. E., Purnama Edra, A., Harijoko, A., & Anggara, F. (2018). Emplacement temperature of the overbank and dilute-detached pyroclastic density currents of Merapi 5 November 2010 events using reflectance analysis of associated charcoal. *Journal of Applied Geology*, 3(1), 41. <https://doi.org/10.22146/jag.42445>
- Wickham, H. (2009). *ggplot2: Elegant graphics for data analysis*. Springer-Verlag New York.

- Williams, R., Branney, M. J., & Barry, T. L. (2014). Temporal and spatial evolution of a waxing then waning catastrophic density current revealed by chemical mapping. *Geology*, 42(2), 107–110. <https://doi.org/10.1130/G34830.1>
- Wilson, C. J. N. (1980). The role of fluidization in the emplacement of pyroclastic flows: An experimental approach. *Journal of Volcanology and Geothermal Research*, 231–249. [https://doi.org/10.1016/0377-0273\(80\)90016-7](https://doi.org/10.1016/0377-0273(80)90016-7)
- Wilson, C. J. N. (1984). The role of fluidization in the emplacement of pyroclastic flows, 2: Experimental results and their interpretation. *Journal of Volcanology and Geothermal Research*, 20(1–2), 55–84. [https://doi.org/10.1016/0377-0273\(84\)90066-0](https://doi.org/10.1016/0377-0273(84)90066-0)
- Wilson, C. J. N. (1985). The Taupo eruption, New Zealand. II. The Taupo Ignimbrite. *Philosophical Transactions of the Royal Society of London A: Mathematical, Physical and Engineering Sciences*, 314, 229–310. <https://doi.org/10.1098/rsta.1985.0020>
- Wilson, C. J. N. (1993). Stratigraphy, chronology, styles and dynamics of late Quaternary eruptions from Taupo volcano, New Zealand. *Philosophical Transactions of the Royal Society of London A: Physical, Engineering and Science*, 343(1668), 205–306. <https://doi.org/10.1098/rsta.1993.0050>
- Wilson, G., Wilson, T. M., Deligne, N. I., & Cole, J. W. (2014). Volcanic hazard impacts to critical infrastructure: A review. *Journal of Volcanology and Geothermal Research*, 286, 148–182. <https://doi.org/10.1016/j.jvolgeores.2014.08.030>
- Wohletz, K. H. (1983). Explosive volcanism. In *Journal of Volcanology and Geothermal Research* (Vol. 17). [https://doi.org/10.1016/0377-0273\(83\)90014-4](https://doi.org/10.1016/0377-0273(83)90014-4)
- Woods, A. W., Bursik, M. I., & Kurbatov, A. V. (1998). The interaction of ash flows with ridges. *Bulletin of Volcanology*, 60(1), 38–51. <https://doi.org/10.1007/s004450050215>
- Wormsbecker, M., & Pugsley, T. (2008). The influence of moisture on the fluidization behaviour of porous pharmaceutical granules. *Chemical Engineering Science*, 63(16), 4063–4069. <https://doi.org/10.1016/j.ces.2008.05.023>
- Wright, J. V., & Walker, G. P. L. (1981). Eruption, transport and deposition of ignimbrite: A case study from Mexico. *Journal of Volcanology and Geothermal Research*, 9(2–3), 111–131. [https://doi.org/10.1016/0377-0273\(81\)90001-9](https://doi.org/10.1016/0377-0273(81)90001-9)
- Wright, J. V., Smith, A. L., & Self, S. (1981). A terminology for pyroclastic deposits. In S. Self & R. S. J. Sparks (Eds.), *Tephra studies* (NATO Advanced Study Institutes Series, Vol. 75). Springer. https://doi.org/10.1007/978-94-009-8537-7_33
- Xu., Y. (2019). Approach to the erosion threshold of cohesive sediments, *Ocean Engineering*, 172:183–190, <https://doi.org/10.1016/j.oceaneng.2018.11.036>.

- Yamamoto, T., Nakamura, Y., & Glicken, H. (1999). Pyroclastic density current from the 1888 phreatic eruption of Bandai volcano, NE Japan. *Journal of Volcanology and Geothermal Research*, 90(3–4), 191–207. [https://doi.org/10.1016/S0377-0273\(99\)00025-6](https://doi.org/10.1016/S0377-0273(99)00025-6)
- Yang, T., Sun, H., Cao, Y., Luo, C., & Dodd, T. J. H. (2024). Gravel-inlaid mud clasts as indicators of transport processes of subaqueous sediment gravity flows. *Sedimentology*, 472, 0037–0738. <https://doi.org/10.1016/j.sedgeo.2024.106741>
- Yehuda, T., & Kalman, H. (2020). Geldart classification for wet particles. *Powder Technology*, 362, 288–300. <https://doi.org/10.1016/j.powtec.2019.11.073>
- Yu, A. B., & Hall, J. S. (1994). Packing of fine powders subjected to tapping. *Journal of Powder Technology*, 10.
- Zhou, X., Kuiper, K. F., Wijbrans, J. R., Boehm, K., & Vroon, P. (2020). Eruptive history and $^{40}\text{Ar}/^{39}\text{Ar}$ geochronology of the Milos volcanic field, Greece. *EGU Geochronology*, 3(1), 273–297. <https://doi.org/10.5194/gchron-2020-30>
- Zimanowski, B., Büttner, R., Lorenz, V., & Häfele, H. G. (1997). Fragmentation of basaltic melt in the course of explosive volcanism. *Journal of Geophysical Research: Solid Earth*, 102(B1), 803–814. <https://doi.org/10.1029/96JB02935>
- Zimanowski, B., Wohletz, K., Dellino, P., & Büttner, R. (2003). The volcanic ash problem. *Journal of Volcanology and Geothermal Research*, 122, 1–5. [https://doi.org/10.1016/S0377-0273\(03\)00045-0](https://doi.org/10.1016/S0377-0273(03)00045-0)
- Zrelak, P. J., Pollock, N. M., Brand, B. D., Sarocchi, D., & Hawkins, T. (2020). Decoding pyroclastic density current flow direction and shear conditions in the flow boundary zone via particle-fabric analysis. *Journal of Volcanology and Geothermal Research*, 402, 106978. <https://doi.org/10.1016/j.jvolgeores.2020.106978>
- Zwaan, F., et al. (2022). Analogue modelling of basin inversion: A review and future perspectives. *Solid Earth*, 13, 1859. <https://doi.org/10.5194/se-13-1859-2022>

Appendix A - Supplementary Material for Chapter 3

Supplementary Material 3A

Geomechanical data (BTD, SAoR, DAoR) for V1 – 6 (Tung 1 – 6) can be found under Walding et al., 2024 Supplementary Material B. GitHub (https://github.com/nwalding/Walding-et-al.-2024_SupplementaryMaterial).

Supplementary Material 3B

Online Resource 3B.1 ([Cohesional behaviours in pyroclastic material and the implications for deposit architecture | Bulletin of Volcanology \(springer.com\)](#)) Pocketing features in the deposit followed by explosive channelling. Annotated frames are seen in Fig 3.5c and d.

Online Resource 3B.2 ([Cohesional behaviours in pyroclastic material and the implications for deposit architecture | Bulletin of Volcanology \(springer.com\)](#)) Drying profile throughout the deposit followed by explosive cracking. Annotated frames are seen in Fig 3.5e.

Appendix B - Supplementary Material for Chapter 4

Supplementary Material 4A

Experimental Methodology

Bulk and tapped densities

Bulk and tapped density measurements assess the mass and volume relationships of powdered or granular material, both in their initial and compacted states, respectively (Amidon et al. 2017). Tapped density experiments reveal the maximum achievable density through packing. Changes in bulk and tapped density measurements can be influenced by the cohesive properties of particles (Deb et al. 2018) and can be affected by the shape and size of the material (Amidon et al. 2017). Given the irregular and angular characteristics of volcanic ash (Table 4.1), it is important to note that not all interstitial spaces between particles are eliminated. In this study, we determined the bulk and tapped density of dry samples to characterize their cohesivity before the introduction of water, following the methodology outlined in the United States Pharmacopeia from 2015.

Bulk density (ρ_b) was obtained by pouring 100 g of the volcanic material into a 250 mL cylinder and levelling it as needed. The unsettled volume was measured, and bulk density was calculated using Equation S4A. 1. This procedure was repeated three times for each sample.

$$\rho_b = \frac{m}{V_o} \quad [S4A.1]$$

$m = \text{mass (g)}$

$V_o = \text{unsettled apparent volume (mL)}$

To calculate tapped density, the cylinder was tapped at a rate of 150 taps per minute, with volume measurements taken every minute until it reached a stable level. The tapped density (ρ_t) is calculated from the unsettled apparent volume and the final tapped volume, (Eq. S4A. 2), where m is *mass (g)*, V_o is the *unsettled apparent volume (mL)* and V_f is the *final tapped volume (mL)* (Moondra et al. 2018).

$$\rho_t = \frac{m}{V_f} \quad [S4A. 2]$$

$m = \text{mass (g)}$

$V_f = \text{final tapped volume (mL)}$ (Moondra *et al.* 2018)

Important parameters for understanding flowability behaviours can be calculated from the bulk and tapped density results. The Carr's Index (CI; Eq. S4A.3) and Hausner Ratio (HR; Eq. S4A.4) serve as indicators of a material's flowability and interparticulate behaviours (Hausner, 1981) and are valuable tools for assessing a material's ability to fluidise and flow (see Table S4A.1). Carr's Index assesses a material's strength and compressibility (Moondra *et al.* 2018), while the Hausner Ratio gauges the packing density of the material and its susceptibility to compaction from external forces (Yu and Hall, 1994; Abdullah and Geldart, 1999). A low Hausner Ratio suggests better flowability.

$$CI = 100 \left(\frac{\rho_t - \rho_b}{\rho_t} \right) \quad [S4A. 3]$$

$$HR = \frac{\rho_t}{\rho_b} \quad [S4A. 4]$$

Table S4A.1 Correlation between Carr's Compressibility Index, the Hausner Ratio, and flowability characteristics. From (Gorle and Chopade, 2020).

CI	HR	Flowability
≤ 10	1.00 – 1.11	Excellent
11 – 15	1.12 – 1.18	Good
16 – 20	1.19 – 1.25	Fair
21 – 25	1.26 – 1.34	Passable
26 – 31	1.35 – 1.45	Poor
32 – 37	1.46 – 1.59	Very Poor

> 38	>1.60	Very Very Poor
------	-------	----------------

Angle of repose

This method involves determining the Static Angle of Repose (SAoR) to assess the flowability of a material (Al-Hashemi and Al-Amoudi, 2018). The SAoR is related to the static friction coefficient and angle of internal friction of a material and the results of Angle of Repose analysis can be used to understand the flowability of the material (Table S4A.2).

Table S4A.2. Flowability assessment using angle of repose results (Beakawi Al-Hashemi & Baghabra Al-Amoudi, 2018).

Flowability	Angle of Repose (°)
Very free flowing	< 30
Free flowing	30 - 38
Fair to passable flow	38 - 45
Cohesive	45 - 55
Very Cohesive (non-flowing)	> 55

To determine the SAoR, 100 g of material was released from a funnel held 3.5 cm over a circular platform with an average diameter of 8.5 cm. The height of the cone formed by the material is measured and the angle of repose is calculated using Equation S4A.5 (Jan et al. 2015). Where the material does not release freely from the funnel, it is lightly agitated to facilitate release. Where the height of the cone reaches the base of the funnel, the funnel was moved incrementally to accommodate the growing cone. This process is repeated three times.

$$SAoR (^{\circ}) = \tan^{-1} \frac{2h}{D} \quad [S4A. 5]$$

$h = \text{height (mm)}$

$D = \text{base diameter (mm)}$

Supplementary Material 4B

Excel Spreadsheet of all geomechanical data and uncertainty/error calculations in measurements for the experiments is available on GitHub

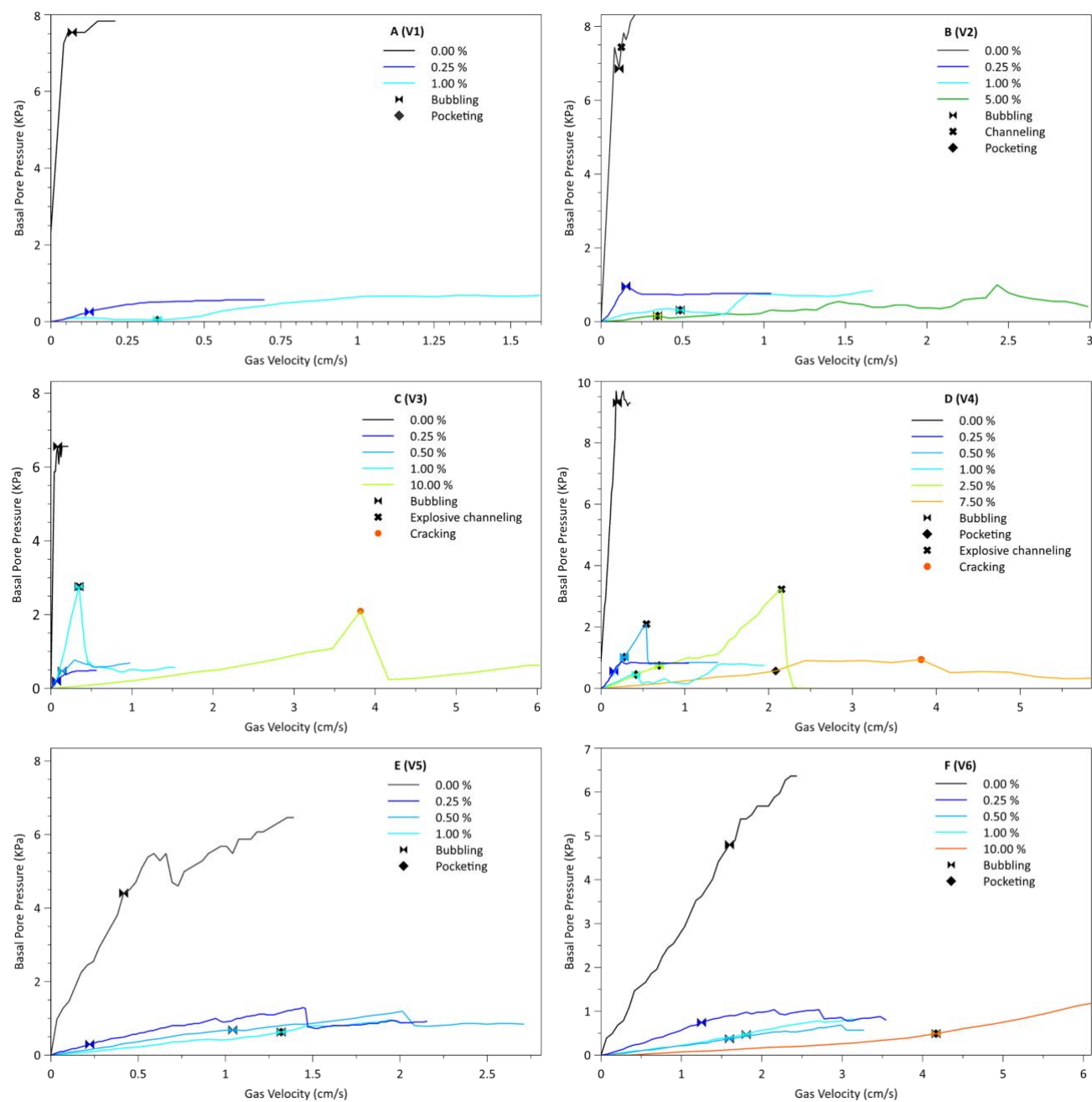
(https://github.com/nwalding/Walding-et-al.-2024_SupplementaryMaterial).

Supplementary Material 4C

Fluidisation videos showing diffusive cracking behaviour observed in the fluidisation experiments of material. Colima 0.5 wt.% moisture. Other fluidisation videos can be found in the Google Drive link on GitHub (https://github.com/nwalding/Walding-et-al.-2024_SupplementaryMaterial).

Supplementary Material 4D

Figure S4D.1: Fluidisation profiles of Tung 1 to 6 (V1 – V6 in Chapter 3) with increasing moisture (0.00 – 10.00 %). Symbols show gas escape structure formation



Supplementary Material 4E

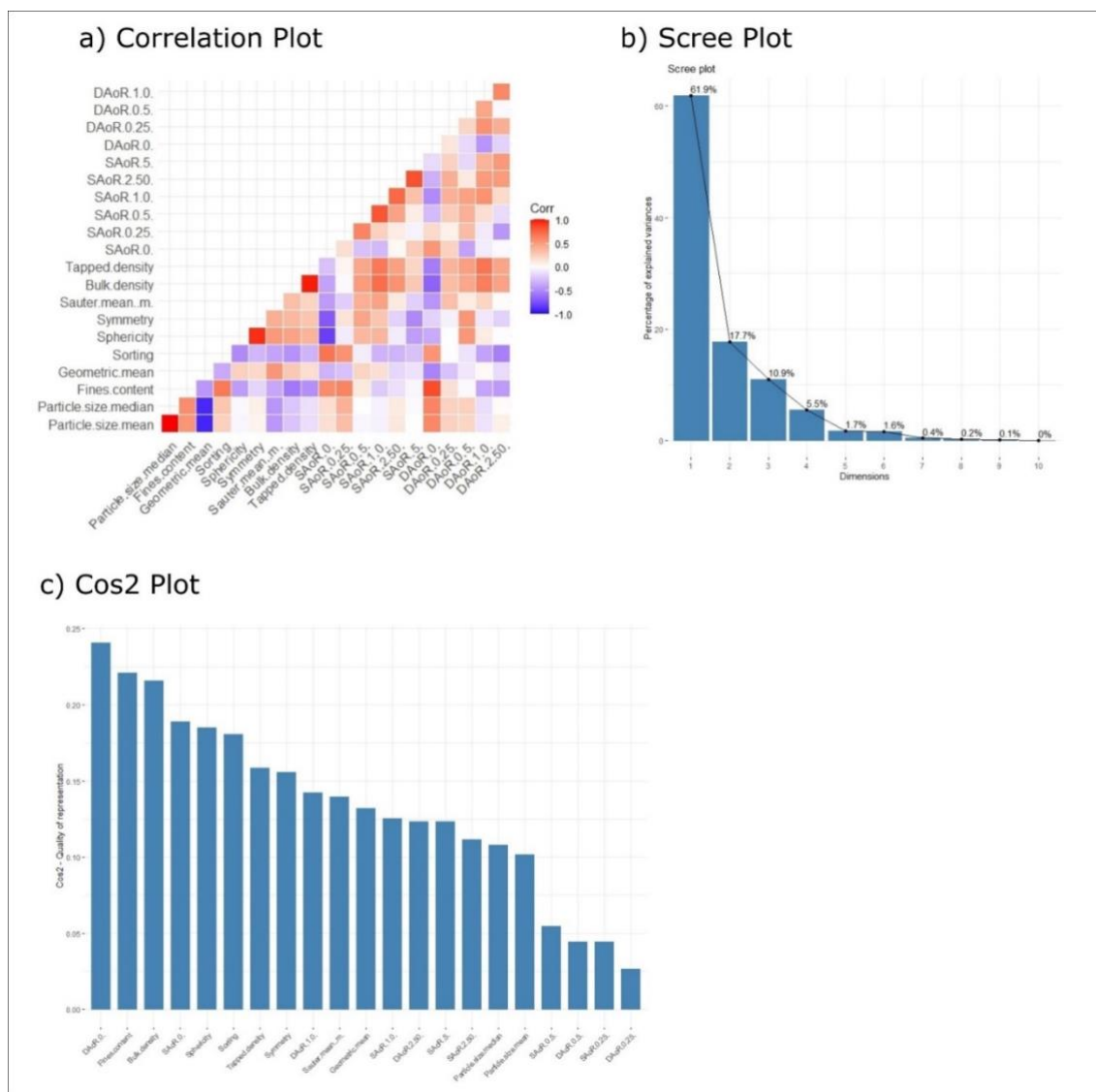


Figure S4E.2 a) the correlation plot shows the result of the correlation matrix (i.e., how related the results are) with the higher value (1) being more closely related than the lower value (0). B) the scree plot shows that the first 2 components can be considered the most significant since they contain a total of 80 % of the total information of the data. C) Cos2 calculations show how much of each variable is represented in each component. The higher the value, the overall better representation of the variable on that component.

Appendix C - Supplementary Material for Chapter 5

Supplementary Material 5A:

Table S5A.1: Accretionary lapilli and pellet description of Brown et al, (2010, 2012) shown against the descriptions used within this work. See Brown et al. (2010, 2012) and references therein for detailed overview.

Aggregate name	Description	This study
PC1	Fragile, irregular-shaped ash clusters. Poorly preserved in ash fall deposits.	
PC2	Fragile coated particles covered in fine ash particles. Poorly preserved in ash fall deposits.	
AP1	Massive or poorly structured pellets. Subspherical or slightly oblate in shape. Can show compaction, disaggregation or fragmentation. Clast-supported fall deposits	Ash Pellets
AP2	Subspherical core surrounding by thin concentric ash laminae. Found in PDC flow deposits and rare in clast-supported fall layers.	Accretionary Lapilli
AP3	Ash particles formed from liquid drops.	

Supplementary Material 5B:

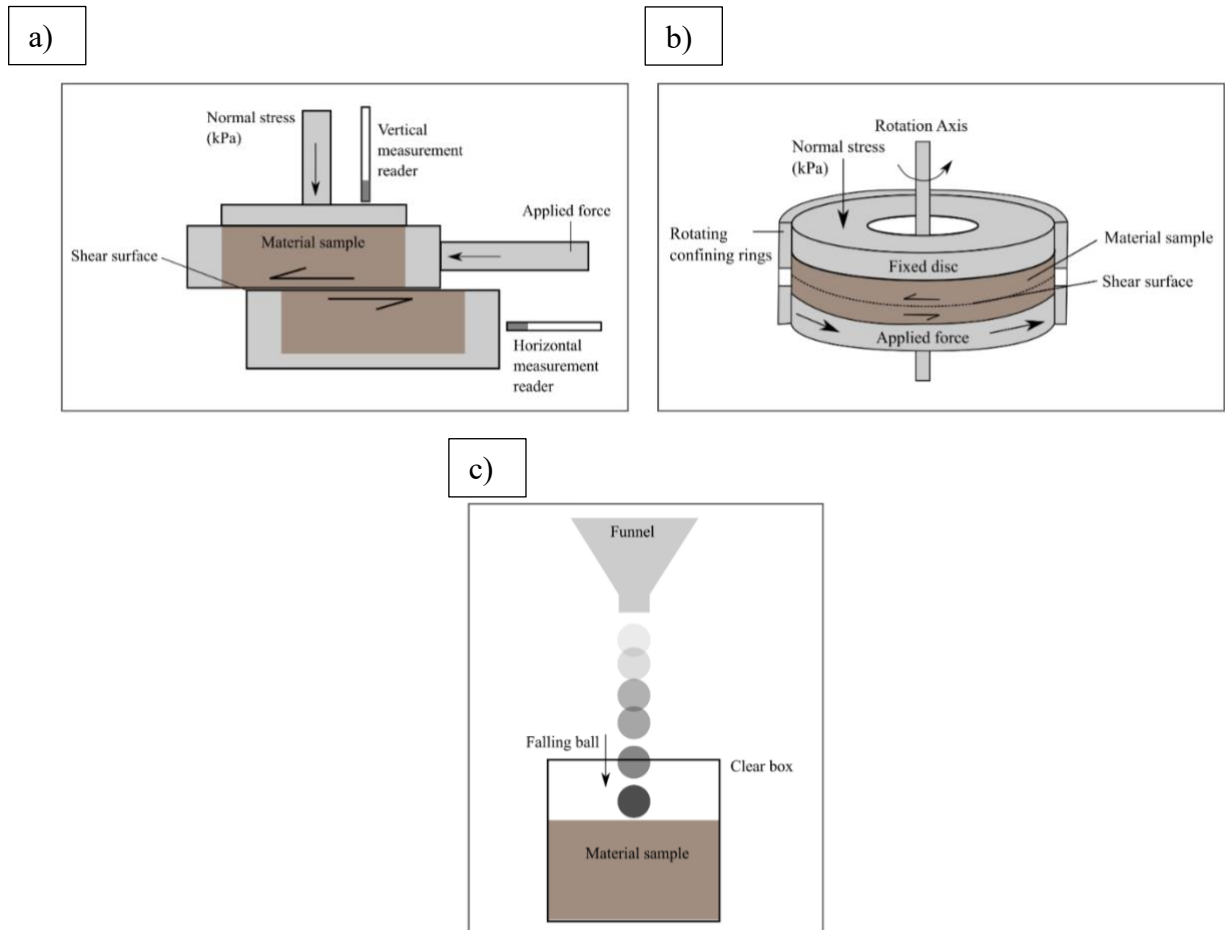
Table S5B.1: Lithofacies name, description and interpretation of formation of the material observed in this work.

Lithofacies Name	Description	Interpretation
MTacc/dsTacc	Massive fine to coarse ash with frequent to abundant accretionary lapilli. Accretions of fine concentric ash rings surround a core. Poorly to moderately sorted. Range from 3 to 30 mm in size. (Note T= Tuff; used here for units comprising > 20 % ash, ds = diffusely stratified)	Aggregates of ash formed initially as pellets in a moist co-ignimbrite cloud or in areas of high electrostatic attraction. As the pellet falls into the lower regions of a PDC, it is thermally lofted, forming thin concentric ash layers around the core, becoming accretionary lapilli.
T	Fine to coarse lithofacies, predominantly ash (< 2 mm) with subordinate lithic and pumice clasts. (Note Tuff used for units comprising > 50 % ash, Le Maitre et al., 2002)	“Dry” fallout of ash associated with dilute PDC.
mLT / LT/ILT	Poorly sorted fine to coarse ash with sub-angular to sub-rounded lithic and pumice lapilli. Can be massive lapilli tuff or stratified in nature. (Note Tuff used for units comprising < 50 % ash)	Deposition from the main body of a pyroclastic density current.
mpL	Massive lapilli deposit. Lapilli are angular to subangular pumice.	Pumice fall deposit from eruption column fallout.
pelT	Well sorted layers (~10 cm) of ash pellets less than 10 mm in diameter. Pellets do not show concentric laminations.	Pellets formed by the sticking together of ash by moist co-ignimbrite cloud.
lBr	Lithic-rich (> 50 wt.%) deposit. Poorly sorted, comprising ash (2 mm) to boulder (> 64 cm) sized lithics. Angular to rounded in nature.	Lithic-rich deposition from the main body of a high-energy pyroclastic density current.

Le Maitre, R. W., Streckeisen, A., Zanettin, B., Le Bas, M. J., Bonin, B., Bateman, P., & Lameyre, J. (2002). *Igneous rocks. A classification and glossary of terms*, 2. Cambridge University Press.

Supplementary Material 5C

Figure S5C.1 of schematic figures showing the configuration and set-up of the a) direct shear box b) ring shear c) drop test experimental methods used in this work. Direct shear box figure adapted from Wijeyesekera et al., 2013. Ring shear figure adapted from Sadrekarimi and Olson, 2009.

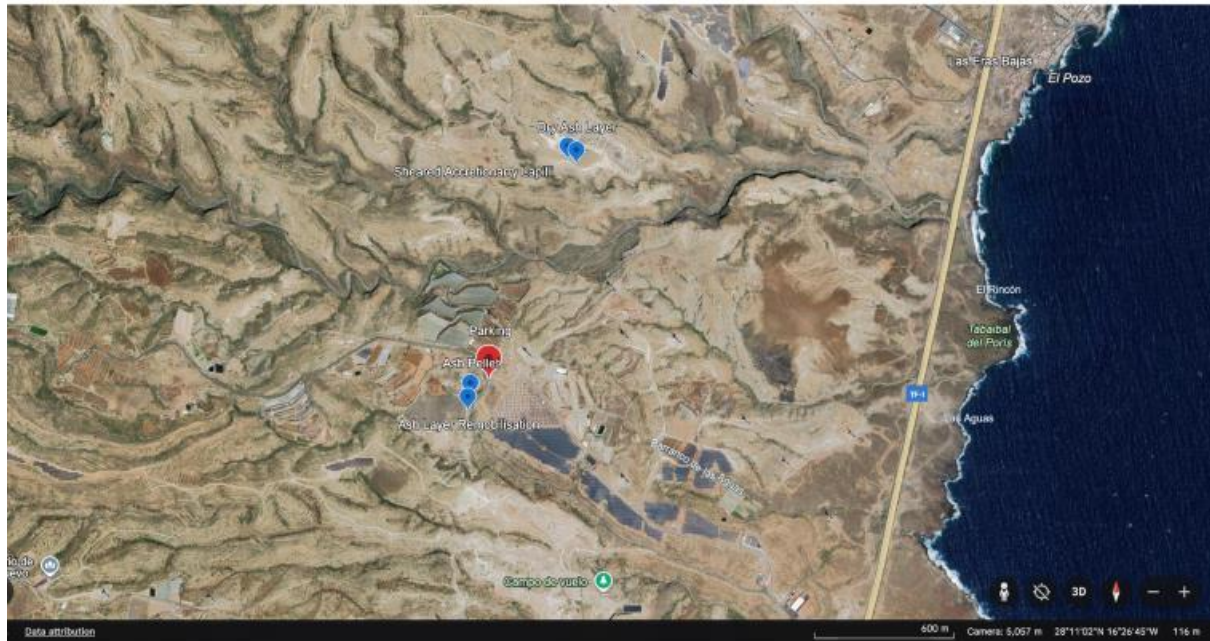


Sadrekarimi, A., & Olson, S. M. (2009). A new ring shear device to measure the large displacement shearing behavior of sands. *ASTM International, Geotechnical Testing Journal*, 32(3), 197–208. <https://doi.org/10.1520/GTJ101733>

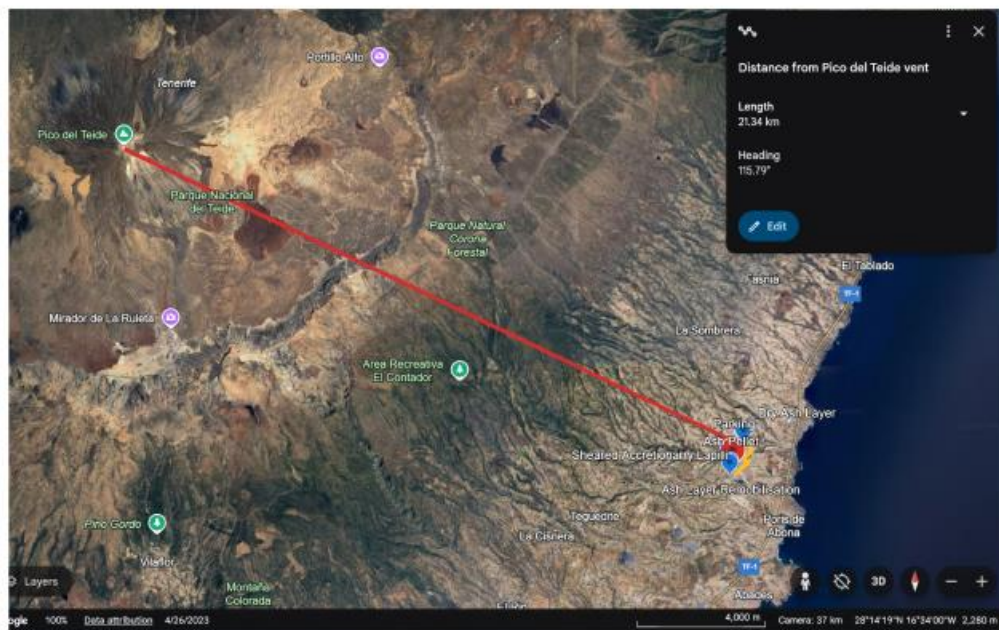
Wijeyesekera, D. C., Siang, A. J. L. M., & Yahaya, A. S. B. (2013). Advanced statistical analysis for relationships between particle morphology (size and shape) and shear (static and dynamic) characteristics of sands. *International Journal of Geosciences*, 4(10A). <https://doi.org/10.4236/ijg.2013.410A004>

Supplementary Material 5D:

All Localities



Deposits - distance from vent



Dry Ash Layer - Get to



Deposit Overview



Location at Montana Magua. Camera is facing East. Arrow points to roughly where the dry ash layers are. Nemi is ~ 1.65 m tall.

Supplementary Material 5E:

Sheared Accretionary lapilli layer - Get to



Deposit Overview



Location at Montana Magua. Camera is facing North West. Arrow points to roughly where the sheared layers are. No Scale.



Location at Montana Magua. Camera is facing East. Arrow points to roughly where the sheared layers are. Nemi is ~ 1.65 m tall.

Supplementary Material 5F:

Ash Pellet Layer - Get to



Ash remobilisation layer on quarry wall. Arrow points to roughly where the layer is. Road direction is towards the South. Matt is ~ 2.00 m tall and is holding a 1.00 m scale.

Supplementary Material 5G:

Ash Remobilisation Layer,- Get to

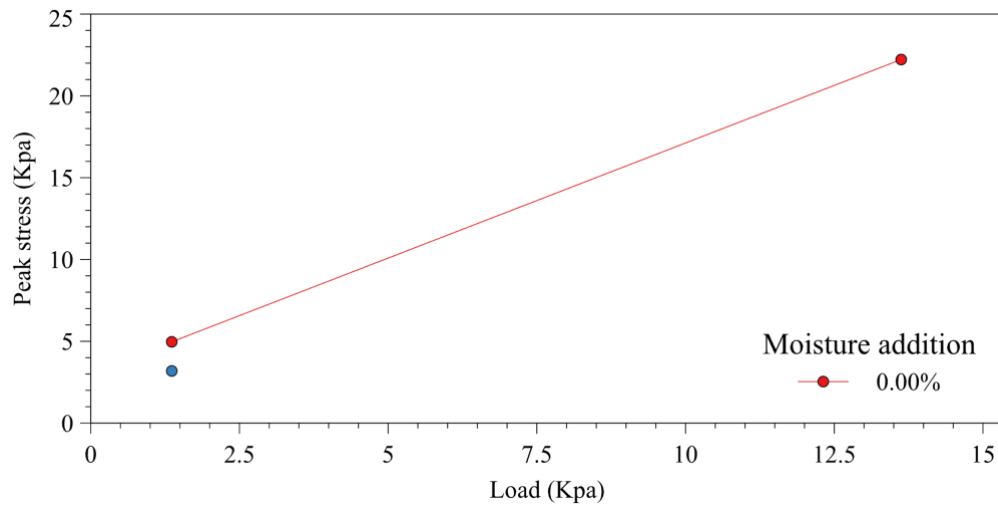


Ash pellet layers on quarry wall. Arrow points to where the upper pellet layer is. Road direction is towards the South. Matt is ~ 2.00 m tall.

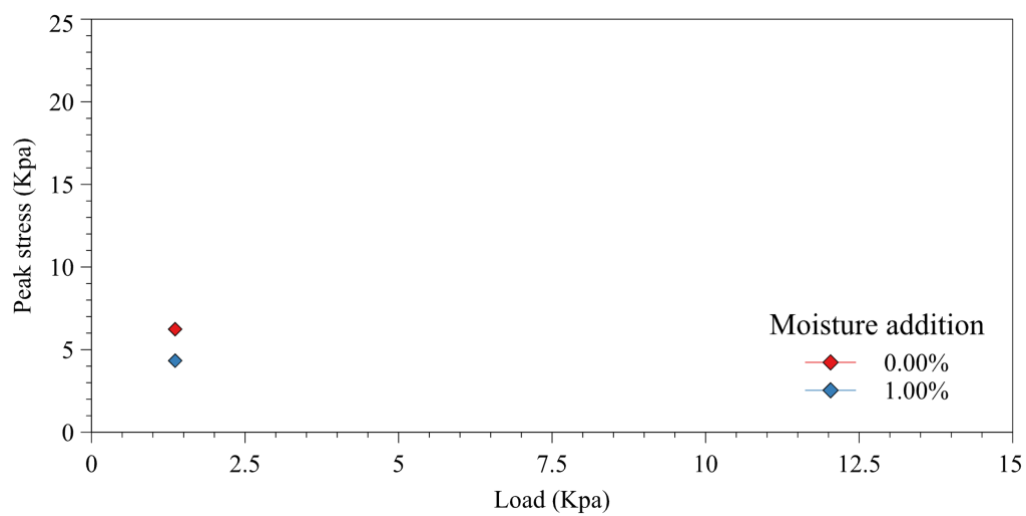
Supplementary Material 5H:

Figure S5H.1 showing the results from the a) 0.5 mm/min tests (circle) and b) 1 mm/min tests (diamond) on Colima sample. Results both show similar peak stress values, even though a full suite was unable to be completed due to time constraints. Therefore, we can conclude that shear rate is not affecting our results.

a)



b)



Supplementary Material 5I:

The samples used ranged in size and sorting parameters (Table 2). Tung 1 (V1), Tung 4 (V4), Tung 5 (V5) (Fig. S5I.1) all display similar peak shear stress values across all moisture addition and all load weights. This is reflected in the Mohr-Coulomb results as consistent (i.e., within range of natural variation) cohesion and internal friction values (Fig. S5I.1). All samples showed similar sphericity and symmetry values, which may suggest that these parameters have a significant control on the shearing behaviour of material. During shearing, the results showed a decrease in vertical displacement and compaction across all samples and moistures.

The results from the direct shear test gave inconclusive results on the effect of moisture on shear stress. It was determined that the peak shear result was not being reached in the experiments due to the limited shear distance available in the apparatus or due to the material being used. Therefore, the use of the ring-shear on a wider variety and finer range of samples was adopted to shear the material for a large distance in hopes of obtaining clearer peak shear stress values.

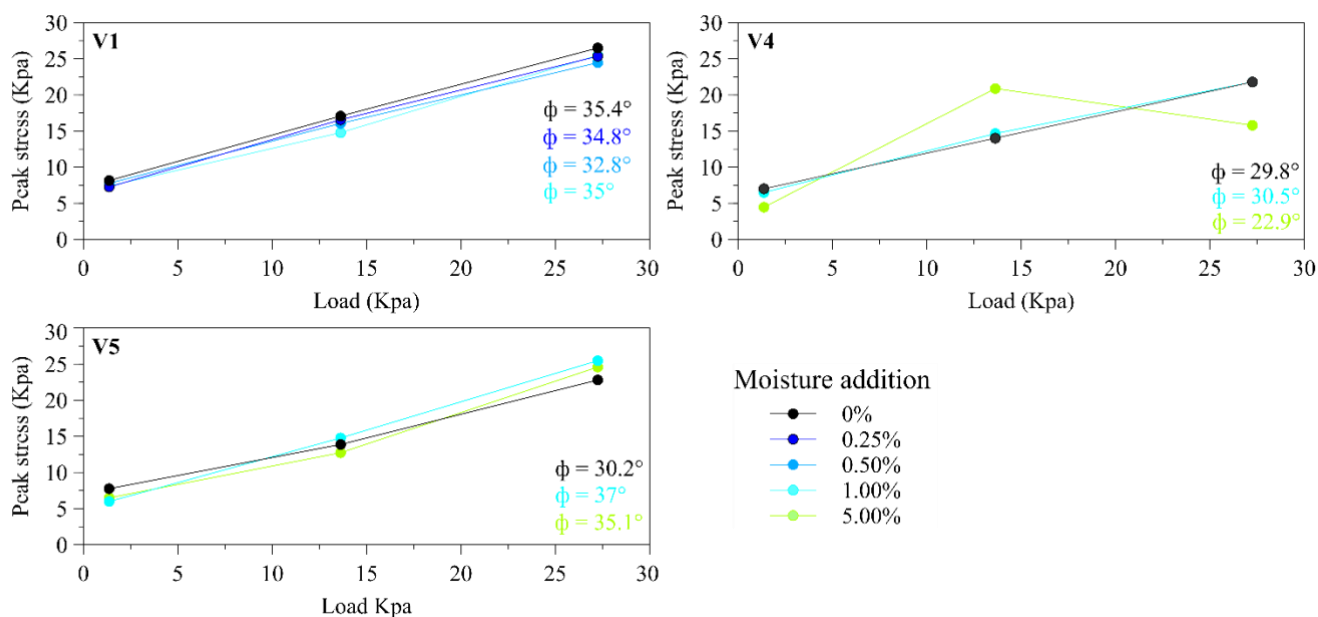


Figure S5I.1 showing the Mohr-Coulomb analysis of the peak shear results for Tung 1(V1), Tung 4 (V4) and Tung 5 (V5) at 0, 0.25, 0.50, 1 and 5 wt.% moisture and where ϕ is the angle of internal friction value.

Supplementary Material 5J

Table S5J.1 This table shows ball penetration depth (mm), ball bounce height (mm), and shear thickening with increasing moisture. ‘-’ is where the ball does not bounce off the deposit. SD = Standard Deviation.

Sample Name	Moisture (%)	Ball Penetration Depth (mm)	Ball Bounce Height (mm)	Shear Thickening
Atitlan 1	0	40 (SD = 0)	-	-
	15	40 (SD = 0)	-	-
	30	28 (SD = 2.4)	-	-
	40	26 (SD = 1.9)	-	-
	50	40 (SD = 0)	-	-
Colima	0	40 (SD = 0)	-	-
	15	35 (SD = 1.2)	-	-
	25	33 (SD = 3.6)	-	-
	30	40 (SD = 0)	-	-
Taupo 1	0	40 (SD = 0)	-	-
	15	33 (SD = 2.2)	-	-
	40	20 (SD = 3.3)	-	-
	50	19 (SD = 4.1)	6	Yes
	60	40 (SD = 0)	-	-
Taupo 2	0	40 (SD = 0)	-	-
	15	40 (SD = 0)	-	-
	40	31 (SD = 0.5)	-	-
	70	14 (SD = 2.4)	6.5	Yes
	90	40 (SD = 0)	-	-

Tung 6	0	39 (SD = 0.9)	-	-
	15	40 (SD= 0)	-	-
	30	38 (SD = 0.5)	-	-
	40	32 (SD = 0.8)	-	-

Supplementary Material 5K:

Uncertainty and Error for the direct shear, ring shear and drop tests can be found here:
<https://github.com/nwolding/SupplementaryMaterial-5K>

Appendix D - Supplementary Material for Chapter 6

Supplementary Material 6A

Particle size analyses of the sample were performed using a CAMSIZER X2 (University of Bristol), which utilizes particle imaging to determine both the shape and size characteristics of dry materials. The CAMSIZER X2 offers a maximum resolution of 0.8 μm per pixel.

The sphericity (SPHT) of particles is calculated using Eq. S6B. 1, where P represents the measured circumference of the particle, and A represents the area projected by the particle. A perfect sphere would have an SPHT value 1 (Liu et al., 2015).

$$SPHT = \frac{4\pi AP}{U^2} \text{ (S6B.1)}$$

Symmetry is measured by how evenly the particle is distributed around its centreline, with perfectly symmetrical particles having a value of 1, while asymmetrical particles have values less than 1. The particle size and shape data obtained from the CAMSIZER were further processed using GRADISTAT (Blott and Pye, 2001) to analyse particle characteristics. This was done through the moments' method (Inman, 1952) to compute parameters such as the logarithmic and geometric mean $((\bar{x}) \Phi)$, median (Φ) , range (μm), sorting index $((\sigma) \Phi)$, sorting (σG) , skewness $((Sk) \Phi)$, kurtosis $((K) \Phi)$, and the geometric mean (μm).

The Sauter mean diameter (D_{32}) was also calculated, representing the mean particle diameter in relation to the surface area and volume of the particles, and is calculated using Eq. S6B. 2 (Breard et al., 2019).

$$D_{32} \text{ (mm)} = 2 - [\mu_m(\Phi) + \frac{\ln 2}{2} \sigma^2(\Phi)] \text{ (S6B.2)}$$

Here, μ_m is the geometric mean, and σ^2 is the geometric standard deviation (Eq. S6B. 1, Breard et al., 2019 ,in Φ units). Following the methodology outlined in Breard et al. (2019), the D_{32} (mm) and fine content ($< 63 \mu\text{m}$, %) of the material was calculated.

Table S6B.1 Material properties of ballotini used in these experiments. These include logarithmic particle size mean and particle size median, particle range, fines content ($< 63 \mu\text{m}$), geometric mean (Φ), and employ the method of moments for calculating mean, sorting, sphericity, symmetry, skewness, and kurtosis. The Sauter mean diameter is computed

following the methods outlined in Breard et al (2019). The Geldart Group Classification (Geldart, 1973) is also determined based on the logarithmic mean particle size.

Material	Particle Size Mean (\bar{x}) \emptyset	Particle Size Median \emptyset	Particle Size Range (μm)	Fine s Content (%)	Sorting Index (σ) \emptyset	Sorting (σ_G)	Sphericity	Symmetry	Skewness (Sk) \emptyset	Kurtosis (K) \emptyset	Sauter Mean (mm)	Geometric Mean (μm)	Geldart Group
Ballotini	3.43	3.61	20 - 655	14.78	0.62	Moderately Well Sorted	0.90	0.93	-0.46	4.72	0.08	92.7	A, B, C

Supplementary Material 6B

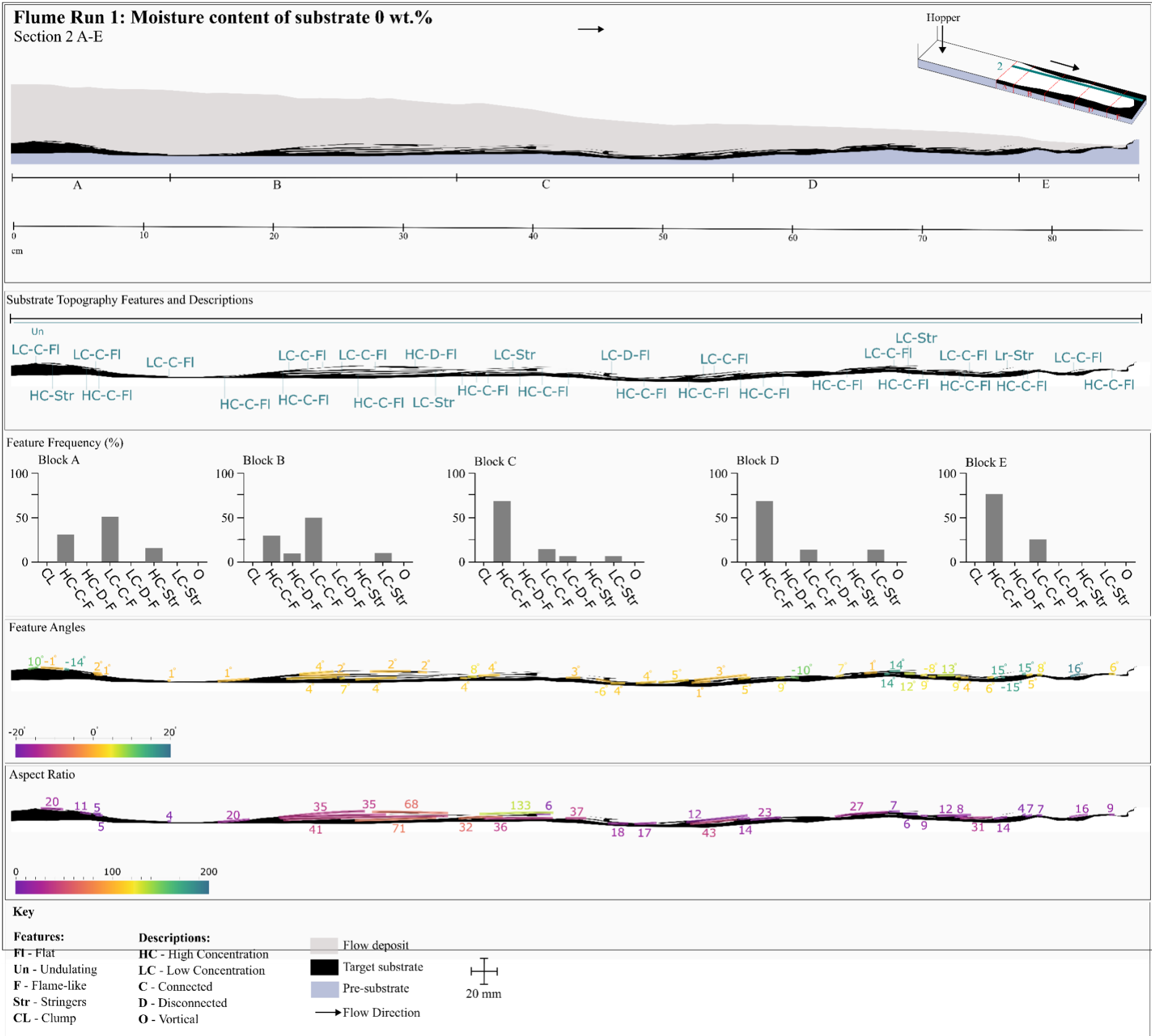
Method: Dyeing Ballotini

- 10 kg ballotini was weighed and then water was added until the ballotini was completely saturated.
- ~250 mL of acrylic paint was added to the mixture and mixed thoroughly.
- Material was set in an oven at 80 ° for up to 48 hours.
- Once dried, the material was manually broken apart and sieved to remove clumps.
- A “dye transfer test” should then be completed to check the bleed of the dyed ballotini. To do this, a clear beaker should be filled with the un-dyed ballotini, and then the dyed ballotini mixture added on top. Slowly pour water onto the sample and note any significant dye transfer.
- If there is any dye transfer, then the dyed ballotini may benefit from being washed in water and dried out again to remove any remaining paint pigment.

It should be noted that the process of dyeing the ballotini may in turn effect the properties of individual particles (e.g., their roughness, size, interactions etc.). This could in turn effect the bulk behaviour of the ballotini material being used. Due to time constraints this was not explored. Future work would benefit from looking at various dyeing techniques on the particle properties of the ballotini used.

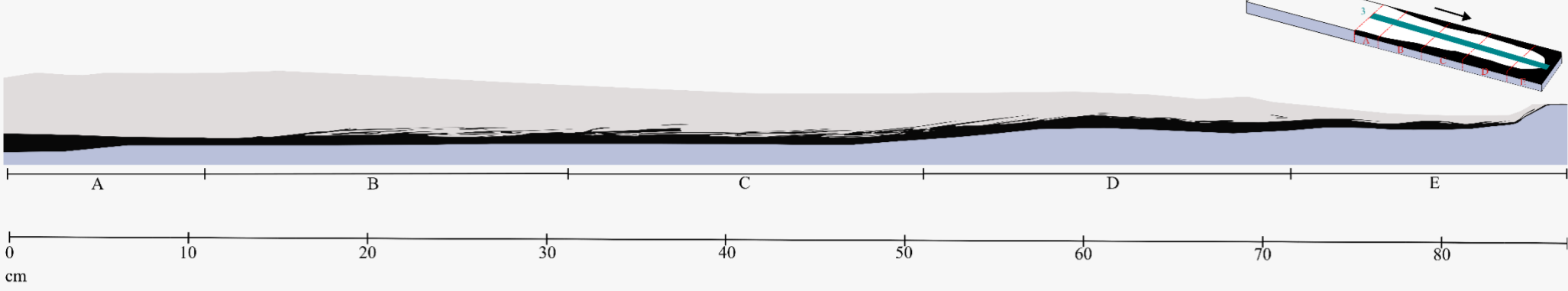
Supplementary Material 6C

Figure S6C.1 Flume Run 1: Dry (0 wt.%) substrate panels showing a) section 2 and b) 3.

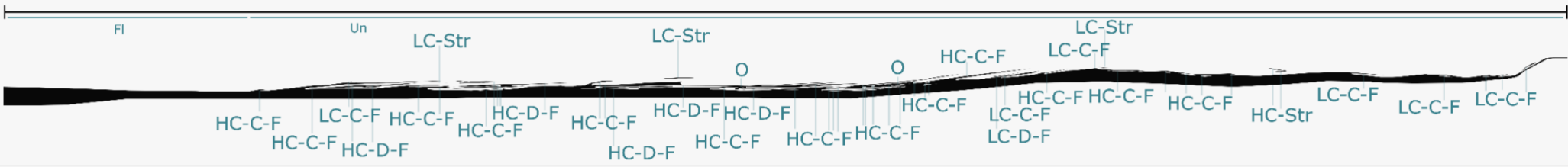


Flume Run 1: Moisture content of substrate 0 wt.%

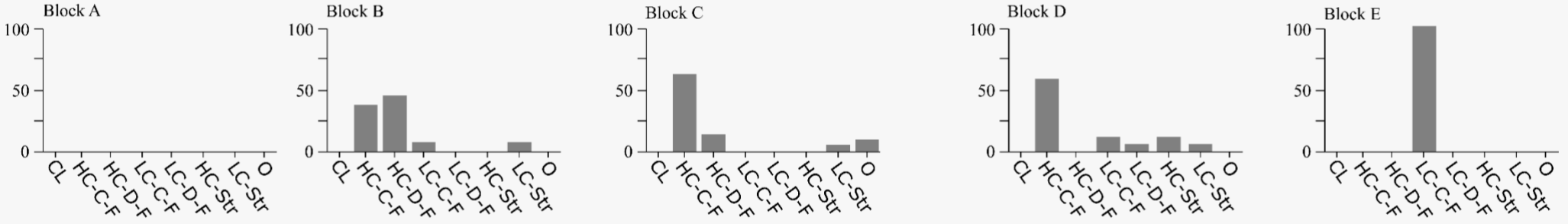
Section 3 A-E



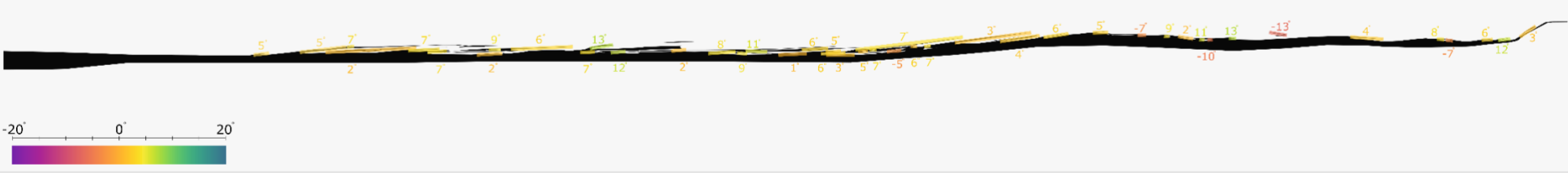
Substrate Topography Features and Descriptions



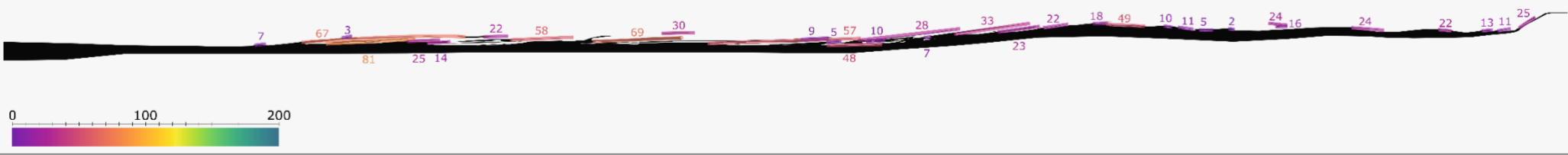
Feature Frequency (%)



Feature Angles



Aspect Ratio

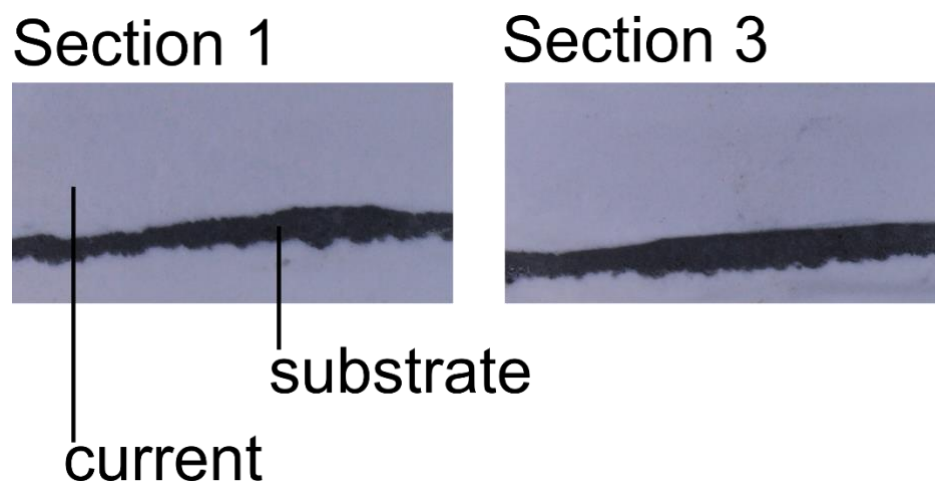


Key

Features:	Descriptions:	
FI - Flat	HC - High Concentration	Flow deposit
Un - Undulating	LC - Low Concentration	Target substrate
F - Flame-like	C - Connected	Pre-substrate
Str - Stringers	D - Disconnected	Flow Direction
CL - Clump	O - Vortical	

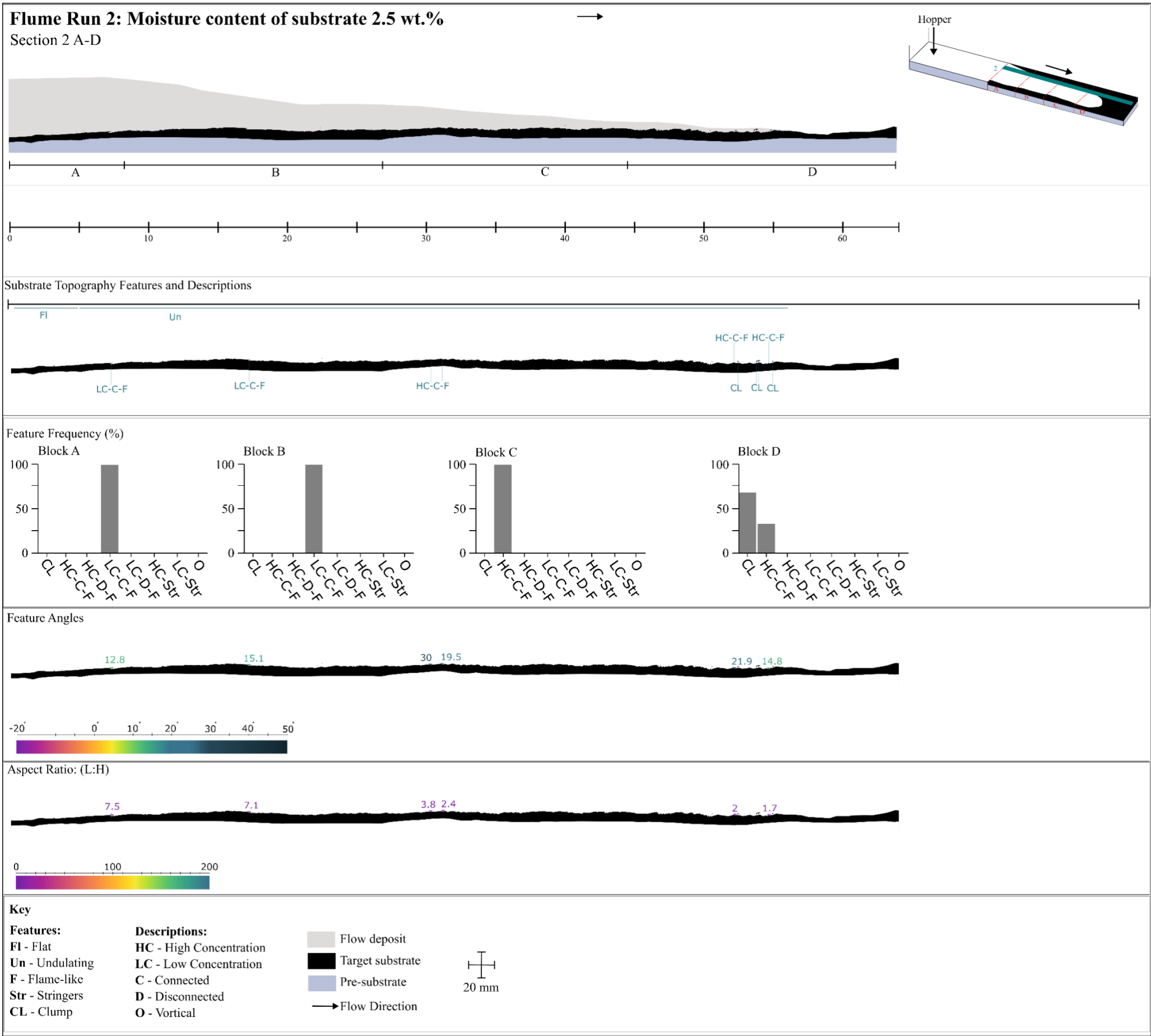
Supplementary Material 6D

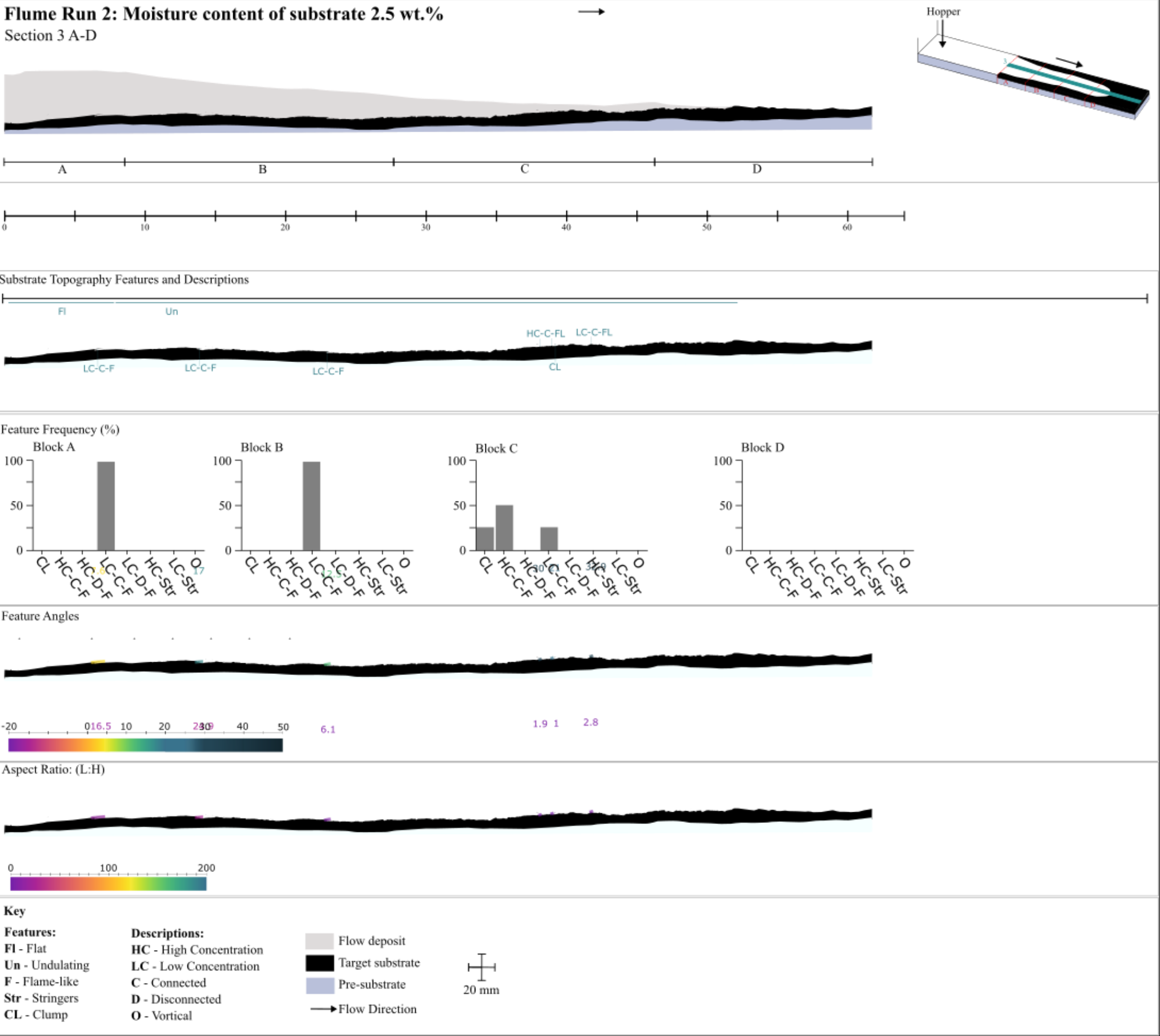
Figure S6D.3 1 current-substrate contact at a) section 1 (side-wall) where small topographic depressions are seen and b) section 3 where small topographic depressions have been sheared resulting in a planar contact.



Supplementary Material 6E

Figure S6E.2 Flume Run 2: Dry (2.5 wt.%) substrate panels showing of section a) 2 and b) 3.





Supplementary Material 6F

Videos of currents can be found here:

<https://drive.google.com/drive/folders/1gaQR7gbiFMe2yfv1Jjq-wlqV21FUQYgJ?usp=sharing>

Supplementary Material 6G

Figure S6G.4 Flume Run 1, 0 wt.% substrate. Pulse initiation, propagation and overtaking of the flow front.

